UNIVERSITÀ DEGLI STUDI DI PADOVA

UNIVERSITÀ DEGLI STUDI DI PADOVA

DIPARTIMENTO DI INGEGNERIA INDUSTRIALE

SCUOLA DI DOTTORATO DI RICERCA IN
SCIENZA ED INGEGNERIA DEI MATERIALI
CICLO XXV

Study and development of high release refractory materials for the SPES project

Direttore della Scuola :
CH.MO PROF. GAETANO GRANOZZI

Supervisori :
CH.MO PROF. PAOLO COLOMBO
CH.MO DR. ALBERTO ANDRIGHETTO

Dottorando :
STEFANO CORRADETTI

CONTENTS

Introduction 1

Introduzione 3

Chapter 1 The SPES project for the production of Radioactive Ion Beams

1.1. Introduction 5

1.2. Radioactive Ion Beams production 8

1.2.1. The In-Flight Separation technique 9

1.2.2. The Isotope Separation On-Line technique 10

1.3. The SPES project at LNL 13

1.4. Applications of Radioactive Ion Beams research 18

1.4.1. Nuclear physics 18

1.4.2. Nuclear astrophysics 19

1.4.3. Solid state physics 20

1.4.4. Nuclear medicine 20

Chapter 2 The SPES target

2.1. General aspects of an ISOL target 23

2.1.1. Isotopes production in an ISOL target 23

2.1.2. Isotopes release from an ISOL target 25

2.1.3. Diffusion and effusion 28

2.1.4. ISOL target requirements 31

2.1.5. Materials for ISOL targets 34

2.2. The SPES target 36

2.2.1. The target layout 36

2.2.2. The target performance 40

Chapter 3 The SPES UC_X target for the production of neutron-rich isotopes

3.1. Introduction: carbides 43

3.2. Uranium carbide 46

3.2.1. General properties 46

3.2.2. Synthesis 48

3.2.3. Thermal properties 49
3.2.4. Reactivity 52
3.2.5. Uranium carbide as a ISOL target 53
3.3. On-line test of SPES UC_X target prototypes at HRIBF 55
3.3.1. Introduction: the OLTF at HRIBF 55
3.3.2. Target – ion source (TIS) system at OLTF 57
3.3.3. 1st test at HRIBF: "Standard" UC_X target prototype 59
3.3.4. 2nd test at HRIBF: "Low density" UC_X target prototype 77
3.4. Towards new UC_X on-line tests: a "medium density" target prototype 92
3.5. Conclusions 94

Chapter 4 Targets for the production of proton-rich isotopes at SPES

4.1. Introduction 97
4.2. Boron carbide targets for the SPES project 100
4.2.1. Boron carbide 101
4.2.2. B_4C SPES target prototypes 107
4.3. Lanthanum carbide targets: from standard synthesis to foams production 122
4.3.1. Lanthanum carbide 122
4.3.2. A complete LaC_X SPES target prototype 124
4.3.3. Lanthanum carbide foams 132
4.4. Conclusions 148

Conclusions 151

Appendix A Yield calculation with γ-ray spectrometry

A.1. Experimental setup 153
A.2. Yield calculation 154

Appendix B Thermal conductivity estimations for refractory materials

B.1. Experimental setup 157
B.2. Direct and inverse problem description 158
B.3. Thermal conductivity of graphite samples 161

References 165

Introduction

Throughout the last century, theoretical and experimental research made by the international nuclear physicists community has led to important advancement in the knowledge of the mechanisms that govern the behavior and stability of the nuclei. The technological improvements necessary to support this research has often opened the way to new applications in other field of science and industry which directly reflects in our common life experience.

Nowadays, Europe is becoming more and more a leader in both theoretical and experimental nuclear physics, as testified by the presence on its territory of several institutes and laboratories dedicated to this field of research, like CERN (*Organisation Européenne pour la Recherche Nucléaire*), the world's largest particle physics laboratory. Italy, represented mainly by INFN (*Istituto Nazionale di Fisica Nucleare*), is one of the main members of this community.

One of the most important projects supported by INFN is SPES (*Selective Production of Exotic Species*), which aim is to develop a facility for the production of radioactive ion beams (RIBs) in one of the four national laboratories of INFN, LNL (*Laboratori Nazionali di Legnaro*).

The facility is designed to produce and deliver to users both proton-rich and neutron-rich nuclei (range of mass 80-160 amu) to be used for nuclear physics research, as well as other applications in different fields of science. The generation of the aforementioned isotopes will occur inside a properly designed target, which represents the core of the whole project. The choice of the proper material for the target, both in terms of composition and properties, is of vital importance in determining the quantity and type of the produced isotopes.

In this work, the synthesis and characterization of different types of target materials are presented. The results of experimental tests performed on some of the produced materials, in configurations very similar to those intended for the final SPES facility are also reported.

Chapter 1 gives a general overview of the SPES project and its context whereas chapter 2 introduces the main topics related to the on-line behavior of the SPES target, relative to both its layout and to the properties of the material constituting it. Chapter 3 is focused on uranium carbide, which will be used at SPES to produce neutron-rich isotopes; after a description of its main physicochemical properties, the results of two on-line tests performed on target prototypes made of this material is reported and discussed into detail. In chapter 4 the synthesis methods and release-related properties of two potential materials to be used as SPES targets for the production of proton-rich isotopes, boron and lanthanum carbides, are presented.

Introduzione

Nel corso dell'ultimo secolo, la ricerca teorica e sperimentale condotta dalla comunità internazionale in fisica nucleare ha portato ad importanti passi avanti nella comprensione dei meccanismi che governano il comportamento dei nuclei e della loro stabilità. In molti casi, le innovazioni tecnologiche che si sono rese necessarie per supportare tali ricerche hanno aperto la strada verso nuove applicazioni scientifiche ed industriali con ripercussioni dirette nella vita di tutti i giorni.

Attualmente, l'Europa è sempre più leader nel campo della fisica nucleare, teorica e sperimentale, come testimoniato dalla presenza nel suo territorio di svariati istituti e laboratori dedicati a questa specifica area di ricerca, come ad esempio il CERN (Organisation Européenne pour la Recherche Nucléaire), il più grande laboratorio al mondo per la fisica delle particelle. L'Italia, principalmente rappresentata dall'INFN (Istituto Nazionale di Fisica Nucleare), è uno dei principali membri di questa comunità.

Uno dei progetti più importanti finanziato dall'INFN è SPES (Selective Production of Exotic Species), la cui finalità è la costruzione di una facility per la produzione di fasci di ioni radioattivi, in uno dei quattro laboratori nazionali dell'INFN, LNL (Laboratori Nazionali di Legnaro).

La facility è progettata per produrre e fornire agli utenti isotopi proton-rich e neutron-rich (massa compresa fra 80 e 160 amu) utilizzabili per esperimenti di fisica nucleare, ma anche per altre applicazioni in diversi settori scientifici. La formazione di tali isotopi avverrà all'interno di uno specifico bersaglio (target), che rappresenta il cuore dell'intero progetto. La scelta dell'opportuno materiale per il target, sia in termini di composizione che di proprietà è di vitale importanza nel determinare la quantità e tipo di isotopi prodotti.

In questo lavoro, vengono descritte nel dettaglio la sintesi e caratterizzazione di diversi tipi di materiali proposti come target, ed inoltre vengono riportati i risultati di test sperimentali condotti su alcuni di essi, ottenuti in modalità molto simili a quelle a cui saranno sottoposti nella facility SPES.

Il capitolo 1 fornisce una presentazione generale del progetto SPES e del contesto scientifico ad esso legato, mentre nel capitolo 2 viene descritto nel dettaglio il comportamento operativo del target SPES, con particolare riferimento alla sua geometria e alle proprietà del materiale che lo costituirà. Nel capitolo 3 vengono presentate le proprietà del materiale scelto come bersaglio per produrre isotopi neutron-rich, ovvero il carburo di uranio; vengono inoltre

presentati i risultati di un test sperimentale di produzione di isotopi da parte di un prototipo di target SPES costituito di tale materiale. Il capitolo 4 descrive la sintesi e caratterizzazione di carburi di boro e lantanio, con particolare riferimento alle proprietà riconducibili alla capacità di rilascio di isotopi; tali materiali rappresentano dei potenziali target SPES per la produzione di isotopi proton-rich.

Chapter 1

The SPES project for the production of Radioactive Ion Beams

1.1. Introduction

Nuclear physics studies the properties and stability of the atomic nucleus, which concentrates in itself most of the mass of the atom (more than 99.9%). In general terms, a nucleus is composed of nucleons, which can be divided into two categories: positively charged particles (protons, p) and neutral particles (neutrons, n), whose masses are very similar to each other ($1.67 \cdot 10^{-27}$ Kg). These particles are bound together by the strong interaction, the most intense above all the fundamental forces acting in nature – the others are gravitation, electromagnetism and weak interaction - thus guaranteeing the stability of the nucleus.

The effect of the ratio between number of protons (Z) and neutrons (N) in determining the stability of one particular nucleus is well represented in the nuclide chart shown in fig. 1, in which the black squares indicate the stable or extremely long-lived nuclei, forming the so-called "valley of stability" [1]. For low Z, stable nuclei are those with N = Z, since in this case the interaction between protons and neutrons is slightly stronger than the proton-proton and neutron-neutron ones. When the mass number $A \geq 40$ (where $A = Z + N$), the stability curve diverges from the ideal N = Z line towards the nuclei with N > Z (neutron-rich nuclei), because the electrostatic repulsion between protons tend to prevail over the other stabilizing forces, so that more neutrons – which are non-charged particles not contributing to electrostatic repulsion – are needed to stabilize the nucleus. For extremely high values of A, and consequently very big atomic radii, strong interaction tend to lose its efficacy with respect to electrostatic repulsion, thus drastically limiting the stability of the so-called Super Heavy Elements (SHE).

Nuclei with the same number of protons – so nuclei of the same element - but with different number of neutrons are called isotopes, and to distinguish between them one must indicate clearly their mass number, in the form ${}^{A}_{Z}E$, where E is the element symbol and Z is optional since it is univocally associated to the element.

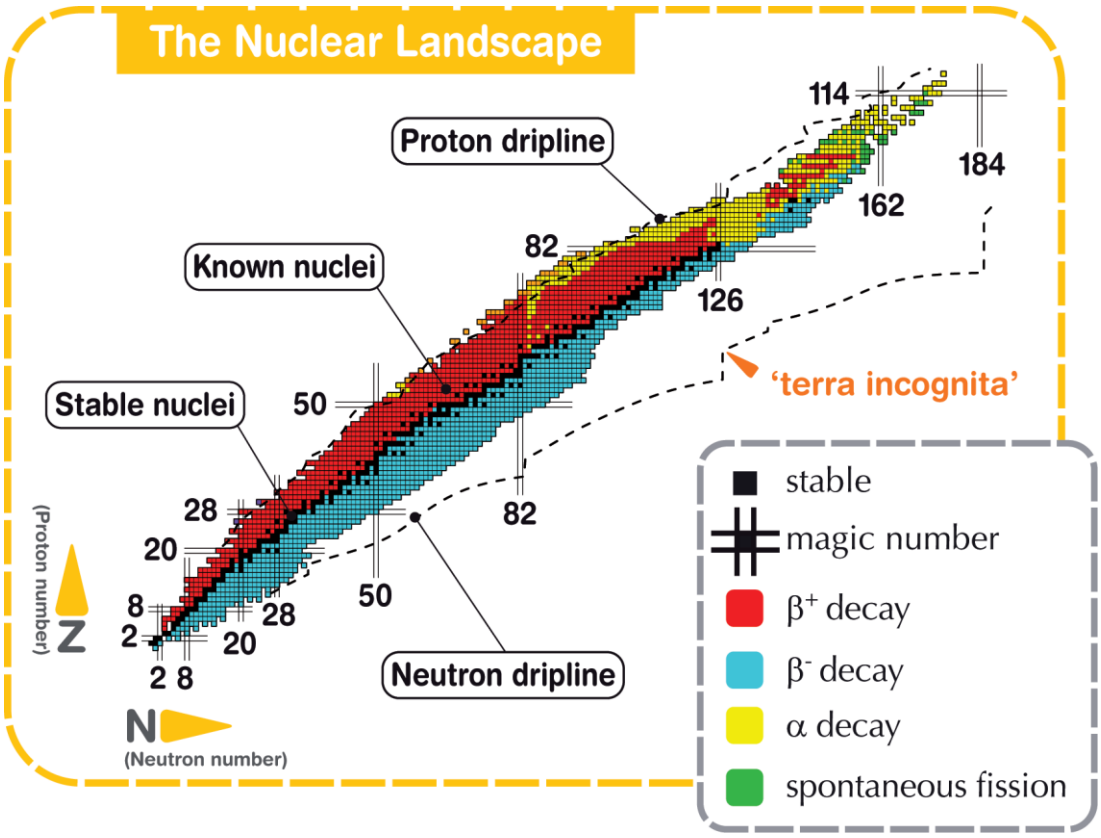

Fig.1 – Chart of the nuclides [2].

Nuclei far from the "valley of stability", so characterized by shortage or excess of neutrons (proton-rich and neutron-rich, respectively), are unstable and decay emitting different types of particles or electromagnetic radiation depending on their nature. Basically, four main types of decay can occur [1]:

- Alpha decay (yellow squares in fig. 1), which happens for elements with Z > 83, is characterized by the emission by a nucleus of a α particle, which is a ^{4}He nucleus consisting of 2 protons and 2 neutrons. The result of this loss is a variation in both Z and A, according to the scheme:

  $Z_D = Z - 2$

  $A_D = A - 4$

  where Z_D and A_D are the atomic number and mass number after decay, respectively.

- Beta decay, which can occur according to two different reactions:

  $n \rightarrow p^+ + \beta^- + \bar{\nu}$

  $p^+ \rightarrow n + \beta^+ + \nu$

The first mode of decay, called β^-(blue squares in fig.1), consists in the conversion of a neutron into a proton, with the emission of an electron (β^- particle) and a antineutrino $\bar{\nu}$. In this way, Z is increased by 1, whereas A doesn't change. This kind of decay is a prerogative of the neutron-rich nuclei, because undergoing this process several times they can move towards the valley of stability eliminating their excess of neutrons.
The second mode is called β^+, and is common in the case of proton-rich (more exactly neutron-deficient) nuclei which tend to transform protons into neutrons to regain stability (red squares in fig. 1), emitting a β^+ particle (positron) and a neutrino ν.

- Spontaneous fission (green squares in fig. 1), in which a heavy nucleus tend to spontaneously break forming two large fragments, like in the case of ^{252}Cf, which is commonly used as a source of both fission fragments and neutrons: ${}^{252}_{98}\mathrm{Cf} \rightarrow {}^{140}_{54}\mathrm{Xe} + {}^{108}_{44}\mathrm{Ru} + {}^{1}_{0}n + \mathrm{Q}$
where Q represents the energy formed in the process.

- Gamma ray emission, which is not a decay like those above described since no change in Z or A is obtained during this process. γ-rays are emitted from a nucleus right after a α or β decay, since in these processes the newly formed nucleus (called the daughter) is usually in an excited state, and tend to lose its excess energy by emitting high frequency electromagnetic radiation.

At present, approximately 3600 radioactive nuclei, commonly called "exotic nuclei" have been studied in terms of nuclear properties and can now be more or less easily produced in several facilities all over the world. However, theoretical calculations predict the existence of more than 6000 unstable nuclei, to be found between the neutron and proton "driplines" reported in Fig. 1. Beyond these boundaries, the instability of a nucleus is so high that it tends to immediately decay emitting nucleons.

Among all the techniques used to investigate the properties of nuclei far from stability, the use of Radioactive Ion Beams (RIBs) have been gaining a significant scientific interest due to the large number of species which can be produced and the possibility to use them for studies in different fields of science. In the next paragraph, a general description of a facility for RIB production is given, together with general details on the SPES project, whose goal is the construction of a RIB facility at INFN-LNL (*Istituto Nazionale di Fisica Nucleare – Laboratori Nazionali di Legnaro*) [3].

1.2. Radioactive Ion Beams production

Nowadays, facilities for the production of RIBs allow the detailed study of exotic nuclei, both from a nuclear physics view but also opening the way to their application in different fields of science.

In a general view, the production of RIBs consists of two very different phases: the generation of the exotic species, obtained usually by means of a nuclear reaction occurring in a well confined area, and the transport of the produced species to a dedicated experimental area, during which various operations of identification and purification of the desired beam are performed.

With the technical advances and improvements in the layout of modern RIB facilities, the quality of the produced beams is becoming more and more a strategic parameter, expecially in the case of very short-lived isotope. The factors that can act against the possibility to obtain pure beams of a desired isotope with a sufficient yield (generally quantified in terms of ions per second to the experimental user) are:

- Low production cross sections of the reaction chosen to produce the isotopes;
- Contamination from unwanted species that form in production site;
- Short half-lives, which is generally the case of very neutron-rich or proton-rich nuclei, since their distance from the valley of stability determines a fast decay.

At the present, two main techniques can be exploited to produce and deliver to users radioactive ion beams: the “In-Flight Separation technique” and the “Isotope Separation On-Line (ISOL) method”.

In the next section a brief comment on the In-Flight technique will be given, whereas the ISOL technique will be discussed in more detail, since it is the methodology adopted in the framework of the SPES project.

1.2.1. The In-Flight Separation technique [4]

The In-Flight Separation technique is based on the nuclear reaction between a primary beam and a lighter production target, in order to produce a secondary beam of radioactive ions, as indicated in fig. 2. Usually, the primary beam has energies of several tens of MeV/u (u = mass of a nucleon ~ $1.66 \cdot 10^{-27}$Kg) so that its interaction with the primary target results in a fragmentation reaction. The produced fragments are then selected using electro-magnetic devices and sent to the experimental areas. In this kind of facility the beam transport system represent a fundamental element: it has to suppress the intense primary beam transmitted through the primary target and in the same time to guarantee an high quality secondary beam transportation.

An example of secondary radioactive ion beam obtainable using this technique is ^{17}F, using ^{16}O as a primary beam, according to the scheme ${}^{2}_{1}H({}^{16}_{8}O, {}^{17}_{9}F)n$, which indicates that the reaction of a ^{16}O with a target containing deuterons (for example a deuterated polymer) produces ^{17}F and neutrons.

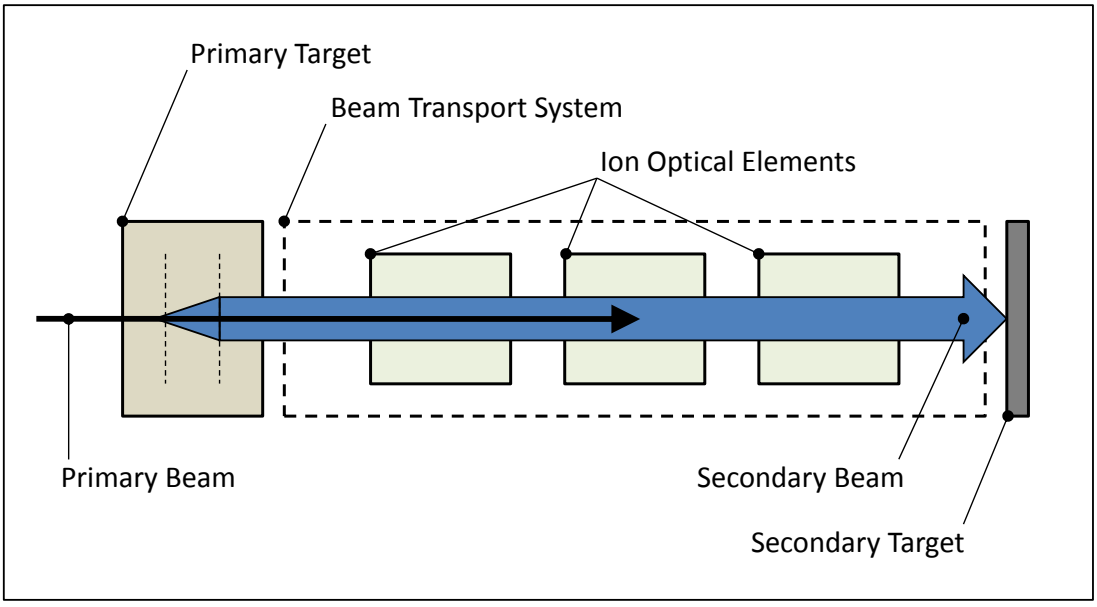

Fig.2 – Schematic representation of the In-Flight Separation technique [5].

This method provides isotopes not very far from stability without limitations due to lifetimes or chemical properties; it allows also for an easy variation of the energy of the reaction products within a certain range and can be implemented in existing heavy-ion accelerators. On the other side the main disadvantages are the low beam quality, due to contamination coming from the primary beam, and the low number of ion species that can be produced.

1.2.2. The Isotope Separation On-Line technique [6,7]

In a ISOL facility, the radioactive isotopes are produced in a heated target and then transported from the target to an ion source; once ionized they can be extracted, selected using a dipole magnet and subsequently accelerated to the required energy. The production sequence is designed to be:

- Efficient: the production of the very exotic nuclei inside the target it is not usually problematic; to avoid to the loss of nuclei due to decay, any manipulation step (ionization, purification, acceleration, transport to the detection system) has to be very efficient.

- Fast: if the species of interest are short-lived exotic nuclei, the losses due to radioactive decay between the moment of production and the arrival at the experimental set-up should be kept to a minimum.

- Selective: in the nuclear reaction process unwanted nuclei are produced in a high quantity; moreover ISOL systems often produce beams of isotopes from the target material itself or from other components of the target – ion source system, due to the conditions at which these devices are exposed. As a consequence the separation process should distinguish between the wanted and the unwanted species with efficacy. One defines the unwanted species as contaminants which are called isobaric if they are characterized by the same mass-over-charge ratio with respect to the ions of interest.

- Highly productive: once the target material has been chosen, to improve the production rate the highest primary beam intensities have to be delivered, ensuring anyway the capability of the target to dissipate the power due to the primary beam action.

In figure 3 a schematic representation of a ISOL facility is reported, characterized by the fundamental and characteristic steps of the ISOL technique: production, thermalization, ionization, extraction, mass separation, cooling, charge-state breeding and acceleration. The section of the facility comprehending target, catcher, transfer line and ion source is commonly referred to as “target-ion source system”. Both physical (production cross section, decay – half life, ionization potential, …) and chemical (molecular formation probability, volatility, …)

properties of the nuclei of interest and of the target materials adopted are important to determine the success of each step in reducing the delay time, which is the average time the radioactive atoms spend from the moment of production to the moment of arrival at the experimental area. In some cases two or more steps are embedded in a single phase, like for example in the case of production and thermalization. Each single step is described as follows.

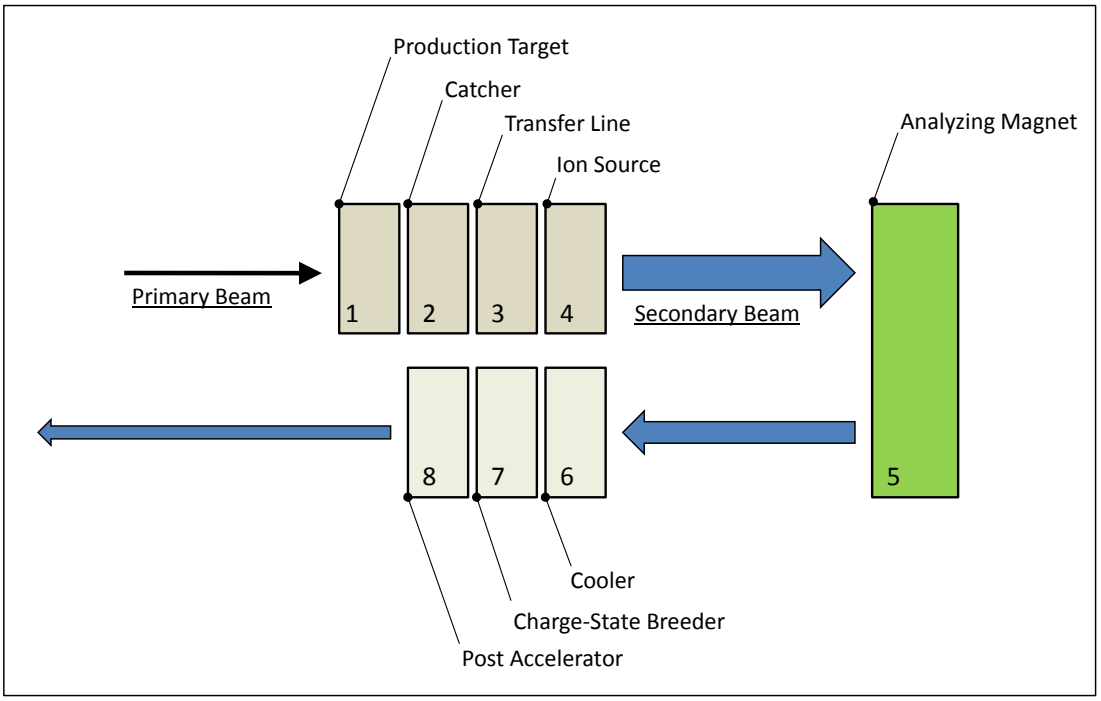

Fig.3 – Schematic representation of the ISOL technique [5].

- Production target. A primary beam of light or heavy ions, electrons or neutrons hits a target to produce the desired radioactive ion beams according to different reaction mechanisms. In some cases a converter is used to transform for instance a primary beam of protons or electrons into a flux of neutrons or γ rays, respectively. This flux is then sent onto the target inducing the nuclear reactions of interest. In choosing the target it is fundamental to optimize the beam-target combination with respect to the highest production cross-section and the lowest amount of contaminants, and to use target material that is able to stand the highest possible beam currents without damage.

- Catcher. In some cases the target and the catcher are the same thing; the catcher can be solid or gaseous and is used to stop (thermalize) the exotic nuclei once they are produced by nuclear reactions. After thermalization a part of the radioactive nuclei of interest is able to escape from the catcher and to reach the ion source passing through the transfer

line described in the following paragraph. The mechanisms of diffusion of the radioactive atoms from the target/catcher material and effusion towards the ion source will be discussed into more detail in chapter 2.

- Transfer line. Through the transfer line the radioactive atoms are transported from the target/catcher to the ion source by effusion. The transfer line is kept generally at high temperature to avoid loss of radioactive atoms by sticking on its walls.

- Ion source. Depending on the particular requirements, several different ionization mechanisms are used to transform the radioactive atoms into radioactive ions. In general singly charged positive or negative ions are produced. To allow the acceleration/extraction of the radioactive ions the ion source is put on a positive (in case of beams of positively charged ions) or negative (negatively charged ions) high voltage.

- Analyzing magnet. Once extracted from the ion source the low energy ion beam is mass separated by an analyzing magnet and transported to the focal plan where it can be opportunely focalized. An important property that express the quality of the system is the mass resolving power, defined as $R = M/\Delta M$, where ΔM is the FWHM (*full width at half maximum)* of a beam of ions with mass M in the focal plane of the separator, which has to be maximized in order to better select the desired isotope.

- Beam cooler. A "cooler" is used to improve the optical properties of the ion beam and to bunch it, in order to increase the peak to background ratio of certain applications like laser spectroscopy or to inject the beam into a charge-state breeder. Two kind of devices are used as coolers: "Penning traps" and "Radio Frequency (RF) coolers". The former is based on the storage of ions using a combination of magnetic and electrical fields, the latter using electrical DC (Direct Current) and RF (Radio Frequency) fields.

- Charge-state breeder. In order to have a simpler and more efficient post-acceleration it is useful to produce a multiple charge state ion beam before the injection into the post-accelerator. A charge-state breeder transforms a singly charged ion beam into a multiple charged one. Two types of charge-state breeding ion sources are used: the Electron Beam Ion Source (EBIS) and the Electron Cyclotron Resonance (ECR) ion source. Both are based on an intense bombardment of the beam ions with energetic electrons, with

electron impact ionization [8] yielding ions in higher charge states. The plasma of ions and electrons is confined through electrical and strong magnetic fields.

- Post accelerator. The highly charged ion beam from the charge-state breeder or the beam of singly charged ions is then injected into the post-accelerator. After the post-acceleration step the beam is sent to the experimental users.

1.3. The SPES project at LNL [9]

The facility proposed for the SPES project has two main goals: to provide a radioactive ion beam accelerator system to perform forefront research in nuclear physics by studying nuclei far from stability and to develop an accelerator based interdisciplinary research center. The SPES facility will be mainly devoted to the production of neutron-rich radioactive nuclei with mass number in the range 80-160 by the ^{238}U fission at a rate of 10^{13} fission/s. The production of few selected proton-rich isotopes will be carried out as well. An overview of the SPES facility is presented in figure 4.

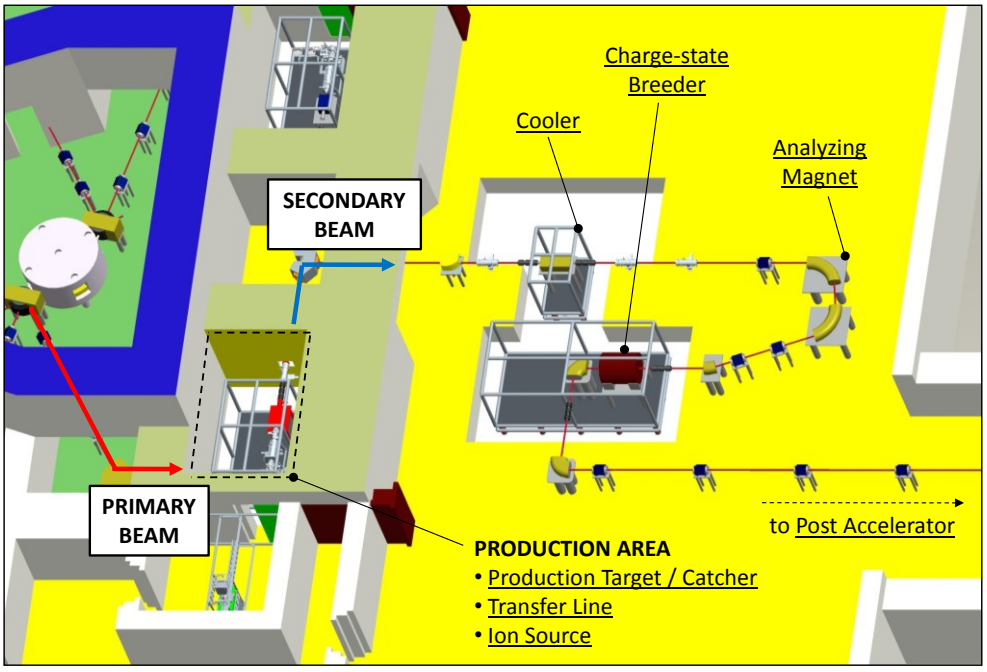

Fig.4 – Overview of the SPES facility.

Neutron-rich ion beams will be produced according to the ISOL technique, using the proton induced fission on a direct target of uranium carbide (see chapter 3), while other types of targets and nuclear reactions will be exploited to produce proton-rich species (see chapter 4). The

primary beam (proton beam) is furnished by a Cyclotron with variable energy (15-70MeV) and a maximum current of 0.750 mA upgradeable to 1.5 mA and splitted on two exit ports.

The SPES facility is designed to supply a second generation of exotic beams able to perform a step toward EURISOL (European ISOL Facility) and to offer a powerful accelerator based system for research in applied physics, nuclear astrophysics, solid-state physics and nuclear medicine (see next paragraph).

A detailed description of each phase of the RIBs production at SPES is described as follows.

- Production. The most critical and innovative element of the SPES project is the production target; its design is carefully oriented to optimize cooling by thermal radiation taking advantage of the high operating temperature of approximately 2000°C. Much effort has been given to the study of the target thermo-electric behavior [10] and the release properties of the target [11]. Experimental work to verify the accuracy of the performed simulations was carried out at HRIBF, the Oak Ridge National Laboratory ISOL facility (USA) [12]. The production target and all the experimental apparatus needed to guarantee its functioning will be designed following the ISOLDE (CERN, Switzerland), the HRIBF (ORNL, USA) and the EXCYT (INFN, LNS, Italy) projects. Special care will be devoted to the safety and radioprotection of the system: the use of up-to-date techniques of nuclear engineering will result in a high safety level of the installation. A detailed analysis on the SPES target requirements and properties will be given in chapter 2.

- Ionization. The isotopes will be extracted and ionized at +1 charge state with an ion source connected with the production target by means of an opportunely designed transfer line. Three types of ionization mechanisms will be exploited to obtain all the radioactive ion beams of interest, depending on their physicochemical properties:

  - Surface ionization, a physical phenomenon according to which when an atom interacts with a hot surface it can lose or gain an electron before leaving the surface as a positive or negative singly charged ion. This technique is efficient to ionize elements with ionization potential (W_i, energy required to remove the outermost electron from an atom or molecule) smaller than 7 eV for the creation of positive ions or with electron affinity (E_A, energy given off when a neutral atom in the gas phase

gains an extra electron to form a negatively charged ion) greater than 1.5 eV for creating of negative ions. The efficiency ε_i of these type of sources can be calculated as:

$$\varepsilon_i = \frac{n_i}{n_0} = \frac{1}{1 + \frac{n_0}{n_i}} \quad (1)$$

where n_i and n_0 are the ion density and neutral density of a certain element, respectively, and are related to each other by the Langmuir equation, reported in (2) in the case of positive surface ionization:

$$\frac{n_i^+}{n_0} = \left(\frac{g_i^+}{g_0}\right) \cdot e^{\left[\frac{(\varphi - W_i)}{kT}\right]} \quad (2)$$

where g_i^+ and g_0 are the statistical weights of the ionic and atomic ground state, T and φ are the temperature and the work function (the minimum energy required to remove an electron from a solid to a point immediately outside from its surface) of the heated surface, respectively, and k is the Boltzmann constant ($1.38 \cdot 10^{-23}$ J/K). This type of ionization is usually obtained forcing the produced element to pass through a so called "hot cavity", a cylindrical tube made of a material with a high φ, for example tantalum (φ = 4.19 eV), tungsten (φ = 4.53 eV) or rhenium (φ = 5.10 eV), kept at high temperature. High ionization efficiencies can be only obtained for elements with Wi < 5.5 eV, like for example alkali and alkaline-earth elements.

- Electron impact ionization, in which the positive ion formation is obtained by the bombardment of the element atoms with energetic electrons, resulting in the loss of one or more electrons from the element outer shells. The evolution of the system in terms of ion density as a function of time can be described as:

$$\frac{dn_i}{dt} = j_e(n_{i-1} \cdot \sigma_{i-1 \to i} - n_i \cdot \sigma_{i \to i+1}) \quad (3)$$

where n_i is the ion density with charge state Q = i, j_e is the electron current density and $\sigma_{i-1 \to i}$ the cross section for impact ionization from charge state (i-1) to i; equation (4.5) is valid for i from 1 to (i_{max}-1), being i_{max} the charge state of the fully stripped ion. To make use of this phenomenon for the ionization of the produced isotopes in ISOL facilities, high temperature plasma ion sources have been developed and successfully used [13]. In this kind of devices, the bombarding electron flux is created by a discharge in a low-pressure environment. In this way a plasma is

produced in which the ions are confined, preventing them from wall collisions and neutralization. One of the most successfully and widely used sources is the forced-electron beam induced arc-discharge (FEBIAD) ion source [14]: in this model the electrons are extracted from a high temperature cathode and accelerated into a low pressure plasma. This type of devices, in general, are not selective: the energy spectrum of the electrons is broad and allows ionization of virtually every element.

- Laser ionization, according to which atoms are stepwise excited by laser photons at precise energy levels, finally becoming positive ions[15]. The ionization process typical consists of two or three steps, everyone characterized by a precise energy level (or wavelength λ) for the laser photons. The aforementioned ionization technique can be performed using commercially available pulsed lasers like Nd:YAG lasers (typical repetition rate 10 Hz), Excimer lasers (100 Hz)[16], copper vapour lasers (10 kHz) and solid-state lasers (10 kHz). Because of the resonant nature of most of these steps, resonant laser ionization is very efficient and chemically selective, resulting in an extremely pure ion beam.

An overview of the applicability of the three aforementioned techniques for the SPES facility is given in fig. 5, which reports the whole set of elements that will be produced form the p-induced ^{238}U fission, clearly indicating the type of source that will be used for their ions production.

The formation of the beam will be guaranteed by an extractor placed right after the ion source, designed so that between its surface and the ion source there will be a 60 kV potential difference, which forces the newly formed ions to follow the path towards the subsequent steps of their transport throughout the facility.

- Separation and transport. A cooler and an high resolution analyzing magnet will be placed in series along the beam line after the extraction of the ions from the ion source to improve the optical quality of the beam and to perform an accurate mass selection, respectively. To optimize the post acceleration, a charge breeder will be introduced: it will increase the charge state of the ion beam before injecting it into the post-accelerator.

- Post acceleration. Two stages of acceleration will be performed: 1) the PIAVE Superconductive RFQ which represents the first reacceleration stage before the injection

into the 2) linear accelerator ALPI (see figure 6). The proper velocity matching needed to enter PIAVE will be furnished by high voltage platforms operating at 250kV. The expected beam on experimental target will have a rate on the order of 10^8-10^9 pps (particles per second) for ^{132}Sn, ^{90}Kr, ^{94}Kr and 10^7-10^8 pps for ^{134}Sn, ^{95}Kr with energies of 9-13 MeV/u.

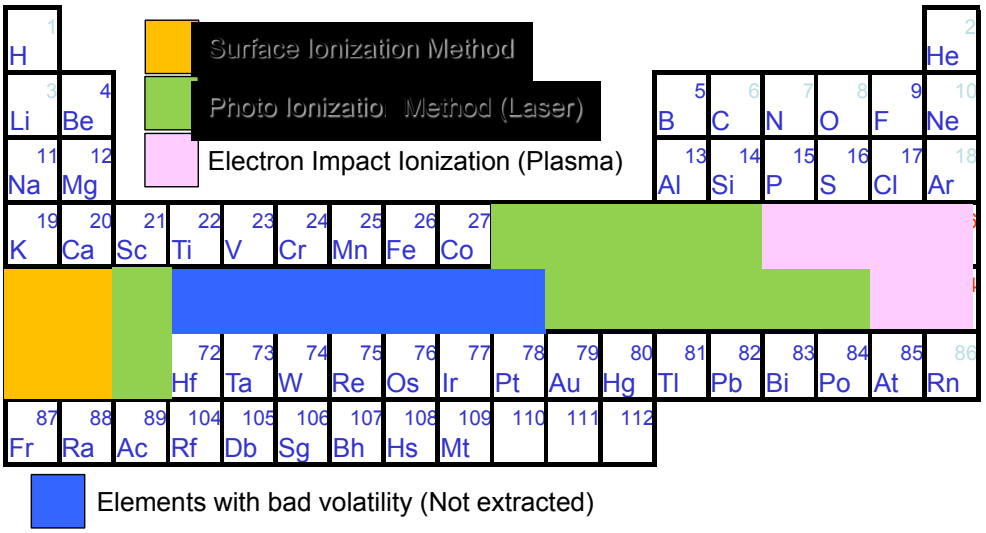

Fig.5 – Ionization of the n-rich isotopes obtained from the ^{238}U fission at SPES.

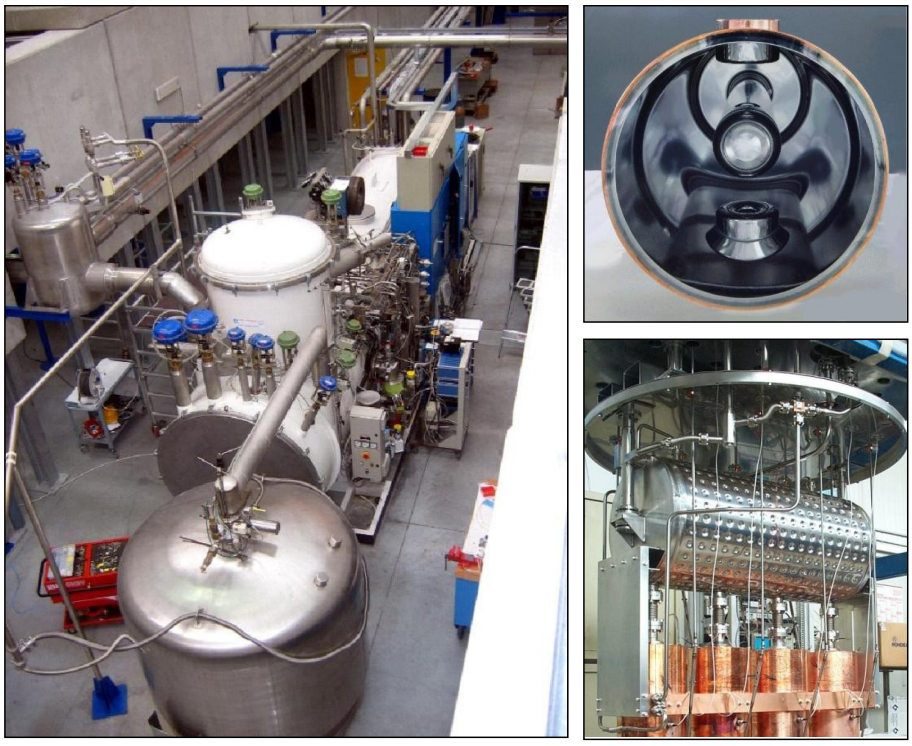

Fig.6 - Some details of the linear accelerator ALPI.

1.4. Applications of Radioactive Ion Beams research [17]

1.4.1. Nuclear physics

Most of the present-day knowledge of the atomic nucleus structure is based on the properties of nuclei that in the chart of nuclides are positioned very close to the "valley of stability" or in the proton-rich side, where the ratio Z/N ratio is not so different to that of stable nuclei. Extrapolating the models based on them to describe the regions far from stability is very puzzling and leads inevitably to wrong suppositions and expectations. Therefore, it is now clear that some of the very "basic truths" of nuclear physics have to be revised and modified.

Among all the examples of deviation from the common accepted rules in describing atomic nuclei, one of the most significant example is the "liquid drop model" failure in the case of the Halo nuclei. The aforementioned model was developed by Bohr and Wheeler to describe the radius R of the atomic nucleus as $R = R_0 A^{1/3}$, where R_0 is a constant equal to 1.2 fm (1 fm = 10^{-15} m). In the case of some nuclei, called Halo, the nuclear radius do not scale with a $A^{1/3}$ dependence, but instead they are appreciably larger than that prediction.

The Halo effect, discovered in the mid-1980's at Lawrence Berkeley Laboratory [18], is related to the presence of two or more external nucleons, (usually neutrons) called valence nucleons, orbiting around a well-defined inert "core" containing all the other nucleons. The most famous Halo nucleus is surely ^{11}Li, composed of two valence neutrons orbiting around a ^{9}Li nucleus. The graph of figure 7 clearly shows the trend of the nuclear radii of Lithium isotopes as a function of the neutron number: the discontinuity of size between ^{11}Li and the other lighter isotopes is evident. In the same figure the ^{11}Li nucleus is compared with other heavier nuclei: ^{48}Ca and ^{208}Pb. The mass-weighted average between the radius of the ^{11}Li external valence neutron's orbit and the radius of the ^{9}Li nucleus is comparable to ^{48}Ca nuclear radius whereas the total space wrapped inside the ^{11}Li external valence neutron's orbit is equivalent to the ^{208}Pb atomic size.

In the framework of nuclear physics many other topics of research are being investigated using radioactive ion beams of exotic nuclei, like for instance, just to name a few: nuclear shell structure description, isospin symmetry, nuclear reactions mechanisms, beta decay, one or two-proton radioactivity, physics of the superheavy elements.

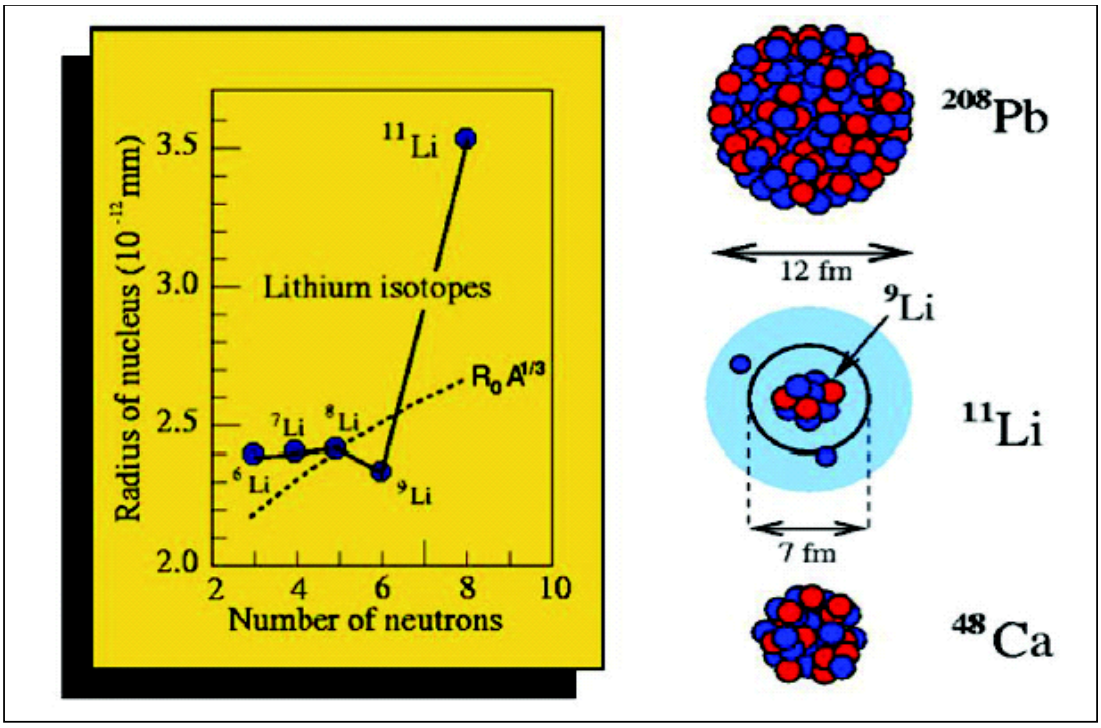

Fig.7 - Lithium isotopes nuclear radii and size comparison between ^{11}Li, ^{48}Ca and ^{208}Pb nuclei.

1.4.2. Nuclear astrophysics

Nuclear astrophysics plays a fundamental role in understanding the structure and composition of the Universe and its many constituents. At the present, the major challenges of experimental nuclear astrophysics are related to the stellar cycles description [19]. The stars produce energy through nuclear reactions between stable as well as unstable nuclei: these processes can either be stable for billions of years or be explosive involving a timescale of seconds. A typical example of burning cycle involving unstable nuclei is the so-called CNO cycle (CNO stands for Carbon-Nitrogen-Oxygen), a set of fusion reactions by which stars convert hydrogen to helium.

To model some steps of these processes nuclear astrophysics must rely on a number of specific characteristics of exotic nuclei. When available, experimental information is used but otherwise scientists must rely on extrapolating nuclear models. The use of radioactive ion beams can either provide this experimental information or can accurately test the applicability of the current nuclear models.

1.4.3. Solid state physics

Radioactive ion beams can be used as a powerful diagnostic tool to furnish detailed information on the environment in which they are implanted [20]. An important application is represented by the Emission Channeling technique, used to study the structure and properties of impurity-defect complexes in solids, particularly in semiconductors whose functioning is deeply influenced by defects.

The technique relies on the emission and movement of charged particles (either α or β) through a single crystal subsequent to the decay of the radioactive ions previously implanted into the crystal. The particles are revealed by 2-dimensional position sensitive detector. The working principle of this analytical method is based on the angle dependence of the intensity of the emitted radiation as a function of the orientation of the host crystal (different crystal axes and planes): from the measured anisotropic intensity distributions the position occupied by the radioactive ions inside the lattice structure of the implanted solid can be determined with a great accuracy.

1.4.4. Nuclear medicine

Nuclear medicine is a branch of medicine that uses radioactive isotopes and relies on the process of radioactive decay in the diagnosis and treatment of disease.

An important application of radioactive ion beams in nuclear medicine is the production of radionuclides to be used for Positron Emission Tomography (PET). PET is a nuclear medicine imaging technique capable of generating three-dimensional images of functional processes undergoing in the human body: it is mainly used in clinical oncology (medical imaging of tumors and the search for metastases) and for neuroimaging.

Radionuclides used for PET are typically isotopes with short half-lives such as ^{11}C (~20 min), ^{13}N (~10 min), ^{15}O (~2 min), and ^{18}F (~110 min), dissolved into compounds involved in the functional process of interest. When introduced into the human body, these radionuclides reach the compound zone of action and undergo β^+ decay emitting a positron for each $p \rightarrow n$ transformation. After travelling up to a few millimeters, the positron with one of the surrounding electrons and annihilation occurs, immediately producing two photons (γ-ray) of characteristic energies moving in exact opposite directions.

By revealing the produced couple of γ-rays with an opportunely designed set of scintillators, after an accurate data elaboration a digital image of the zone of interest can be obtained, thus helping the understanding of the particular process to be analyzed. A schematic representation of the technique is given in figure 8.

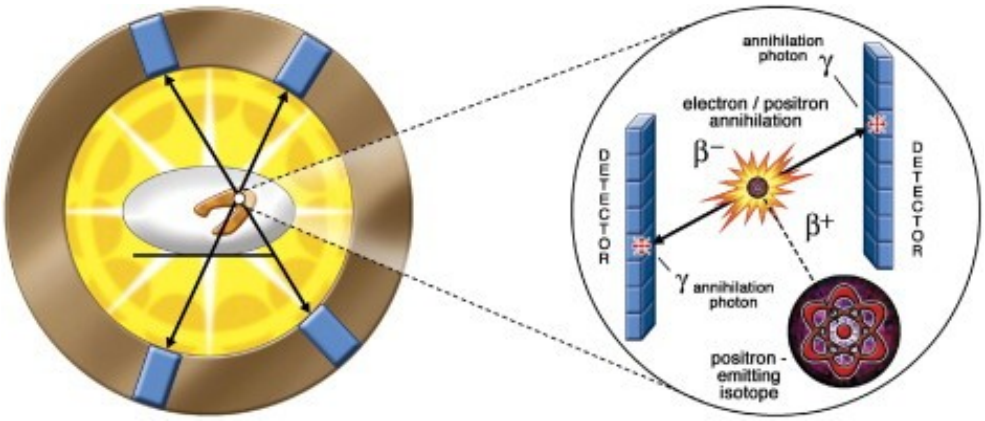

Fig.8 – PET detection system [21].

Chapter 2

The SPES target

2.1. General aspects of an ISOL target

As presented in paragraph 1.2.2, the ISOL technique is based on sequential steps, each one characterized by a specific set of features and operational constraints. Since this work is focused on different aspects of the target production, characterization and testing, a more specific analysis of all the mechanisms in which the target is involved will be given. As already stated, the target is the real core of the entire ISOL facility, since from the interaction between the primary beam and its atoms the radioactive species of interest are created. Moreover, the target chemical and microstructural characteristics are also important in determining the possibility of effectively make use of the produced isotopes, without losing them due to radioactive decay during their "run" towards the ion source. In the following sections two different stages of the RIBs production, both involving the target, will be analyzed in detail: the isotopes production and their release from the target.

2.1.1. Isotopes production in an ISOL target

The isotopes generation inside a ISOL target is obtained by means of a nuclear reaction between a primary beam and a target: it is obvious then that the amount of obtainable species and their abundance are related to some basic features of both the beam and the target nuclei.

Different projectiles with a large variety of energies are used, such as low energy protons and neutrons of 30 to 100 MeV, high-energy protons of 500 to 1500 MeV, heavy ions of 4 to 100 MeV/u, thermal neutrons and electron beams.

The intensity ($I_{production}$) of the reaction products formed in the target is calculated using the following expression [7]:

$$I_{production} = \Phi \, \sigma \, N_{target} \tag{4}$$

where Φ is the primary beam intensity (A, but typically μA or mA), σ is the reaction cross section (usually expressed in cm^2 or barns, 1 barn = 10^{-24} cm^2) and N_{target} is the number of target atoms per surface area (atoms/cm^2).

The cross section σ represents the probability of the interaction between the primary beam and the target nuclei, and it is energy dependent. Since during the passage through the target the beam loses part of its initial energy, the intensity can only be obtained by integrating over the target thickness taking into account this energy loss.

Four main types of nuclear reactions can occur when a primary beam interacts with a target:

- Fission: it is used to produce neutron-rich nuclei in a wide mass range, using ^{235}U, ^{238}U, ^{232}Th or other long lived actinides as target nuclei. Typical primary beams are protons, neutrons, electrons or heavy ions. The interaction results in the nucleus scission forming two species with similar masses, typically in the range between 90 and 150 amu, with emission of by-products such as neutrons. More detail on the fission-produced isotopes will be given when discussing the SPES target features in detail.

- Spallation: in this type of reaction a large number of protons, neutrons and *a* particles are ablated from the target nucleus, resulting in the formation of a new nucleus with similar mass with respect to the original one. For example, a 1 GeV proton beam on a ^{238}U target produces ^{200}Fr, ablating 5 protons and 23 neutrons. Due to this particular mechanism, spallation is commonly used to produce neutron-deficient isotopes.

- Fragmentation: for ISOL systems both target fragmentation, whereby a heavy target is bombarded with a high-energy proton beam and projectile fragmentation, in which a high-energy (energy > 50 MeV/u) heavy-ion beam is sent onto a light target are used. These reactions produce again a wide variety of isotopes, close to the initial target or projectile nucleus as well as very light nuclei.

- Light- and Heavy-ion Fusion Evaporation Reactions or Direct Reactions: with light-ion induced fusion reactions nuclei close to the line of stability on the proton-rich side are produced, like for example the $^{13}C(p, n)^{13}N$ reaction. Heavy-ion fusion evaporation reactions have typically a much lower cross section than the light-ion ones but produce neutron-deficient nuclei very far from the line of stability, like in the case of the

$^{52}Cr(^{142}Nd, 4n)^{190}Po$ reaction. It should be noted that this kind of reactions doesn't involve any fissile material, and so the number of produced isotopes for each kind of target material is very limited with respect to the three aforementioned reactions.

2.1.2. Isotopes release from an ISOL target

As soon as a radioactive nuclide is generated inside the target, it immediately starts to move with a direction and velocity related either to the target microstructure and to the temperature at which the system is kept (diffusion process). At the same time, the produced isotopes start to decay, each one with a well-defined time. Besides travelling through the target, some of the produced species reach its surface and start moving inside the surrounding volume, until they reach, after several collisions, the ion source which is usually directly connected to the target system (effusion process).

Each collision between the particles and the material constituting the target and the surrounding volume leads to the absorption of the nuclide on the hit surface, which is followed generally by its desorption after a certain time (sticking time) [22]. Chemical reaction and re-diffusion inside the target material are possible as well, but the latter is not very common if the surface is kept at high temperature

All the process occurring from the isotopes generation to their effective use are characterized by a certain grade of imperfections (loss of efficiency), but diffusion and effusion, being based on the interaction of the produced particles with the surrounding environment, represent the slowest among all the steps. The optimization of the target release, as well as an accurate design of the target-ion source geometry are therefore of extreme importance to avoid the loss of a big fraction of isotopes which decay before reaching the experimental areas in which they are supposed to be studied or used.

From a general point of view, referring to eq. (4), the final intensity I of the secondary ion beam produced can be expressed as:

$$I = I_{produiction}\,\varepsilon = \Phi\,\sigma\,N_{target}\,\varepsilon \qquad (5)$$

where ε represents the efficiency of the whole ISOL process, so taking into account the efficiencies of every single step of the isotopes production and manipulation. E can be therefore calculated as follows:

$$\varepsilon = \varepsilon_{delay}\, \varepsilon_{ionization}\, \varepsilon_{transport}\, \varepsilon_{cooling}\, \varepsilon_{breeding}\, \varepsilon_{post-acceleration} \quad (6)$$

In the above reported equation:

- ε_{delay} is the probability of survival against radioactive decay during the time needed to extract the ion from the target-ion source system (diffusion and effusion efficiency);
- ε_{ion} is the ionization efficiency;
- $\varepsilon_{transport}$ is the efficiency of both mass separation and transport to the experimental set-up;
- $\varepsilon_{cooling}$ is the beam cooler efficiency;
- $\varepsilon_{breeding}$ is the efficiency of the charge-breeding process;
- $\varepsilon_{post\text{-}acceleration}$ is the efficiency of the post-acceleration step.

If the secondary ion current as a function of time is considered, eq. (5) can be changed into:

$$i(t) = \Phi\, \sigma\, N_{target}\, \varepsilon_{ionization}\, \varepsilon_{transport}\, \varepsilon_{cooling}\, \varepsilon_{breeding}\, \varepsilon_{post-acceleration}\, p(t) e^{-\lambda t} \quad (7)$$

where p(t) is called release function and represents the probability that an atom generated at a time t=0 is released from the ion source and $e^{-\lambda t}$ is the contribution of decay of the radioactive isotopes, with λ being the decay constant, $\lambda = \ln 2 / T_{1/2}$.

p(t) is a term related to the diffusion and effusion processes, and several effort has been done in order to successfully describe it into detail [23, 24, 25]. If we consider the time rate of variation of a population N of a certain isotope (Z,A) formed at t=0, taking into account its production, release and decay, the following expression can be obtained:

$$\frac{dN(t)}{dt} = J(t)P - F(t) - \lambda N(t) + \lambda_n N_n \quad (8)$$

in which J(t) is the flow of primary particles hitting the target, P is the probability of yielding the particular isotope considered per incident proton and $\lambda_n N_n$ is the sum of all the decay channels that feed the population of the (Z,A) isotope, like for example its parent nuclei β^-

decay. The form of the time release flux, F(t), is usually a complex function of the target geometry and depends on the diffusion and effusion phenomena parameters.

The release efficiency ε_{delay} can be obtained as the ratio between the total number of isotopes released from the target and the number of produced isotopes inside the target (N_0):

$$\varepsilon(\lambda, \lambda_n) = \frac{\int_0^\infty F(t)\, dt}{N_0} \tag{9}$$

Equation (9) can be expressed in terms of the release function p(t) as follows:

$$\varepsilon(\lambda, \lambda_n) = \int_0^\infty p(t) e^{-\lambda t} dt \tag{10}$$

The function p(t) can therefore be obtained as:

$$p(t, \lambda, \lambda_n) = \frac{F(t)}{N_0 e^{-\lambda t}} \tag{11}$$

Under the assumption that the release flux F will follow closely to the number of isotopes inside the target, one can express this term as:

$$F(t) = g(t) N(t) \tag{12}$$

where g(t) is a function that characterize the deviation of the function F(t) away from N(t), and it is constant in steady state conditions.

Substituting (12) into (8), assuming that the target is hit by a very short pulse of primary particles, and imposing the boundary condition $N(0)=N_0$, the number of isotopes inside the target can be obtained as:

$$N(t) = e^{-\lambda t - \mu(t)} \left(N_0 + \lambda_n \int_0^t N_n e^{\lambda \tau + \mu(\tau)} d\tau \right) \tag{13}$$

where $\mu(t)$ is defined by

$$\mu(t) = \int_0^t g(\tau) d\tau \tag{14}$$

By combining (8), (12) and (13), $p(t,\lambda,\lambda_n)$ becomes:

$$p(t, \lambda, \lambda_n) = g(t) e^{-\mu(t)} \left(1 + \frac{\lambda_n}{N_0} \int_0^t N_n e^{\lambda \tau + \mu(\tau)} d\tau \right) \tag{15}$$

Eq. (15) is usually expressed in the literature for the special case where $\lambda_n = 0$, in whereby the λ dependence on the release function drops out as well. This assumption implies that the

radioactive decay properties of the particles travelling through the target towards the ion source is not directly related to their release function, and consequently don't affect their release times.

Following this consideration, and supposing steady-state conditions – so assuming for g a constant value - the delay function becomes equal to the one relative to the evacuation of a gas through an orifice from a container, with 1/t being the time constant:

$$p(t) = ge^{-gt} \tag{16}$$

Under this simplifications, p(t) depends only on the diffusion and effusion processes, which themselves show characteristic delay functions, namely $p_D(t)$ and $p_E(t)$, respectively. If one assumes that effusion happens always after diffusion, so that there is no re-diffusion of particles previously escaped from the target, p(t) can be obtained by the following convolution:

$$p(t) = \int_0^t p_D(\tau) p_E(t-\tau) d\tau \tag{17}$$

in which it is supposed that the particle diffuse inside the target material in a time interval $[0,\tau]$ and effuse in the surrounding environment between τ and t.

In the following section, a detailed analysis of diffusion and effusion in the case of radioactive isotopes release will be given.

2.1.3. Diffusion and effusion

Solid state diffusion is governed by Fick's laws, which characterize the flow of particles driven by a concentration gradient. The Fick's first law shown in eq. (18) describes the case in which the flow of particles happens in steady state conditions, with no variation of concentration in time. In this case, the flow goes from the portions of space with higher concentrations towards those with lower concentrations of particles. In a real system such as a ISOL target however, concentration is a function of both space and time, and the variation of concentration in time can be calculated by the Fick's second law reported in eq. (19).

$$\bar{J} = -D\nabla c \tag{18}$$

$$\frac{dc}{dt} = D\nabla^2 c \tag{19}$$

In the above reported equations, $\bar{J}$ is the particle flow, c is the concentration and D the diffusion coefficient, describable with an Arrhenius-like expression:

$$D = D_0 e^{-\frac{E_D}{kT}} \tag{20}$$

in which E_D is the activation energy for the diffusion of a particle inside a matrix, k is the Boltzmann constant and T is the temperature.

In the case of a ISOL target, the solution of the Fick's second law is obtainable defining appropriate boundary conditions, in three different cases:

- target made of spherical grains (common approximation in the case of ceramic targets);
- fiber target;
- target obtained superposing thin foils.

As demonstrated experimentally [26, 27] and also theoretically [28], the diffusive process is faster in the targets made of powders (ceramics), so constituted by the combination of bulk grains and pores: a common approximation of this system is considering the target made of spherical grains of the same dimension.

The release function relative to the diffusion process can be calculated as [27]:

$$p_D(t) = \frac{6\mu}{\pi^2} \sum_{n=1}^{\infty} e^{-n^2 \mu t} \tag{21}$$

where $\mu = \pi^2$ D / r is the diffusion parameter, D the diffusion coefficient and r the grain radius. The diffusion contribution to the delay efficiency can be obtained by integrating equation (10) from time t to infinite:

$$\varepsilon_D(\lambda) = \frac{6\mu}{\pi^2} \sum_{n=1}^{\infty} \frac{e^{-(\lambda + n^2 \mu)t}}{\lambda + n^2 \mu} \tag{22}$$

In a real situation, the assumption of spherical grains with the same radius is clearly not valid: it is possible however by calculating ε_D experimentally to obtain a mean value μ for a specific target kept at a certain temperature.

Once the atoms have diffused and reach the surface of the grain, the subsequent step is the effusion process, which can be modeled as the evacuation of a volume through an orifice, since it describes the erratic path that gas atoms follow when they move freely within a vacuum bounded

(walls) system [29]. This situation can be described as molecular flow, where, in absence of a pressure gradient, atoms don't tend to move with a privileged direction of motion. Thus, trajectories will be straight lines between two consecutive collisions with the system walls.

This process depends on the following parameters [30]:

- the mean number of collision ω with the target material surface and container walls;
- the mean sticking time per collision τ_s, which depends on the temperature and adsorption enthalpy of the system particle-surface;
- the mean flight time between collisions τ_f, which depends on the mass, temperature and target geometry.

The delay function of the effusion process can be expressed as [24]:

$$p_E(t) = \upsilon e^{-\upsilon t} \tag{23}$$

where υ is the time constant of the effusion process. The mean effusion time τ_E can be related to the three aforementioned system properties ω, τ_s, τ_f as:

$$\tau_E = \omega(\tau_s + \tau_f) \tag{24}$$

The sticking time per collision τ_s can be obtained from the Frenkel equation [31, 32]:

$$\upsilon_s = \upsilon_0 e^{\frac{-\Delta H_a}{kT}} \tag{25}$$

in which υ_s is the probability of escape of a particle adsorbed on a surface, υ_0 the vibrational energy of the adsorbed molecules and ΔH_a the adsorption enthalpy. The sticking time can be calculated as the inverse of υ_s:

$$t_s = t_0 e^{\frac{\Delta H_a}{kT}} \tag{25}$$

The effusion contribution to the release efficiency can be calculated in the same way as for equation (22):

$$\varepsilon_E(\lambda) = \int_0^\infty e^{-\lambda t} p_E(t) dt = \upsilon \int_0^\infty e^{-(\upsilon+\lambda)t} dt = \frac{\upsilon}{\upsilon + \lambda} \tag{26}$$

The overall release function (diffusion + effusion) can be obtained substituting eqs. (21) and (23) into equation (17) [25]:

$$p(t) = \frac{6\mu\upsilon}{\pi^2}\sum_{n=1}^{\infty}\frac{e^{-\upsilon t} - e^{n^2\mu t}}{\upsilon + n^2\mu} \tag{27}$$

Eq. (10) can be used to obtain the overall release efficiency, using the p(t) expression of eq. (27):

$$\varepsilon(\lambda) = \frac{3\upsilon}{\upsilon + \lambda}\left(\frac{W\coth(W) - 1}{W^2}\right), \quad W = \pi\left(\frac{\lambda}{\mu}\right)^{\frac{1}{2}} \tag{28}$$

In the particular case of the release of short-lived isotopes, for which $\lambda > \mu$, eq. (28) can be rewritten in the form:

$$\varepsilon(\lambda) = \frac{3}{\pi}\left(\frac{\mu}{\lambda}\right)^{\frac{1}{2}}\left(\frac{\nu}{\nu + \lambda}\right) = \frac{3}{r}\left(\frac{D}{\lambda}\right)^{\frac{1}{2}}\left(\frac{\nu}{\nu + \lambda}\right) \tag{29}$$

If effusion is faster than decay, so that $\nu >> \lambda > \mu$, equation (29) becomes:

$$\varepsilon(\lambda) = \frac{3}{r}\left(\frac{D}{\lambda}\right)^{\frac{1}{2}} \tag{30}$$

in which the release efficiency only depends on the competition between the diffusion process and the radioactive decay.

On the other hand, if the condition $\lambda >> \nu >> \mu$ is fulfilled, which is the case very short-lived isotopes ($\nu > \mu$ is usually verified since diffusion is slower than effusion), release efficiency is inversely proportional to $\lambda^{3/2}$, so remarkably affected by the isotopic decay.

2.1.4. ISOL target requirements

Equation (29) and (7) clearly point out which are the main material properties and conditions that positively affect release efficiency, and more in general the radioactive ion beam yield, which can be increased by:

- reducing the grain size of the target material;
- working at the highest possible operating temperature;

- choosing a material characterized by a low adsorption enthalpy relative to the particle-surface interaction;

- reducing the number of collisions by properly designing the geometry of the system;

- choosing a material with a sufficiently high target nuclei density;

- maximizing the in-target production by selecting a material whose target nuclei interaction with the primary beam has a high cross section for the desired reaction (fission in the case of n-rich isotopes production);

- avoiding the presence of impurities with similar or higher masses with respect to the target nuclei, because they can have a high stopping power without contributing to the desired isotopes production.

The choice of the optimal grain size is strictly related to the sintering process, which can cause grain growth and pore size reduction in the target material. These two phenomena have the effect of increasing the contribution of diffusion to the release, so slowing the process. For this reason, since the initial dimensions of the grains have a remarkable effect on the sintering rate, sub-micron starting powders are not traditionally used for the production of ISOL targets [26].

In order to allow the produced isotopes to diffuse faster inside the target grains, temperature should be kept as high as possible: for each target material, used in high vacuum, the upper limit in temperature is not simply determined by its melting point, but more commonly in terms of its vapor pressure. A material with a high vapor pressure at the operating temperature can have a negative effect on the ion source functioning, due to the presence of unwanted species in the ionization volume. The upper limit in temperature defined by considering vapor pressure is called limiting temperature [33], which can be determined by computing thermal equilibrium composition versus temperature of the particular material under the operation conditions. However, since materials that make up a target must be in contact with each other, thermal dissociation and chemical reactions between different materials can alter the limiting temperature of the target through formation of volatile compounds [33].

Physicochemical and thermal properties are important as well in determining the applicability of a certain material as a fast releasing ISOL target. It is particularly important the comparison between these properties and those of the escaping particles: they should be ideally

very different, in order to limit the particle-surface interaction and adsorption during the release process. Thermal properties to take into particular consideration are emissivity and conductivity, which are important in determining the capability of the target to dissipate the power deposited in it by both the primary beam bombardment and the heating system used to keep it at high temperatures.

Among all the aforementioned requirements, temperature plays a key role in determining the successful release of isotopes, as shown in fig. 9, where the yield (in terms of secondary beam ions/μC) of different bromine isotopes obtained bombarding a uranium carbide target with protons is clearly dependent on the temperature at which the target is kept. This effect will be reported and discussed into more detail in chapter 3.

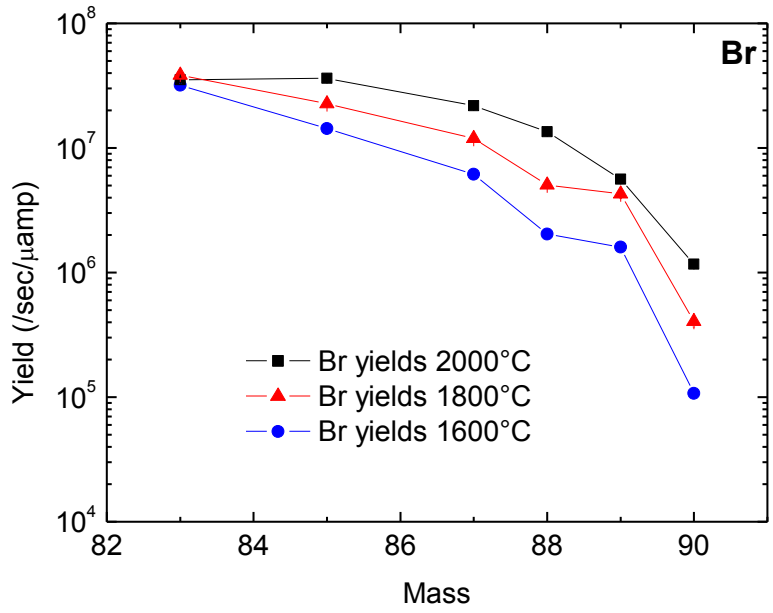

Fig.9 – The importance of temperature in RIBs production: yields of bromine isotopes obtained bombarding a uranium carbide target with protons, keeping the target at three different temperatures (see chapter 3).

Some general geometrical consideration must be done when designing a properly working ISOL target. In particular, the optimal target dimension can be determined from Fick's law, rewritten highlighting the contribution of generation and decay (S(t) and E(t), respectively) of the isotopes to their concentration [33]:

$$\frac{\partial n(t)}{\partial t} = D\nabla^2 n(t) + S(t) - E(t) \tag{31}$$

In which D is assumed to be independent from the concentration n. This equation has different solutions depending on the geometry of the target, the isotope half-life and the diffusion coefficient [33]:

- $x(cm) = \pi(D\,T_{\frac{1}{2}})^{\frac{1}{2}}$ for a plate of thickness x (32)
- $d_r(cm) \cong 4.8(D\,T_{\frac{1}{2}})^{\frac{1}{2}}$ for a rod of diameter d_r (33)
- $d_s(cm) = 2\pi(D\,T_{\frac{1}{2}})^{\frac{1}{2}}$ for a sphere of diameter (34)

2.1.5. Materials for ISOL targets

As already mentioned, the choice of the proper material to be used as a ISOL target is strictly related to the type of process that it will undergo when interacting with the primary beam. In the case of n-rich isotope production, a single target material can provide the whole desired spectra of isotopes, provided that it is fissile and that its interaction with the primary beam of a well-defined energy is characterized by a high enough cross section. On the other hand, to produce proton-rich isotopes, most of the times a single target can produce only a limited spectrum of species. In the following sections, a brief description of the different classes of materials which have been tested as ISOL targets will be given.

- Oxides. Oxide targets are usually constituted by sintered powders, fibers [33] or films deposited onto highly permeable substrates [34]. In order to use them particular attention must be kept to their interaction with the other target components (which are usually made of graphite and tantalum), limiting the contact surface if any kind of reaction is possible, otherwise the occurring of an undesired target-heating system interaction may lead to a decrease in the material limiting temperature. For this reason, when using oxide targets, tungsten or rhenium protective coatings on tantalum are used. As an example, the limiting temperature of Al_2O_3 at the pressure of ~$2.67 \cdot 10^{-4}$ mbar is 1900°C, and the same when in contact with W, but if in contact with Ta the limiting temperature falls down to ~1630°C. The decrease is even more evident if the Al_2O_3 target is put in contact with graphite, in which case the highest operating temperature is of about 1050°C [33]. As a

general rule, metal oxides cannot be put in contact with graphite at high temperature because of the occurrence of the reduction of the oxide to form either pure metal or metal carbide, eliminating huge amounts of CO. Common oxides used as ISOL targets are HfO_2[35], ZrO_2, Al_2O_3, CaO and MgO[36]. They are mostly used for the production of p-rich noble gases like Ar, or for p-rich fluorine beams like ^{17}F or ^{18}F.

With respect to carbides, oxides can be produced with a great purity, and they guarantee short delay between the primary beam bombardment and the maximum release. However, the release of species is slower than from carbides, and long-term operation of oxides is limited by the fact that they usually sinter at the operating temperatures, so having a negative effect on the release of short-lived isotopes.

- Borides. Several attempts have been made to use borides as ISOL targets, but the most refractory ones have shown a too slow release. In some cases, as for CaB_6 [36], the release was fast, but the amount of impurities contained in the material was too high, thus causing malfunctions in the ion source functioning.

- Sulfides. Only a few sulfides are sufficiently refractory to be used as ISOL targets. In particular, CeS has been used for the production of p-rich chlorine and phosphorous isotopes such as ^{33}Cl, ^{34}Cl [35], ^{29}P, ^{30}P [33], especially used in astrophysics experiments. CeS shows the same issues of reactivity seen in the case of oxides. It has the same limiting temperature in isolation, in contact with Ta and W, of 1900°C. However, when in contact with C, its limiting temperature falls to 1800°C. ThS is another example of refractory sulfide, in which the presence of the fissile Th atom opens the way for different reactions than in CeS. However, the contact with graphite must be avoided, since it lowers limiting temperature by 100°C with respect to the isolated material (from 2000°C to 1900°C).

- Pure metals. Metals, either in the form of sintered powders or thin foils have been extensively used as ISOL targets, especially for spallation based production. The most used metals belong to groups 4 and 5 of the periodic table, since they possess very high limiting temperatures and guarantee fast release of isotopes [26]. Particularly interesting is the case of the RIST target [37], developed and tested at ISOLDE, made of 3600 discs of 25 μm thick tantalum, with a hole in the middle of their surface, which has shown good release efficiencies for short-lived isotopes [38].

Liquid metal targets have been tested at HRIBF [35]: in particular the production of arsenic and gallium isotopes was carried out using liquid germanium as a target, whereas liquid nickel was used to obtain copper isotopes. Liquid metal targets offer some advantages with respect to solid ones: diffusion rates are several orders of magnitude faster, and convection currents can enhance the release of the produced nuclei by bringing them closer to the liquid surface. However, designing and effectively using liquid metals requires special attention to their interaction with the support material, since they tend to be very corrosive. In order to obtain a fast release of isotopes from the target, the liquid should form a thin layer on top of the support surface, but the high surface to volume ratio enhances the presence of vapor inside the vacuum chamber and consequently affects the performance of the ion source.

- Carbides. Since the early 70's, the research on materials for ISOL targets have been focused to carbides, and many off-line [26] and on-line [27] tests have been done to demonstrate their capability of fast releasing of short-lived isotopes. Nowadays uranium carbide is the most used ISOL target, because it combine the vast spectra of isotopes produced by the uranium fission with excellent thermal properties which allow to use it in the harsh conditions required by the ISOL technique in order to favor the isotopes release. To obtain a faster release of isotopes, often the material used as a target consists in a dispersion of the desired carbide in a matrix of excess carbon, which has proven to have a positive effect on release [36]. A more detailed analysis on carbides and specifically on uranium carbide and its properties will be given in chapter 3.

2.2. The SPES target

2.2.1. The target layout

In paragraph 1.3 a brief presentation of the SPES facility was given; its more critical part is surely the production area, where the primary proton beam (PPB) is converted into a radioactive ion beam (RIB). The SPES production area is constituted by the production target (that with the transfer line composes the target block), the ion source and all the experimental apparatus needed for their functioning which constitutes the target chamber and the front end, as shown in figure 10.

The target chamber is used to contain and support the target – ion source complex in a high vacuum environment, providing both the water for the cooling system and the electrical current needed to heat by Joule effect the production target and the ion source. A detailed internal view of the target chamber is given in figure 11.

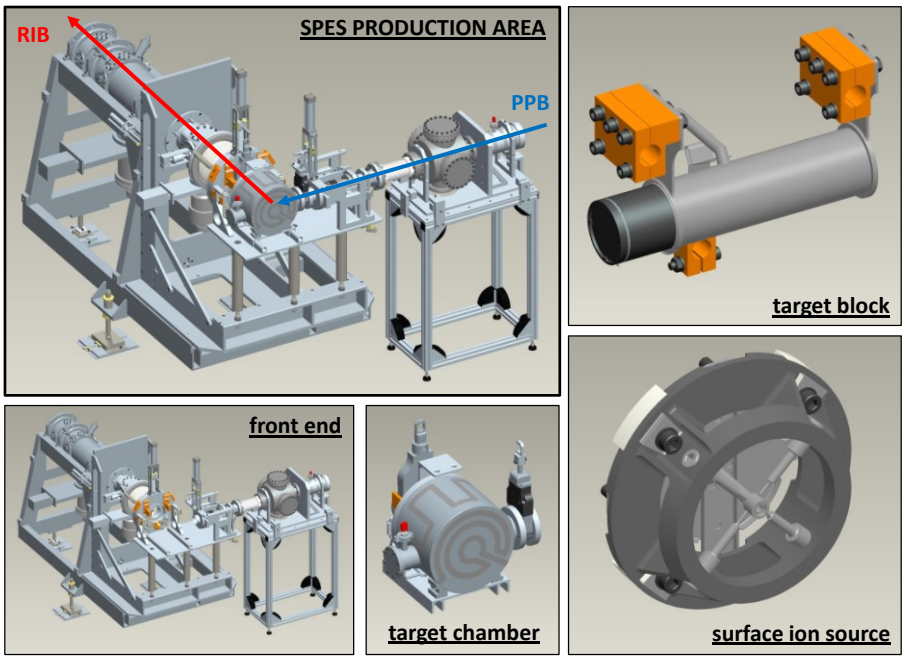

Fig. 10 – The main components of the SPES production area [5].

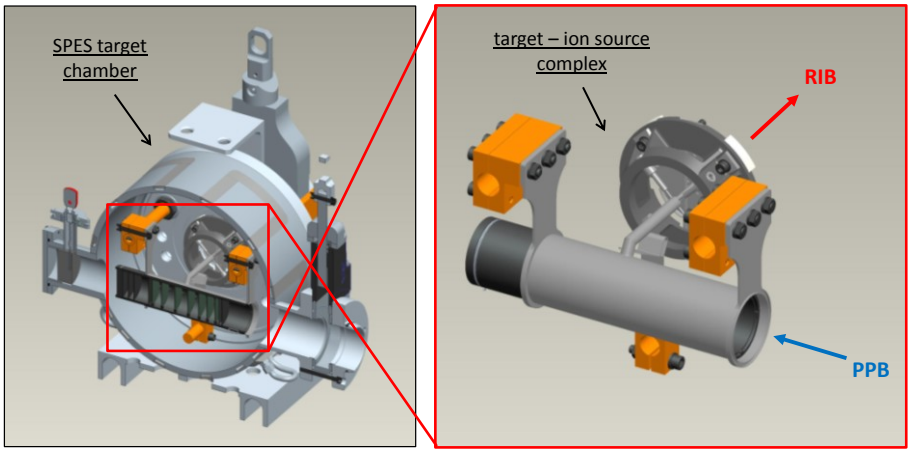

Fig. 11 – The SPES target chamber and the target – ion source complex [5].

The production target is composed of 7 co-axial discs made of uranium carbide characterized by an external diameter and a thickness equal to 40 and 1.3 mm, respectively: they are spaced in the axial direction in order to promote the dissipation (by thermal radiation) of the heat deposited by the primary proton beam, as shown in figures 12 and 13.

Two thin (0.2 mm) circular windows made of graphite are located at the proton beam entrance to prevent the undesired emission of the nuclear fragments, while four circular graphite dumpers, with thickness ranging from 0.8 mm up to 10 mm, stop the proton beam at the rear side of the target [39]. All discs, windows, and dumpers are located inside a tubular hollow box made of graphite, having an external diameter and an average length of 49 and 200 mm, respectively. Fig. 13 shows a graphite box loaded with 7 silicon carbide discs used for thermal studies in [5].

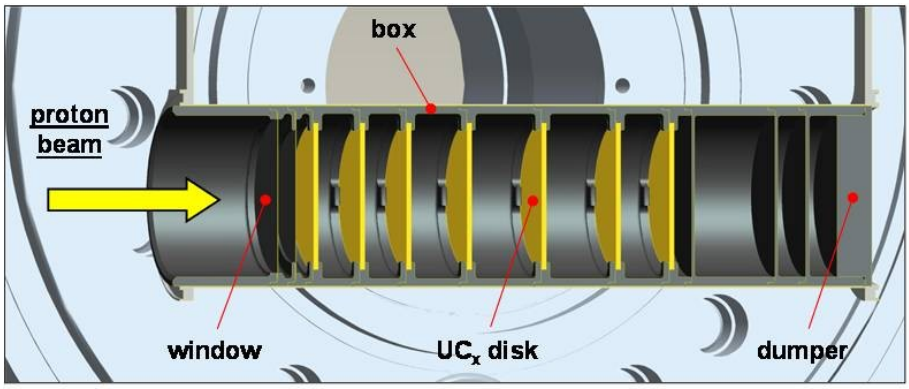

Fig. 12 – CAD representation of the SPES production target [5].

Fig. 13 –SPES graphite box loaded with 7 SiC discs and graphite dumpers and windows [5].

The box is positioned inside the target heating system, which is composed of a tantalum tube with an average length of 200 mm, an external diameter and a thickness of 50 and 0.35 mm, respectively. It is welded at its edges to two tantalum wings, which are directly connected to copper clamps (see fig. 14), through which an electric current delivered by a 10 kW power supply (maximum current I_{MAX} = 1000 A and maximum potential ΔV_{MAX} = 10 V) heats by Joule effect the Ta tube. Tantalum was chosen to build the heating system because it is an highly corrosion resistant transition metal with very good thermal and electrical conductivity (thermal conductivity and electrical resistivity at room temperature equal to 57 W/(m·K) and $1.34 \cdot 10^{-7}$ Ω·m, respectively, both increasing with temperature increase) and capable of operating at very

high temperatures: considering a working pressure of 10^{-4} Pa, Ta starts to sublimate at approximately 2200°C [40]. Moreover thanks to its low emissivity (0.15 at 1000°C and 0.26 at 2000°C), tantalum is able to screen efficiently the target box, limiting the cooling effect by thermal radiation.

Another important component of the target block is the transfer line (fig. 15), through which the radioactive atoms are transported from the production target to the ion source by effusion. The transfer line itself is generally kept at high temperatures to increase the mobility of the atoms but in some cases it can be water-cooled with the aim to improve the selectivity of the system. When the transfer line works at high temperatures it is heated by Joule effect making use of the same electrical circuit adopted to heat the ion source.

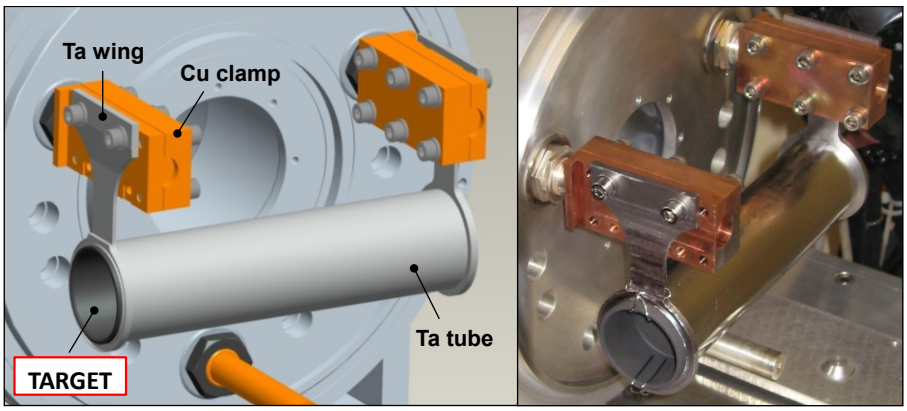

Fig. 14 – CAD representation (left) and picture (right) of the target heating system [5].

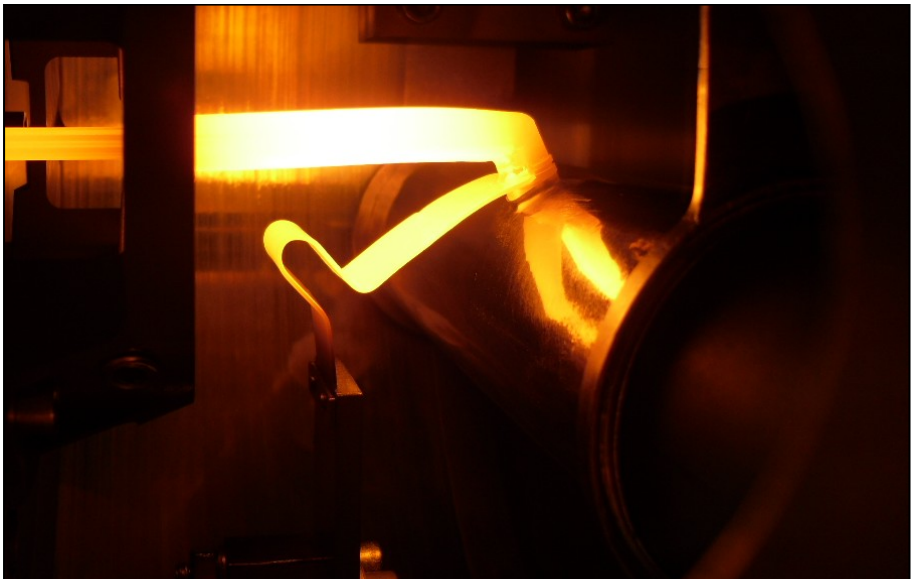

Fig. 15 – Transfer line heated at 2000°C. On its left side the hot cavity (smaller size tube) of the surface ion source can be noticed. On its right side, the transfer line is connected to the unheated target heating system [5].

2.2.2. The target performance

The interaction of the primary beam with the ^{238}U atoms is expected to give a fission rate of 10^{13} fissions/s, as shown in figure 16. In order to achieve this result, the energy and intensity of the primary proton beam are 40 MeV and 200 μA, respectively, leading to a power level of approximately 8 kW to be dissipated by the target.

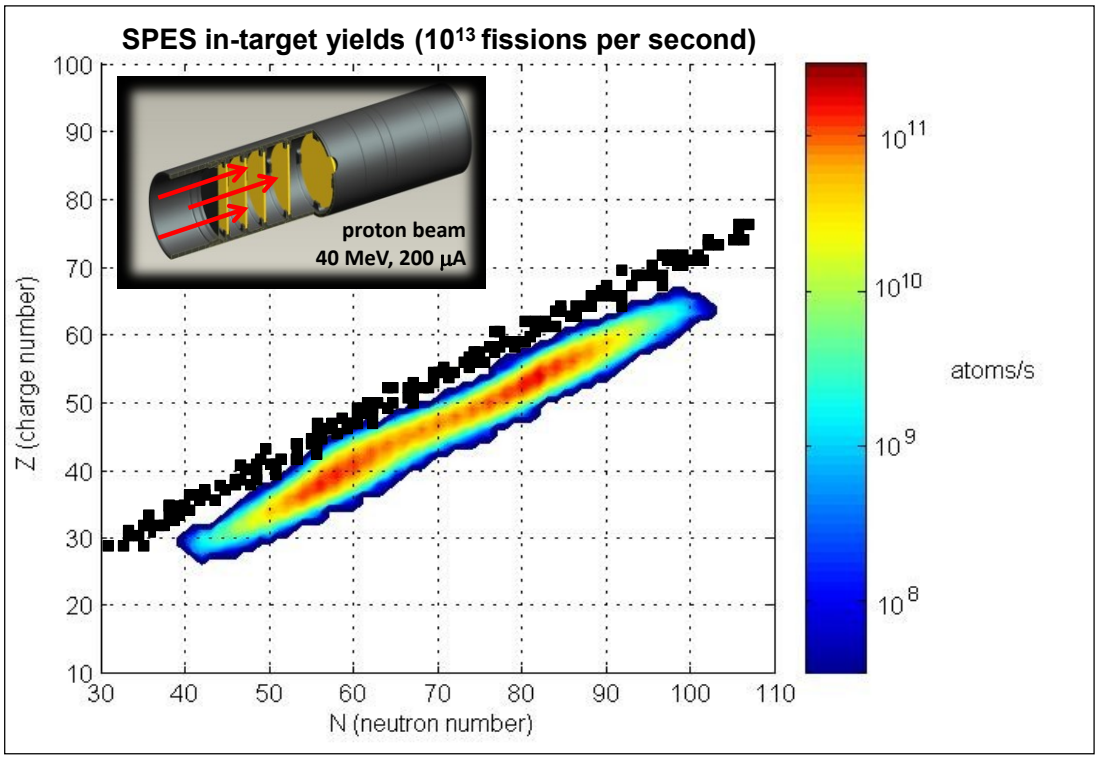

Fig. 16 – In-target isotope production as determined from eq. (4).

Huge effort [5, 10] have been made in order to characterize the contribution of the proton beam power to the target temperature, which should be as close as possible to 2000 °C to enhance diffusion and effusion, as previously seen in paragraph 2.1.4. If one considers only a graphite box as the one that will be used to contain the 7 SPES discs, the proton beam bombardment itself is not sufficient to make the discs reach 2000 °C [5], since graphite emissivity is very high [41] ($\varepsilon > 0.8$) and tend to exchange heat with the water-cooled surrounding chamber. However, the heating system described in 2.2.1 has proven to be capable of heating and shielding at the same time the graphite box, thus allowing the discs to reach the desired temperature. Fig. 17 reports the expected temperature distribution inside the target box at the current of 1300 A (the maximum current that can be applied to the heater in the off-line tests performed to characterize the SPES target-ion source) as calculated numerically in [5]. The

effect of the combined proton beam – heating system on the temperature of the 7 uranium carbide discs is shown in fig. 18.

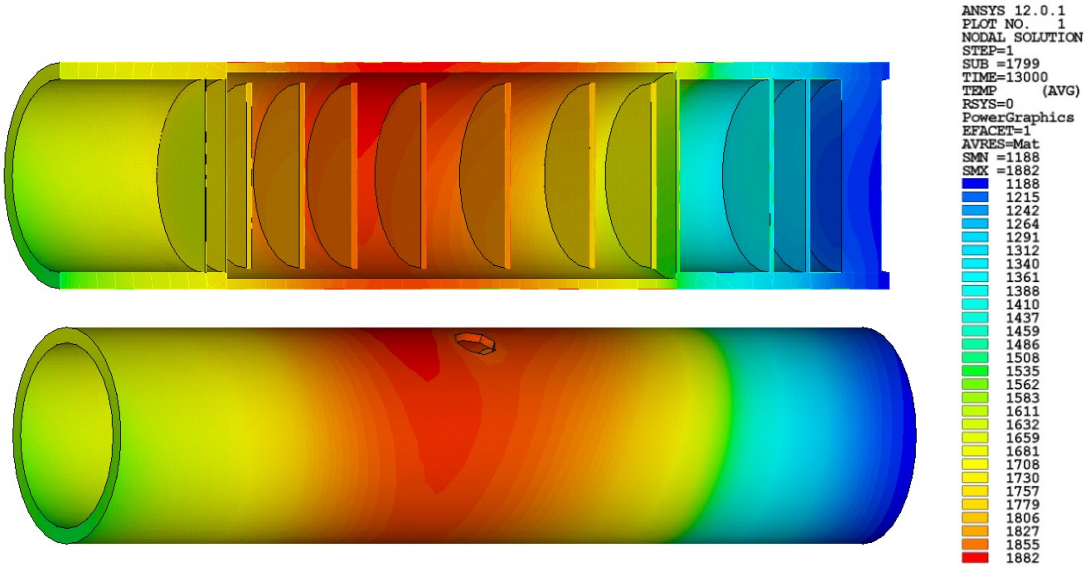

Fig. 17 – Temperature plot [°C] of the production target at 1300A without proton beam on target [5].

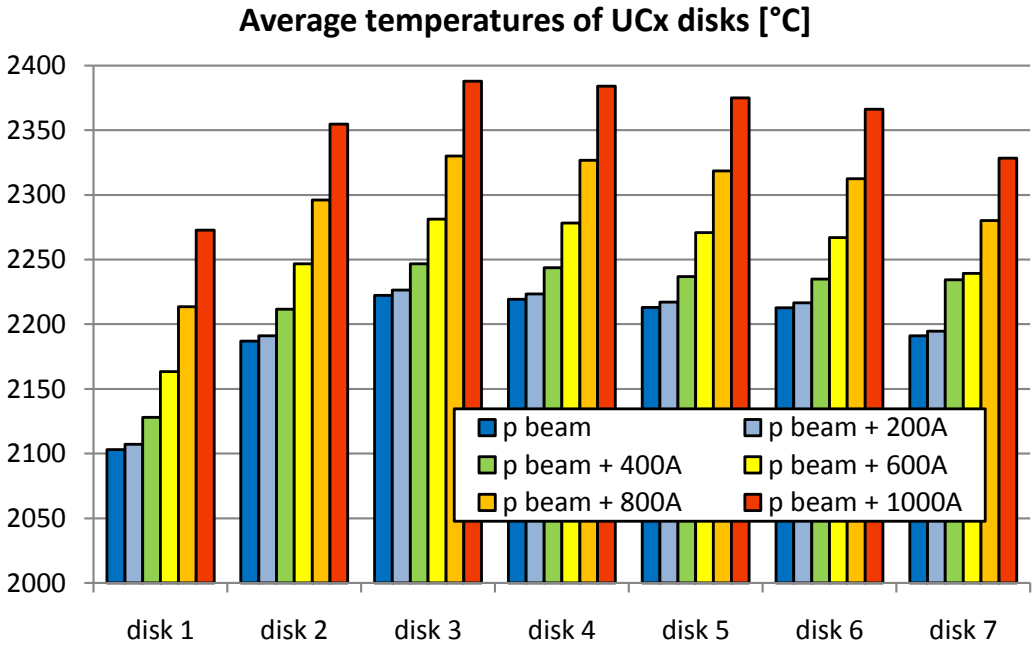

Fig. 18 - Average temperatures of the discs considering the proton beam thermal load and additional current applied to the target heating system [5].

Figs. 17 and 18 can be used to describe of the target heating procedure during an on-line experiment: usually before the proton beam bombardment the target system is heated up in order

to let all its components outgas at the maximum reachable temperature using the heating system, thus improving the vacuum conditions inside the target chamber, which are important for the ion source functioning. During the first stages of the proton beam bombardment, the heating system is gradually switched off, so that the proton beam reaction with the target can itself keep the discs above 2000 °C.

Chapter 3

The SPES UC_X target for the production of neutron-rich isotopes

As anticipated in chapter 2, the SPES target for the production of n-rich isotopes will be constituted of thin uranium carbide discs. The use of this type of material will allow to make use of the ^{238}U atoms fissionability and at the same time working at high operating temperatures, T > 2000°C in high vacuum, factors that have a positive effect on the isotopes release from the target and allow for an efficient heat dissipation through irradiation (power dissipation governed by the Stefan-Boltzmann's law, so depending on T^4). Before describing into details the production and testing of different uranium carbide target prototypes, a general introduction on carbides and more specifically on uranium carbide is given in the following paragraphs.

3.1. Introduction: carbides

Carbides, and in particular actinide carbides, surely represent the most used targets for ISOL facilities (see paragraph 2.1.5).

Generally speaking, a carbide is a compound formed by carbon with other elements with lower or about equal electronegativity [42, 43]. Most of these compounds can be considered ceramics, and some of them are actually refractory, since they possess high thermal and chemical stability and can therefore be used in extreme environments.

Although the synthesis of carbides is a relatively easy and well-known process, particular attention must be given to the oxygen contamination, which can have a huge impact on the material properties even at extremely low concentrations [44]. Oxygen dissolution in the material can occur rapidly if the carbide lattice is not saturated by carbon atoms, or more slowly during a process in which carbon atoms are gradually removed from the lattice. In order to diminish the quantity of dissolved oxygen in the carbide lattice, a high temperature thermal treatment in high vacuum (up to 2000 °C at pressures of ~10^{-6} mbar) can be performed.

The synthesis methods adopted to obtain carbides include:

- Direct reaction of a metal with carbon, which is carried out at high temperature (T > 2000 °C), allows the formation of relatively pure carbides of different stoichiometries. However metal powders, especially those of alkali and alkaline-earth metals are highly reactive towards air so that the incorporation of oxygen in the final carbide can occur.

- Carbothermal reduction, which is the reaction of a metal oxide with a carbon source (graphite, charcoal, pyrolitic carbon) at high temperature. This reaction is typically carried out in high vacuum in order to limit the oxygen contamination of the material. More details about this type of synthesis will be given in this chapter, since it is the main production route for the SPES target prototypes described in this work.

- Reaction of the metal with gaseous hydrocarbons, which is typically used to obtain thin films. This method requires a lower temperature with respect to the direct metal-carbon reaction, but the high purity gas needed for the reaction can be expensive. Moreover, the metal powder must be finely ground, in order to increase the surface available for the solid-gas reaction, but in this way the possibility of oxygen contamination and uptake in the final carbide is enhanced.

- Sol-gel process, which uses a liquid reactive precursor or the metal that is converted to the final product by chemical and thermal means. The metal precursor is initially put in contact with a well-defined solvent, in order to form a colloidal suspension, which is then transformed into a gel (constituted by a liquid dispersed in an interconnected solid phase). The gel is then dried to obtained a solid metal precursor-carbon precursor mixture and subsequently fired (pyrolized) to form the final carbide [45]. The temperatures required for this process are generally lower than those of the other production processes.

Carbides can be classified in four general categories [43], which are described as follows.

- Salt-like carbides, which are formed with carbon and the most electropositive elements, found in groups 1, 2, 3 of the periodic table, with the addition of Al and several lanthanides and actinides. The difference in electronegativity in most cases – with the exception of Al and Be – between metal and carbon is higher than 2 so resulting in a metal-carbon atomic bond which is at least 50 % ionic. These type of carbides can be further classified according to the anionic form of carbon, which can be either C^{4-}, C_2^{2-} or

C_3^{4-}. The first case is relative to the so-called methanides, such as Al_4C, which evolve methane on hydrolysis:

$$Al_4C_3 + 12H_2O \rightarrow 4Al(OH)_3 + 3CH_4 \quad (35)$$

The most known and better characterized methanides are Al_4C_3 and Be_2C: the first is obtained from the reaction between beryllium oxide and carbon at 2000 °C, the latter is synthesized from the direct reaction between aluminum and carbon in an electric arc furnace.

Alkaline, alkaline-earth and lanthanide carbides containing the C_2^{2-} anion are commonly called acetylides, since they release acetylene when in contact with water, like in the case of CaC_2:

$$CaC_2 + 2H_2O \rightarrow Ca(OH)_2 + HCCH \quad (36)$$

Lanthanide carbides can be obtained by heating a mixture of M_2O_3 (where M is the lanthanide element) and carbon in an electric furnace, or by direct combination of M and C by means of an electric arc fusion in inert atmosphere [46]. They are highly reactive towards water and on hydrolysis release complex mixtures of hydrocarbons. Most of the lanthanide carbides have a CaC_2-like structure, obtained from the distortion of a NaCl-like cubic cell to tetragonal due to the presence of two carbon atoms in the cell edge. However, with respect to CaC_2, the lanthanide (and some actinide such as UC_2) carbides show a higher C-C bond length, and the metal in their structures is essentially trivalent. These two aspects indicate that not only two, but three electrons are shared in the metal-carbon bond, thus resulting in an enhanced electrical conductivity in lanthanide carbides with respect to other salt-like carbides. More details on the chemistry of UC_2 and LaC_2 will be given in the following.

The C_3^{4-} anion is found in lithium and magnesium carbides, Li_4C_3 and Mg_2C_3, which yield several hydrocarbons such as methylacetylene and propadiene on hydrolysis [46].

- Covalent carbides, which are formed by elements that approach carbon closely in size and electronegativity. Although some carbides like Be_2C are partially covalent, only SiC and B_4C are considered covalent carbides. These two types of carbides, in particular B_4C, will be described in more detail in chapter 4.

- Interstitial carbides, formed when the difference in electronegativity and also in size between the metal atom (usually a transition metal) and carbon is large. This allows the carbon atoms to occupy the octahedral interstices of the close-packed metal lattice without significant distortions. The bonding is partly covalent and ionic, but mostly metallic which explains why the interstitial carbides closely resemble metals [43]. The electron band structure and other characteristic of the pure metal are not altered by the insertion of the carbon atoms, which at the same time further stabilize the metal lattice, thus increasing hardness and raising the melting point [42]. Interstitial carbides indeed have the highest melting point over all binary compounds, very high hardness and unusually high thermal and electrical conductivity for ceramic materials. If the atomic radius of the metal is sufficiently high, monocarbides (MC, like for example in TaC, ZrC, HfC) are formed; in most cases however, a metal can form several interstitial carbides with different stoichiometries. The transition metal interstitial carbides are generally chemically inert at room temperature, and only attacked by oxidizing acids and hydrofluoric acid [47], but however they show oxidation at high temperature [48].

- Intermediate carbides, which are formed by carbon with different elements of groups 6, 7, 8 and 9 such as manganese, nickel, iron, cobalt and chromium. The atomic radius of the metal is in these cases too small to accommodate the carbon atom in interstitial sites without severe distortion of the lattice. As a consequence of that, carbon atoms are close enough for carbon-carbon bond and carbon chains to form. These carbides are hydrolyzed by water or dilute acids, to produce hydrocarbons and hydrogen, and are not refractory, the only exception being Cr_3C_2. These carbides are considered intermediate between interstitial and salt-like carbides.

3.2. Uranium carbide

3.2.1. General properties

As already reported in literature in early works by Rundle et al. and Litz et al. [49, 50], uranium carbide exists in three stoichiometric phases: UC, U_2C_3 and UC_2. Fig. 19 reports the uranium-carbon phase diagram at atmospheric pressure, as taken from [51].

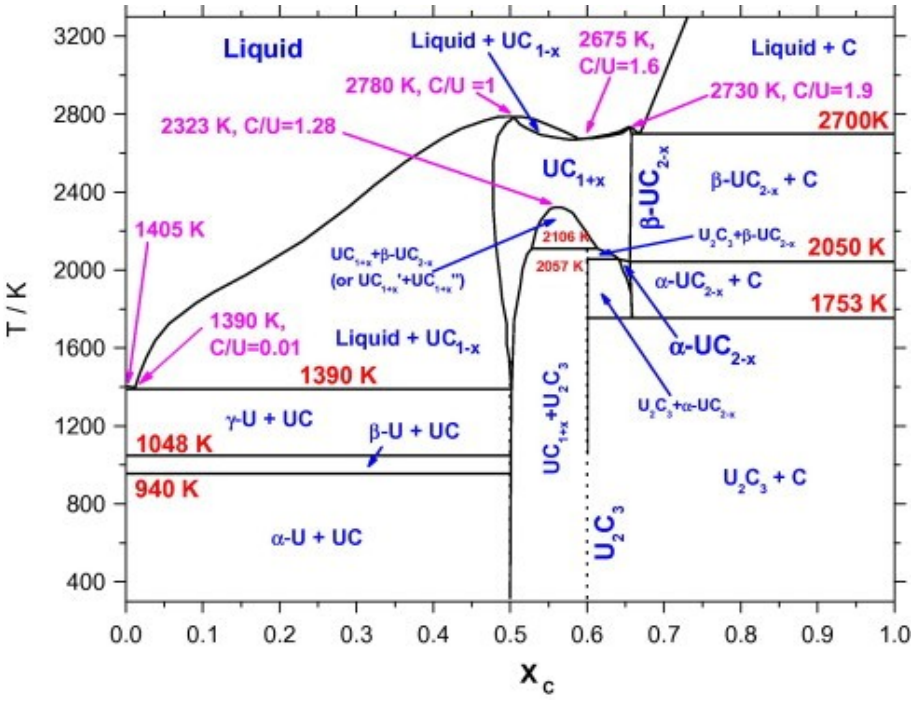

Fig. 19 – U-C phase diagram at atmospheric pressure, after [51].

Uranium monocarbide (UC) is face-centered cubic with rock-salt structure, a_0 = 4.96 Å [52], and it is the most stable phase from room temperature up to about 2500 °C. Its properties have been extensively studied since it is used as a nuclear fuel due to its favorable characteristics [53] such as high uranium density, high melting point and thermal conductivity. In addition to that, it maintains its crystallographic structure in a large domain of nonstoichiometry at high temperatures. At T > 1130 °C indeed it can exist in both hypostoichiometric and hyperstoichiometric forms, generally indicated as $UC_{1\pm X}$.

Uranium sesquicarbide (U_2C_3) is cubic body centered with Pu_2C_3 strucure, a_0 = 8.1 Å [54], metastable at low temperature [55], where UC+C are the stable phases. Its window of phase stability goes from approximately 900 °C up to 1820 °C, where it decomposes to form UC and UC_2. The existence of a so wide range of stability should suggest the possibility to obtain it from raw materials in the same way as UC and UC_2 are formed (see next paragraph). However, when trying to perform such synthetic processes, the carbide phase of the composition C/U = 1.5 is always found to be a mixture of UC and UC_2 [56].

Uranium dicarbide (UC_2) is stable at high temperatures, since it forms above 1480°C and melts at about 2427°C. In this range of existence, two polymorphs of UC_2 have been observed: the high temperature cubic form (β-UC_2) and the low temperature tetragonal form (α-UC_2). The martensitic phase transformation $\alpha UC_2 \rightarrow \beta UC_2$ occurs at approximately 1777°C (see fig. 18,

2050 K). Both forms have a range of hypostoichiometry (namely αUC_{2-x} and βUC_{2-x}), the limits of which are determined by their equilibrium with U_2C_3.

Table 1 reports some physical and chemical properties of the three aforementioned uranium carbides [57].

Table 1 – Properties of the three types of uranium carbide.

	UC	**U_2C_3**	**UC_2**
Theoretical density (g/cm^3)	13.63	12.70	11.28
Uranium density (g/cm^3)	12.97	11.81	10.25
Melting point (°C)	2507	1820 (dec.)	2427
Crystal structure	NaCl - FCC	BCC	β: NaCl - FCC α: CaC_2 - Tetragonal
Lattice parameter	a_0 = 4.96 Å	a_0 = 8.10 Å	β: a_0 = 5.49 Å α: a = 3.52 Å, c = 5.99 Å

3.2.2. Synthesis

Synthetic routes to produce bulk uranium carbide samples, either for research or to be used as nuclear fuel have been known and exploited since several decades [50, 58]. The main methods are equal to those described for a generic carbide, and comprehend [59]:

- Arc melting of metallic uranium with carbon or solid state reaction of intimately mixed U and C powders at high pressure, according to:

$$xU + zC \rightarrow U_xC_z \tag{37}$$

  in which z/x can be equal to 1, 1.5 or 2 depending on the type of uranium carbide formed, z/x = 1 in the solid state reaction.

- Alkan route, which consists of the following steps:

$$U_{massive} + \frac{3}{2} H_2 \xrightarrow{250\,^{\circ}C} UH_3 \quad (38)$$

$$UH_3 \xrightarrow{600\,^{\circ}C} U_{powder} + \frac{3}{2} H_2 \quad (39)$$

$$U_{powder} + CH_4 \xrightarrow{600\,^{\circ}C} UC + 2H_2 \quad (40)$$

Dehydriding UH_3 and carburization of the uranium powder formed to UC are carried out in a stream of methane (or propane) gas at 600 – 700 °C. This method is chosen to produce sinterable UC powder, which is cold-pressed and sintered under inert atmosphere. The use of propane produces a purer carbide product, since it contains less nitrogen and oxygen with respect to commercial methane. By varying parameters such as gas flow, temperature and time, any degree of substoichiometry can be attained, but it is difficult to produce hyperstoichiometric carbide with this process [59].

- Carbothermal reduction of uranium oxide with carbon:

$$U_xO_y + (z+y)C \rightarrow U_xC_z + yCO \quad (41)$$

in which the carbon required for the reaction can be either graphite or other precursors. This type of reaction will be better analyzed in the next paragraphs since it is the most commonly used for the production of uranium carbide targets for ISOL facilities, and therefore it has been extensively used for SPES target prototypes production [60].

In addition to the aforementioned techniques, uranium sesquicarbide can be obtained either applying mechanical stresses onto a UC-UC_2 mixture or by heating it a 1500 – 1600 °C, or by the reaction of UC and carbon in vacuum, or again by the partial decarburization of UC_2 using MgO as a reducing agent [56].

3.2.3. Thermal properties

Thermal properties are important in determining the behavior of a uranium carbide based target when exposed to the extreme conditions required to obtain a fast release of radioactive

isotopes. Not only material sensitivity to strong temperature gradients has to be considered, but also the effect of working in high vacuum must be taken into account.

- Thermal conductivity. In literature very few data are available relatively to thermal conductivity of the different types of uranium carbide. The most important contribution to this field of research was given by R. De Coninck et al. [61, 62, 63], who obtained thermal conductivity values for UC, UC_2 and U_2C_3 performing thermal diffusivity measurements using the laser-flash technique [64]. More recently, thermal conductivity measurements on UC_2 have been performed by Greene and co-authors [65] in the framework of the research on targets for ISOL facilities. Thermal diffusivities and conductivities of the three types of carbide are reported in table 2, together with the temperature interval in which they have been obtained. Density of the analyzed samples is also indicated for the two different UC_2 measurements found in literature, as a percentage relative to the theoretical density (TD).

Table 2 – Thermal diffusivity and conductivity of the three types of uranium carbide.

	Thermal diffusivity, α (m^2/s)	**Thermal conductivity, k (W/m·K)**
UC	$5.7 \cdot 10^{-6} \div 6.1 \cdot 10^{-6}$ (1000 ÷ 2200 °C) [61]	20 ÷ 25 (1000 ÷ 2200 °C) [61]
UC_2	$3.8 \cdot 10^{-6}$ (600 ÷ 2060 °C) [62] --	13 ÷ 20 (600 ÷ 2060 °C) [62] ρ = 99.5 % TD 5 ÷ 8 (1500 ÷ 1880 °C) [65] ρ ~ 44% TD
U_2C_3	$3.2 \cdot 10^{-6}$ (790 ÷ 1790 °C) [63]	11 ÷ 16 (790 ÷ 1790 °C) [63]

- Thermal expansion coefficient. Early high temperature neutron diffraction experiments allowed the determination of α for U_2C_3 and the two polymorphs of UC_2 [66], whereas an important contribution to the calculation of α for UC and U_2C_3 was given by Mendez-Peñalosa and Taylor [67, 68]. Table 3 reports mean thermal expansion coefficient values found in literature.

- Vapor pressure. This property, as already stated, is extremely important in determining the possibility to use a target at high temperature in a high vacuum environment. Fig. 20 shows the vapor pressure of uranium over different uranium carbide compositions [44].

Table 3 – Mean thermal expansion coefficient of the three types of uranium carbide.

	Mean thermal expansion coefficient, α ($°C^{-1}$)
UC	$1.1 \cdot 10^{-5}$ (20 ÷ 1000 °C) [58] $1.2 \cdot 10^{-5}$ (20 ÷ 2000 °C) [67]
UC_2	β: $2.5 \cdot 10^{-5}$ (1765 ÷ 2300 °C) [66] α: $1.8 \cdot 10^{-5}$ (1000 ÷ 1765 °C) [66]
U_2C_3	$1.4 \cdot 10^{-5}$ (1100 ÷ 1730 °C) [66] $1.2 \cdot 10^{-5}$ (20 ÷ 1700 °C) [68]

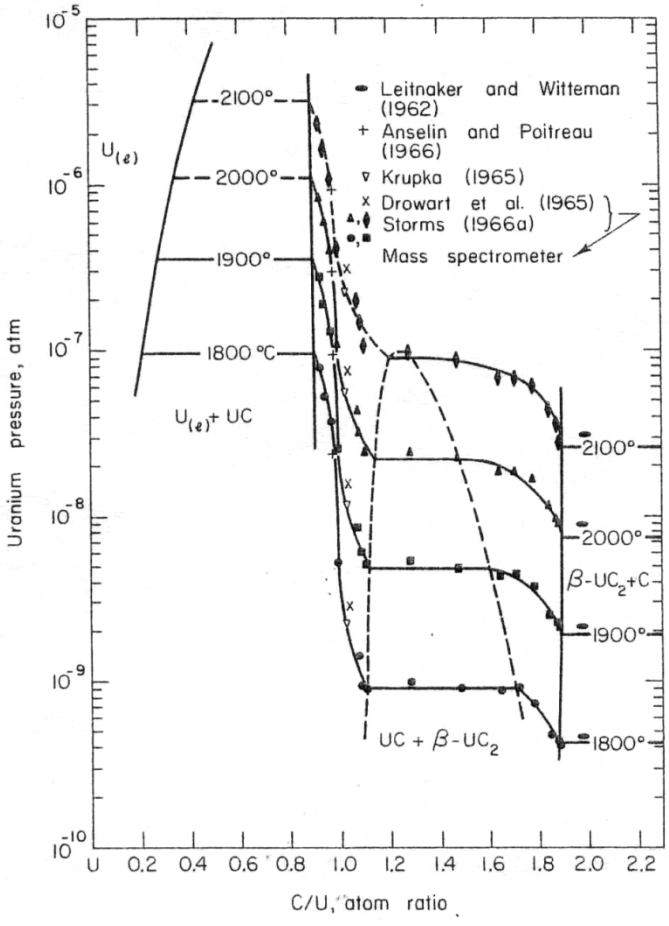

Fig. 20 – Uranium vapor pressure over different uranium carbides, after [44].

It is verified that for carbides with C/U < 1 at different temperatures obviously different values of vapor pressure are obtained, and that these values are constant throughout all the compositional range considered. However, when approaching C/U = 1, a rapid

decrease of vapor pressure is observed. It is known that in the C/U < 1 case sublimation of uranium is the main phenomenon occurring, whereas for C/U > 1 the release of $UC_2(g)$ and a small quantity of $UC_4(g)$ have been observed [44]. Since the uranium carbide used for ISOL targets have usually the UC_2 + xC composition [60], it is important to determine whether they can sustain high vacuum – high temperature conditions: values reported in fig. 20 show that for U:C = 1:2 at 2000 °C, the uranium vapor pressure is approximately 10^{-5} mbar (10^{-8} atm), so compatible with the operational requirements for the common ion sources used for the radioactive ion beams production.

3.2.4. Reactivity

Even if uranium carbide is used as a target for ISOL facilities in conditions of high vacuum, reactivity issues must be taken into account, since UC and UC_2 are difficult to prepare free from oxygen and nitrogen contamination [69, 70]. Moreover, since there is a great difference in weight between uranium and the interstitials (C, N and O), a very small weight percentage of the latter represents a substantial atomic percentage [69]. Both oxygen and nitrogen are found in solid solution in the monocarbide structure. The presence of impurities within the uranium carbide structure can deform the unit cell geometry [49], and in the case of UC_2, might have also a stabilizing effect on this phase at room temperature [71].

- Reactivity towards nitrogen. UC and UC_2 can react with nitrogen above 550 °C, to form mainly U_2N_3, but also UN and traces of UN_2 [72]. UC_2 reactivity seems to be higher than that of UC [72]. Above 1200 °C, virtually all the C atoms in UC can be substituted by N atoms, causing the UC lattice contraction to occur. In the U/C = 1 case, the increase of N atoms concentration causes the lattice parameter to approach that of UN. Nitrogen is insoluble in UC_2 and U_2C_3; however, its presence can inhibit the U_2C_3 formation, and moreover it can favor the UC_2 formation from UC [44].

- Reactivity towards oxygen. Oxygen solubility in uranium carbide depends on several factors, the most important of which are their stoichiometries, the thermal treatment temperature and the CO pressure during their production (if they are produced by means of the carbothermal reduction synthesis seen in paragraph 3.2.2). Solubility studies performed on the UC-O_2 system are complicated by the easy hydrolysis of uranium carbides, so that the revealed oxygen can be either attributable to its dissolution inside the

carbide or it can have been deposited on the material surface during its manipulation. UC powder can contain a significant amount of oxygen even if kept at room temperature [44], and can ignite above 300 °C to form U_3O_8 [73]. Below 230 °C, UC reactivity with oxygen can lead to the formation of UO_3, UO_2 and free carbon [74]. At low oxygen pressures ($\sim 10^{-4}$ mbar), heating at 900 °C of UC causes the growth of UC_2 and UO_2 layers on its surface [44], with liberation of CO and CO_2 [74].

- Reactivity towards water. Bradley and Ferris [75, 76, 77] as well as Pollard et al. [78] studied in detail the reaction of the different uranium carbides with water between room temperature and 100 °C. Hydrolysis of UC yields UO_2 and a gas mixture composed mainly of methane, with a minor amount of hydrogen and ethane, with traces of C_3 to C_6 saturated hydrocarbons. UC_2 reaction with water is faster than in UC, and yields mainly hydrogen (40% vol.), 15% vol. methane and 45% vol. of C_2 to C_6 both saturated and unsaturated hydrocarbons. The formation of these reaction products is an indirect confirmation of the presence of C_2 units in the dicarbide lattice. In the case of U_2C_3 hydrolysis, the main reaction products are hydrogen and ethane, with minor amounts of methane and other alkanes, alkenes and alkynes.

3.2.5. Uranium carbide as a ISOL target

Since early experiments with radioactive ion beams, graphite matrices containing uranium carbide have been a natural choice as targets, exhibiting short delay times for a variety of fission produced elements [79, 80, 27].

Although several types of uranium carbide have been used in ISOL facilities, nowadays uranium carbide dispersed in excess graphite, namely UC_X, is the most used target for the production of RIBs [60, 81, 82]. The most common synthetic route to obtain it is the already described in paragraph 3.2.2 carbothermal reduction of a primary uranium compound, which is performed under vacuum in order to [60]:

- Obtain the desired reaction at lower temperatures with respect to the same process carried out under inert atmosphere.

- Enhance the formation of pores resulting from the gas generation (mainly CO) during the reaction at T > 1000 °C.

Other ways to obtain usable uranium carbide based targets are the deposition of UC_X onto refractory matrixes [83] or arc melting of metallic uranium and carbon [81, 82].

In the case of the carbothermal reduction synthesis, much effort has been made in order to characterize the effect of the starting precursors properties on the final carbide characteristics [60] and release behavior [81]. Several aspects have been investigated, such as:

- Differences in the final material microstructure changing type of uranium oxide, namely UO_2, UO_3 or U_3O_8 [60].

- Effects in the final material release and microstructure of using uranium oxalates in place of uranium oxides [81].

- Effects of the type of carbon excess, in particular in the case of fibers [81] or nanotubes [84], on the release of isotopes from the target.

- Differences between UC_2-based and UC-based targets [81][82].

The effect of changing type of uranium oxide as a starting material has been investigated by L. Biasetto and co-authors [60] by studying the following reaction, using UO_2, U_3O_8 and UO_3 as uranium sources, keeping the n/x ratio equal to 4:

$$U_xO_y + (z + y + n)C \rightarrow U_xC_z + nC + yCO \quad (42)$$

Mass spectrometry studies performed during the occurrence of the reaction showed that U_3O_8 and UO_3 decomposed to UO_2 before the start of the reaction (42), and therefore the final samples did not differ one another in terms of grain size and porosity. The use of reaction (42) resulted in a porosity of more than 60%, which was mostly open, so favorable for application as a ISOL target.

The use of oxalate and carbon nanotubes as metal and carbon precursors, respectively, was successfully tested in the development of lanthanum carbide [85, 86, 87], which was suggested as a substitute of uranium carbide for preliminary bench tests on the production and characterization techniques developed at SPES [60]. The use of such precursors resulted in a

final material with a controlled amount of porosity, with dimensions ranging from few nanometers to some microns.

The influence of the type of uranium carbide used as a target was recently analyzed by B. Hy et al. [81], who showed that UC_2-based targets possess generally better release than UC-based targets, especially when their production results in a higher porosity with respect to monocarbide targets. This work clearly highlights the direct relation between porosity and release, especially at low temperature.

3.3. On-line test of SPES UC_X target prototypes at HRIBF

3.3.1. Introduction: the OLTF at HRIBF

After demonstrating the capability to produce and successfully characterize uranium dicarbide-graphite porous materials as targets for the SPES project in [60], the attention has been moved to the possibility of performing on-line tests of such kind of materials. In particular, in order to obtain information about the capability of the material to produce and release radioactive isotopes in conditions as similar as possible to those of the SPES facility, two UC_X target prototypes were tested at HRIBF.

As introduced in 1.3, HRIBF is a ISOL radioactive ion beam facility of Oak Ridge National Laboratory (ORNL) [88]. Among all the worldwide ISOL facilities, it is the most similar to SPES, and the most suitable to test SPES targets, for three main reasons:

- The two facilities have the same energy of the primary proton beam, 40 MeV.

- The layout of SPES and HRIBF, especially in terms of target-ion source geometry and parameters, is very similar.

- A part of HRIBF is dedicated to on-line test of targets and ion sources, the OLTF (On-Line Test Facility).

For this reason, a collaboration between SPES and HRIBF has been active since 2007, when a silicon carbide SPES target prototype was tested [12].

OLTF is primarily used for the development and characterization of targets and ion sources to be used for the production of radioactive ion beams at the HRIBF. The general layout of the OLTF is presented in fig. 21.

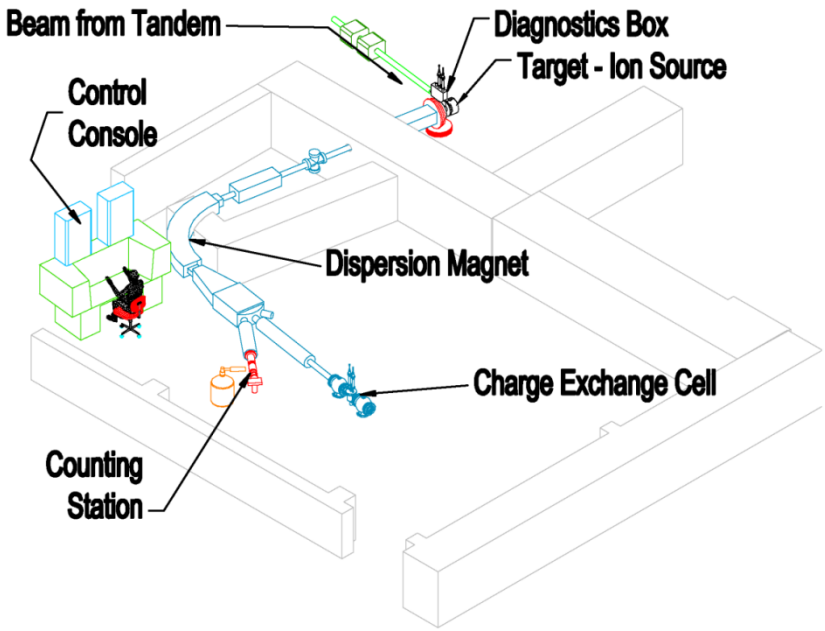

Fig. 21 – Layout of the OLTF at HRIBF.

OLTF consists of a high voltage platform for the ion source, a versatile extraction system, a beamline with electrostatic elements for focusing and steering the beam, a dipole magnet for mass analysis, and beam diagnostics. The RIB production target and ion source (commonly named TIS) are contained in an enclosure on the high voltage platform, which can operate at either positive or negative potential up to 60 kV. The extraction electrode can be moved along the extracted beam axis; just downstream, rigidly coupled with the electrode, there is an Einzel lens. After that, a set of vertical and horizontal electrostatic steerers are used to center the beam. Mass analysis of the extracted beam is accomplished with a 90° dipole electromagnet with a nominal mass resolution, $M/\Delta M = 2000$. Ion beams with energies up to 50 keV and mass up to 270 amu can be analyzed and delivered to the diagnostics station after the dipole magnet.

Faraday cups and beam profile monitors are used to control the beam intensity, shape, and position during operation. A retractable Faraday cup is occasionally inserted to measure the total beam intensity before the mass analysis magnet. After the bending magnet, a Faraday cup at the

focal point is used to measure the beam current of a single mass, which is useful to optimize the tune of the system before the beam is directed to the diagnostic counting station where the yields are measured. The beam is then focused onto a moving tape collector, which uses a 8 mm wide, aluminized Mylar tape that is incorporated into a Faraday cup. After some predetermined collection time, the tape is moved along the line to a counting position, where the γ-rays from the decay of the collected beam particles are detected using a high-purity Ge detector. The yield in terms of atoms/μC of each isotope is then calculated as described in Appendix A.

3.3.2. Target – ion source (TIS) system at OLTF

For the two tests performed at HRIBF the same target-ion source system was used, corresponding to the standard TIS used at OLTF to perform on-line preliminary tests on materials that will be used as targets for the generation of RIBs. As shown in fig. 22, the TIS used in these tests has a very similar layout to that of the SPES final configuration, previously reported in figs. 10-13.

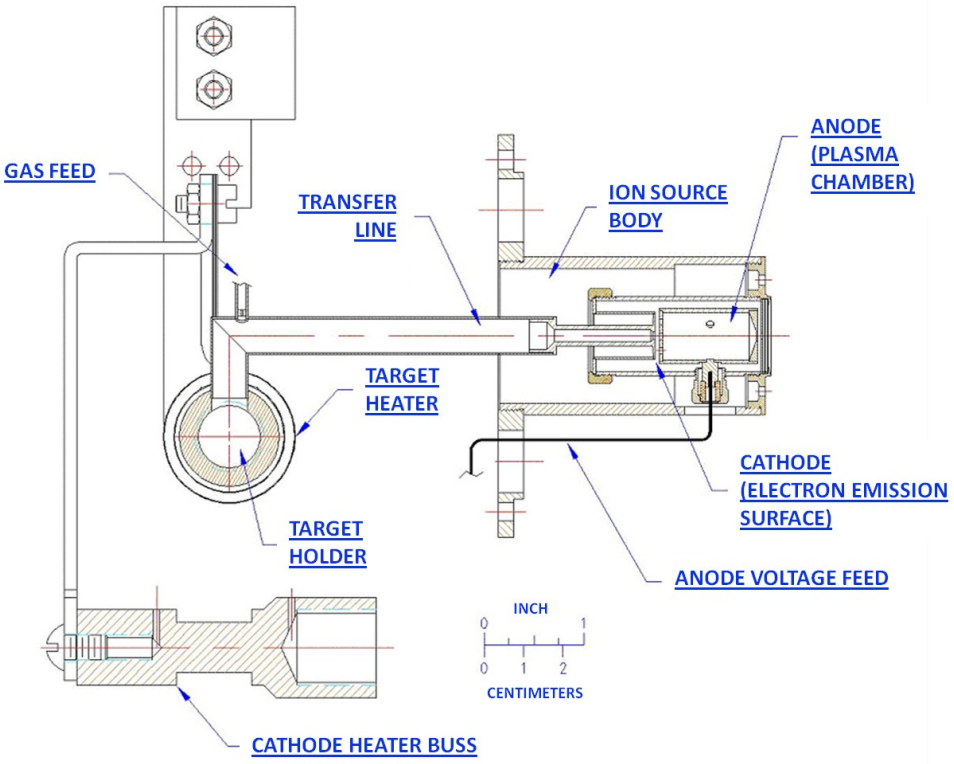

Fig. 22 – Target - ion source system of the OLTF.

In both the tests, seven UC_X target discs were held in a graphite holder that was inserted into a tantalum heater. The whole system was closed inside a water cooled vacuum chamber shown in fig. 23. The discs were downscaled from the original SPES optimal diameter (40 mm) to about 13 mm, and the same was done with the graphite box, in order to fit the geometrical constraints of the OLTF target heater. More details on the discs characteristics in the two different tests will be given in the following paragraphs.

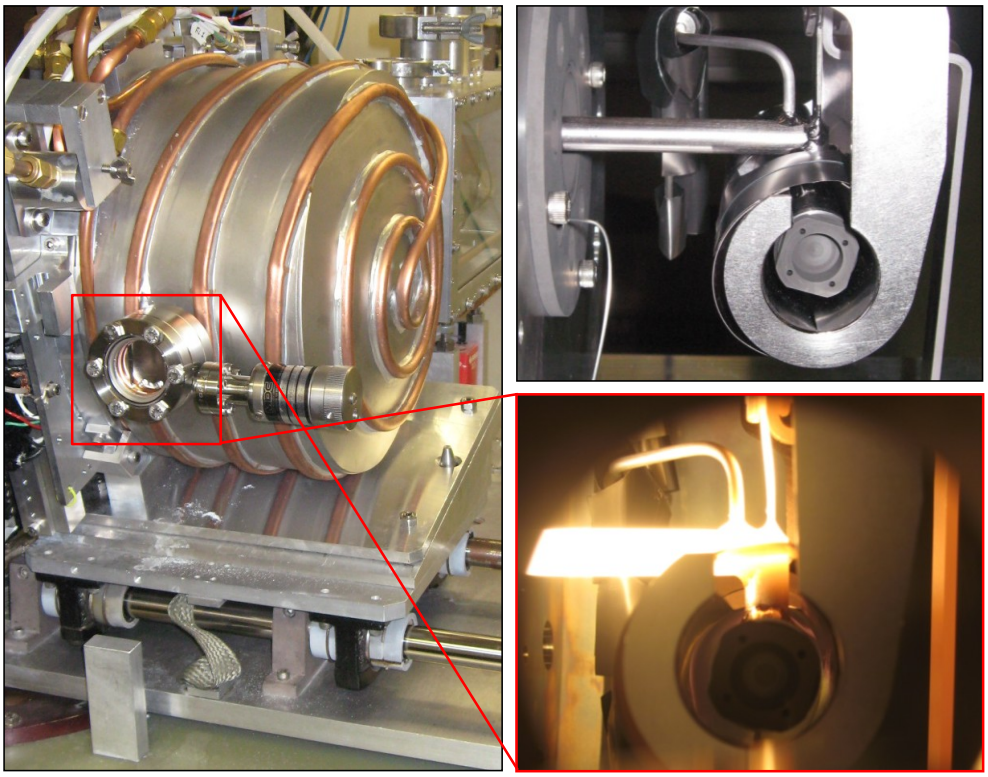

Fig. 23 – Left: water cooled vacuum chamber; up right: graphite box, containing discs, placed inside the tantalum heater; bottom right: view of the target - ion source system from a lateral viewport mounted on the chamber [5].

The isotope production from the two different targets was obtained by bombarding them with a 40 MeV, 50 nA beam of protons coming from a Tandem electrostatic accelerator [89] over a period of about five days. In order to evaluate the effect of temperature on the isotope yields, γ-ray spectra relative to a predefined set of isotopes were collected (see Appendix A) at three different target temperatures: 2000 °C, 1800 °C and 1600 °C.

Temperatures of the target and transfer line were measured before the beginning of the proton beam bombardment using an optical pyrometer through a glass viewport on the TIS enclosure (see fig. 23). A beam of 50 nA protons impinging on a target does not cause a significant heat generation [84], so temperature was considered constant throughout all of each measurement campaign.

The target holder was coupled to the ion source through a hot tantalum transfer line that had a minimum temperature of 1800° C. The ion source used for the experimental tests was the Electron Beam Plasma Ion Source (EBPIS) [90] which provides efficient ionization of a wide range elements. The EBPIS was developed at HRIBF and was based on the FEBIAD (Forced Electron Beam Induced Arc Discharge) ion source [91]. This type of ion source is well suited for RIB production and is capable of operating at temperatures up to 2200 °C and with pressures up to the range of 2 x 10^{-4} mbar. It is equipped with standard Xe and Kr leaks to periodically monitor the ionization performance during on-line operations. This gas feed tube is directly welded on the transfer line. In fig. 21 it is possible to distinguish the main components of the EBPIS: the cathode and the anode. The former, heated to 2000 °C ÷ 2200 °C by Joule effect, emits electrons from its surface (thermionic emission). The latter, kept at a positive voltage (about 150 V), constitutes the plasma chamber and attracts the electrons produced by the cathode. By this route it allows for the ionization of the radioactive isotopes (coming from the transfer line and entering the anode) by means of the electron impact ionization mechanism [7]. Like most of the plasma ion sources, the EBPIS is not isotope-selective as the energy of the electrons accelerated towards the plasma chamber allows the first ionization of virtually every element; as a consequence of that, the amount of unwanted species in the radioactive ion beam is considerably large. Particularly important is the presence of isobaric contaminants (species which have the same mass number of the desired isotope) which cannot be filtered by the mass separator magnet.

3.3.3. 1st test at HRIBF: "Standard" UC_X target prototype

The first material tested on-line at HRIBF represents the "standard" target material that will be used at SPES. During the last few years, its synthesis and characterization were successfully described into detail [60]. Although the production of the discs to be tested was completed before the beginning of this research work, a brief description of the experimental procedure followed to obtain them will be given for the sake of clarity.

Material synthesis and properties

"Standard" uranium carbide discs were obtained starting from uranium dioxide, UO_2, and graphite as uranium and carbon sources, respectively. The UO_2 powder (mean grain size < 300 μm) was purchased from CERAC Inc. (Milwaukee, WI, USA) and graphite (powder mean grain

size < 45 μm) from Sigma-Aldrich. Both the powders were used as received, under an inert atmosphere guaranteed by the use of a glove-box (O_2 and H_2O < 1 ppm), shown in fig. 24. They were manually ground and mixed in an agate mortar, according to the stoichiometry of the following equation:

$$UO_2 + 6C \rightarrow UC_2 + 2C + 2CO \tag{43}$$

which is a particular case of eq. (42).

Fig. 24 – Glove box used for the manipulation and storage of uranium compounds.

In order to obtain mechanically stable and safely manageable samples, 2 wt. % of phenolic resin – in the form of a 10 wt. % solution in acetone – was added as a binder to the powder mixture. After mixing it to the reaction precursors, the powders were placed in a 13 mm diameter mold and subsequently cold pressed in a uniaxial hydraulic press placed outside the glove-box, at 750 MPa for 1 hour.

The thermal treatment of the produced pellets was performed under high vacuum (10^{-6}-10^{-7} mbar) in a furnace entirely designed and developed at LNL, currently working at Padova University, briefly described as follows.

The samples to be treated are placed on a graphite crucible connected to copper clamps, through which the electrical current provided by a power supply (I_{MAX} = 1000 A, V_{MAX} = 10 V)

can pass, thus heating the crucible by Joule effect. Heat dispersion is minimized by using a shielding system made of alumina plaques and tantalum foils which completely surrounds the crucible, leaving space only for its connection to the copper clamps, and for a small hole through which the temperature and emissivity of the sample is measured, by means of a dual frequency infrared pyrometer [41], operating in the range between 1000 °C and 3000 °C, extrapolating values of T < 1000 °C. The whole system is placed inside a water-cooled, bell-shaped steel chamber evacuated using a rotary and a turbomolecular pump placed in series. The process undergoing is typically monitored by means of a penning trap which measures the pressure inside the chamber (in the 10^{-3} – 10^{-7} mbar range) and by a Quadrupole Mass Spectrometer that gives information about the gases formed during the thermal treatment. Fig. 25 shows the main components of the high temperature furnace.

The thermal treatment was carefully designed in order to make the reaction (43) occur by removing CO from the reaction chamber, without reaching pressure values that could compromise the functioning of the pumping system, and at the same time favor the consolidation of the green pellets by sintering.

More into details, the treatment consisted of three phases [60]:

- Slow heating (2 °C/min) up to 1200°C, dwell time of 24 hours at 1200 °C, to promote and possibly complete the carbothermal reaction (43).

- Heating (2 °C/min) up to 1600°C, dwell time of 4 hours at 1600°C, to sinter the carburized powders.

- Cooling to room temperature (2 °C/min).

Fig. 26 reports the measured pressure inside the chamber during the treatment [92]. A clear gas evolution was found to occur at low temperature, and can be attributable mainly to water release, as found by mass spectrometry [60], and clearly indicated in figure. Water was probably generated inside the chamber either by desorption from the precursors powders or during the crosslinking of the phenolic resin used as a binder. Moreover, a certain amount of the produced gas at low temperature can be attributed to the resin decomposition, which occurs at temperatures between 350 °C and 800 °C, as obtained by thermal gravimetric analysis [60]. For T > 1000 °C, two main peaks can be observed and they can be both attributed to the carbothermal reduction reaction, liberating CO as indicated. Their position in terms of

temperature in the graph reported in fig. 26 corresponds to the plateaus of the heating ramp. The particular shape of the CO evolution pattern for T > 1000 °C (two peaks at different temperatures) can be ascribed to the presence of a gradient in temperature within the treated samples, since they were placed in contact with the graphite crucible only with their bottom surfaces.

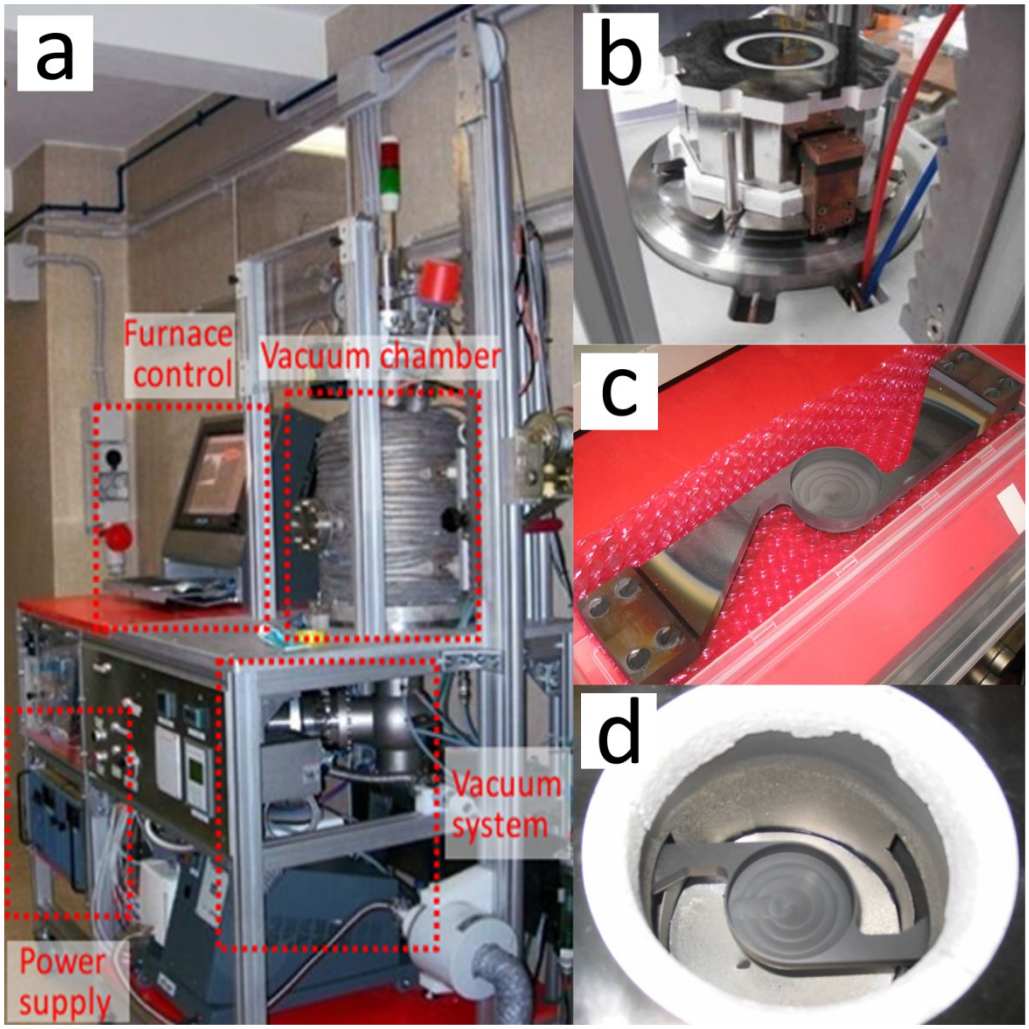

Fig. 25 – a) High vacuum – high temperature furnace, b) Shielding system placed inside the vacuum chamber, c) graphite crucible, d) graphite crucible - shielding system assemble.

Previous X-Ray Diffraction (XRD) investigations revealed that by means of reaction (43) performed in the above described experimental setup, the final composition of the treated samples consisted of α-UC_2, graphite and a minor amount of UC. The obtained XRD spectrum is shown in fig. 27, marked as UO2C [60]. The presence of the monocarbide may be attributed to the precipitation of carbon from the uranium dicarbide during the slow cooling from the sintering temperature, as reported in literature [49].

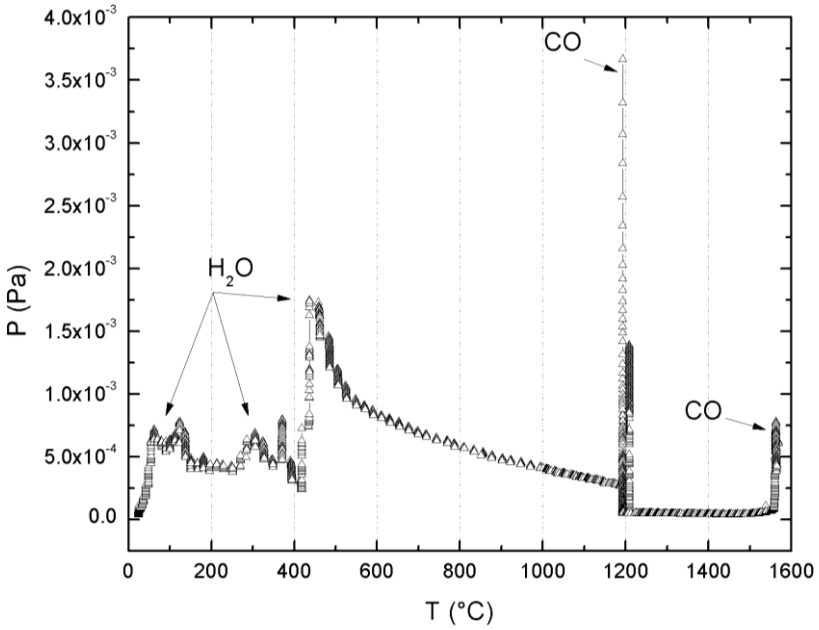

Fig. 26 - Pressure inside the reaction chamber upon carburization and sintering of the "standard" UC_X pellets [92].

Fig. 28 [92] shows a Scanning Electron Microscope (Philips XL-30, SEM) image of the surface of one of the discs. In the reported micrograph it is clear that the material was composed of two phases, as confirmed by Energy Dispersive Spectroscopy (EDS): uranium dicarbide ("white" grains) and residual graphite ("black" aggregates).

Even if the temperature reached during the thermal treatment was high enough to make the sintering of the carbide powders to occur, a significant amount of residual porosity was found in the final samples, and evaluated as follows:

$$P_{tot} = 1 - \frac{\rho_{bulk}}{\rho_{th}} \tag{44}$$

In eq. (44) P_{tot} represents the total porosity of the sample, ρ_{bulk} is its bulk density (calculated by the weight over volume ratio) and ρ_{th} is the theoretical density of the UC_2+2C mixture, calculated as the weighted average of the two components theoretical densities, taking into account the values of 11.2 g/cm^3 and 1.9 g/cm^3 for UC_2 and graphite, respectively [60].

Table 4 reports the main characteristics of the "Standard" pellets used for the first on-line test at HRIBF. Among the values reported in the table, mass thickness is a fundamental property to take into account when trying to compare yields obtained in different online test, since it is directly related to the amount of interaction between the primary particles and the uranium atoms throughout all the disc thickness (th in the following), being it calculated as:

$$Mass\ thickness = \rho_{bulk} \cdot th \tag{45}$$

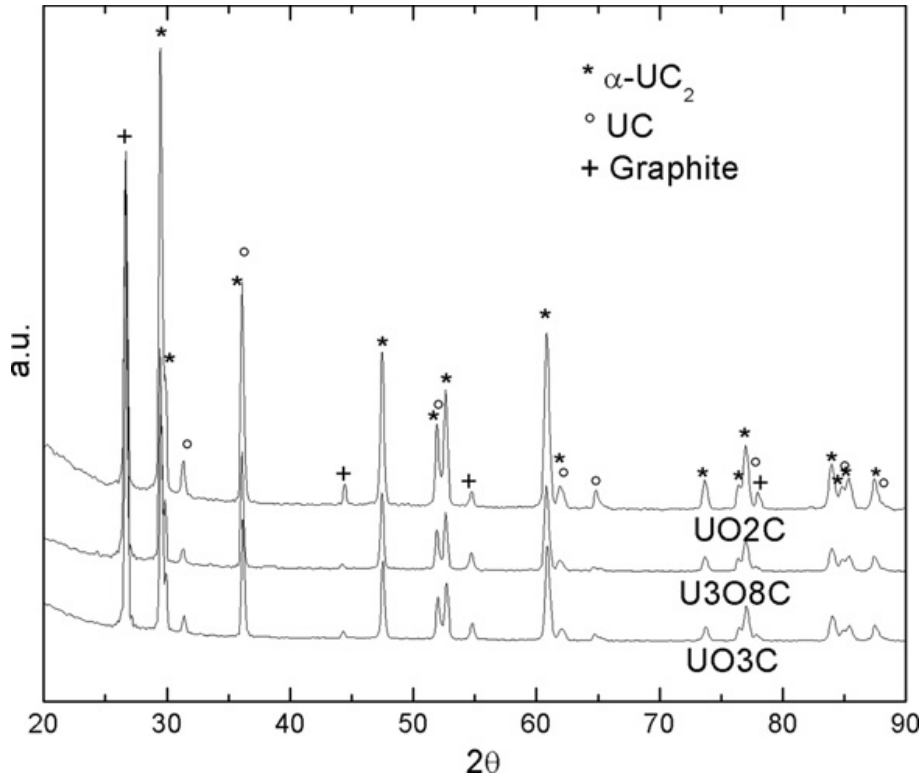

Fig. 27 – XRD patterns of UC_X samples, after [60]. UO2C: composition used in the "standard" UC_X targets.

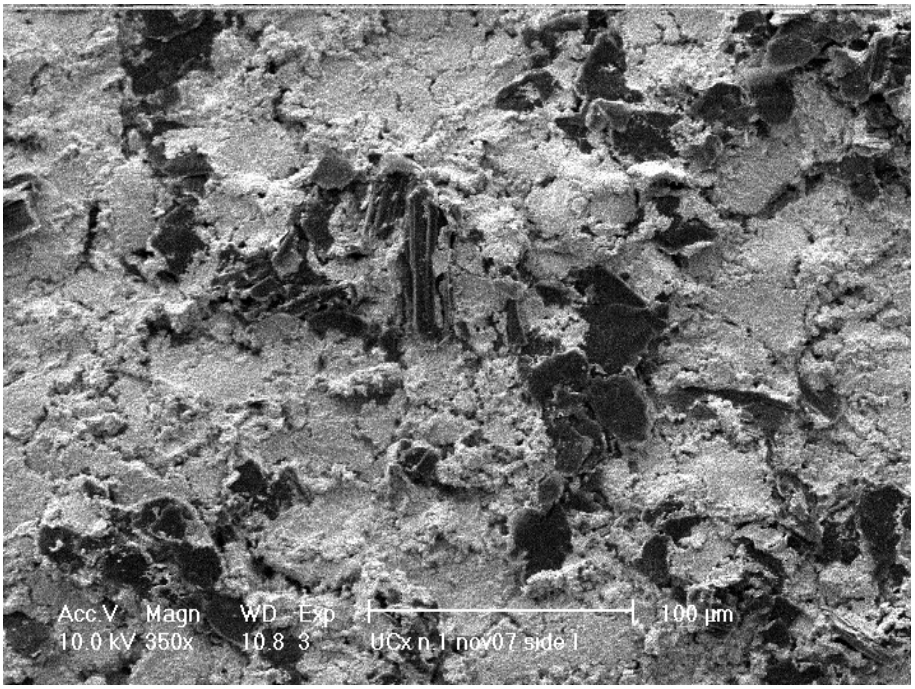

Fig. 28 – SEM micrograph of the surface of a "standard" UC_X disc.

Table 4 – Average properties of the "Standard" UC_X pellets used for the online test.

	"Standard" UC_X properties
Bulk density (g/cm^3)	4.25 ± 0.24
Disc diameter (mm)	12.50 ± 0.07
Mass thickness (g/cm^2)	0.41 ± 0.04
Total porosity (%)	58 ± 1

Online test at HRIBF

Fig. 29 (left) shows the seven UC_X discs used for the test, placed in vertical position inside the aforementioned graphite box, which was closed at its extremities by a graphite window (where the proton beam enters the target) and three dumpers which constitute the primary beam stopping zone, as reported in fig. 29 (right).

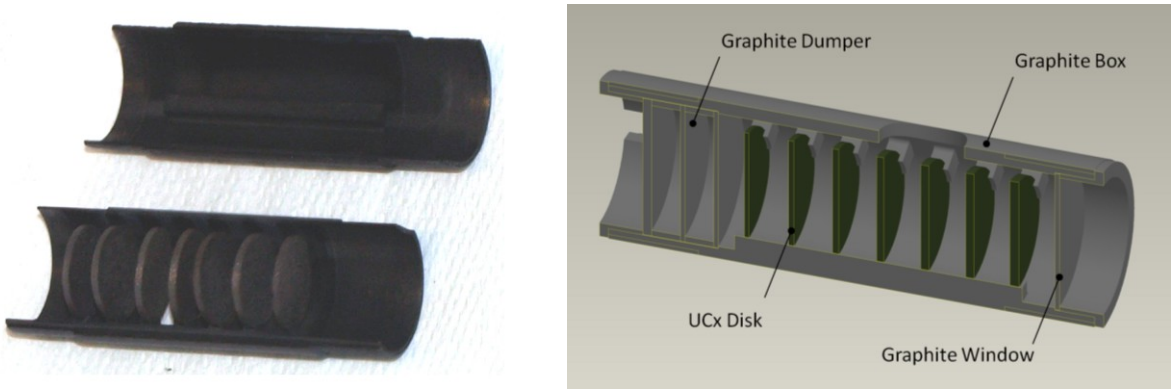

Fig. 29 – Left: seven "standard" UC_X discs placed inside the graphite box, right: box complete layout.

The so assembled graphite box was placed inside the OLTF target heating system, as shown in fig. 30 (left). A threaded graphite cap was added to one of the box extremities in order to fix and secure it (fig. 30, right).

Once the aforementioned procedures were completed, thermal characterization of the target-ion source system was performed for one week. This process had both the aim collect useful data and measurements to study the thermal electric behavior of the target - ion source system [5, 92] and to slowly out-gas the target and the ion source. It is indeed expectable that by means of the aforementioned production technique, reaction (43) may not be perfectly completed; moreover, during the target shipping and handling, oxidation or water adsorption could have occurred. For these reasons, a subsequent slow heating at high temperature was

necessary to remove all the producible gas (mainly CO and H_2O) from the tested discs without compromising the heating system and the ion source functioning.

However, in the particular case of the "Standard" UC_X discs, the out-gassing from the target was small, allowing the chamber pressure during the heating to be always good for the TIS correct functioning (~ 10^{-6} mbar).

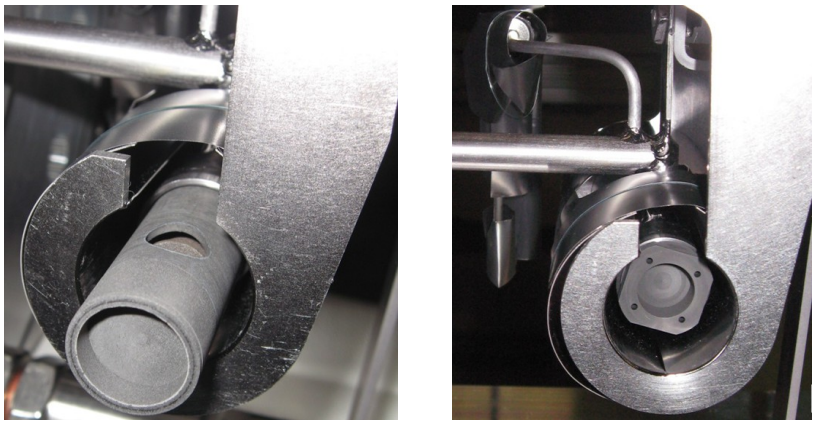

Fig. 30 – Left: target box installation in the OLTF heating system, right: graphite cap used to secure the box.

After the completion of a week of off-line out-gassing and thermo-electrical tests [5], the target temperature was raised up to 2000 °C, and the UC_X discs were irradiated by a 50 nA, 40 MeV beam of protons. After measuring the yield of the produced isotopes at this temperature, the same collection was done at 1800 °C and 1600 °C, to determine the effect of temperature on the release of particles from the target. For each temperature, after the collection of the desired and predetermined set of isotopes of interest, holdup-time measurements were performed on two particular nuclides, ^{92}Sr and ^{128g}Sn. For each isotope, this type of measurement was carried on measuring the intensity of its main γ-peak in steady state conditions (proton beam on target with constant current intensity), and measuring how fast was the γ-signal decay when the proton beam was suddenly switched off, thus interrupting the fission-based isotope production. This method is particularly useful when characterizing the release properties of a target, and can in some cases be used also to predict the ISOL yield of a particular isotope knowing the yield of another isotope of the same element and its holdup-time behavior [93].

Fig. 31 gives an overview of the produced isotopes spectrum at 2000 °C, with a clear indication of the order of magnitude of their yield, expressed as ions/μC (ions/μA*s).

A total number of 77 isotopes of 21 different elements were obtained; most of them were found also at 1800 °C and 1600 °C. Table 5 reports the yields of a selected number of produced and collected ions [92, 94], with a very broad half-life spectrum, from short-lived ($T_{1/2}$ ~ 1 s) to

very long-lived isotopes ($T_{1/2}$ > 1 h). The uncertainties ΔYield reported in table 5 were calculated taking into account both statistical and systematic errors.

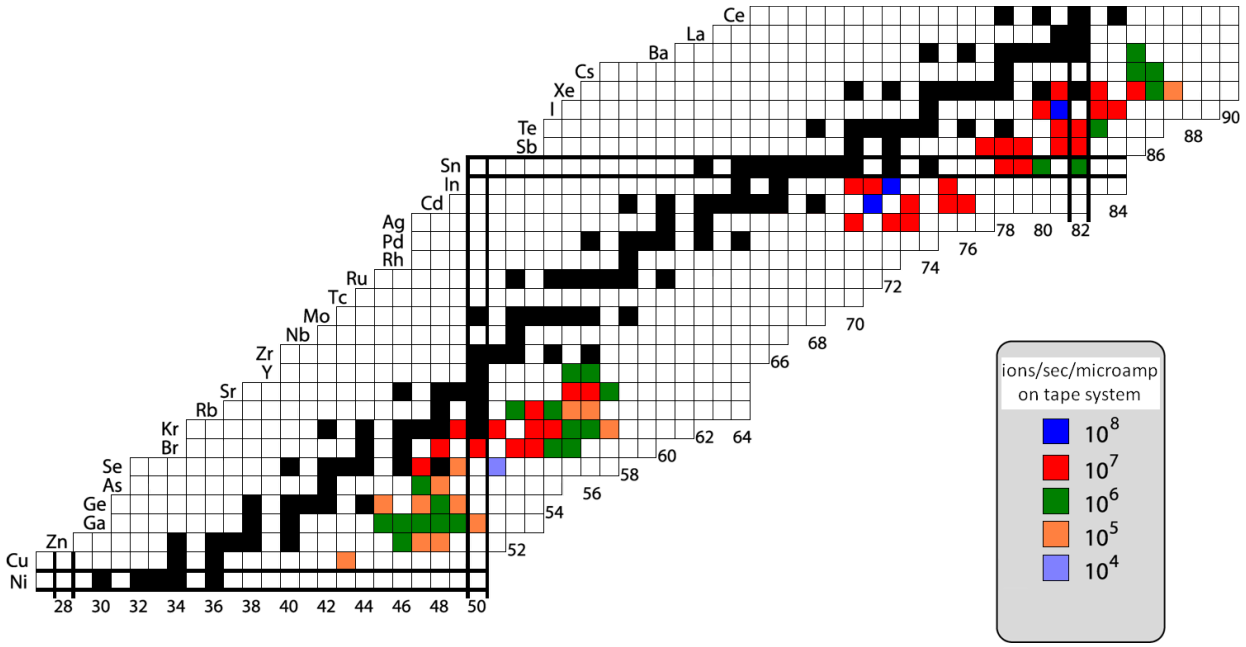

Fig. 31 – Radioactive isotopes obtained with a "Standard" UC_X target at 2000 °C.

As anticipated in paragraph 1.3 (fig. 5), the spectrum of the obtainable and extractable isotopes at SPES will be divided in two zones: a low-mass (from Ni to Y) and a high-mass region (from Ag to La), whereas transition metals in the Zr-Pd interval will not be obtained since they are too refractory to be extracted from the target. This aspect was confirmed in this experimental test, as shown in fig. 31. It is important to underline that the obtainment of this huge amount of data represented a key milestone in the SPES target development since it was the first on-line evidence that a target with its innovative geometry is capable of producing and quickly releasing fission products. What follows is a detailed analysis on the influence of half-life and temperature on the calculated yield of isotopes belonging to a significant group of the produced elements. Half-life is a key parameter when considering release from an irradiated target, since it determines whether there is sufficient time to escape to the ion source avoiding decay or not, while temperature is extremely important for diffusion, effusion and ionization, as explained in chapter 2. These aspects were clearly verified in this test, as can be noticed in figures 32 to 39, in which the yields of different elements and isotopes are reported, with respect to isotopic mass and to half-life. For isotopes which present isomeric states, the yield reported is relative to the state with the higher gamma signal, and reported in the graphs marked as "m" or "g" for metastable and ground state, respectively. The elements chosen for this detailed analysis

are representative of the different groups produced during the experiment [94]: alkali, alkaline-earth metals, transition metals, metalloids, halogens and noble gases.

Table 5 – Yields of a selected group of isotopes at 2000 °C, 1800 °C and 1600 °C.

Isotope	$T_{1/2}$	2000 °C		1800 °C		1600 °C	
		Yield (/s*μA)	ΔYield (/s*μA)	Yield (/s*μA)	ΔYield (/s*μA)	Yield (/s*μA)	ΔYield (/s*μA)
^{121}Ag	0.78s	$5.53*10^{6}$	$1.44*10^{5}$	$3.06*10^{6}$	$1.22*10^{5}$	$4.40*10^{6}$	$1.64*10^{5}$
^{81}Ga	1.22s	$2.20*10^{5}$	$6.55*10^{3}$	$1.97*10^{5}$	$6.04*10^{3}$	$1.56*10^{5}$	$5.10*10^{3}$
^{120g}Ag	1.23s	$1.52*10^{7}$	$4.32*10^{5}$	$1.17*10^{7}$	$4.78*10^{5}$	$1.29*10^{7}$	$4.99*10^{5}$
^{124}Cd	1.29s	$8.24*10^{6}$	$1.63*10^{5}$	$5.18*10^{6}$	$1.91*10^{5}$	$4.20*10^{6}$	$1.21*10^{5}$
^{78}Zn	1.47s	$1.22*10^{5}$	$3.62*10^{3}$	$1.09*10^{5}$	$2.94*10^{3}$	$8.09*10^{4}$	$3.00*10^{3}$
^{123m}Cd	1.82s	$1.08*10^{7}$	$1.60*10^{5}$	$8.11*10^{6}$	$1.64*10^{5}$	$7.12*10^{6}$	$1.35*10^{5}$
^{92}Kr	1.84s	$1.55*10^{6}$	$2.42*10^{4}$	$5.68*10^{5}$	$9.08*10^{3}$	$1.86*10^{5}$	$3.24*10^{3}$
^{90}Br	1.91s	$9.94*10^{5}$	$4.01*10^{4}$	$4.06*10^{5}$	$3.88*10^{4}$	$1.07*10^{5}$	$3.87*10^{3}$
^{119}Ag	2.10s	$2.96*10^{7}$	$2.47*10^{5}$	$2.45*10^{7}$	$3.66*10^{5}$	$2.05*10^{7}$	$2.81*10^{5}$
^{93}Rb	5.80s	$3.25*10^{5}$	$1.03*10^{4}$	$1.92*10^{5}$	$7.40*10^{3}$	$8.98*10^{4}$	$4.33*10^{3}$
^{123g}In	5.98s	$1.22*10^{8}$	$2.03*10^{6}$	$1.23*10^{8}$	$3.15*10^{6}$	$8.82*10^{7}$	$2.28*10^{6}$
^{72}Cu	6.60s	$2.19*10^{5}$	$4.30*10^{3}$	$2.54*10^{5}$	$5.45*10^{3}$	$1.48*10^{5}$	$3.17*10^{3}$
^{133m}I	9.00s	$1.04*10^{7}$	$1.54*10^{5}$	$5.41*10^{6}$	$1.75*10^{5}$	$2.75*10^{6}$	$8.90*10^{4}$
^{88}Br	16.30s	$1.15*10^{7}$	$2.31*10^{5}$	$5.05*10^{6}$	$1.08*10^{5}$	$2.03*10^{6}$	$3.08*10^{4}$
^{79g}Ge	19.00s	$1.31*10^{6}$	$4.05*10^{4}$	$1.05*10^{6}$	$5.13*10^{4}$	$8.25*10^{5}$	$3.40*10^{4}$
^{81}As	34.00s	$7.15*10^{5}$	$1.59*10^{4}$	$3.95*10^{5}$	$9.86*10^{3}$	$1.45*10^{5}$	$5.50*10^{3}$
^{132}Sn	39.70s	$2.14*10^{6}$	$2.80*10^{4}$	$1.60*10^{6}$	$3.27*10^{4}$	$8.49*10^{5}$	$3.14*10^{4}$
^{120m}In	47.30s	$4.23*10^{7}$	$1.02*10^{6}$	$4.10*10^{7}$	$1.22*10^{6}$	$2.37*10^{7}$	$8.66*10^{5}$
^{140}Cs	1.06m	$1.44*10^{6}$	$4.85*10^{4}$	$6.84*10^{5}$	$4.81*10^{4}$	$1.21*10^{5}$	$5.30*10^{3}$
^{94}Sr	1.23m	$6.30*10^{6}$	$1.91*10^{5}$	$1.90*10^{6}$	$7.59*10^{4}$	$8.50*10^{5}$	$8.90*10^{4}$
^{133}Sb	2.50m	$9.77*10^{6}$	$3.72*10^{5}$	$6.10*10^{6}$	$3.30*10^{5}$	$3.95*10^{6}$	$2.29*10^{5}$
^{137}Xe	3.83m	$4.58*10^{7}$	$2.88*10^{6}$	$5.92*10^{7}$	$4.46*10^{6}$	$6.25*10^{6}$	$4.32*10^{5}$
^{93}Sr	7.45m	$1.10*10^{7}$	$1.12*10^{5}$	$8.16*10^{6}$	$8.44*10^{4}$	$2.11*10^{6}$	$3.95*10^{4}$
^{95}Y	10.30m	$2.05*10^{6}$	$6.66*10^{4}$	$9.28*10^{5}$	$5.13*10^{4}$	$1.71*10^{5}$	$4.00*10^{3}$
^{141}Ba	18.30m	$2.48*10^{6}$	$3.24*10^{5}$	$1.97*10^{6}$	$2.54*10^{5}$	/	/
^{83g}Se	22.40m	$3.30*10^{6}$	$3.23*10^{4}$	$4.71*10^{5}$	$5.33*10^{3}$	$5.74*10^{4}$	$1.05*10^{3}$
^{134}Te	41.80m	$4.90*10^{7}$	$7.70*10^{6}$	$4.53*10^{7}$	$8.12*10^{6}$	$3.39*10^{7}$	$5.81*10^{6}$
^{134g}I	52.50m	$1.40*10^{8}$	$2.77*10^{7}$	$1.41*10^{8}$	$2.59*10^{7}$	$6.93*10^{7}$	$1.43*10^{7}$
^{87}Kr	1.27h	$1.09*10^{7}$	$1.04*10^{6}$	$1.40*10^{7}$	$8.57*10^{5}$	$6.69*10^{6}$	$4.72*10^{5}$

Values reported in the above table show that uncertainties higher than 10% were obtained for some long-lived isotopes (^{141}Ba, ^{134}Te and ^{134g}I), mainly due to huge differences between

their half-life and the efficient measurement time. This reflected in a low number of counts in the γ-ray spectra, thus resulting in high values of statistical errors.

All the isotopes detected at 2000 °C were clearly observed also at the lower temperatures, the only exception being ^{141}Ba, whose γ-peaks were not present in the spectrum obtained for mass 141 at 1600 °C. This result confirms the good efficiency of the SPES multi-foil target in the production and release of radioactive species, even at low temperature and for short half-lives. However, as can be noticed in table 5 and in fig. 32-39, in most cases a simple correlation can be found: the higher the temperature, the higher the yield, so yield increases can be mainly attributed to improved release efficiency of the target at higher temperatures. Some exceptions to this rule however still occur in the presented data like, for example, in short-lived silver isotopes, for which temperature seems not to be significantly affecting the calculated yields.

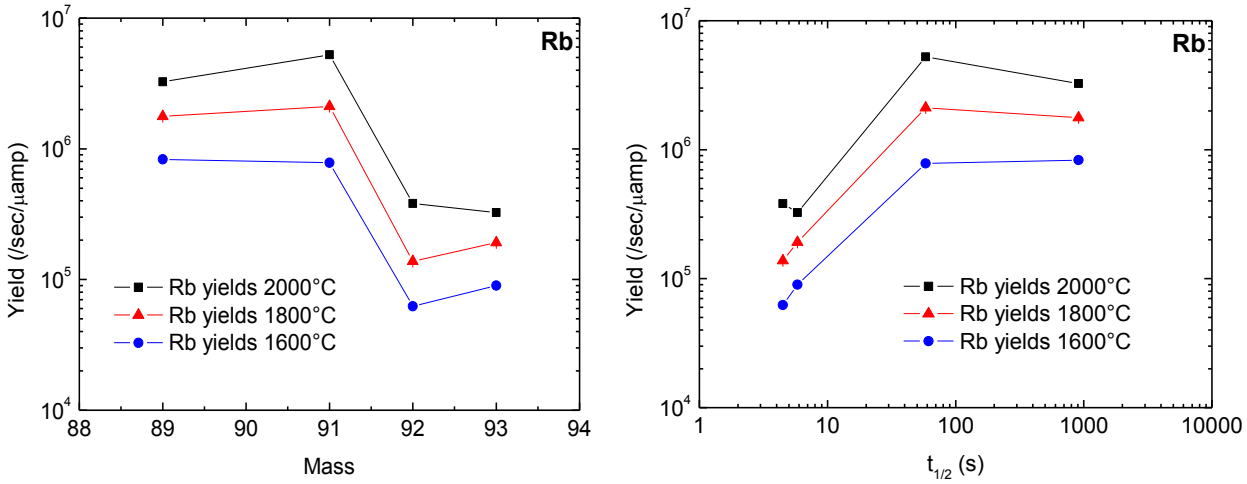

Fig. 32 – Ion yields of Rb isotopes at different temperatures. Left: yield *vs.* mass. Right: yield *vs.*$t_{1/2}$.

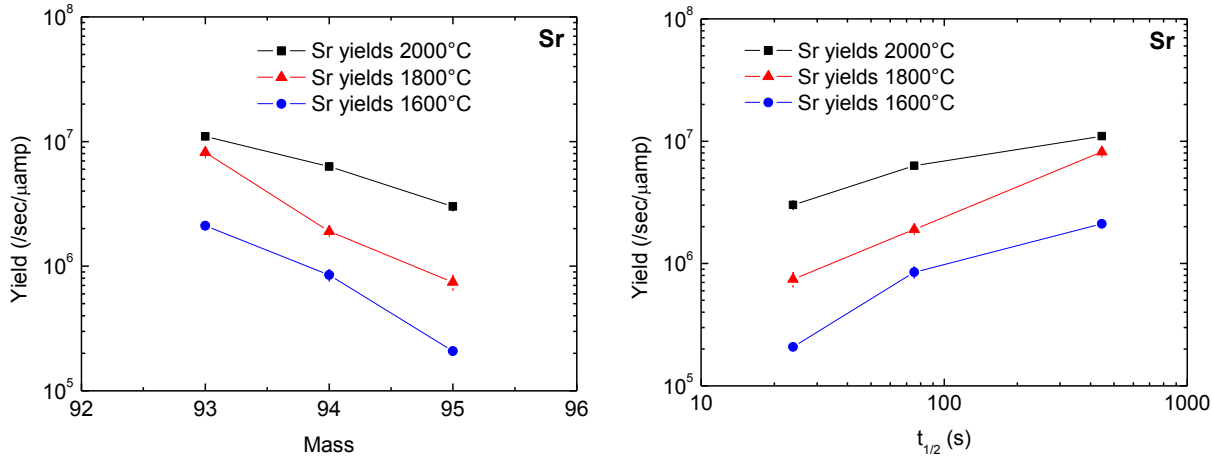

Fig. 33 – Ion yields of Sr isotopes at different temperatures. Left: yield *vs.* mass. Right: yield *vs.*$t_{1/2}$.

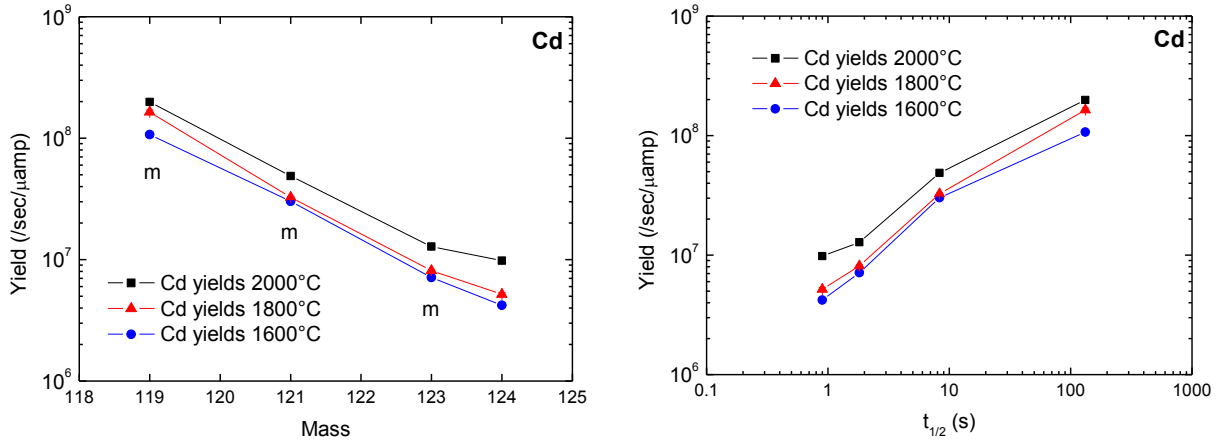

Fig. 34 – Ion yields of Cd isotopes at different temperatures. Left: yield *vs.* mass. Right: yield *vs.*$t_{1/2}$.

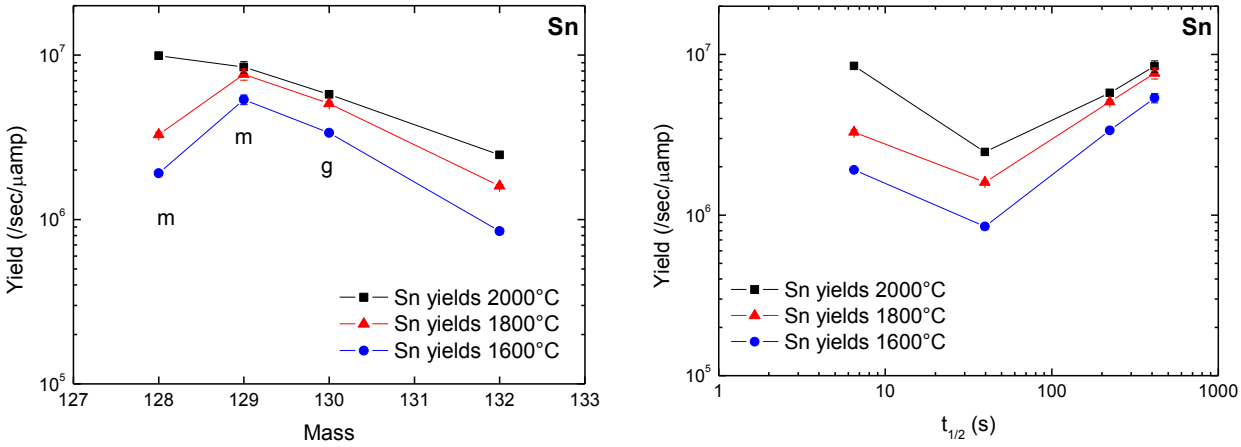

Fig. 35 – Ion yields of Sn isotopes at different temperatures. Left: yield *vs.* mass. Right: yield *vs.*$t_{1/2}$.

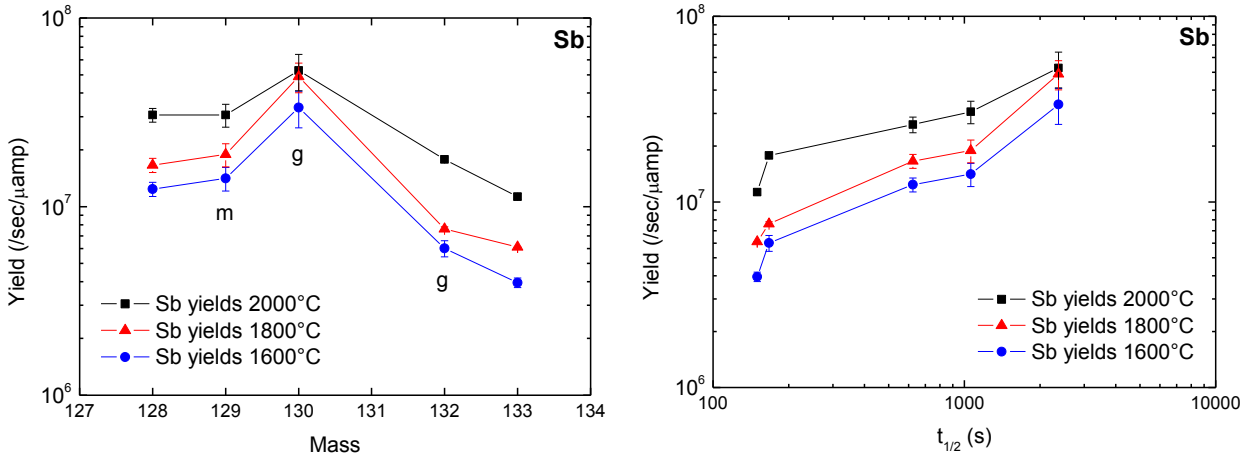

Fig. 36 – Ion yields of Sb isotopes at different temperatures. Left: yield *vs.* mass. Right: yield *vs.*$t_{1/2}$.

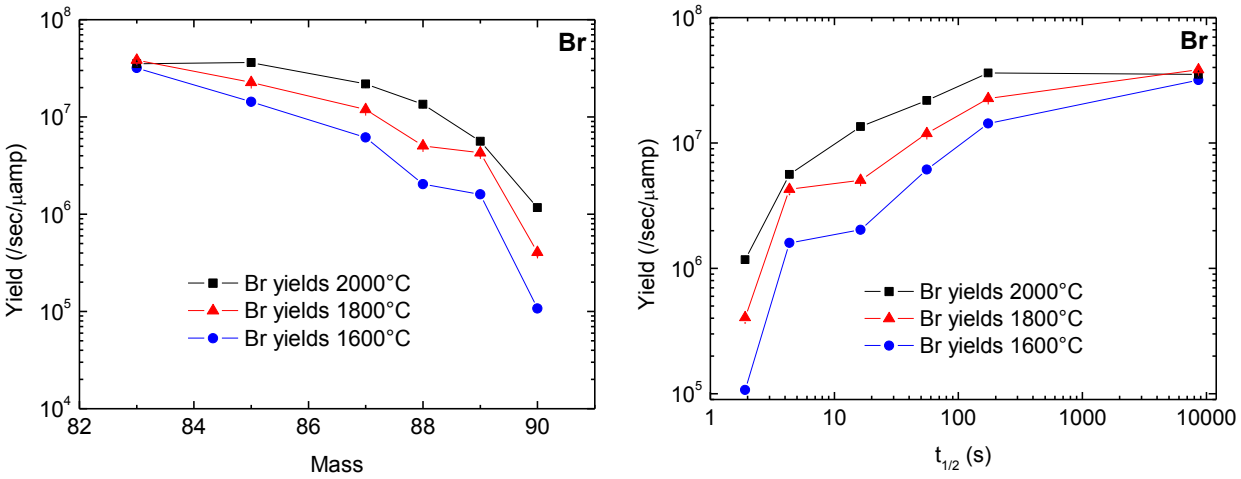

Fig. 37 – Ion yields of Br isotopes at different temperatures. Left: yield *vs.* mass. Right: yield *vs.*$t_{1/2}$.

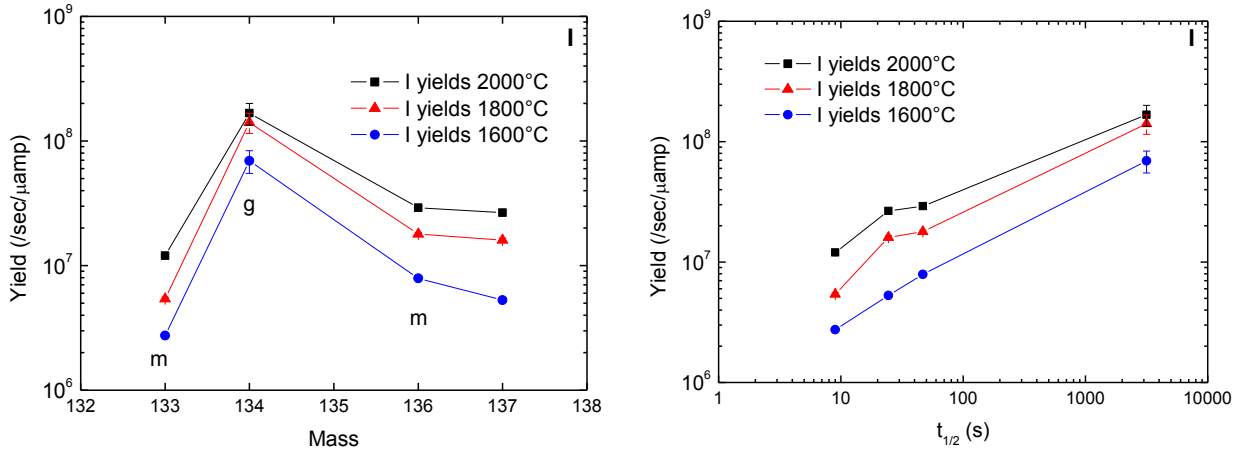

Fig. 38 – Ion yields of I isotopes at different temperatures. Left: yield *vs.* mass. Right: yield *vs.*$t_{1/2}$.

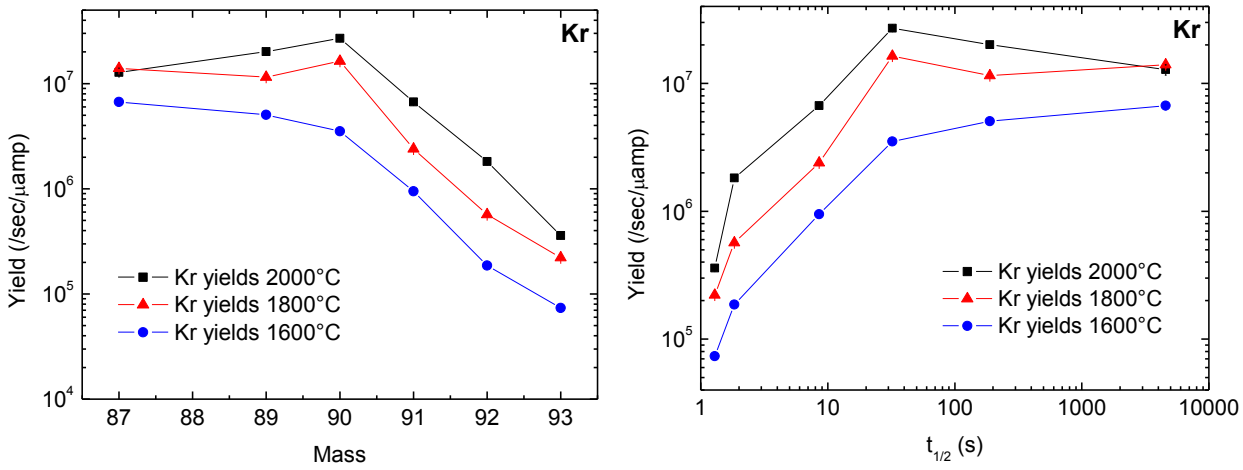

Fig. 39 – Ion yields of Kr isotopes at different temperatures. Left: yield *vs.* mass. Right: yield *vs.*$t_{1/2}$.

As reported in [95], Cs, Rb and Ba should possess the highest production cross-section among all the species generated in the UC_X target irradiated with 40 MeV protons, but in this test

their yields were found to be clearly lower than other elements. This aspect is strictly related to the fact that the plasma ion sources like EBPIS are not effective to ionize the alkaline and alkaline-earth elements: for these isotopes, a overall plasma ionization efficiency less than 10% can be expected [92]. On the other hand, the use of EBPIS has resulted in high yields of elements like Kr, Xe, Ag and Sn, as suggested by plasma ionization efficiencies reported in [96].

The trends reported in figs. 32 to 39 suggest another simple consideration about the calculated yields: they tend indeed to increase with increasing half-lives of the isotopes, as expected from the fact that long-lived species can diffuse into crystalline grains and effuse out of the target for more time without decaying. As a matter of fact, not only half-life has to be considered when comparing yields, but also production rate must be taken into account, since it can be very diverse for different isotopes of the same element.

In the case of rubidium (fig. 32), ^{91}Rb ($T_{1/2}$ = 58 s) was found to be the isotope with the highest yield at 1800 °C and 2000 °C – the maximum in yield vs. half-life curve - whereas at 1600 °C the yield values of ^{91}Rb and ^{89}Rb ($T_{1/2}$ = 15.2 m) are very close to each other. Another apparent discrepancy can be noticed at 2000 °C where, unlike the data for 1600 °C and 1800 °C, ^{92}Rb ($T_{1/2}$ = 4.5 s) yield was observed at a higher intensity than the longer-lived ^{93}Rb ($T_{1/2}$ = 5.8 s, about 17% difference in yield). The latter effect is probably due to local instabilities in proton beam current and ion beam tuning, the former depends on the fact that ^{91}Rb is, together with ^{90}Rb (not revealed in this experiment), the most produced rubidium isotope by proton-induced fission of ^{238}U at similar energies to those used in this test [97], so its experimental yields are higher or comparable to those of longer-lived isotopes such as ^{89}Rb. This effect is less pronounced at 1600 °C, where the diffusion-effusion mechanism is slower, so half-life has a greater impact on the yield.

A more linear trend in yield vs. half-life was found for strontium (fig. 33), whose three detected isotope yields are clearly different depending on half-life and temperature. In the case of the longest-lived among them, ^{93}Sr ($T_{1/2}$ = 7.5 m), the yield at 1800 °C is closer to that at 2000 °C with respect to the two other isotopes. This phenomenon (divergence of the yields at different temperatures for short-lived isotopes and convergence for longer-lived ones) was found in almost all the detected elements, as can be noticed in figs. 34 to 39, and underlines the importance of operating at the maximum sustainable temperature to increase the yield of short-lived isotopes. For instance, in the case of ^{95}Sr ($T_{1/2}$ = 24.4 s), yields at 1600 °C and 2000 °C have a difference of more than one order of magnitude.

In the case of cadmium isotopes (fig. 34), a clear temperature effect is found for short-lived isotopes ($T_{1/2}$ < 10 s), for which the yield values obtained at 1600 °C and 1800 °C are similar and

clearly lower than those at 2000 °C. However, in this case the convergence between 1800 °C and 2000 °C data is found for shorter half-lives than in the case above described (^{119m}Cd, $T_{1/2}$ = 2.2 m). Cadmium, as well as the aforementioned silver, is one of the most volatile elements produced in this experiment, so its yields at 1600 °C and 2000 °C do not differ of more than one order of magnitude, even in the case of the shortest-lived isotopes (^{124}Cd, $T_{1/2}$ = 1.3 s).

Graphs reported in fig. 35 show a good reproducibility in terms of yield vs. mass for tin isotopes at the three different temperatures. An exception can be found for ^{128m}Sn ($T_{1/2}$ = 6.5 s), whose yield is considerably higher at 2000 °C with respect to the other two temperatures. This aspect is clearer if yield vs. $T_{1/2}$ is considered, since ^{128m}Sn is the shortest-lived tin isotope that was observed, and thus is the most sensitive to temperature due to the diffusion and effusion mechanisms. Again, a general temperature dependence of yield can be seen in yield vs. $T_{1/2}$ graph (fig. 35, right), in which for the longest-lived isotopes, yields at 1800 °C and 2000 °C are very close, whereas for $T_{1/2}$ lower than 100 s the two curves tend to consistently diverge. This half-life effect seems to be less important for yields obtained at 1600 °C, since they are clearly lower than those at 1800 °C for the whole $T_{1/2}$ spectrum considered. The yields of ^{128m}Sn are higher than the yields for ^{132}Sn ($T_{1/2}$ = 39.7 s), even though the half-life of the former is much shorter than that of the latter, due to the difference in production rate of these two isotopes in the target. The production rate of ^{128m}Sn was indeed estimated to be about 84 times higher than the production rate of ^{132}Sn [97].

Analogously, for Sb and I the same half-life effect is found: at the three different temperatures, increasing $T_{1/2}$ results in higher yields of antimony and iodine isotopes (figs. 36 and 38, respectively). Again, the curves obtained at 1800 °C and 2000 °C shown in yield vs. $T_{1/2}$ graphs tend to converge for half-lives higher than 1000 seconds (39.5 m for ^{130g}Sb, 52.0 m for ^{134g}I).

Bromine yield trend with respect to mass (fig. 37, left) is in good agreement with that reported by Kronenberg et al. [82] for a UC_X target irradiated with 40 MeV protons at HRIBF. As shown in fig. 37, right, for half-lives greater than 1 hour, like in the case of ^{83}Br ($T_{1/2}$ = 2.4h), differences between yields at different temperatures become less considerable, and values at 1600 °C, 1800 °C and 2000 °C can be considered equal, within experimental error bars. For short half-lived isotopes, for example the very neutron-rich ^{90}Br ($T_{1/2}$ = 1.9 s), differences of one order of magnitude can be found between yields at 2000 °C and 1600 °C, like in other aforementioned elements. In these cases, a diffusion governed release process from the target can be suggested, with a remarkable influence of temperature in the short-lived isotopes yields.

The Kr yields reported in fig. 39 show a particular trend with respect to mass and half-life: while at 1800 °C and 2000 °C the calculated values reach a maximum for ^{90}Kr ($T_{1/2}$ = 32.3 s) and then decay for higher half-lived isotopes, at 1600 °C the yields continue to increase as half-life increases, with the highest value found for ^{87}Kr ($T_{1/2}$ = 1.3 h).

The results of the holdup-time measurements are presented in figs. 40 and 41 for ^{92}Sr and ^{128g}Sn, respectively. In order to compare the results of the release at the different temperatures, the data were normalized by dividing the γ count values by the initial value, obtained before the shutting down of the proton beam (steady state conditions). These two particular isotopes were chosen to perform the analysis since they are long-lived ($T_{1/2}$ = 2.7 h for ^{92}Sr and $T_{1/2}$ = 59.1 m for ^{128g}Sn) and their parent isotopes are short-lived ($T_{1/2}$ in the order of seconds for ^{92}Kr, ^{92}Rb and ^{128}In), so that they have a negligible effect on the measured γ count. Experimental holdup-time data can be fitted by a simple two-exponential decay function [93], which describes the isotopic release by means of two components: the first one is related to the fast escape from the target, whereas the second describes the delayed part of release (tail). Each component is characterized by its time parameter, t_f for fast release, t_s for the slow tail [98]. These values, reported in table 6, were obtained fitting the experimental data with a function of the type (A and B are fitting constants, y_0 depends on the background level during the measurements):

$$Counts = y_0 + A \cdot e^{-\frac{t}{t_f}} + B \cdot e^{-\frac{t}{t_s}} \tag{45}$$

Table 6 – Fitting parameters for the holdup-time measurements of ^{92}Sr and ^{128g}Sn.

Isotope	2000°C					1800°C					1600°C				
	y_0	FAST		SLOW		y_0	FAST		SLOW		y_0	FAST		SLOW	
		A	t_f (s)	B	t_s (s)		A	t_f (s)	B	t_s (s)		A	t_f (s)	B	t_s (s)
^{92}Sr	0.06	0.94	227	--	--	0.06	0.16	345	0.78	1223	0.06	0.10	355	0.84	3626
^{128g}Sn	0.08	0.60	29	0.32	132	--	--	--	--	--	0.08	0.31	92	0.61	297

At 2000 °C the release of ^{92}Sr (fig. 40) is so fast that the data were fitted using a single-exponential function, whereas at lower temperature the presence of two components in the decay is evident as the release tails extend over the measurement time. The temperature effect on release is clearly testified by the fitting parameters: the lower the temperature, the higher the contribution of the slow tail (B) and the time parameters t_f and t_s. Low initial γ-counts make fitting ^{128g}Sn data (fig. 41) more complicated because of the effect of the background. In fact, the count rate was about one-tenth of the counting rate observed in the ^{92}Sr holdup-time

measurements. However, is it quite clear that the ^{128g}Sn release at 1600 °C is slower than the release at 2000 °C, as indicated by the fit parameters reported in table 6 (A > B at 2000 °C, A < B at 1600 °C, time parameters lower at 2000 °C than those at 1600 °C).

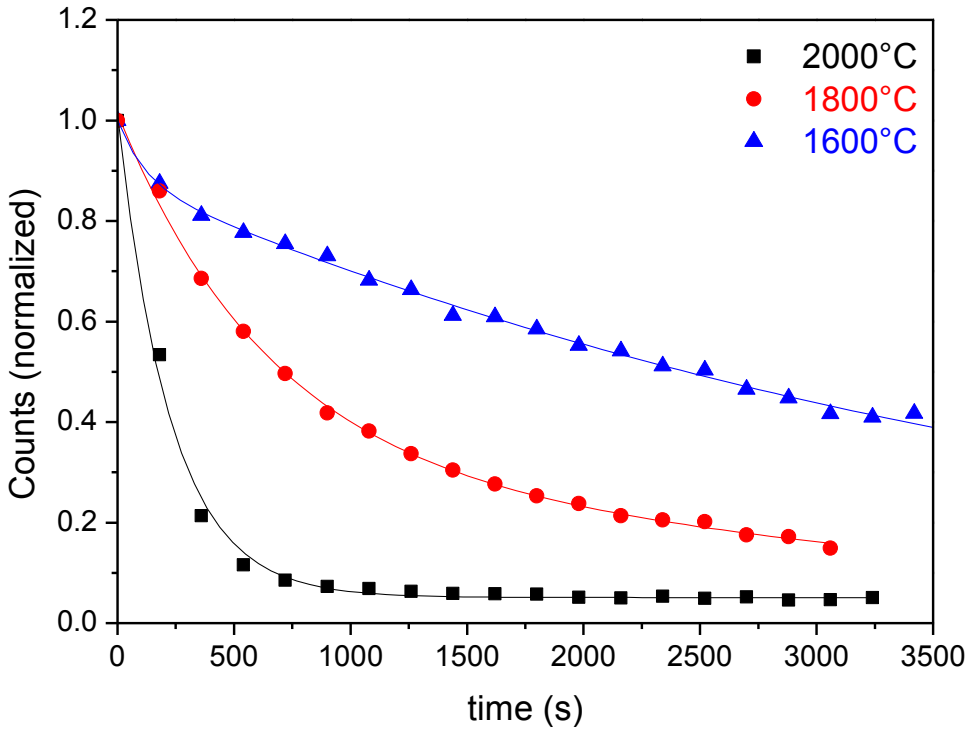

Fig. 40 – ^{92}Sr holdup-time measurements at three different temperatures.

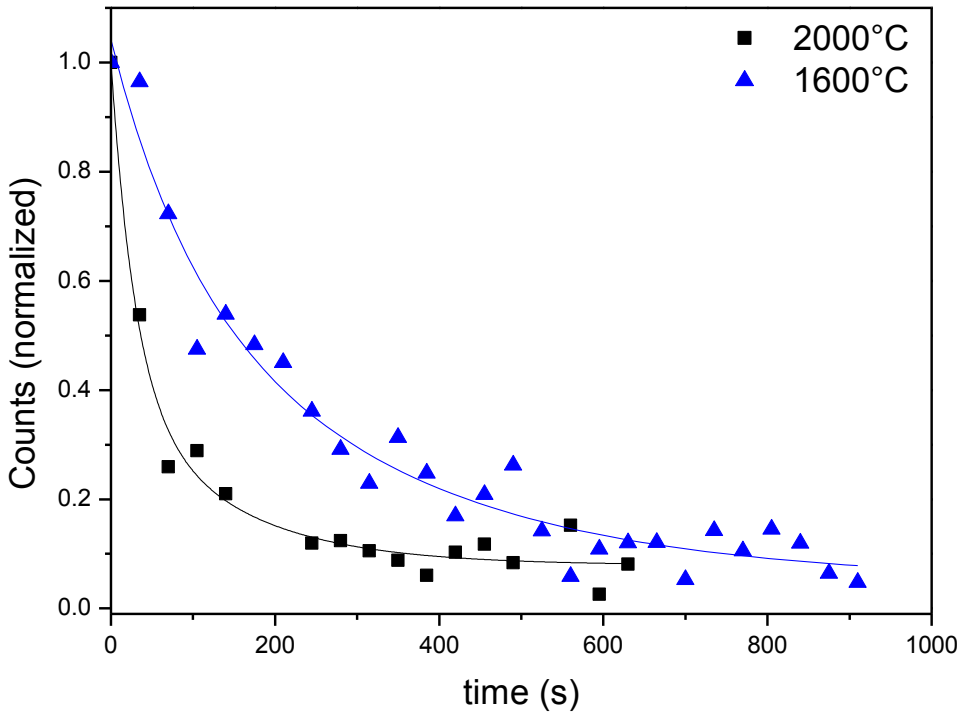

Fig. 41 – ^{128g}Sn holdup-time measurements at two different temperatures.

After data collection, following a week of cooling time, a visual inspection on the used target was done, and no significant structural changes or breakdown were observed, as shown in fig. 42. This aspect highlights the good thermo-mechanical behavior of the SPES thin disc target at 2000 °C, even if it has to be considered that in the real conditions it will be bombarded with a 4000 times higher proton beam current intensity, which itself will heat the target up to more than 2000 °C.

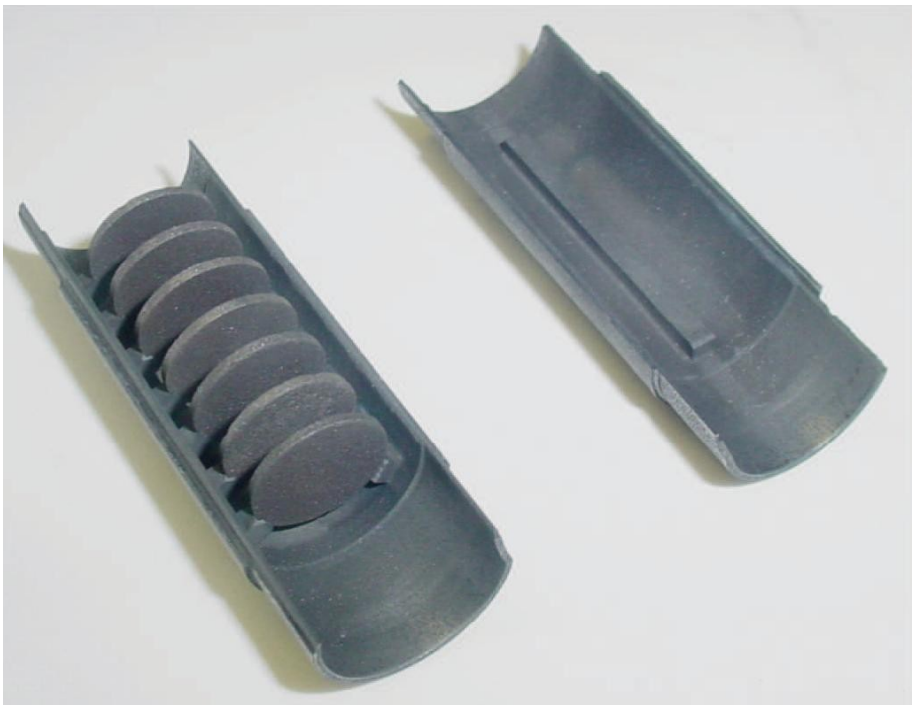

Fig. 42 – Seven “standard” UC_X discs after the online test.

3.3.4. 2nd test at HRIBF: "Low density" UC_X target prototype

The aim of the second test made at HRIBF was to obtain yield and release data of a different type of target material to be proposed as an alternative to the "standard" UC_X. The idea behind the synthesis of the second type of target material was the introduction in the reactive precursors mixture of a certain quantity of carbon nanotubes (CNTs) to replace the same exact quantity of graphite of eq. (43). In this way, the $UC_2 + 2C$ stoichiometry of the final carbon-dispersed uranium carbide wasn't changed, so that the only modifications introduced with respect to the "standard" material were relative to the partial graphite substitution with CNTs. The use of CNTs was motivated by the fact that past investigations made on lanthanum carbide (LaC_X, see chapter 4) demonstrated that the use of carbon nanotubes in place of graphite as carbon source can have significant effects on the material microstructure.

Lanthanum carbide was tested mainly as a benchmark for the production of uranium carbide as SPES targets, since it possesses similar properties to UC_X but without radioactivity issues. In particular, the reaction which can be used to produce it is very similar to eq. (43), as will be shown in chapter 4. With respect to the "standard" lanthanum carbide, obtained using graphite as a carbon source [85, 86], the use of CNTs gave rise to highly porous samples possessing high specific surface area (30 m^2/g, instead of 1.6 m^2/g for standard LaC_X) and consequently pores in the micro ($d<2$ nm) and meso ($2 \text{ nm}<d<50$ nm) range [87]. In addition, this meso- and micro-porosity was interconnected (open porosity), so in principle acting beneficially on the isotopes release, owing to the higher escape probability for the produced species enabled by the presence of empty cavities connected one another. On the other hand, this type of microstructure could detrimentally affect the thermal and mechanical properties of the material compared to its bulk form, since the presence of micro-meso pores could locally introduce abrupt changes in a particular mechanical or thermal feature, such as Young modulus or thermal conductivity. Basing on these considerations, the attention has been moved to the production of highly porous UC_X, to be tested online.

Material synthesis and properties

The possibility to combine nanotubes with metal carbides has been investigated in the last ten years. The main difficulty in the synthesis of such systems is related to the control and purity of the nano-junction between the nanotubes and the metal carbide. Moreover, CNTs have been tested to reinforce various ceramics, cermets, metals and alloys because they possess many

unique mechanical and physical properties [99, 100, 101, 102]. The two main difficulties in such applications are related to:

- The poor dispersability of the pristine multi-walled carbon nanotubes (MWCNTs) in the precursors mixture and the consequent severe structure inhomogeneities.

- The poor connectivity between CNTs and the ceramic matrix.

In the present test, multi-walled carbon nanotubes (MWCNTs) were tested, together with graphite, as carbon sources for the carbothermal reduction of uranium dioxide, eq. (43). The choice of using MWCNTs instead of single-walled carbon nanotubes (SWCNTs) was driven by two main reasons: the remarkably lower cost of MWCNTs compared to SWCNTs, and the presence of the multi walls available for carbothermal reaction.

The experimental steps performed to prepare the pellets to be thermal treated was basically the same as in the "standard" UC_X target production, with the only difference that in this case the carbon source was composed by 50% wt. graphite and 50% wt. nanotubes. MWCNTs, with outer average diameter of 8–15 nm and lengths up to 50 μm were purchased from Guangzhou Heji Trade Co. (China). Before mixing them with the other reagents (UO_2, graphite and 2% wt. phenolic resin binder), they were thermally treated at 500°C for 5 hours in air flow (20 mL/min).

The thermal treatment of the samples was performed in a high vacuum (10^{-5}-10^{-7} Pa) furnace using the experimental setup already described in paragraph 3.3.3. Differently from the "standard" UC_X synthesis, the heating cycle was divided into four steps:

- Slow heating (2 °C/min) up to 1075 °C, dwell time of 16 hours at 1075 °C, to promote the carbothermal reaction (43).

- Slow heating (2 °C/min) up to 1200 °C, dwell time of 16 hours at 1600 °C, to possibly complete the reaction.

- Heating (2 °C/min) up to 1800 °C, dwell time of 7 hours at 1800 °C, to sinter the carburized powders.

- Cooling to room temperature (2 °C/min).

The choice of dividing the reaction step into two different dwellings was motivated by the reaction kinetics, which can be analyzed considering the vacuum levels in the reaction chamber, shown in figure 43. It is clear that the release of CO in this case started for T > 1000 °C, and after the 16 hours dwelling the reaction wasn't completed, since a huge pressure peak was revealed at T > 1075 °C. With respect to the "standard" UC_X production, in this case the CO evolution inside the chamber started at lower temperatures, due to enhanced reactivity of the system obtained by using carbon nanotubes as a carbon source. On the other hand, the use of two different carbon sources and the consequent inhomogeneity of the structure resulted in a more chaotic CO evolution, with peaks arising for T > 1200 °C and T > 1600 °C. The maximum temperature reached during this process was actually higher than that of the "standard" UC_X production, with the aim of improving the consolidation by sintering of the crumbly structure obtained by pressing the UO_2-graphite-MWCNTs mixed powder.

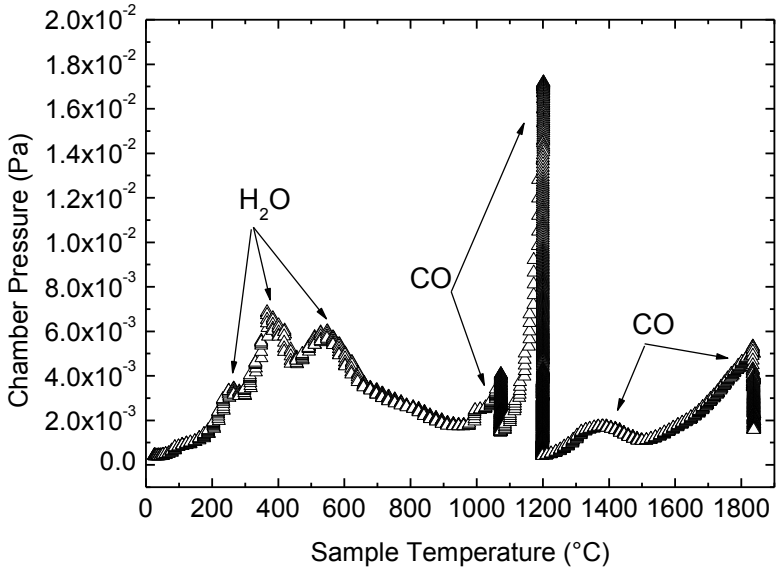

Fig. 43 - Pressure inside the reaction chamber upon carburization and sintering of the "low density" UC_X pellets.

Even if no XRD data were collected on these samples, their structure can be thought as a mix between the one shown in the XRD pattern of fig. 27 ("standard" UC_X, carbon source 100% graphite) and the one reported in fig. 44, relative to a UC_2+2C sample obtained from UO_2 and a carbon source made entirely of MWCNTs. For this reason, the actual structure of a "low density" UC_X sample should consist of UC_2 grains, a minor amount of UC, residual graphite and carbon nanotubes.

The SEM image shown in fig. 45 (surface of one of the discs) highlights the presence of a uranium carbide porous matrix interrupted by carbon blocks (black particles). Two higher

magnification images (fig. 46) show the presence of residual graphite blocks and carbon nanotubes, both acting as carbon sources and nucleating site for the formation of UC_2 grains.

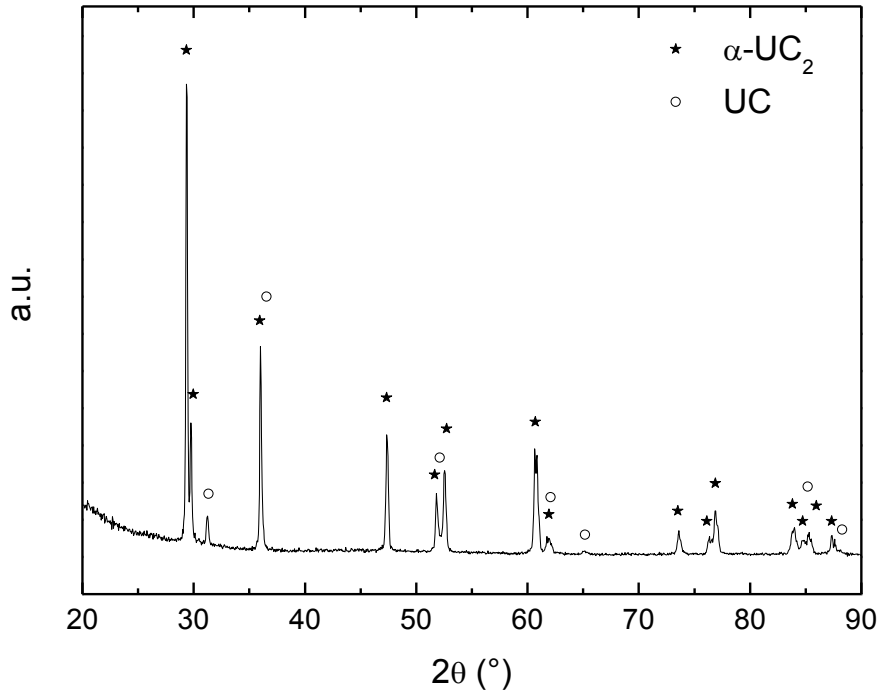

Fig. 44 – XRD pattern of a UC_X sample obtained from UO_2 and a MWCNTs. Courtesy of L. Biasetto.

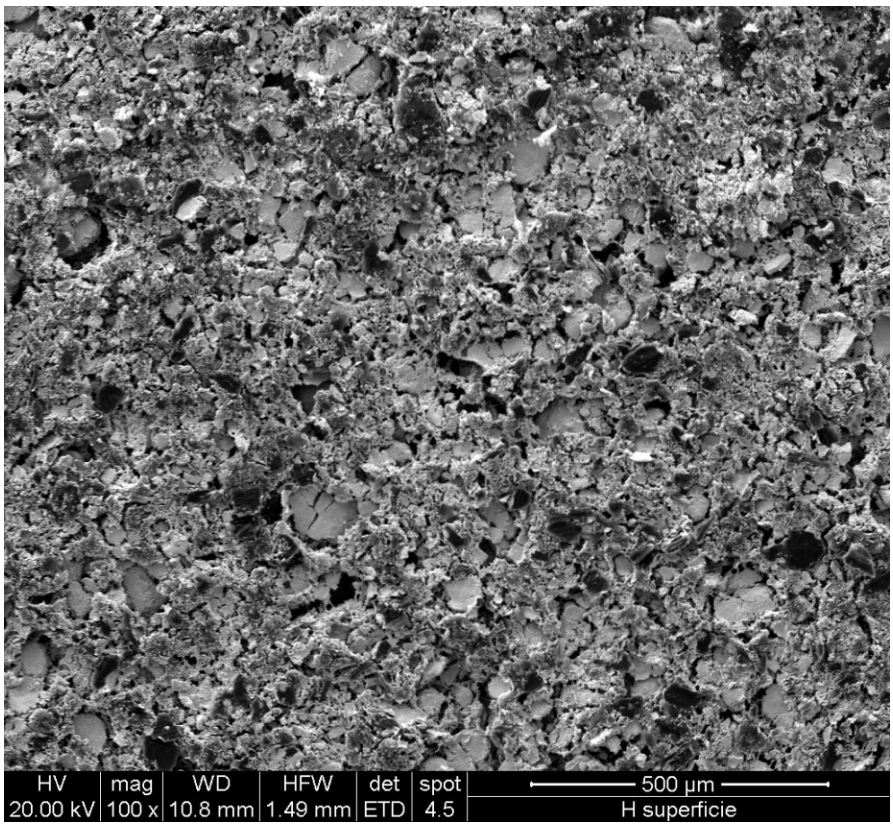

Fig. 45 – SEM micrograph of the surface of a "low density" UC_X disc.

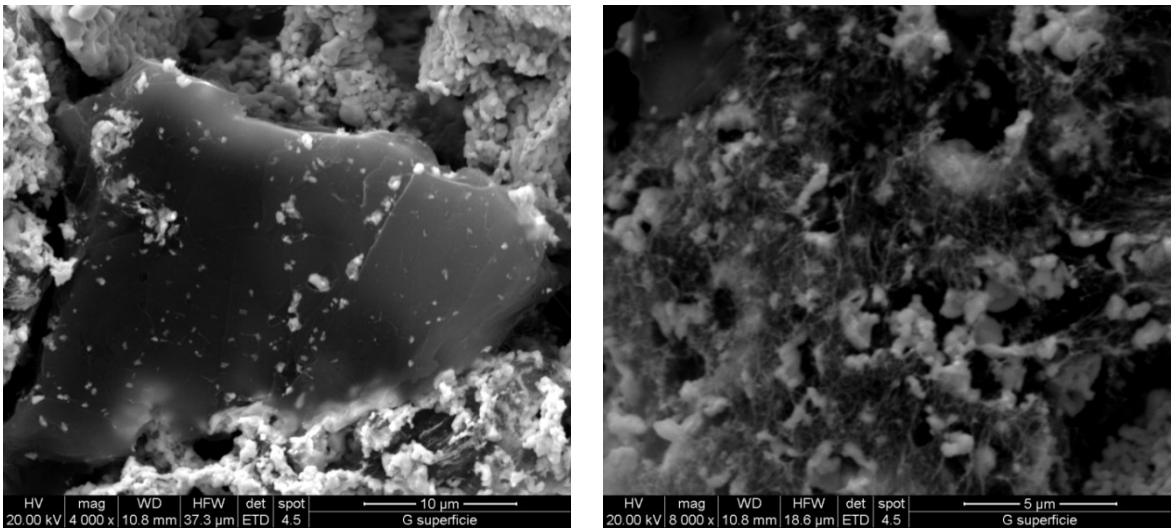

Fig. 46 – SEM micrographs of the surface of a "low density" UC_X disc. Left: detail on a graphite grain, right: detail on CNTs.

Table 7 reports the main properties of the "low density" UC_X discs. The value of the mass thickness per disc was kept constant in order to obtain the same amount of interaction between the primary beam and the ^{238}U atoms with respect to the "standard" UC_X target. The main difference between the two tested targets is, as expected, the density of the sintered structure, which in this case is lower thanks to the aforementioned effect of increasing porosity when using CNTs in place of graphite.

Table 7 – Average properties of the "low density" UC_X pellets used for the online test.

	"Standard" UC_X properties
Bulk density (g/cm^3)	2.59 ± 0.41
Disc diameter (mm)	13.07 ± 0.29
Mass thickness (g/cm^2)	0.41 ± 0.13
Total porosity (%)	75 ± 1

Online tests at HRIBF

Fig. 47 shows the seven UC_X discs used for the test (left) ant the target-ion source setup in which the graphite box was placed to be heated and irradiated (right). The experimental conditions under which the test was performed are substantially equal to those of the first test. In this case however, during the first heating to outgas the system (without proton beam on target)

and during the measurement at 2000 °C a huge gas evolution from the target was measured. A mass spectrum of the revealed species is shown in figure 48.

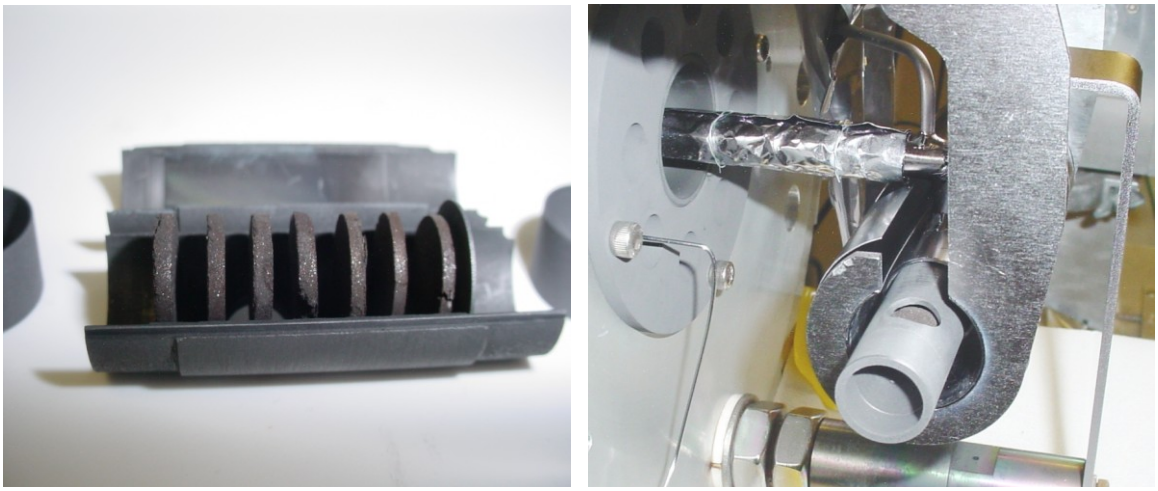

Fig. 47 – Left: seven "standard" UC_X discs placed inside the graphite box, right: target box installation in the OLTF heating system.

It is clear that the spectrum shown in figure 48 is dominated by mass 28, which can be either due to the presence of residual N_2 (which can be related to the presence of residual O_2, visible peak at mass 32, O_2^+) or more probably mainly ascribed to the presence of a huge CO outgassing from the target, due to the undergoing of the incomplete reaction (43). An evidence of this phenomenon is the presence of a considerable CO_2^+ signal at mass 44. Other important contributions to the mass spectrum are C^+, O^+, Ca^+ (mass 12, 16 and 40, respectively) and a peak system centered at about mass 56, probably originated by the sublimation of heated stainless steel components present inside the reaction chamber (Fe-Cr-Ni stable isotopes have masses in the range 50-64). Aluminum as well, in the form of Al+ ions, was originated from the evaporation of material constituting the water cooled target chamber. Peaks around mass 84 are those relative to the krypton gas which is introduced into the chamber by means of a calibrated leak, in order to check the correct functioning of the ion source by measuring the current of ^{84}Kr at the diagnostic station and comparing it to that obtained in the EBPIS optimal working conditions.

Analogously to what shown in paragraph 3.3.4, figure 49 reports an overview of the produced isotopes spectrum at 2000 °C, indicating the order of magnitude of the yields of the 83 isotopes revealed, belonging to the same 21 elements found in the "standard" UC_X online test.

The yield of the same isotopes shown for the previous test in table 5 are reported in table 8.

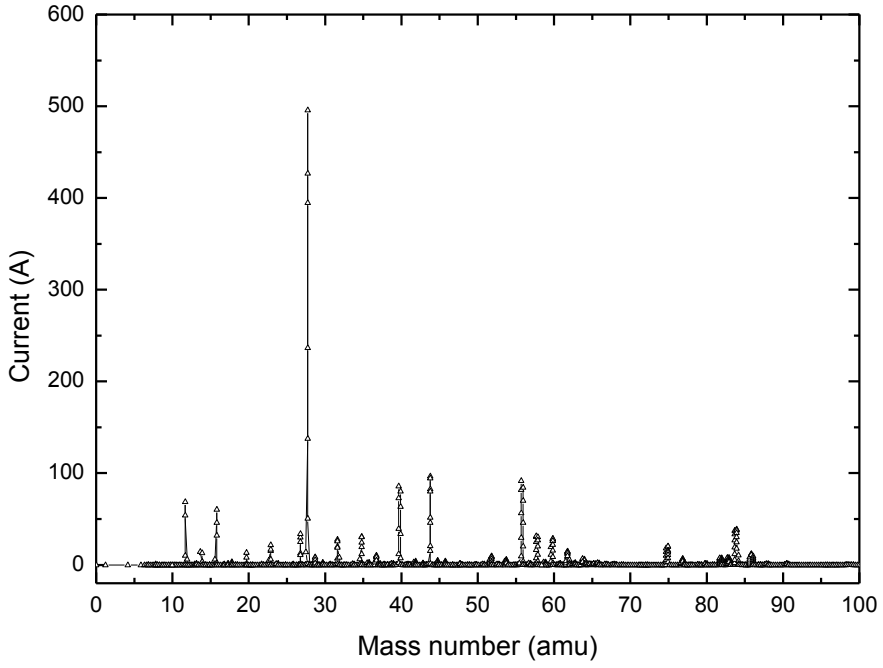

Fig. 48 – Mass spectrum obtained with no proton beam on the target kept at 2000 °C.

Values reported in table 8 show a general trend of increasing yield with temperature, due to faster diffusion and effusion mechanisms. Some exceptions are however present, certainly more than those found in the "standard" UC_X test. These variations can be attributable to:

- temporary variation of proton beam current and tuning parameters that weren't easily detectable and thus not taken into account during the yield calculations;

- the aforementioned outgassing from the target, particularly important at 2000 °C and at 1800 °C, less pronounced at 1600 °C, which could have locally decreased the ion source performance.

The production and release performance of this type of target will have certainly to be analyzed in more detail in future tests on the actual SPES conditions (higher primary beam current), in order to define specifically in which situations and for the fulfillment of which requirements a "low density" target can be preferred to a "standard" one, if any. However, the obtainment of a huge amount of on-line data for a second type of target represents a successful achievement for the SPES project in the main framework of informing the international nuclear physics community on which are the capabilities of the facility in terms of type and quantity of producible RIBs.

Yield vs. mass and vs. half-life trends relative to the same elements described in 3.3.3 are reported in figs. 50-57.

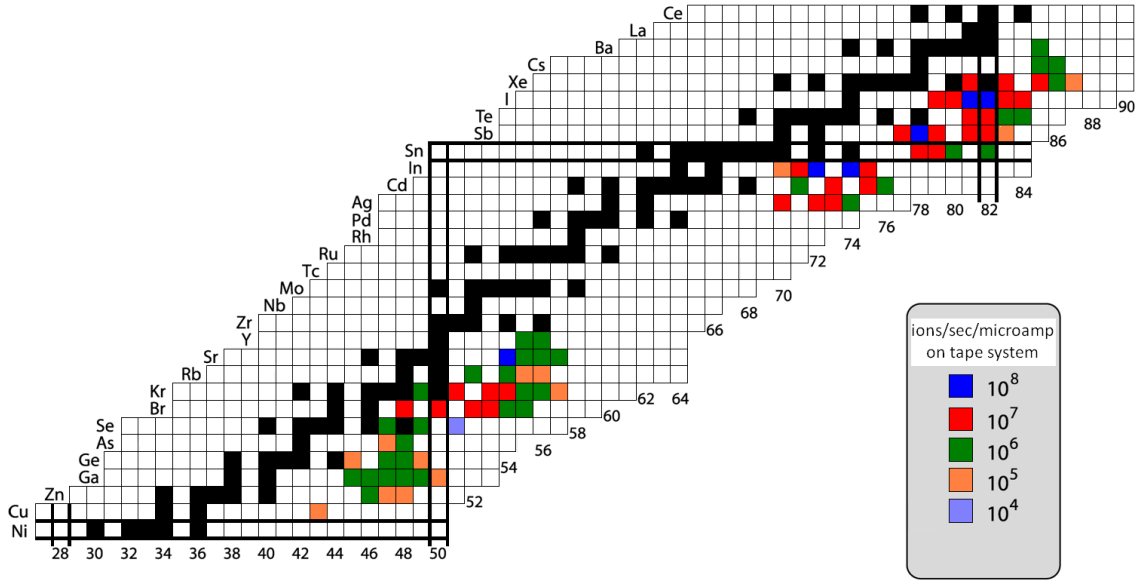

Fig. 49 – Radioactive isotopes obtained with a "low density" UC_X target at 2000 °C.

The general trend noticeable in figs. 50-57 is very similar to that found in the case of the "standard" target, i.e. yield increases with temperature and half-life. However, in many cases, a remarkable difference in yield has been found between the two experiments. A direct comparison between the data is in any case difficult, due to non-perfectly equal working conditions in the two tests, derived by the fact that they were conducted in different years, trying to replicate as much as possible the same operational parameters but not avoiding at all the presence of turbulence or instabilities in both the primary beam current and ion source performance (that is especially the case of the "low density" target test in which ion source was found to work with lower efficiency than in the case of the "standard one").

Data reported in table 9 represents a qualitative comparison between the absolute yields at different temperatures of the elements described in figs. 32-39 and 50-57 in the two tested targets. Data marked as "standard" indicate that for the particular element considered the average difference between the "standard" and the "low density" yields is higher than 10%, vice versa for the "low density" case. When the difference is lower than 10%, the "≈" symbol is used. Even taking into account the aforementioned intrinsic incomparability of the two tests, some considerations can be done on the reported data. It is clear that the yields relative to the "standard" target seem to be higher than the "low density" at higher temperatures, 2000 °C and 1800 °C. It is not completely clear if this behavior represents a limitation in the use of a CNTs-containing target, or it is only a matter of system performance at high temperature affected by the

CO outgassing from the target, since at 1600 °C the "low density" target seem to work at least as well as the "standard" one. An apparently strange deviation from this general trend was found in the case of tin, whose yields are almost always higher in the "low density" target. This aspect will have to be analyzed more into detail in future dedicated tests, since tin is by far the most requested element for nuclear physics experiments at the SPES facility [103].

Table 8 – Yields of a selected group of isotopes at 2000 °C, 1800 °C and 1600 °C.

		2000 °C		1800 °C		1600 °C	
Isotope	**$T_{1/2}$**	**Yield (/s*μA)**	**ΔYield (/s*μA)**	**Yield (/s*μA)**	**ΔYield (/s*μA)**	**Yield (/s*μA)**	**ΔYield (/s*μA)**
^{121}Ag	0.78s	$2.29*10^{6}$	$2.82*10^{5}$	$1.08*10^{6}$	$6.18*10^{4}$	$2.03*10^{6}$	$9.48*10^{4}$
^{81}Ga	1.22s	$2.22*10^{5}$	$8.02*10^{3}$	$1.55*10^{5}$	$5.14*10^{3}$	$1.14*10^{5}$	$3.94*10^{3}$
^{120g}Ag	1.23s	$8.04*10^{6}$	$8.60*10^{5}$	$4.86*10^{6}$	$2.69*10^{5}$	$6.83*10^{6}$	$3.46*10^{5}$
^{124}Cd	1.29s	$2.63*10^{6}$	$2.50*10^{5}$	$1.80*10^{6}$	$1.19*10^{5}$	$1.45*10^{6}$	$7.42*10^{4}$
^{78}Zn	1.47s	$8.96*10^{4}$	$4.27*10^{3}$	$5.39*10^{4}$	$1.81*10^{3}$	$4.02*10^{4}$	$1.41*10^{3}$
^{123m}Cd	1.82s	$5.01*10^{6}$	$2.78*10^{5}$	$3.40*10^{6}$	$1.12*10^{5}$	$3.14*10^{6}$	$8.36*10^{4}$
^{92}Kr	1.84s	$7.14*10^{5}$	$3.62*10^{4}$	$4.08*10^{5}$	$1.86*10^{4}$	$2.00*10^{5}$	$4.50*10^{3}$
^{90}Br	1.91s	$7.95*10^{5}$	$8.99*10^{4}$	$3.65*10^{5}$	$3.04*10^{4}$	$7.29*10^{4}$	$3.37*10^{3}$
^{119}Ag	2.10s	$1.42*10^{7}$	$1.90*10^{5}$	$2.01*10^{7}$	$2.44*10^{5}$	$1.88*10^{7}$	$2.34*10^{5}$
^{93}Rb	5.80s	$1.92*10^{5}$	$6.63*10^{3}$	/	/	$1.21*10^{5}$	$6.50*10^{3}$
^{123g}In	5.98s	$6.42*10^{7}$	$5.45*10^{6}$	$4.40*10^{7}$	$1.77*10^{6}$	$4.19*10^{7}$	$1.41*10^{6}$
^{72}Cu	6.60s	$1.13*10^{5}$	$3.42*10^{3}$	$1.33*10^{5}$	$2.86*10^{3}$	$1.00*10^{5}$	$2.83*10^{3}$
^{133m}I	9.00s	$1.11*10^{7}$	$3.42*10^{6}$	$5.05*10^{6}$	$2.06*10^{5}$	$4.55*10^{6}$	$1.88*10^{5}$
^{88}Br	16.30s	$1.17*10^{7}$	$5.98*10^{5}$	$4.85*10^{6}$	$1.29*10^{5}$	$1.40*10^{6}$	$3.05*10^{5}$
^{79g}Ge	19.00s	$1.22*10^{6}$	$7.02*10^{4}$	$7.51*10^{5}$	$3.97*10^{4}$	$4.89*10^{5}$	$2.64*10^{4}$
^{81}As	34.00s	$6.25*10^{5}$	$2.01*10^{4}$	$2.06*10^{5}$	$7.78*10^{3}$	$1.47*10^{5}$	$6.05*10^{3}$
^{132}Sn	39.70s	$2.82*10^{6}$	$1.94*10^{5}$	$1.03*10^{6}$	$2.51*10^{4}$	$1.13*10^{6}$	$2.78*10^{4}$
^{120m}In	47.30s	$2.37*10^{7}$	$1.89*10^{6}$	$1.70*10^{7}$	$6.45*10^{5}$	$1.71*10^{7}$	$6.68*10^{5}$
^{140}Cs	1.06m	$1.12*10^{6}$	$1.38*10^{5}$	$5.70*10^{5}$	$2.38*10^{4}$	$2.07*10^{5}$	$9.40*10^{3}$
^{94}Sr	1.23m	$2.37*10^{6}$	$2.78*10^{5}$	$6.48*10^{5}$	$3.63*10^{4}$	$1.85*10^{5}$	$1.14*10^{4}$
^{133}Sb	2.50m	$9.01*10^{6}$	$2.81*10^{6}$	$4.41*10^{6}$	$2.22*10^{5}$	$5.80*10^{6}$	$2.49*10^{5}$
^{137}Xe	3.83m	$3.52*10^{7}$	$1.01*10^{7}$	$1.12*10^{7}$	$4.32*10^{6}$	$4.40*10^{6}$	$2.53*10^{5}$
^{93}Sr	7.45m	$5.18*10^{6}$	$1.12*10^{5}$	$1.41*10^{6}$	$2.29*10^{4}$	$6.06*10^{5}$	$1.83*10^{4}$
^{95}Y	10.30m	$1.34*10^{6}$	$1.61*10^{5}$	$3.17*10^{5}$	$2.58*10^{4}$	$4.69*10^{4}$	$1.80*10^{3}$
^{141}Ba	18.30m	$1.88*10^{6}$	$1.29*10^{5}$	$3.82*10^{5}$	$1.97*10^{4}$	/	/
^{83g}Se	22.40m	$1.89*10^{6}$	$5.06*10^{4}$	$1.90*10^{5}$	$3.13*10^{3}$	$7.20*10^{4}$	$1.42*10^{3}$
^{134}Te	41.80m	$4.37*10^{7}$	$1.70*10^{6}$	$3.69*10^{7}$	$5.34*10^{5}$	$2.43*10^{7}$	$4.83*10^{5}$
^{134g}I	52.50m	$6.88*10^{7}$	$2.52*10^{6}$	$7.53*10^{7}$	$1.05*10^{6}$	$4.91*10^{7}$	$9.46*10^{5}$
^{87}Kr	1.27h	$6.67*10^{6}$	$1.04*10^{6}$	$4.96*10^{6}$	$7.78*10^{5}$	$2.41*10^{6}$	$2.91*10^{5}$

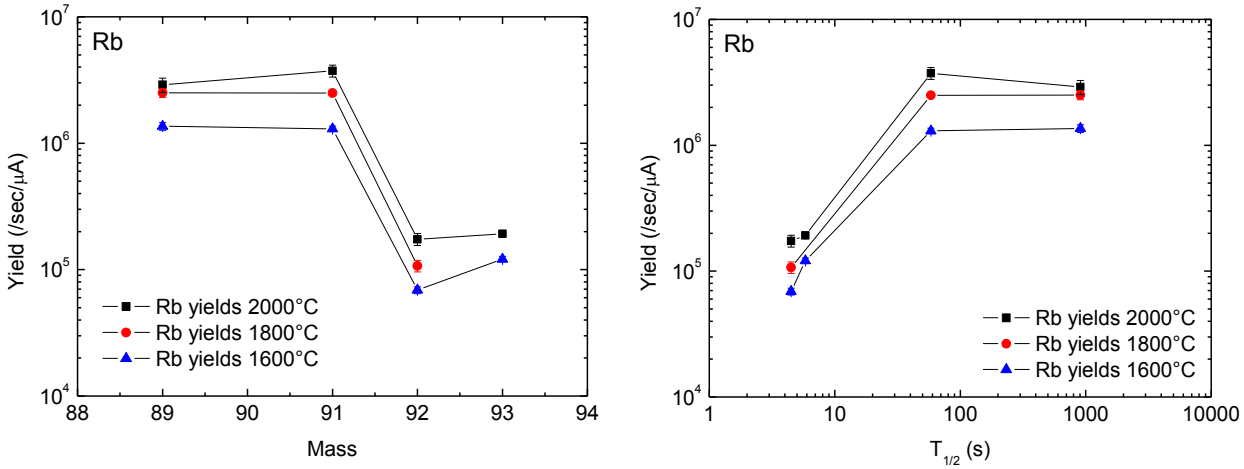

Fig. 50 – Ion yields of Rb isotopes at different temperatures. Left: yield *vs.* mass. Right: yield *vs.*$t_{1/2}$.

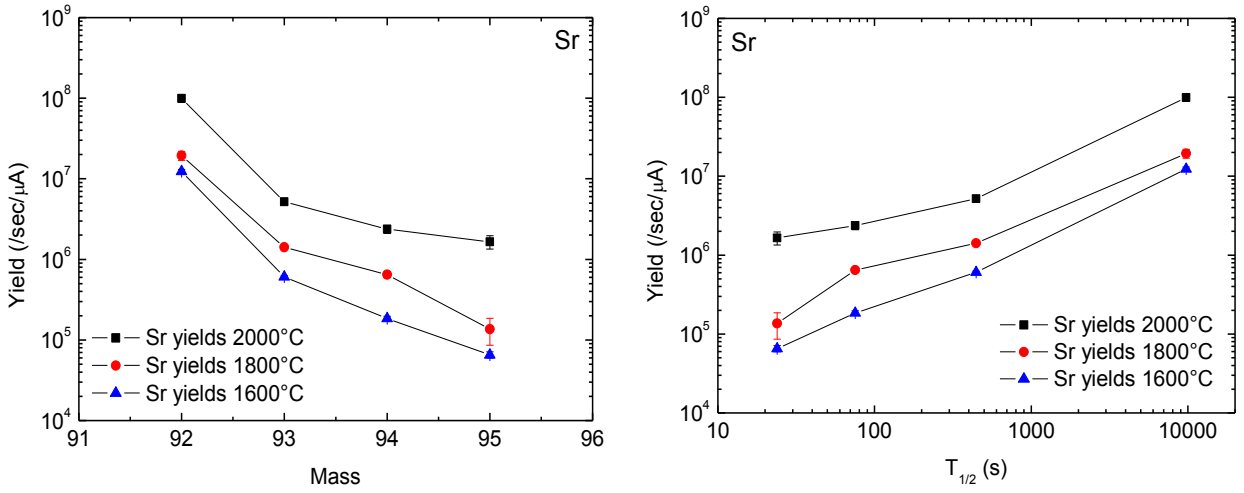

Fig. 51 – Ion yields of Sr isotopes at different temperatures. Left: yield *vs.* mass. Right: yield *vs.*$t_{1/2}$.

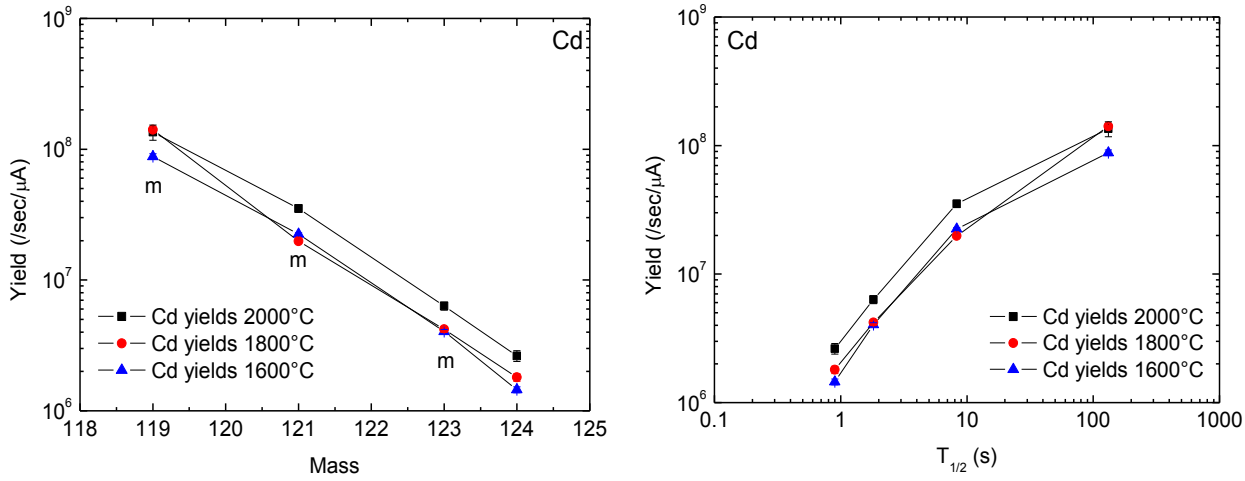

Fig. 52 – Ion yields of Cd isotopes at different temperatures. Left: yield *vs.* mass. Right: yield *vs.*$t_{1/2}$.

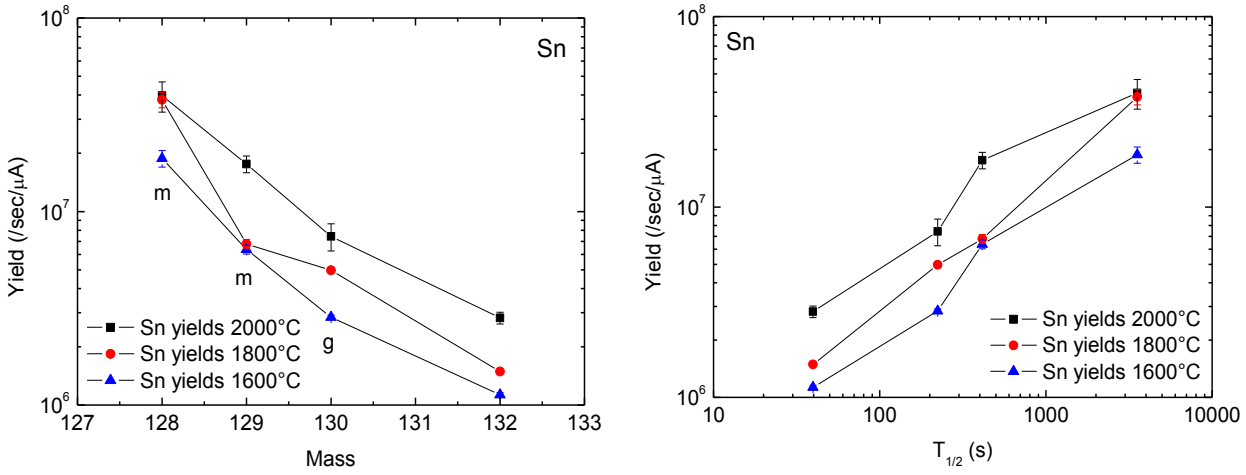

Fig. 53 – Ion yields of Sn isotopes at different temperatures. Left: yield *vs.* mass. Right: yield *vs.*$t_{1/2}$.

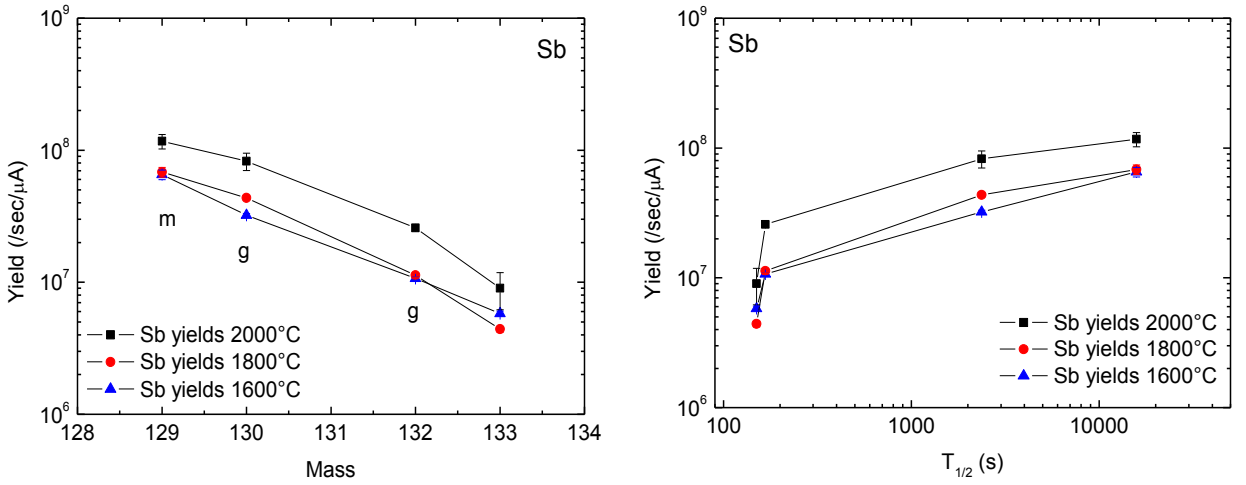

Fig. 54 – Ion yields of Sb isotopes at different temperatures. Left: yield *vs.* mass. Right: yield *vs.*$t_{1/2}$

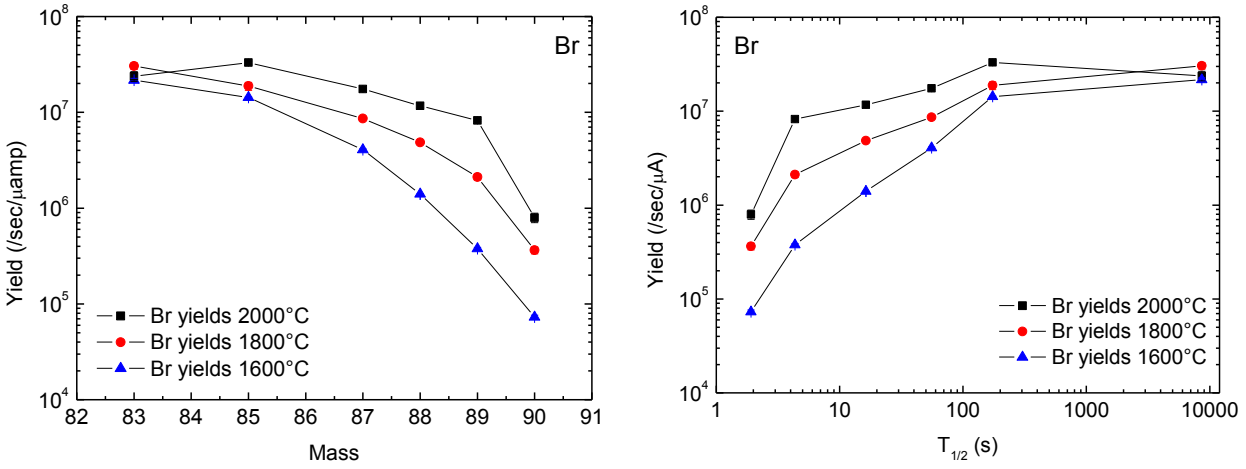

Fig. 55 – Ion yields of Br isotopes at different temperatures. Left: yield *vs.* mass. Right: yield *vs.*$t_{1/2}$

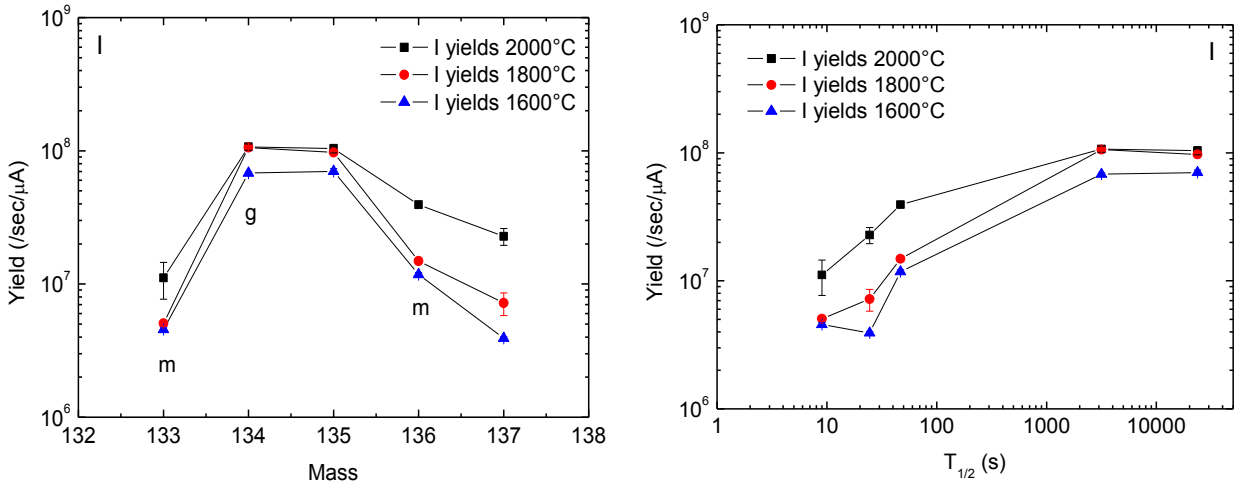

Fig. 56 – Ion yields of I isotopes at different temperatures. Left: yield *vs.* mass. Right: yield *vs.*$t_{1/2}$

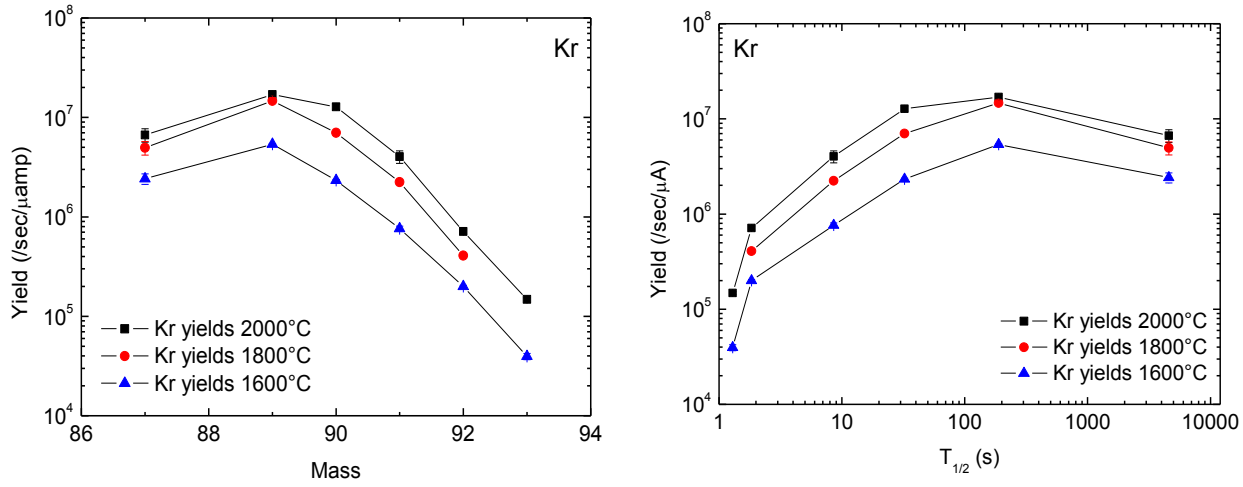

Fig. 57 – Ion yields of Kr isotopes at different temperatures. Left: yield *vs.* mass. Right: yield *vs.*$t_{1/2}$

Table 9 – Comparison between the yields of the two tested targets.

Element	Higher Y at 2000 °C	Higher Y at 1800 °C	Higher Y at 1600 °C
Rb	Standard	Low density	Low density
Sr	Standard	Standard	Standard
Cd	Standard	Standard	Standard
Sn	Low density	≈	Low density
Sb	≈	≈	Low density
Br	Standard	Standard	Standard
I	Standard	Standard	Low density
Kr	Standard	Standard	Standard

Table 10 reports the fitting time parameters, relative to eq. (45), used to characterize the holdup-time behavior of the target in the case of ^{92}Sr and ^{128g}Sn, whose release trends are shown in figs. 58 and 59, respectively.

Table 10 – Fitting parameters for the holdup-time measurements of ^{92}Sr and ^{128g}Sn.

Isotope	2000°C					1800°C					1600°C				
	y_0	FAST		SLOW		y_0	FAST		SLOW		y_0	FAST		SLOW	
		A	t_f (s)	B	t_s (s)		A	t_f (s)	B	t_s (s)		A	t_f (s)	B	t_s (s)
^{92}Sr	0.04	0.48	186	0.48	1149	0.04	0.46	204	0.50	1313	0.04	0.09	113	0.87	1713
^{128g}Sn	0.00	1.00	53	--	--	0.00	1.00	101	--	--	0.00	0.56	54	0.45	419

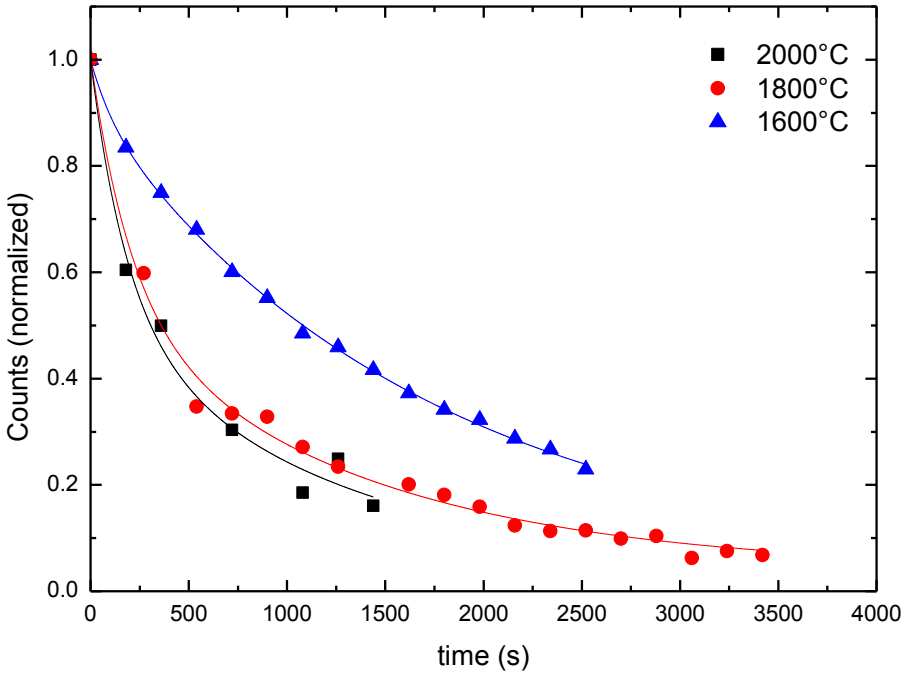

Fig. 58 – ^{92}Sr holdup-time measurements at three different temperatures.

A direct comparison between the holdup-time measurement trends of the two targets should be more significant than the comparison between the absolute yields, because data are normalized on the steady state yield, thus measuring only the rate of decay of the main γ signal of a particular isotope, so directly taking into account the release capabilities of the target.

In the case of ^{92}Sr, the direct comparison between figs. 40 and 58 show clearly that the release is faster in the case of the "standard" target at 2000 °C, whereas for lower temperatures the "low density" target seems to release the isotope more rapidly. This aspect is clearly deductible from the A, B and time parameters reported in tables 6 and 10. Data relative to ^{128g}Sn seem to confirm what shown in table 9, since the release at 2000 °C from the "low density"

target is faster than that from the “standard” one, whereas at 1600 °C the two releases look very similar, even if their time parameters are different.

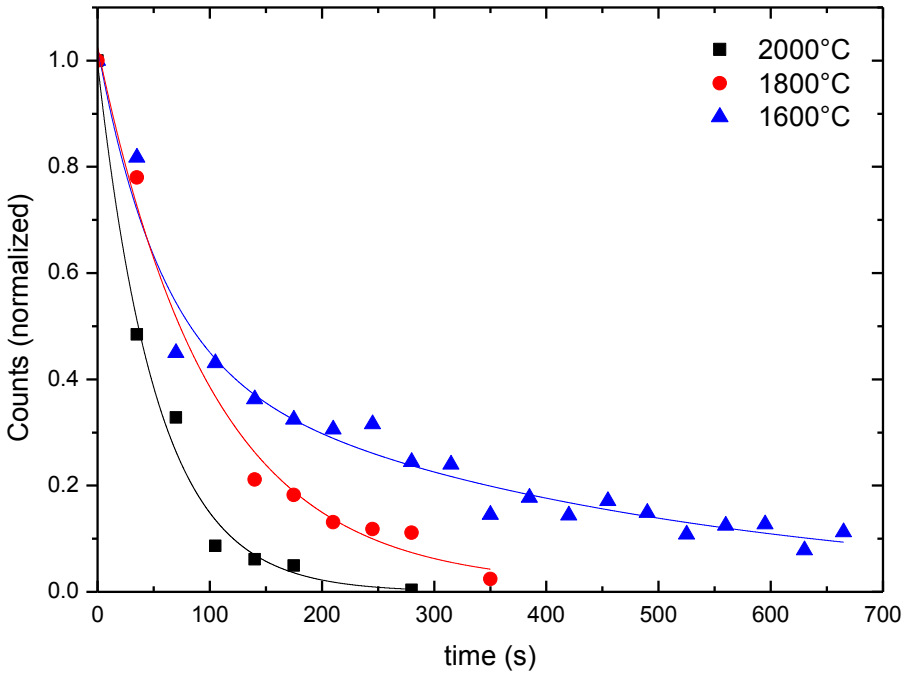

Fig. 59 – ^{128g}Sn holdup-time measurements at three different temperatures.

Fig. 60 – Seven “low density” UC_X discs after the online test.

After the test, the target box was easily disassembled in order to visually inspect the target discs. Analogously to the previous test, this operation was very important in order to check if any major damage on the discs had happened, especially on their central part, which was the one hit

by the proton beam and determined the overall target behavior in terms of both stopping power and cross section for the p-^{238}U reaction. A certain loss of material from the target was observed, especially from the discs named #2 in fig. 60, but the amount of damage occurred was with any probability non influential on the target behavior, since it was in major part a consequence of the box extraction from the TIS system and the subsequent disc removal from the box.

3.4. Towards new UC_X on-line tests: a "medium density" target prototype

During the construction and development of SPES in its final layout, new on-line tests on different facilities will be carried out in order to test the performances of the SPES target when exposed to irradiation in high-power conditions. Besides testing the thermo-structural behavior and properties of the target-ion source system, these tests will be useful to further expand the knowledge about the release behavior of the UC_X thin discs, taking as a starting point for comparison the two low-intensity on-line tests described above. The research and development on materials will obviously be not limited to the "standard" UC_X target, since many properties and parameters of both the target composition and microstructure can be changed in order to better characterize the release from a thin-disc based target. By doing this, the SPES community will obtain practical information to refer when choosing the correct target, depending on the type of experiment or study the RIBs will be produced for.

In this general framework, taking into account the types of UC_X produced for the previously described on-line tests, a new type of target material was produced. In this case, with respect to the "standard" UC_X composition, the production process was modified in order to keep constant the final material composition, UC_2+2C as a result of equation (43), but increasing the density of the target disks by reducing their total porosity. The obtainment of on-line data on this type of target will allow for a better characterization of the relation between the UC_X microstructure properties and the obtainable yield of isotopes.

The production process developed for the production of the new type of material, namely "medium density" UC_X, consists of the following steps:

- UO_2, graphite and phenolic resin mixing, uniaxial cold pressing into pellets in the same conditions described in 3.3.3;
- Thermal treatment up to 1600 °C in high vacuum with the same heating cycle as in 3.3.3;
- Manual grinding into powders of the sintered pellets, cold pressing into discs;
- High vacuum sintering at 1800 °C of the pressed pellets.

Table 11 reports the properties of the produced discs, as obtained from the first thermal treatment and after the second sintering process. One of the produced pellets and a graphite box containing seven "medium density" discs are shown in figure 61.

Table 11 – Average properties of the "medium density" UC_X pellets.

	First thermal treatment	**Second sintering**
Bulk density (g/cm^3)	4.19 ± 0.20	6.19 ± 0.39
Disc diameter (mm)	12.72 ± 0.05	12.93 ± 0.10
Mass thickness (g/cm^2)	0.48 ± 0.05	0.41 ± 0.06
Total porosity (%)	59 ± 1	39 ± 1

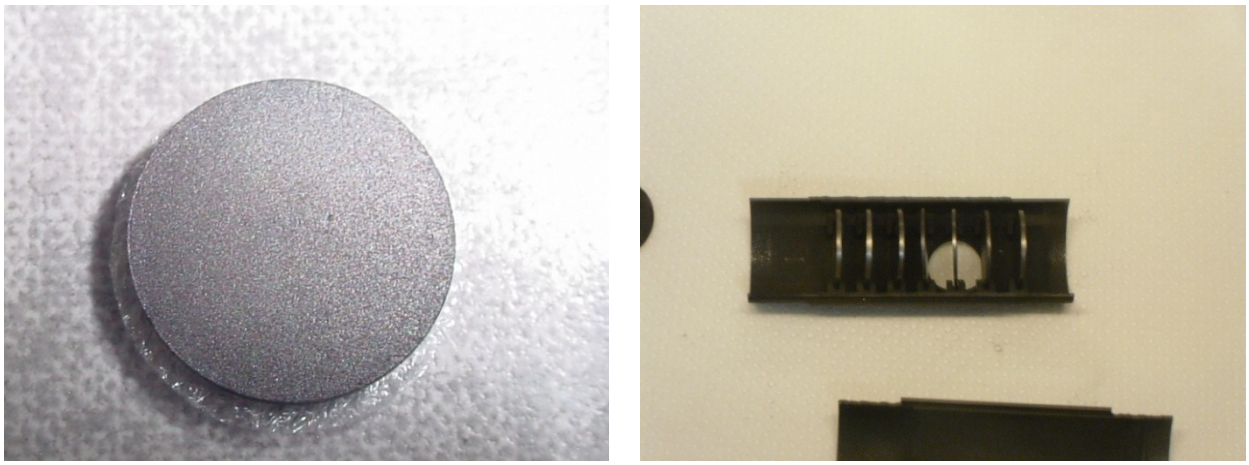

Fig. 61 – Left: "medium density" UC_X pellet, right: target prototype containing seven discs.

Values reported in table 11 show the effect of the second sintering process on the disc physical properties: as expected, a density increase of almost 50% was obtained, thus reducing the total porosity to less than 40%. In order to prepare a target that could be used in the same conditions as the two previously described ones, the mass thickness of a single disc was kept equal to the value reported in tables 4 and 7. The obtainment of a new type of target material with the same composition as the standard one but with different properties could lead the way towards new on-line tests to perform on SPES target prototypes.

3.5. Conclusions

Uranium carbide is the most used target material for the generation of Radioactive Ion Beams with the ISOL technique, due to its excellent thermal properties combined with the possibility to exploit the p-induced uranium fission reaction to generate a huge number of isotopes of several different elements.

The research and development of target prototypes for the SPES project has been focused in the past in the synthesis of carbon dispersed uranium carbides, namely UC_X, which were successfully off-line characterize, in order to highlight the main properties of the material and to describe into detail the production process of the SPES target pellets.

In order to have a direct evidence of the performance of the UC_X target designed according to the SPES layout (seven separate thin discs), two on-line tests were performed at the HRIBF facility of the Oak Ridge National Laboratory. In these experiments, two different types of UC_X were irradiated by protons of the same energy as in the future SPES facility – 40 MeV - and their fission products were extracted, ionized, mass separated and revealed by means of gamma spectrometry, in order to obtain the yields of several isotopes coming from the target. A further release characterization was carried out by means of holdup-time measurements on two different long-lived isotopes. The first tested material represent the "standard" UC_X designed to be used in the final SPES facility, obtained from the high temperature carbothermal reduction of uranium dioxide using graphite as a carbon source; the second one was obtained reacting the same uranium oxide with a 50%-50% wt. mixture of graphite and multi-walled carbon nanotubes, with the aim of obtaining a "low density" UC_X possessing a higher amount of open interconnected pores to favor the release of isotopes from its matrix.

The experimental results showed that both the targets can be successfully used to produce and release several tens of radioactive isotopes of more than 20 elements, with half-lives from less than one second to up to several hours. The obtainment of such a huge quantity of on-line data represented a key milestone in the SPES target research and development, since it was the first experimental evidence of the good on-line behavior of the innovative SPES target-ion source system, previously off-line characterized in detail. Both the materials survived to a week of low intensity (50 nA) proton beam bombardment at high temperatures – the tests were performed at 2000 °C, 1800 °C and 1600 °C – without significant damage, proving the efficiency of the separate thin disc system in working at high temperatures under irradiation.

A yield vs. temperature and vs. half-life characterization was performed for most of the produced isotopes, highlighting the importance of working at the highest possible temperature in order to obtain a better release of short-lived species from the target.

Some differences were found between the isotope yields and release properties of the two targets, both depending on the actual material microstructure and on the operational anomalies found during the two experimental tests, which added a non-quantifiable degree of uncertainty in the calculated data.

A qualitative comparison between the yields of the two experiments suggests that the "standard" target seem to release more radioactive species than the "low density" one at the highest operative temperatures, 2000 °C and 1800 °C, while at 1600 °C the yields of the two targets are comparable. The investigations made in the two tests did not completely clarify whether this behavior is due to bad release properties of the CNTs-containing target or it is only caused by the CO outgassing from it, negatively affecting the ion source performance. In the case of the extremely strategic tin isotopes – in terms of experiment requests at the future SPES facility - however, yields were found almost always higher in the "low density" target. This behavior was confirmed studying the holdup-time of ^{128g}Sn released from the two systems.

Chapter 4

Targets for the production of proton-rich isotopes at SPES

4.1. Introduction

Differently from neutron-rich species, which can all be produced from the proton induced fission of uranium, the production of proton-rich isotopes requires a more specific choice of the target material, since they are not obtained from a fission reaction. The interaction of low energy particles (as the protons that will be used at SPES) with a non-fissile atom can indeed only lead to the formation of products that are those close in mass and charge to the target nuclei. For this reason, in most cases each proton-rich beam requires a dedicated target [35].

Several proton-rich isotopes have been produced and are nowadays being delivered to experiments in ISOL facilities, obtained from the interaction of protons with different targets, such as:

- Oxides like CaO (production of p-rich isotopes of C, Ne, Ar [104, 105]), HfO_2 (for $^{17-18}F$ experiments at HRIBF [35]), ZrO_2 (p-rich isotopes of elements from Cu to Kr [106, 107]), CeO_X and La_2O_3 (p-rich Xe isotopes [107]), Al_2O_3 ($^{26-27}Si$ production [35]). In most cases, oxides are used in the form of fibrous sheets.

- Carbides, such as SiC (used for the production of p-rich Ne, Na [108], Mg [109], F [108] and Al [35] isotopes), LaC_X (p-rich isotopes of In [6], Cd [110] and Xe [108]), Sc_2C_3 (p-rich K, Mg and Ar [108]), VC ($^{32-37}Ar$ production [108]).

- Metal foils of Nb [111], Ta and Zr [108], used to produce large set of isotopes of alkali, alkaline-earth and transition metals.

- Molten metals such as germanium [108] and nickel [35], used to produce p-rich isotopes of Ga [90] and Cu.

- Cerium sulfide, used at HRIBF in the form of a thin film deposited onto a tungsten-coated graphite matrix, to produce proton-rich isotopes of Cl [35].

For the production of proton-rich isotopes at SPES, several targets have been proposed and an estimation has been made on which isotopes will be produced by irradiating them with 40 MeV protons [112]. What follows in tables 12 to 14 is a detailed list of targets and producible species, supposing a 200 μA proton beam on target; SIS, LIS and PIS represent surface, laser and plasma ion source, respectively.

It is important to underline that the beams of proton-rich isotopes will be the first to be produced at SPES, in particular those of aluminum, fluorine and beryllium. The list of proposed materials is limited to solid targets, since no gaseous or liquid targets are planned to be used at SPES.

Table 12 – Proton-rich beams of light elements produced at SPES.

Isotope	$T_{1/2}$	Post-accelerated yield estimation (ions/s)	Candidate targets	Ion source
^{7}Be	53.29 d	$2.0*10^{7}$	B_4C – HfO_2 – ZrO_2 – Al_2O_3	LIS – PIS
^{17}F	1.08 m	$2.0*10^{7}$	HfO_2 – ZrO_2 – Al_2O_3	PIS
^{18}F	1.83 h	$2.0*10^{6}$	HfO_2 – ZrO_2 – Al_2O_3	PIS
^{21}Na	22.48 s	/	Al_2O_3 – SiC – CeS	SIS
^{22}Na	2.60 y	/	Al_2O_3 – SiC – CeS	SIS
^{22}Mg	3.86 s	/	Al_2O_3 – SiC – CeS	LIS – PIS
^{23}Mg	11.30 s	/	Al_2O_3 – SiC – CeS	LIS – PIS
^{24g}Al	2.07 s	/	SiC	LIS
^{25}Al	7.18 s	$1.0*10^{4}$	SiC	LIS
^{26m}Al	6.35 s	$1.0*10^{4}$	SiC	LIS
^{26}Si	2.21 s	$1.0*10^{3}$	Al_2O_3 – CeS	PIS
^{27}Si	4.16 s	$1.0*10^{3}$	Al_2O_3 – CeS	PIS
^{29}P	4.10 s	/	SiC – CeS	PIS
^{34g}Cl	1.53 s	$5.0*10^{3}$	CeS	PIS

Among the materials proposed in the following tables, SiC has already been successfully tested as a SPES target prototype, during an on-line irradiation experiment at HRIBF in very similar conditions to those reported in this work for UC_X [12]. The results highlighted the

possibility to obtain ^{26m}Al beams from a 15 mm diameter SiC target prototype made of 7 separated discs, kept at 1800 °C and irradiated with a 42 MeV, 12 μA proton beam. The tested material was purchased from Saint-Gobain (Hexoloy SC) and cut into thin discs of thickness ranging from 0.5 mm to 1 mm. Due to its easy availability and considering the good results obtained on the target prototype, this type of SiC will be probably used as a SPES target for the production of p-rich Al isotopes without further investigations on its synthesis process. The same material used for the on-line test is commonly used to characterize the thermo-electrical performances of the SPES target-ion source complex in dedicated off-line investigations [5], using the set-up shown in fig. 12.

Table 13 – Proton-rich beams of medium mass elements produced at SPES.

Isotope	$T_{1/2}$	Post-accelerated yield estimation (ions/s)	Candidate targets	Ion source
^{73}As	80.30 d	$2.90*10^2$	ZrC – ZrO_2	LIS
^{74}As	17.77 d	$3.78*10^3$	ZrC – ZrO_2	LIS
^{78}Br	6.46 m	$6.02*10^2$	ZrC – ZrO_2	PIS
^{83}Rb	86.20 d	$7.10*10^4$	ZrC – ZrO_2	SIS
^{84g}Rb	32.80 d	$8.02*10^5$	ZrC – ZrO_2	SIS
^{85g}Sr	64.90 d	$4.46*10^3$	ZrC – ZrO_2	SIS

Table 14 – Proton-rich beams of heavy elements produced at SPES.

Isotope	$T_{1/2}$	Post-accelerated yield estimation (ions/s)	Candidate targets	Ion source
^{126}I	80.30 d	$3.66*10^5$	LaC_X – CeS	PIS
^{131}Cs	9.69 d	$1.64*10^5$	LaC_X – CeS	SIS
^{132}Cs	6.47 d	$1.79*10^6$	LaC_X – CeS	SIS
^{131g}Ba	11.50 d	/	LaC_X – CeS	LIS
^{133}La	3.91 h	/	CeS	LIS
^{134}La	6.67 m	/	CeS	LIS
^{135}La	19.40 h	$4.56*10^2$	CeS	LIS
^{136}La	9.90 m	$5.60*10^4$	CeS	LIS
^{135g}Ce	17.76 h	/	LaC_X – CeS	SIS

The synthesis of all the other proposed targets will require specific routes, depending on their properties and on the particular form in which they will be used (powder targets, fibrous

sheets, foams). In this work, the attention has been focused on the production of carbides, since as already stated they possess the most favorable release and thermo-mechanical properties among all the classes of materials that can be used in ISOL facilities. In particular, boron carbide and lanthanum carbide synthesis and characterization will be reported in the following paragraphs.

4.2. Boron carbide targets for the SPES project [113]

Among the feasible proton-rich beams to be produced at SPES (see tables 12-14), ^{7}Be represents an important choice due to its applications, mainly in astrophysics experiments but also in materials science and medicine [114]. Particularly significant is their use in determining the cross section of the direct-capture reaction $^{7}Be(p,\gamma)^{8}B$, used in astrophysics to calculate the expected neutrino flux from the sun [115]. ^{7}Be can also be successfully used as a tracer in high-sensitivity wear analysis in materials science [116] and medicine studies [117].

Due to its long half-life ($T_{1/2}$ = 53 d), ^{7}Be can be produced by on-line (ISOL) [118] or by off-line techniques [114], using a wide variety of targets and impinging beams, such as high energy protons on graphite [114], protons on lithium-based targets [35, 119] or on SiO_2 [120], neutrons on graphite [121].

For the production of ^{7}Be beams in the SPES facility, boron carbide (B_4C) is being considered as a suitable target, since it is characterized by a set of favorable thermo-mechanical properties that will be described in the following paragraph. Moreover, since boron is close in mass to beryllium, its interaction with protons should result in an easier formation of proton-rich beryllium isotopes with respect to other types of target. For this reason, a high rate of production of ^{7}Be isotopes is expected.

Inoue et al. [122] reported the formation of ^{7}Be isotopes during proton bombardment of natural boron nuclei, with a 10 mb cross section for the reaction $^{nat}B(p,x)^{7}Be$ in conditions of 40 MeV proton impinging beam. In the aforementioned reaction, x represents the various sub-products of the interaction of the protons with the two different isotopes present in natural boron, ^{10}B (19.8 at.%) and ^{11}B (80.2 at.%).

4.2.1. Boron carbide

General properties

Boron carbide is a compositionally disordered material that is known to exist as a single phase in a wide range of composition, which extends from $B_{10.4}C$ (about 8.8% at. C) to B_4C (20% at. C) [123, 124]. Among them, B_4C is the most commonly used since it possesses better mechanical, thermal and electrical properties.

The crystal structure of boron carbide has been investigated in a huge number of studies involving X-Ray and neutron diffraction and NMR analysis [124]; the most widely accepted structure of boron carbide is rhombohedral, consisting of 12-atom icosahedra located at the corners of the unit cell. The longest diagonal of the rhombohedral cell contains a three atom linear chain made of boron and carbon atoms. At the highest carbon concentration (B_4C), the structure consists of $B_{11}C$ icosahedra and C-B-C chains, whereas near the composition $B_{13}C_2$ ($B_{6.5}C$) it is composed of $B_{11}C$ icosahedra and a C-B-B chain. For lower carbon concentrations, some of the $B_{11}C$ icosahedra are replaced by B_{12} ones, maintaining the central C-B-B chain.

Table 15 reports some physical properties of three boron carbide compositions [123, 124, 125]. Figs. 62 and 63 show the B-C phase diagram and a diagram of the boron carbide structure, respectively [126, 124].

Table 15 – Properties of three boron carbide compositions.

	$B_{10.4}C$	**$B_{6.5}C$**	**B_4C**
Theoretical density (g/cm^3)	2.46	2.49	2.52
Atoms per unit cell	15.3	15.2	15
Melting point (°C)	2075	2400	2450
Crystal structure	Rhombohedral B_{12} icosahedra CBB chain	Rhombohedral $B_{11}C$ icosahedra CBB chain	Rhombohedral $B_{11}C$ icosahedra CBC chain
Lattice parameter	a_R = 5.213 Å α = 65.650° V_R = 112.43 Å^3	a_R = 5.205 Å α = 65.350° V_R = 111.30 Å^3	a_R = 5.170 Å α = 65.683° V_R = 109.77 Å^3

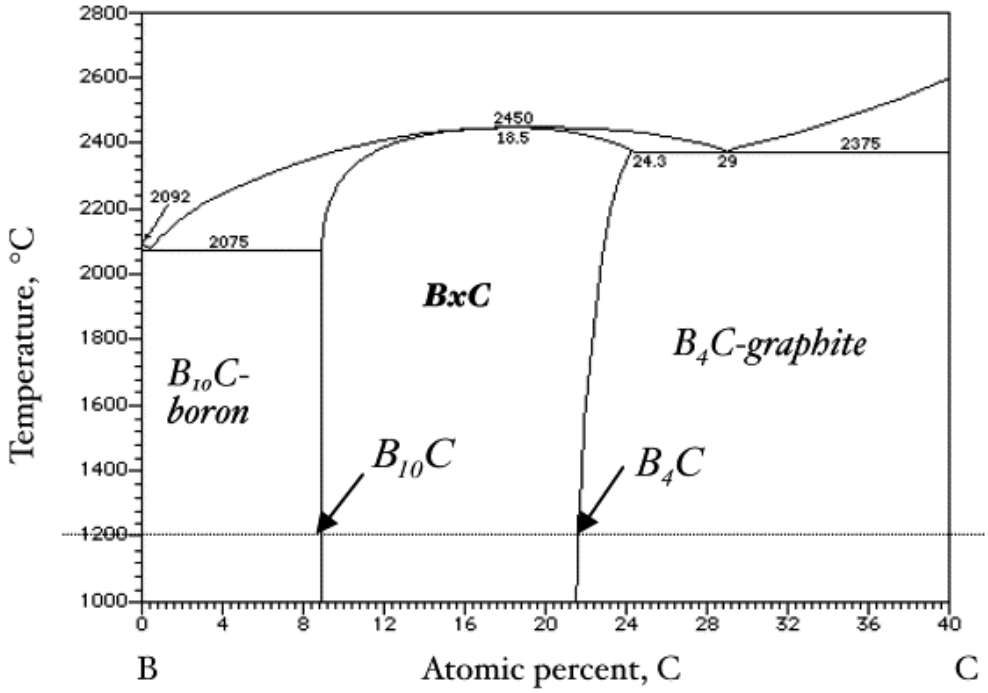

Fig. 62 – B-C phase diagram, after [126].

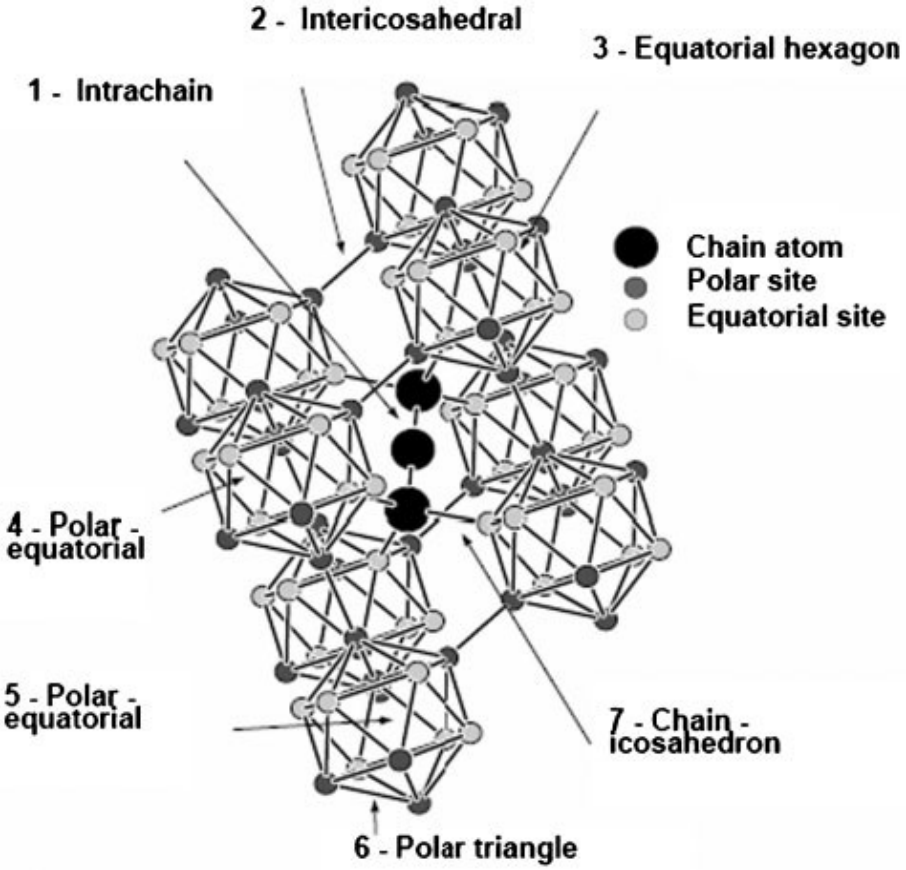

Fig. 63 – Boron carbide structure, after [124].

Synthesis

Boron carbide can be prepared by several different reactions, including [124]:

- Carbothermal reduction of boric acid and boron trioxide, which is the most common commercial method for the production of B_4C, overall represented as follows:

$$4H_3BO_3 + 7C \rightarrow B_4C + 6CO + 6H_2O \quad (46)$$

The reaction proceeds in three sub-steps [127]:

$$4H_3BO_3 \rightarrow 2B_2O_3 + 6H_2O \quad (47)$$

$$B_2O_3 + 3CO \rightarrow 2B + 3CO_2 \quad (48)$$

$$4B + C \rightarrow B_4C \quad (49)$$

On heating, at T < 200 °C, boric acid converts to boron oxide releasing water. The reaction (48) becomes thermodynamically feasible above 1400 °C, but the temperature in the reaction furnace is usually maintained above 2000 °C in order to enhance the rate of the overall reaction, which is highly endothermic, needing 16800 kJ/mol B_4C [128]. Common carbon sources include petroleum coke, charcoal, carbon active and graphite [124]. The process can be carried out in tubular furnaces, especially for laboratory scale experiments, whereas for large scale production of boron carbide electric arc or Acheson type furnaces are used. In the first case, a remarkable boron loss can occur due to localized electric arcs which result in very high temperatures (evaporation of boron oxides), and the resulting boron carbide has usually to undergo laborious crushing and grinding operations in order to reduce the obtained chunks size. The latter furnace type uses a graphite rod as a heating element surrounding which the reactants (boric acid and a carbon source) are charged, and on top of which B_4C forms. In each run, only a small portion of the charge gets converted to carbide and the balance material is recirculated in further runs. Some quantity of boron oxides however escapes to the atmosphere along with the gaseous reaction products (mainly CO). For this reason, $H_3BO_3 \rightarrow B_4C$ conversion in each run is low and boron loss is high. Although this kind of process has a

low yield it is the most common commercial method because of the simple equipments and cheap raw reagents.

- Magnesiothermic reduction of B_2O_3, carried out at temperatures higher than 1000 °C in a high pressure hydrogen or argon atmosphere, following the overall reaction [123]:

$$2B_2O_3 + 6Mg + C \rightarrow B_4C + 6MgO \quad (50)$$

The products of the reaction are processed by aqueous methods to remove magnesium oxide, but usually the carbide is contaminated with magnesium borides formed as stable compounds. This reduction technique yields very fine amorphous powder, which is well suited for use in the fabrication of sintered products. The addition of metallic sulphates like K_2SO_4 as catalysts has been found to reduce the reaction temperature to about 700 °C. Though thermodynamically favored with respect to the standard carbothermal reduction, the high cost of magnesium makes this process inconvenient for regular large scale production.

- Synthesis from elements, as in eq. (49) which suffers from the high cost of elemental boron and so employed for specific applications, such as ^{10}B enriched or very pure boron carbide. In the first case, the common commercial reactions, in particular the carbothermal reduction route, being characterized by boron loss in form of gaseous products and boron hold-up in the reaction furnace, cannot be used. The reaction is tipically carried out in inert or vacuum atmosphere at temperatures higher than 1500 °C, or in the case of spark plasma synthesis at T between 1000 °C and 1200 °C [124].

- Vapor phase reaction between a boron halide, typically BCl_3, and a carbon source which can be either a hydrocarbon gas such as CH_4, C_2H_4, C_2H_6 and C_2H_2 or carbon tetrachloride, CCl_4. Hydrogen is present as well in the atmosphere; it reacts with the halogen forming hydrogen chloride, as in the following reactions:

$$4BCl_3 + CCl_4 + 8H_2 \rightarrow B_4C + 16HCl \quad (51)$$

$$4BCl_3 + CH_4 + 4H_2 \rightarrow B_4C + 12HCl \quad (52)$$

This process has been extensively studied and developed for the production of boron carbide powders, whiskers as well as films deposited by different types of CVD techniques.

- Synthesis from polymeric precursors, which is particularly interesting since it enables the possibility to obtain boron carbide at lower temperatures than those required by other techniques. B_4C powders have been obtained from a boron and carbon containing polymer, using boric acid as boron source and various types of carbon sources such as citric acid [129, 130, 131] or different alcohols [132, 133, 134]. Typically, the process involves the formation of a gel which is subsequently dried and pyrolized to obtain B_4C powders. More detail on this type of synthetic reaction will be given in the following paragraphs, since the SPES boron carbide target prototypes were produced following this route.

Thermal properties

Thermal properties of boron carbides are very dependent on the carbon and boron relative concentration [124]. Heat capacity increases with decrease in carbon within the homogeneity range (8.8% at. C ÷ 20% at. C). This behavior is due to the change in lattice vibration mode produced by a lower stiffness of the three-atom C-B-B chain with respect to C-B-C [135]. Thermal conductivity of B_4C falls with temperature like most crystalline ceramics. On the other hand, thermal conductivity of boron carbide with low carbon is relatively lower and temperature independent, a more characteristic behavior of amorphous materials [136]. This behavior can be explained assuming that the thermal conductivity is dominated by the transfer of vibrational energy through the inter-icosahedral chains rather than within the softer icosahedra. When the C-B-C chains are inhomogeneously replaced by C-B-B chains (increasing the boron content) a transition takes place from crystal-like transport to glass-like transport. Moreover, thermal conductivity decreases by increasing B content because B-B bonds are much softer than C-B bonds [135]. When ^{10}B isotope replaces ^{11}B in boron carbide, thermal conductivity increases, due to the increase in the bonding energy per unit mass and the phonon velocity [137, 138]. Table 16 reports some thermal properties of three boron carbides. Data relative to boron-rich boron carbide are given for the B_9C composition.

Table 16 – Thermal properties of three boron carbide compositions.

	B_9C	$B_{6.5}C$	B_4C
Heat capacity (J/mol·K)	\	\	~ 50 ÷ 140 (25 ÷ 1430 °C) [135]
Thermal diffusivity ($\cdot 10^{-6}$ m^2/s)	~ 1.2 ÷ 1.3 (300 ÷ 1500 °C) [136]	~ 1.3 ÷ 1.4 (300 ÷ 1500 °C) [136]	~ 4.2 ÷ 1.8 (350 ÷ 1500 °C) [136] ~ 3.8 ÷ 2.7 (600 ÷ 1000 °C) [139]
Thermal conductivity (W/m·K)	~ 5.5 (350 ÷ 1450 °C) [136]	~ 6.0 (350 ÷ 1450 °C) [136]	~ 12.5 ÷ 6.5 (200 ÷ 1450 °C) [136] ~ 29 ÷ 12 (RT ÷ 1000 °C) [139]
Mean thermal expansion coefficient ($\cdot 10^{-6}$ $°C^{-1}$)	\	\	5.7 (25 ÷ 1700 °C) [140] 4.8 (25 ÷ 800 °C) [141]

Reactivity

Due to its low standard enthalpy of formation (-38.9 to -71.5 kJ/mol), boron carbide is a very stable compound [123]. The reaction with wet air of fine B_4C powders is slow, forming species like B_2O_3, HBO_3 and H_3BO_3 at the surface of the powders. In the case of hot-pressed samples, oxidation starts at 600 °C and results in the formation of a thin transparent B_2O_3 film, which cracks after cooling. Up to 1200 °C, the oxidation process is limited by the diffusion of reagents through the formed oxide layer.

Boron carbide is not attacked by cold chemical reagents; it is oxidized by hot oxidizing acids (HNO_3, H_2SO_4, HCl, etc.) and fused salts. Chlorine attacks B_4C at 600 °C, and bromine attacks it at 800 °C, giving boron trihalides, BCl_3 and BBr_3.

B_4C reacts with metal oxides at elevated temperatures to form metal borides; it also reacts with many metals like iron, nickel, titanium, titanium and zirconium to form carbides and borides at 1000 °C. Substitutional compounds can be obtained formed by boron carbide with aluminum or silicon additions.

4.2.2. B_4C SPES target prototypes

For the development of a carbon dispersed boron carbide target for the SPES project, two different synthetic reactions have been investigated, both using boric acid as a boron source, and citric acid or phenolic resin as carbon sources, respectively. The first type of reaction was chosen in consideration of the good results already found by several researchers, in particular Sinha and co-workers [129], and besides representing a feasible synthetic route for porous B_4C/C targets, it also can be seen as a reference as for process parameters to develop new production methods.

The second type of synthesis was introduced considering the potential beneficial effects of using a polymeric carbon source. Indeed, the thermal decomposition of the phenolic resin provides free carbon from a ring-based molecular structure of carbon atoms. This type of precursor might modify the thermodynamics of the carbothermal reaction [142], as will be explained in the following paragraphs.

Material synthesis

B_4C powders were prepared starting from two different synthetic routes described in the following.

- Boric acid – citric acid synthesis (BA-CA)

  Boric acid (ACS Reagent, Sigma Aldrich) and citric acid (ACS Reagent, Sigma Aldrich) were used as boron and carbon sources, respectively, used as received. The expected dissociation reaction of the two precursors to form B_2O_3 and C and the overall carbothermal reduction of the obtained boron oxide during the thermal treatments can be respectively expressed as [131]:

$$2H_3BO_3 \rightarrow B_2O_3 + 3H_2O, \quad T > 170\ °C \tag{53}$$

$$C_6H_8O_7 \rightarrow 3C + 4H_2O + 3CO, \quad T > 220\ °C \tag{54}$$

$$2B_2O_3 + 7C \rightarrow B_4C + 6CO, \quad T > 1000\ °C \tag{55}$$

The overall stoichiometry of the reaction to obtain a carbon-free boron carbide requires a theoretical 12:7 (1.7:1) molar ratio between boric and citric acid. However, as pointed out by Sinha et al. [129], carbothermal process to obtain B_4C is inherently characterized by loss of boron, so that an excess of boric acid in the initial solution may avoid the occurrence of a too large amount of free carbon in the final composition. As already described in 4.2.1 this aspect is strictly related to the presence of highly volatile reactive boron suboxide species such as B_2O_2 and BO gases during the reaction advancement [142]. For this reason, boric acid/citric acid molar ratio of 2.2:1 was used [130], which corresponds to a weight ratio between boric acid and carbon of 3.7:1, in order to obtain a limited amount of free carbon in the final carbide. A boric acid solution (2.5 M) was obtained by dissolving $B(OH)_3$ in distilled water at 80 °C; solid citric acid powders were then slowly added to the solution, under continuous stirring. To promote the formation of a B-O-C containing gel [130], the temperature of the solution was raised up to 105 °C and the pH was kept at 2.5 by adding few drops of an ammonia solution (28% aq solution, analytical grade, Carlo Erba Reagents). After slow solvent evaporation (about 1 hour), the obtained yellowish gel was dried in an oven at 60 °C overnight and subsequently ground. The powders were then put in an alumina crucible inside a tube furnace, where they underwent a primary thermal treatment. In order to favour both decomposition of the precursors and carbothermal reduction, the primary thermal treatment was divided into two different steps:

- heating up to 800 °C (0.75 °C/min) in low vacuum (10^{-2} mbar by means of a rotary pump), to decompose the precursors into highly reactive boron and carbon sources;

- slow heating (1 °C/min) up to 1500 °C in argon flow with rotary pump still running (1 mbar pressure in the tube), to favor the carbothermal reaction avoiding the aforementioned boron suboxides evacuation from the reactive system.

The obtained dark grey powders were then formed into discs with 13 mm diameter and about 1 mm thickness by uniaxial cold pressing at 450 MPa. Phenolic resin (about 10% wt.) was added as binding agent in order to afford mechanically stable samples. The pressed pellets were then put on a graphite plate and sintered in high vacuum up to 1900 °C with 2 °C/min heating rate and 4 hour dwelling.

- Boric acid – phenolic resin synthesis (BA-PR)

The starting solution was prepared by dissolving boric acid (the same reagent used for BA-CA synthesis) and phenolic resin (Dynea, 860 series) in ethanol at 80 °C under magnetic stirring. The composition of the initial mixture was obtained by keeping the same $B(OH)_3$/C weight ratio of the BA–CA case, considering that the used phenolic resin has a carbon yield of 45% of its initial weight (measured by TGA-DTA analysis, shown in fig. 64).

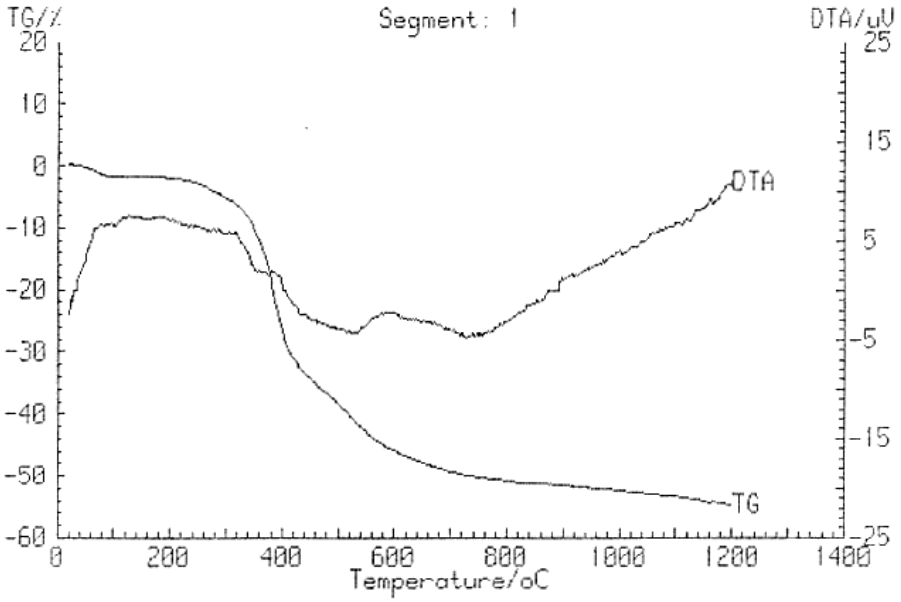

Fig. 64 – TGA-DTA (in Ar) analysis of the used phenolic resin up to 1200 °C.

As reported in [132], white deposits on the walls of the reaction beaker were observed. These residues were most probably composed of still unreacted boric acid spurting out on the beaker walls during thorough mixing and boiling, while in Hasegawa et al. [132] they were identified as borate esters of hydroxybenzylalcohol produced by the known reaction of boric acid and ethanol. However, in the present case only the following reaction between boric acid and ethanol can occur:

$$H_3BO_3 + 3CH_3CH_2OH \rightarrow B(OCH_2CH_3)_3 + 3H_2O \quad (56)$$

leading to triethylborate ester formation, which is a liquid at room temperature and its boiling point is 120 °C [143]. For this reason, the observed deposits cannot be ascribed to this compound. It is however likely that a not controllable loss of boron through

evaporation of volatile esters occurred during the heating step to produce the BA-PR solution. Once the solvent evaporation was complete, the orange solid obtained was ground to powders in an agate mortar and further ground in a planetary ball-mill. After that, the powder underwent the same thermal treatment described for BA–CA.

Characterization techniques

The crystalline phases obtained after sintering were analysed by XRD, while their morphology and composition were investigated using a SEM-EDS equipment.

Free carbon in the final B_4C/C composite was determined according to the method published by Alizadeh et al. [144], described in the following.

Being W_1 the pellet weight after sintering, each sample was burned at 700 °C for 30 minutes in air, allowing for free carbon removal. The remaining powder, weighted as W_2, can be considered as composed of boron carbide and a minor amount of boron oxide, namely B_2O_3 which according to literature is by far the main oxidation product of B_4C in dry air [145]. To remove B_2O_3, the powder was washed with hot water and then dried and weighted as W_3. In this way, the difference

$$W_2 - W_3 = W_4 \tag{57}$$

yields the amount of B_2O_3, which allows to calculate the oxidized boron carbide weight (W_5), according to the main B_4C oxidation reaction in dry air [145]:

$$B_2C + 4O_2 \rightarrow 2B_2O_3 + CO_2 \tag{58}$$

The sum

$$W_3 + W_5 = W_6 \tag{59}$$

gives the total boron carbide content (oxidized and unoxidized), so the difference

$$W_1 - W_6 = W_7 \tag{60}$$

yields the amount of residual carbon. In this way, the fractional content of boron carbide and carbon in the sample (f_{B4C} and f_C, respectively) can be obtained as:

$$f_{B_4C} = \frac{W_6}{W_6 + W_7} \tag{61}$$

$$f_C = 1 - f_{B_4C} = \frac{W_7}{W_6 + W_7} \tag{62}$$

The bulk density (ρ_{bulk}) of the sintered samples was calculated by the weight over volume ratio, while the theoretical density (ρ_{th}) was obtained using the expression:

$$\rho_{th} = f_{B_4C} \cdot \rho_{B_4C} + f_C \cdot \rho_C \tag{63}$$

where ρ_{B4C} and ρ_C are the theoretical densities of the two components (respectively 2.52 g/cm³ for boron carbide, 1.90 g/cm^3 for graphite).

The total estimated porosity of the specimens was obtained by the comparison of the bulk and theoretical densities, as in eq. (44).

The theoretical overall weight loss of the two different synthetic routes was calculated taking into account the actual ratios between the starting reagents, referring to (53), (54) and (55) for BA-CA, whereas for BA-PR reactions (53), (55) and the carbon yield of phenolic resin (see fig. 64) were considered. In both cases, the effect of the phenolic binding agent addition before sintering, and its partial decomposition at high temperature, was taken into consideration.

In order to investigate the type of generated porosity, the samples were analysed by nitrogen physisorption at -196 °C. Nitrogen adsorption/desorption isotherms at relative pressures (P/P_0) ranging from 10^{-4} up to 1.0, where P_0 is the saturation pressure of nitrogen at the analysis temperature, were collected. Before the measurement, the specimens were outgassed at 350 °C for two hours in vacuum (10^{-2} mbar). The different types of isotherms and of hysteresis loops were described according to IUPAC classifications [146], which allowed to relate them to different features of the adsorbent materials. The complete isotherms was analysed to calculate the pore size distribution, whereas for specific surface area (SSA) evaluation, data in the relative pressure range of 0.01-0.11 were used, applying the BET method (Brunauer, Emmett, Teller) [147]. The computational method developed by Barrett, Joyner and Halenda (BJH) [148] was used to derive the pore size distribution from the nitrogen isotherms.

Experimental results

Figures 65 and 66 show the main phases of the two materials production. Both the types of samples after the two thermal treatments showed good mechanical stability. During the treatment, volumetric shrinkages of 45% for BA-CA and 35% for BA-PR were measured.

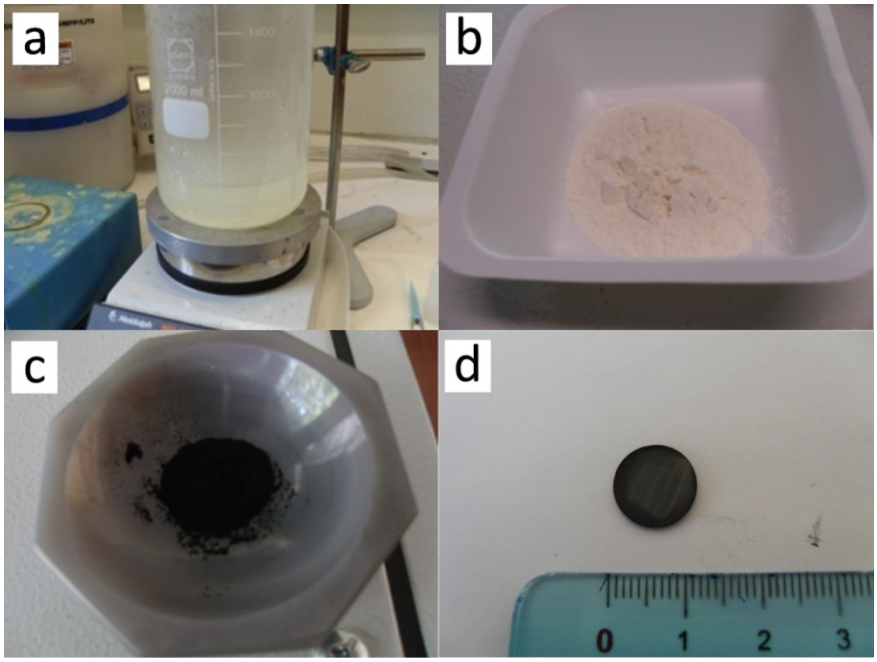

Fig. 65 – BA-CA synthesis. a: gel formation, b: dried and ground powder, c: powder after primary thermal treatment, d: sintered pellet.

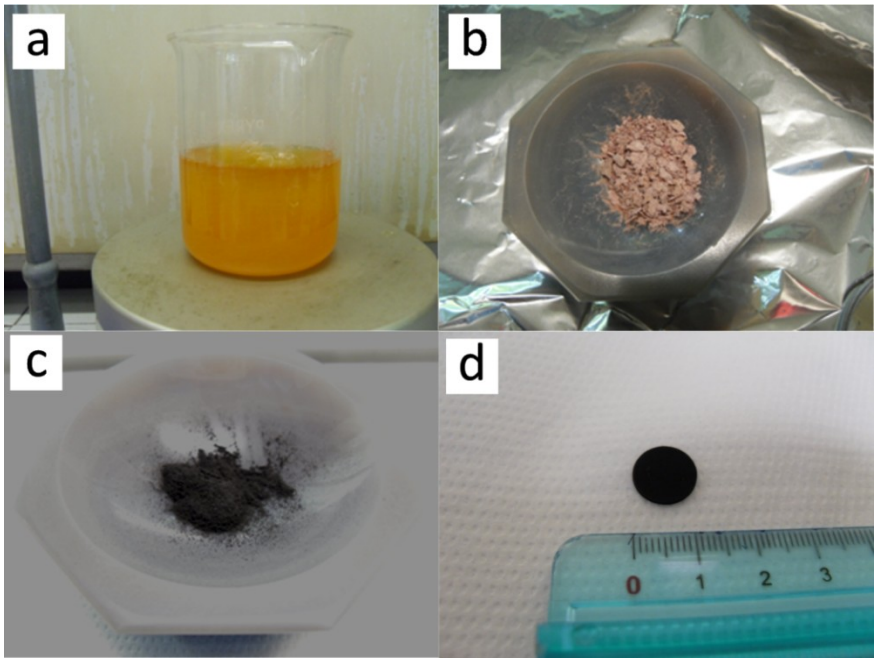

Fig. 66 – BA-PR synthesis. a: reagents suspension, b: dried and ground powder, c: powder after primary thermal treatment, d: sintered pellet.

The XRD patterns obtained on powders of the two samples are shown in figs. 67 and 68. For each sample, both the composition after the primary thermal treatment (bottom side) and the sintering process (top side) is reported. A similar phases evolution can be noticed for the two produced types of samples. After the Ar/vacuum primary treatment, the obtained powders were mainly composed of a dispersion of boron carbide (very sharp peaks for 2θ values of 35° and 38°) in a partially amorphous carbon phase, represented by the broad peaks around 25° and 42°. On the other hand, the subsequent high vacuum (10^{-6} mbar) treatment at higher temperatures (1900 °C) resulted in a more defined XRD spectrum where narrower B_4C and graphite peaks can be observed. The free carbon found in the final samples derived both from the non-stoichiometric ratio of the initial precursors mixture and from the residue of phenolic resin binder used to form the pellets before sintering. The only difference between the two samples is related to the carbon content in the final material, which is higher in the case of the BA-PR composition. This effect is probably due to the aforementioned boron loss during the first steps of the synthesis process, or to a lower interaction between the reactive species, i.e. phenolic resin-derived carbon and boron suboxides, with respect to BA-CA composition, in which the formation of a polymeric gel resulted in a more efficient contact between boron and carbon.

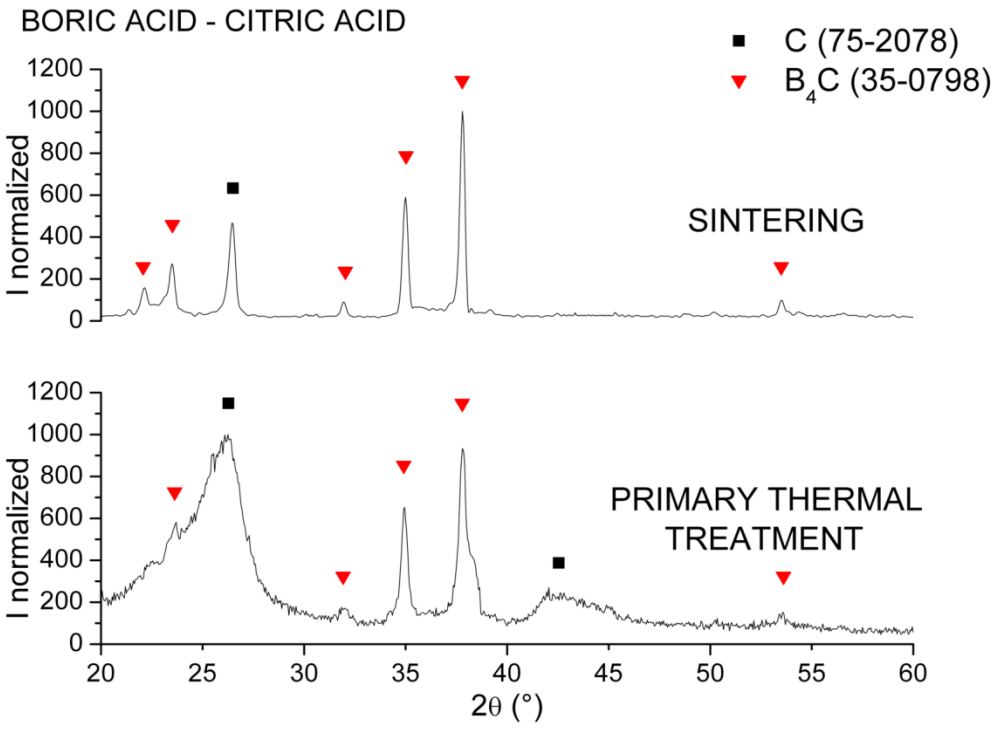

Fig. 67 - XRD pattern of the sample obtained from BA-CA, after the two steps of synthesis. Bottom: sample after primary Ar/vacuum treatment at 1500°C, top: sample after high vacuum 1900°C sintering.

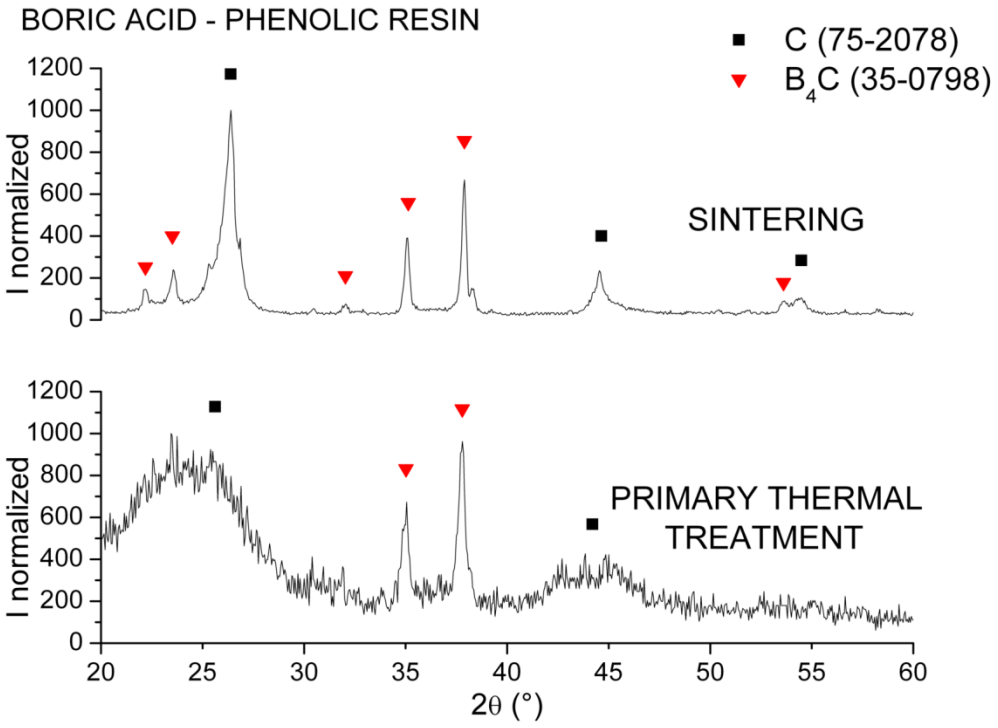

Fig. 68 - XRD pattern of the sample obtained from BA-PR, after the two steps of synthesis. Bottom: sample after primary Ar/vacuum treatment at 1500°C, top: sample after high vacuum 1900°C sintering.

SEM micrographs reported in figures 69 and 70 show the cross-section of the two samples after sintering at low and high magnification. In both cases, the microstructure of samples appears to be composed of randomly distributed macropores with size of the order of a few microns, produced during sample preparation and binder decomposition in the sintering thermal treatment. Moreover, this residual porosity remained in the sintered samples since densification of boron carbide is very difficult, due to the presence of strong covalent bonds, even if a small quantity of residual free carbon should promote sintering [149]. Compositional analysis of the microstructure of the samples fracture section is reported in figures 71 and 72. EDS analysis was carried out on a selected area of the reported SEM images; for each sample, a qualitative carbon/boron amount ratio evaluation was obtained on three different portions of the same section, namely top, middle and bottom, by using the same accelerating voltage and spot size in order to assure that the same depth is being probed by the beam. Errors on weight % composition resulting from EDS analysis can be as high as 10% [150], so EDS in this case was used to discuss qualitatively the trend in C/B ratio between different areas of the same sample or different samples, keeping constant the analytical parameters like accelerating voltage and working distance.

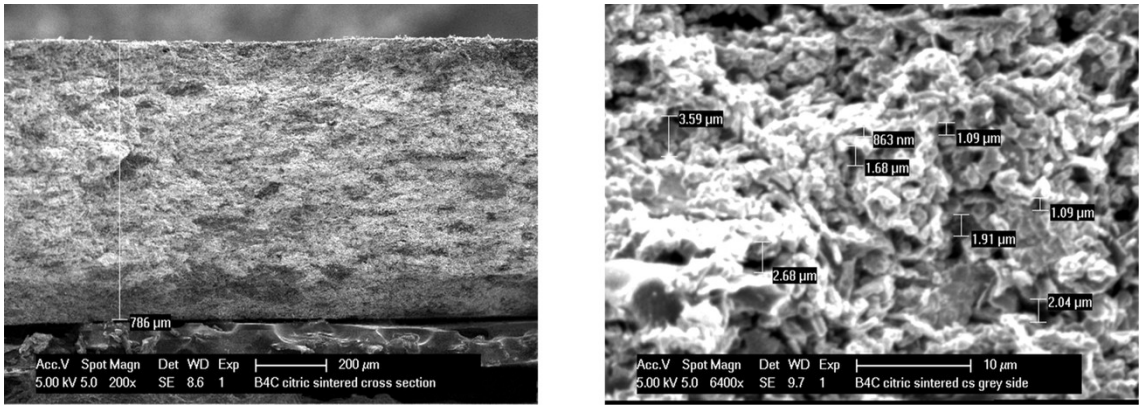

Fig. 69 - SEM micrographs of the sample obtained from BA-CA, after sintering at 1900°C in high vacuum.

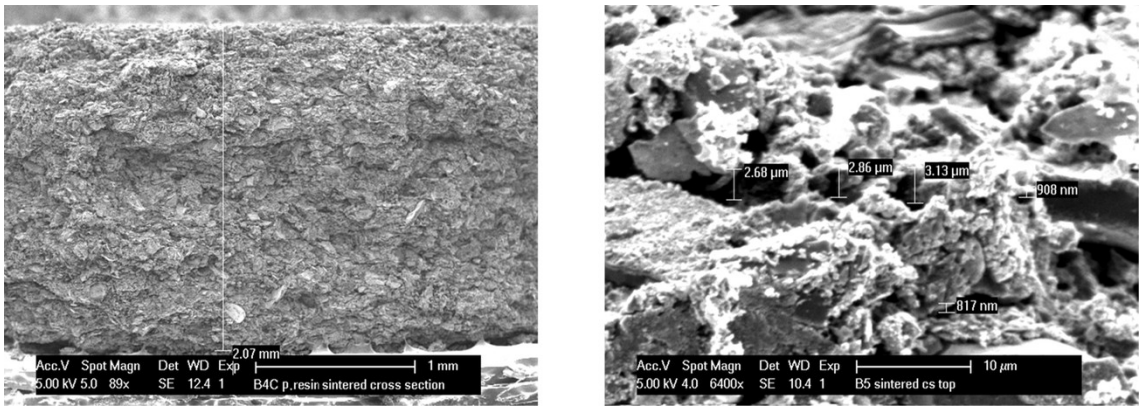

Fig. 70 - SEM micrographs of the sample obtained from BA-PR, after sintering at 1900°C in high vacuum.

The data here reported are in good agreement with XRD analyses concerning the higher amount of free carbon present in the BA-PR samples with respect to the BA-CA samples, as can be observed by comparing the carbon/boron intensity ratio of figures 71 b) and 72 b) (the spectra are normalized on B signal intensity for BA-CA, and on C signal for BA-PR). Furthermore, as clearly shown in fig. 71 a) and c), the relative carbon/boron ratio is higher towards the top and bottom surfaces of the sample, with respect to its inner core (fig. 71 b)), in the case of B_4C/C obtained from BA-CA. This aspect is evident also in the BA-PR sample (see fig. 72). Such gradient in composition could be attributed to enhanced evaporation of boron-containing volatile species such as B_2O_2 and BO [142] from the sample surfaces. No oxygen contamination was present in the samples after high temperature processing.

The surface morphologies reported in figures 71 and 72 suggest important differences in the sintering behaviour of the two types of samples. In the case of the BA-PR system, a low degree of sintering for the boron carbide grains is evident and can be ascribed to the presence of a large amount of free carbon (black macro-clusters), which hinders an efficient grains

consolidation, resulting in an opposite effect with respect to the aforementioned B_4C sintering aid capability of small quantities of residual carbon. On the other hand, the BA-CA sample displays a uniform and continuous texturing, with no appreciable presence of dark graphitic grains. This aspect is evident from the comparison of the two different samples surfaces, reported in figure 73, where SEM images from BA-CA and BA-PR systems collected under the same beam energy and magnification are reported.

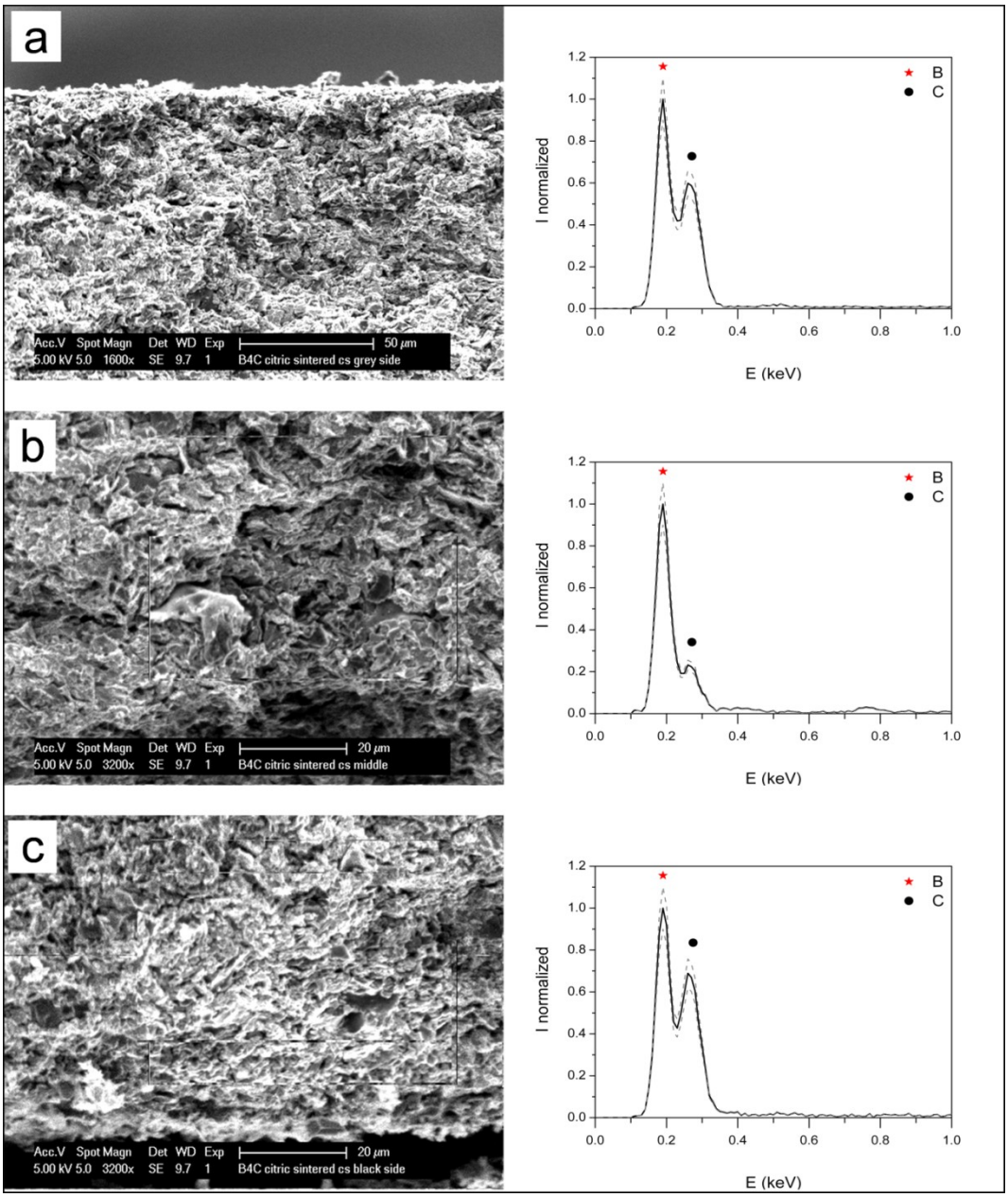

Fig. 71 - EDS analysis performed on SEM micrographs showing a section of one sample obtained from boric acid and citric acid. a) section towards the top surface, b) sample internal structure, c) section towards the bottom surface. For a) and c) EDS data were collected from a selected area located only 5 µm from the external surface edge. Dashed line represents an error band of 5% on the non-normalized data.

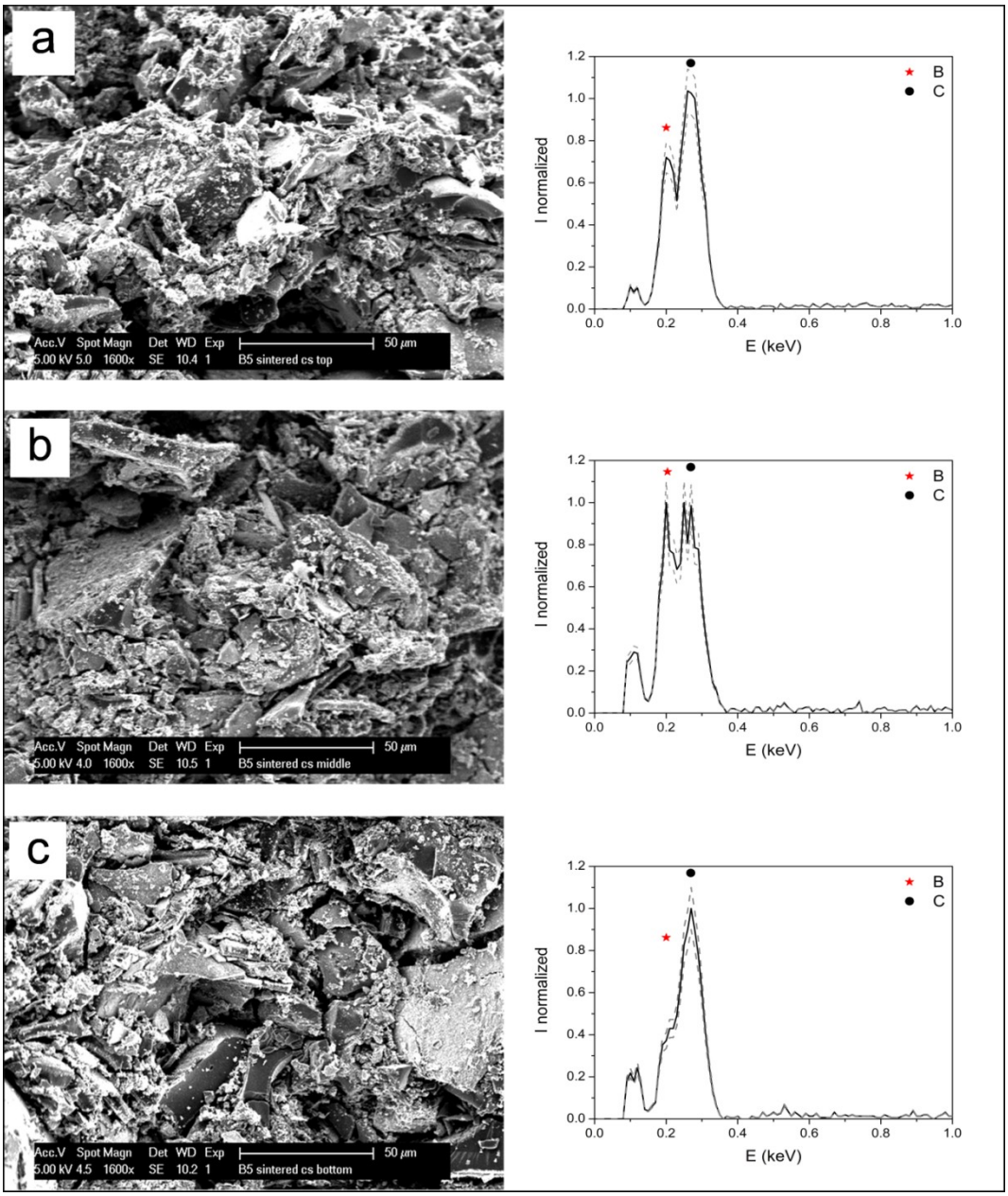

Fig. 72 - EDS analysis performed on SEM micrographs showing a section of the sample obtained from boric acid and phenolic resin. a) section towards the top surface, b) sample internal structure, c) section towards the bottom surface. For a) and c) EDS data were collected upon first 5 µm of material from the external surface edge. Dashed line represents an error band of 5% on the non-normalized data.

An overview of the samples characteristics is reported in table 17, in which the overall weight loss (Δw %) is compared to the theoretical value (Δw_{th} %). Data obtained for BA-CA sample show a good agreement with the predicted weight loss, whereas for the BA-PR sample the difference is remarkable. Also in this case, discrepancies with expected data can be attributed to the same already discussed condition of non-stoichiometry. Table 17 also reports the calculated fraction of B_4C and C in the final sintered pellets, with carbon partly obtained from

the phenolic binder decomposition during the second thermal treatment. In the case of the BA-PR sample, the B_4C fraction was lower than for the BA-CA sample (78.8 wt% against 90.9 wt%).

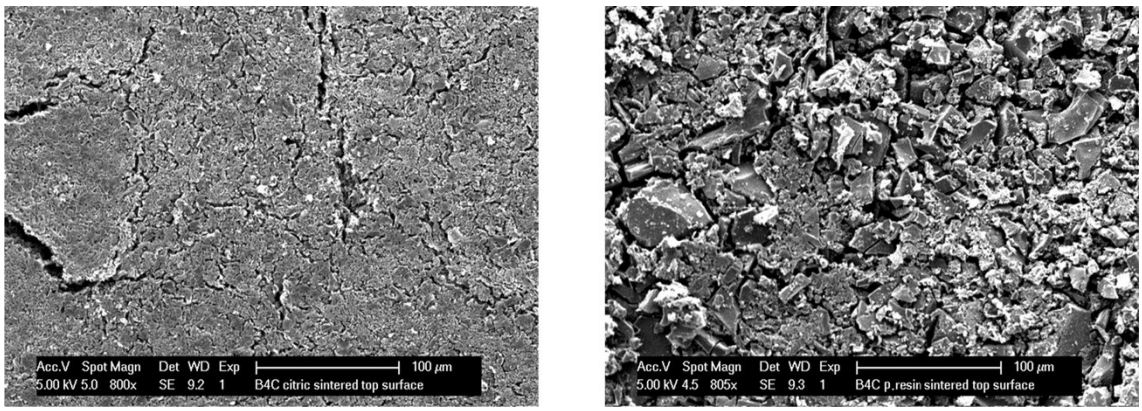

Fig. 73 - SEM micrographs showing the top surface of the BA-CA (left) and BA-PR (right) samples.

Table 17 – Properties of the two types of samples.

	BA-CA	**BA-PR**
Δw % (Δw_{th} %)	-91.5 ± 0.6 (-92.4)	-79.7 ± 0.3 (-88.5)
f_{B4C}(%)	90.9 ± 2.1	78.8 ± 0.6
f_C(%)	9.1 ± 2.1	21.2 ± 0.6
ρ_{bulk} (g/cm³)	1.61 ± 0.07	1.21 ± 0.05
ρ_{th} (g/cm³)	2.46 ± 0.09	2.39 ± 0.03
Estimated porosity (%)	34.6 ± 5.2	49.4 ± 2.7

In Figure 74 the isotherms obtained from N_2 physisorption measurements of samples BA-CA and BA-PR after treatment at 1900 °C in vacuum are reported, whereas table 18 summarizes the most important information concerning the porosity which are derivable from the measurements of both samples. Figure 75 reports the pore size distribution curves derived from BJH model applied to the desorption branch of the isotherm.

According to IUPAC classification [146, 151, 152], and comparing the obtained curves with the reference ones reported in fig. 76, since a change in convexity during adsorption is not easily discernible, the isotherms can be identified as of Type V, thus similar to type IV but characterized by weak interactions between adsorbent and adsorbate, with a very small hysteresis loop, extending over a wide range of relative pressures. Adsorption of N_2 is negligible at low pressures, indicating the absence of micropores. The hysteresis shape for sample BA-CA is close

to type H4, according to Kruk and Jaroniec [153] with almost horizontal branches for adsorption/desorption characteristic of narrow slit-shaped mesopores, whereas the sample BA-PR displays a H3 type of loop, typical of wide and randomly distributed mesopores arising from loosely packed plate-like particles. This interpretation is confirmed by the pore size distribution curves reported in fig. 75. While the BA-CA sample displays a sharp peak in Pore Size Distribution (PSD) at about 40 Å (see also table 18), indicating an almost mono-modal distribution in pores, the sample BA-PR shows an almost featureless PSD graph (very broad pore size distribution).

Table 18 – Porosity parameters of the two samples.

	BA-CA	**BA-PR**
BET SSA (m^2/g)	4.9 ± 0.5	4.5 ± 0.4
Nitrogen uptake (cm^3/g)	0.017 ± 0.001	0.025 ± 0.001
Pore size (mesopores) (Å)	36 ± 5	Very broad

The BET specific surface area (SSA) values of the two types of samples are very close, as can be seen from the data in table 18, whereas the total pore volume, measured as nitrogen uptake at almost saturation pressure and comprehensive also of macropores, is remarkably higher for the BA-PR sample. In addition, the larger pores obtained for BA-PR sample (table 18) are in agreement with low SSA values and high pore volume fraction. This finding supports previous results on the different porosity percentages in the samples, as reported in table 17. The different morphology of the samples can be ascribed to the different structure of the powders employed for reaction: in the case of BA-CA samples, powders are sol-gel derived; in the case of BA-PR samples powders derive from a dried solution.

The successful obtainment of two different boron carbide – carbon systems, with different microstructures but with good enough mechanical stability during handling and supposedly when exposed to high temperature – high vacuum conditions, can be seen as a starting point for future on-line tests on these type of materials. As soon as the facility will be ready for the first on-line isotopes production tests, B_4C/C systems will be among the first tested materials for the obtainment of ^{7}Be beams, together with other types of targets to be used for the production of proton-rich isotopes.

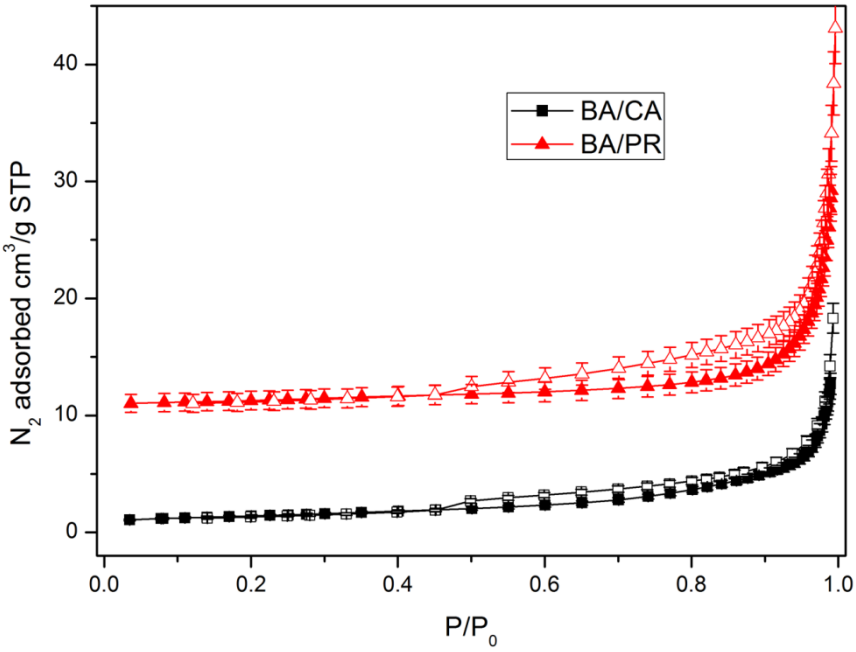

Fig. 74 - N_2 adsorption/desorption isotherms for the B_4C containing samples; the data were stacked on y-axis for the sake of clarity.

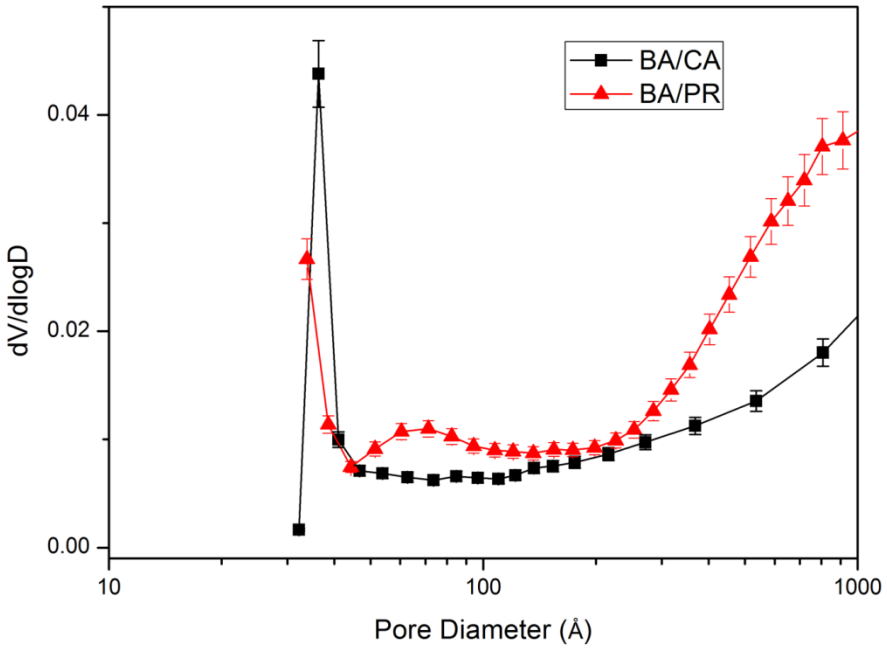

Fig. 75 - Pore size distribution curves.

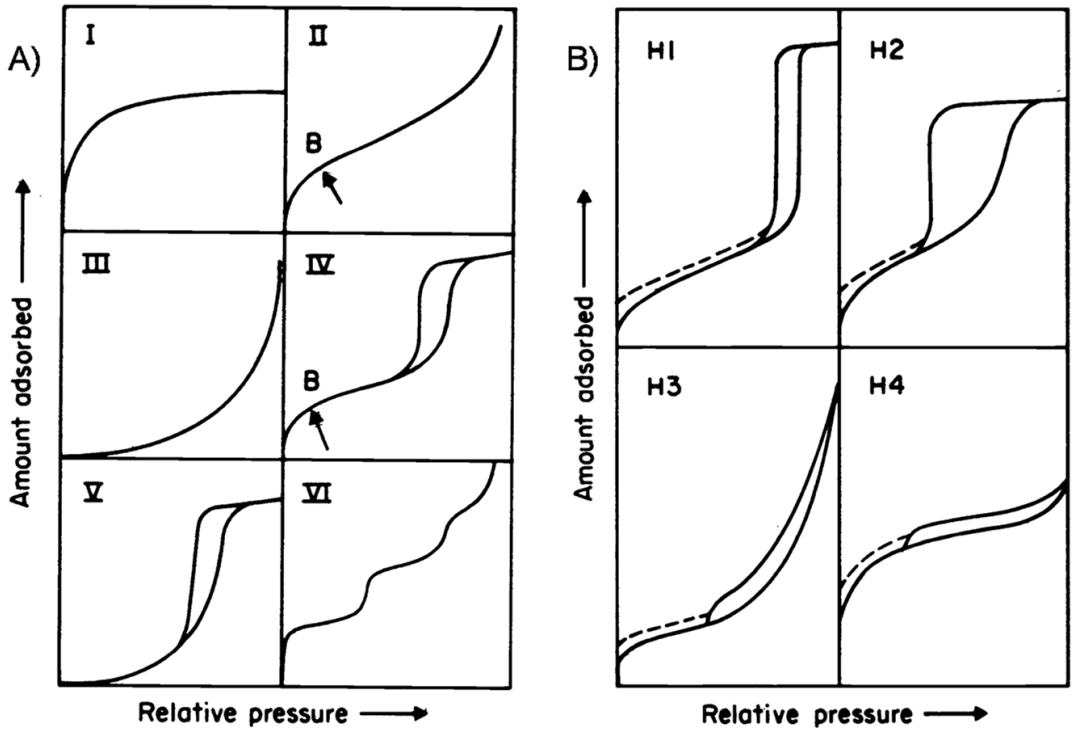

Fig. 76 - The different types of isotherms (A) and of hysteresis loops (B), after [146].

4.3. Lanthanum carbide targets: from standard synthesis to foams production

As anticipated in 3.2.5, lanthanum carbide has been extensively studied at SPES as a test material [85, 86, 87] to obtain information on the synthesis and properties of uranium carbide, since the two materials possess similar properties and therefore analogous production and high temperature performances. Moreover, as showed in 4.1, lanthanum carbide can itself be considered a potential material to obtain heavy proton-rich isotopes in the SPES facility.

The aforementioned experiments performed on various aspects of the lanthanum carbide synthesis and characterization were carried out on rescaled target prototypes, usually of the same dimensions of the UC_X discs used for the online tests described in chapter 3. In the present work, the attention has been moved to the possibility to further improve the processing techniques in order to produce ready-to-use lanthanum carbide targets with the final SPES layout and geometry, in one single thermal treatment. In addition to that, lanthanum carbide was once more used as a test material, to develop ceramic foams possessing very high porosity to be used in future on-line tests to obtain additional experimental data about the relationship between porosity characteristics of different ISOL targets and their release properties.

These two experimental approaches are explained in detail in the following paragraphs.

4.3.1. Lanthanum carbide

Due to its very limited applications, very few experimental data are available about lanthanum carbide, most of them coming from studies carried out during the 50's and 60's. Important contribution to the definition of its crystallographic properties and synthesis techniques were given by F.H. Spedding and co-authors [154, 155] and by Greenwood and Osborn [156]. Differently from uranium carbide, only two stoichiometric forms of lanthanum carbide are known to exist: LaC_2 and La_2C_3. Fig. 77 shows the La-C phase diagram [157], in which the interval of solubility of the two species is found between 11.5% and 14.4% wt. C. While La_2C_3 exists only in the body centred cubic form, LaC_2 can exist in two crystalline forms: the low temperature α-LaC_2 (body centred tetragonal) and the high temperature face centred cubic β-LaC_2. The transition temperature between the two LaC_2 phases was initially found to occur at about 1800 °C [155], while later studies demonstrated that the correct temperature is

1060 °C [158], as reported in fig. 77. This aspect represents an important structural analogy with UC_2, in which a similar martensitic transition takes place at about 1780 °C, as shown in 3.2.1. Because of its high melting point (about 2360 °C), the highest among lanthanum carbides, LaC_2 is surely the most interesting for ISOL RIBs production, and therefore only its properties will be discussed in the following. Table 19 highlights the important physical and microstructural analogies between UC_2 and LaC_2.

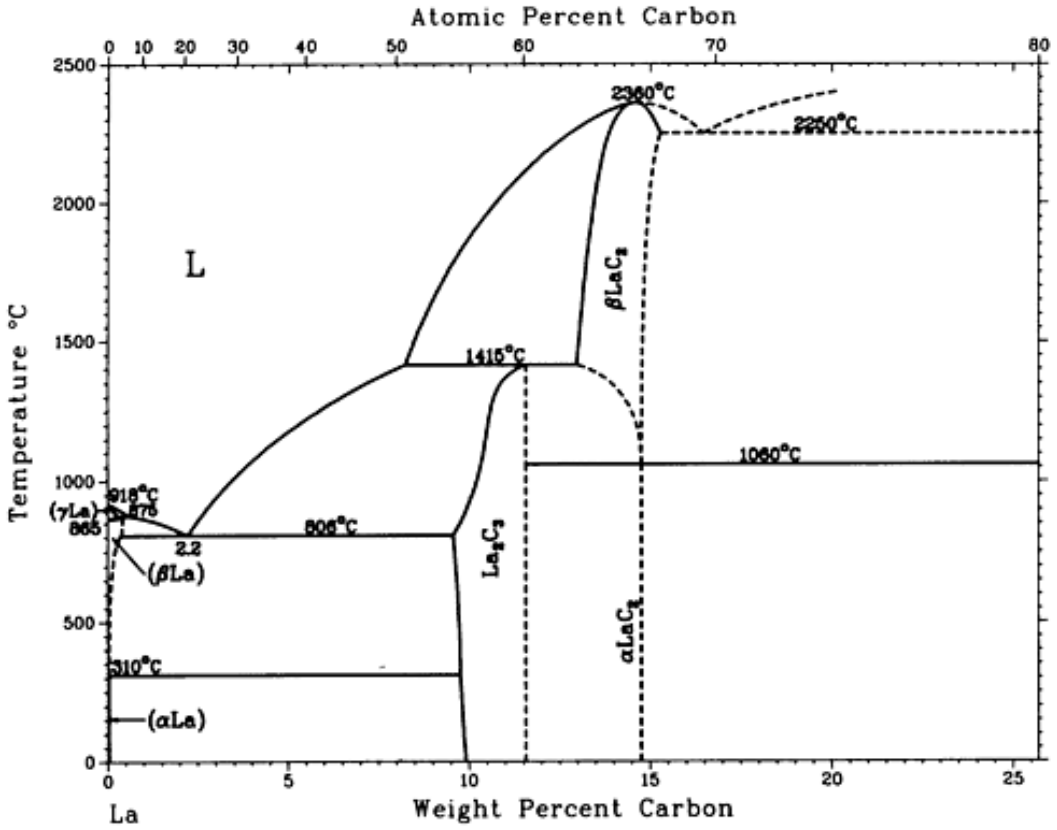

Fig. 77 – La-C phase diagram, after [157].

Lanthanum carbides, in particular LaC_2 can be produced in very similar processes to those used for the UC_2 synthesis, among which the carbothermal reduction of lanthanum sesquioxide is the easiest and more widely used. According to the quantity of carbon used to reduce La_2O_3, the overall process can be written as:

$$La_2O_3 + 6C \rightarrow La_2C_3 + 3CO \quad (64)$$

$$La_2O_3 + 7C \rightarrow 2LaC_2 + 3CO \quad (65)$$

Other feasible processes to produce LaC_2 and La_2C_3 are [155, 156] the direct combination of lanthanum and graphite in electric arc furnaces under inert atmosphere (very pure carbides, but high cost) and the reaction between lanthanum dihydride and graphite at temperatures up to 2200 °C in high vacuum.

As reported in table 19, no data about the thermal conductivity of pure LaC_2 is available in literature. In the following, the results of a new type of experimental technique developed at INFN-LNL to measure the thermal conductivity of refractory samples like LaC_2/C will be presented. A detailed description of the experimental method is given in Appendix B.

Table 19 – Comparison between some LaC_2 and UC_2 properties.

	LaC_2	**UC_2**
Theoretical density (g/cm^3)	5.20	11.28
Melting point (°C)	2360	2427
Thermal conductivity (W/m·K)	\	13 ÷ 20 (600 ÷ 2060 °C) [62] ρ = 99.5 % TD 5 ÷ 8 (1500 ÷ 1880 °C) [65] ρ ~ 44% TD
Crystal structure	HT β: FCC LT α: Tetragonal	HT β: FCC LT α: Tetragonal
Lattice parameter	β: a_0 = 6.02 Å α: a = 4.00 Å, c = 6.58 Å	β: a_0 = 5.49 Å α: a = 3.52 Å, c = 5.99 Å
α → β $T_{transition}$ (°C)	1060	1777

Lanthanum carbide is known to react with oxygen (adsorption rate of O_2 increasing with carbon content) [155] and more heavily with water, at room temperature forming $La(OH)_3$ [159] and a mixture of acetylene, ethane, hydrogen and ethylene [156].

4.3.2. A complete LaC_X SPES target prototype

Early investigations on lanthanum carbide as a SPES target test material [85, 86, 87] were focused on the relationship between the type and stoichiometry of the precursors used in its synthesis and the properties of the obtained product, in terms of composition, microstructure and

thermal properties. In particular, lanthanum oxide and lanthanum oxalate were tested as lanthanum sources, whereas different mixtures of graphite and carbon nanotubes were used as carbon sources. Most of the thermal treatments were performed in the same setup described in 3.3.3, demonstrating the possibility to obtain carbon dispersed lanthanum carbide (LaC_X in the following, where, as in the case of UC_X, LaC_X stands for LaC_2 + nC) operating under high vacuum at temperatures up to 1600 °C. The above mentioned experimental apparatus however allows only for the obtainment of a limited amount of carbide pellets on a single thermal treatment, due to geometric limitations of the heating crucible and the vacuum chamber. More into details, only one 40 mm diameter (or up to three 13 mm rescaled prototypes) disc can be produced at a time. In the future view of producing uranium carbide targets for the running SPES facility, this means that several thermal treatments would have to be performed in such system to obtain a single target, and the handling and storage of a large amount of radioactive material (about 30 g of UC_X) would have to be taken into account. In the case of lanthanum carbide, whose reaction with air and more importantly with water is faster than that of UC_X leading to very severe damage of the produced discs in a short time, the development of a reaction chamber capable of producing seven 40 mm in one single treatment is even more important. Moreover, the geometry and layout of the reaction furnace should ideally resemble those of the irradiation chamber ("target chamber" and "target block" of fig. 10) in order to allow for a fast and safe transfer of the produced disc into the RIBs production area. This aspect directly implicates that the target discs should be thermal treated in vertical position inside a graphite box very similar to that shown in fig. 13.

Details on the newly developed reaction chamber are given in the following, where the production process developed for the obtainment of a complete LaC_X target is described.

Material synthesis

Lanthanum oxide (Sigma-Aldrich) and graphite (the same used for the UC_X production, chapter 3) were used as lanthanum and carbon sources, respectively, according to the reaction:

$$La_2O_3 + 11C \rightarrow 2LaC_2 + 4C + 3CO \quad (66)$$

The choice of this conditions of iperstoichiometry is motivated by the LaC_2:C molar ratio of 1:2, thus equal to that obtained in the UC_X target prototypes.

Before being mixed with graphite, lanthanum oxide was calcinated at 1000 °C for 2 hours in argon flow in order to remove CO_2 and H_2O adsorbed during air exposition, whose massive

release could lead to critical pressure levels in the reaction chamber during the first steps of the thermal treatment to favour reaction (66), compromising the vacuum system performances.

The reagents were ground and mixed inside an agate jar by means of a planetary ball mill. After adding 2% wt. phenolic resin as a binder, the powders were cold pressed into 40 mm diameter discs under a 750 MPa uniaxial pressure. Seven discs were placed vertically inside a graphite box, as shown in fig. 78, and thermal treated in a furnace briefly described as follows.

Fig. 78 – Seven green La_2O_3/C pellets placed in a graphite box.

The main component of the reaction furnace (fig. 79) is a water cooled stainless steel chamber evacuated by means of a rotary and a turbomolecular pump placed in series. In the same configuration of fig. 10, a tantalum heater placed inside the chamber is heated by Joule effect by means of a power supply system capable of providing currents up to 1300 A, with a maximum potential difference of 10 V. The graphite box containing the reactive samples can be placed inside the heater, whose both sides are then closed by means of two graphite bulk disks which act as heat shields and allow for a good temperature homogeneity inside the box. One of the graphite caps has a 5 mm diameter hole through which the temperature of the first thermal treated disc can be measured by means of a pyrometer. The tantalum heater is itself shielded by means of a complex system made of curved tantalum foils, in order to reach temperatures up to 2000 °C inside the reaction box.

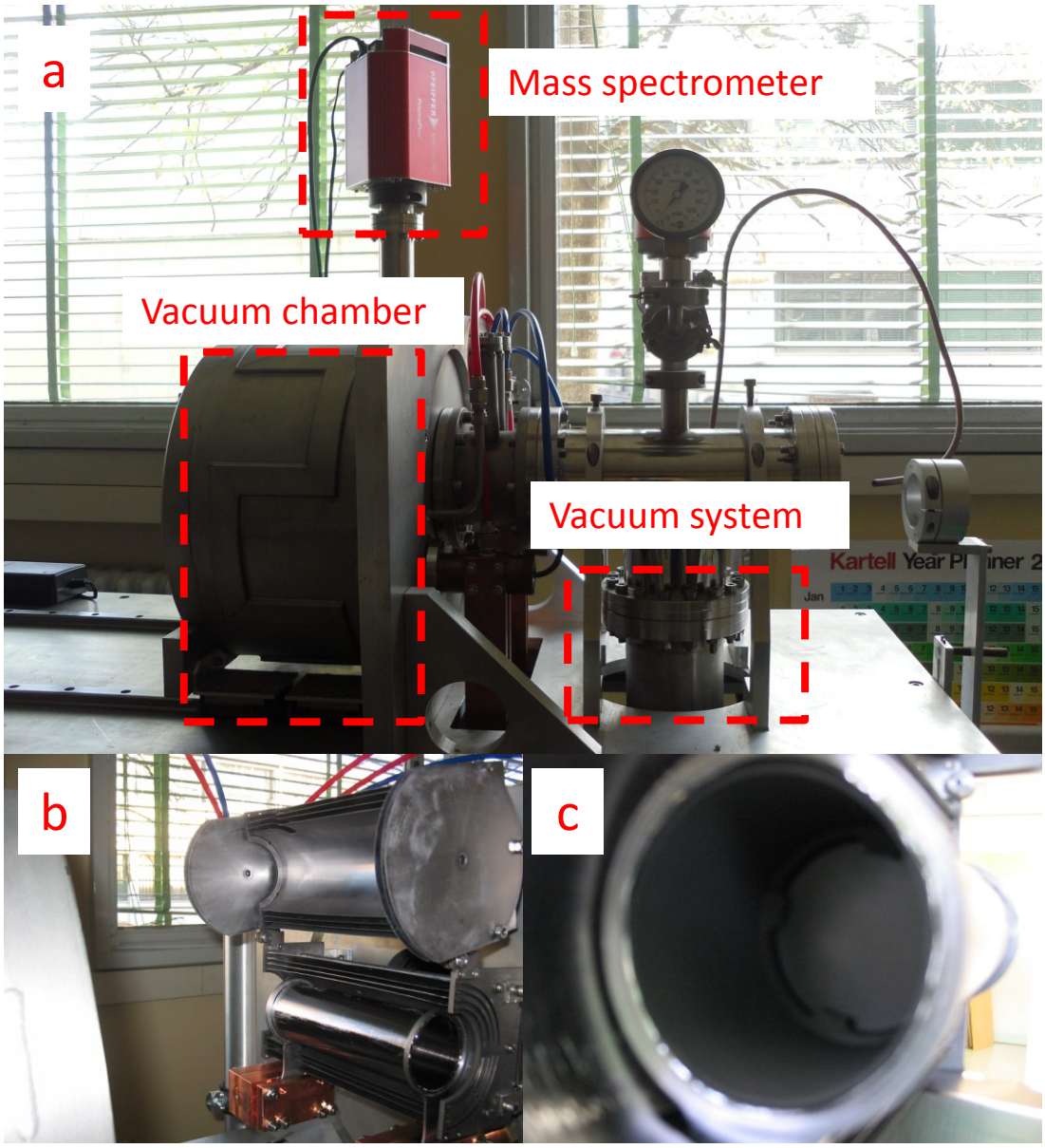

Fig. 79 – Furnace used for high vacuum treatments. a) System overview, b) Open shield showing the cylindrical tantalum heater connected to copper clamps, c) graphite box placed inside the heater for the "vertical" treatments of samples.

The thermal treatment to be performed on the pressed pellets was designed to promote a slow and homogeneous carbothermal reaction throughout the entire target block, allowing for the outgassing of the reaction products without compromising the efficiency of the vacuum pumping system by guaranteeing a pressure always below the $1*10^{-4}$ mbar threshold. The treatment was divided into several steps:

- Slow heating (0.5 °C/min) up to 1000 °C, with intermediate dwell times of 4 hours at 400 °C, 6 hours at 600 °C and 650 °C and 4 hours at 750 °C to slowly release water and other

gases coming from the binder reticulation and decomposition, as well as H_2O and CO_2 adsorbed on lanthanum oxide during mixing and pressing.

- Very slow heating (0.2 °C/min) up to 1600 °C, with intermediate dwell times of 4 hours at 1200 °C, 8 hours at 1350 °C and 8 hours at 1450 °C, to promote the reaction (66) releasing CO.

- 6 hours maintenance at 1600 °C to complete reaction (66) and sinter the obtained material.

- Cooling down to room temperature at 1 °C/min rate.

Experimental results

A typical ongoing of the above described thermal treatment is shown in fig. 80, where the pressure inside the vacuum chamber throughout the experiment is reported. The revealed gas evolution is analogous to that found during the production of UC_X targets reported in chapter 3, with a huge gas evolution below 1000 °C, mainly consisting of CO_2 and H_2O, and the evidence of a CO peak arising for T > 1100 °C (locally interrupted during the aforementioned dwell times).

Fig. 81 shows seven LaC_X discs right after the extraction and opening of the graphite box, performed after venting the furnace from high vacuum to atmospheric pressure fluxing argon into the system. The brown-greenish color of the opaque surface of the discs can be considered itself a proof of occurred reaction (66), since it is the characteristic aspect of LaC_2.

In fig. 82 the results of a XRD analysis performed on powders of one of the discs is reported. During the XRD measurement, the powders were covered with a PEEK thin film (0.25 mm), in order to avoid the contact with air and humidity. It is clear that an important oxygen contamination was present, most probably coming from the sample's contact with air during handling rather, but also from incomplete reaction. However, no clear evidence of La_2O_3 peaks was found. Fig. 83 show a XRD spectrum obtained on a LaC_X sample obtained in a very similar treatment than that above described, but stored in a glove box with nitrogen atmosphere for the preparation of the powders for the XRD investigation, soon after being removed from the reaction chamber. It is clear that the careful control of the air contamination can allow for limiting the oxidation of the formed carbide.

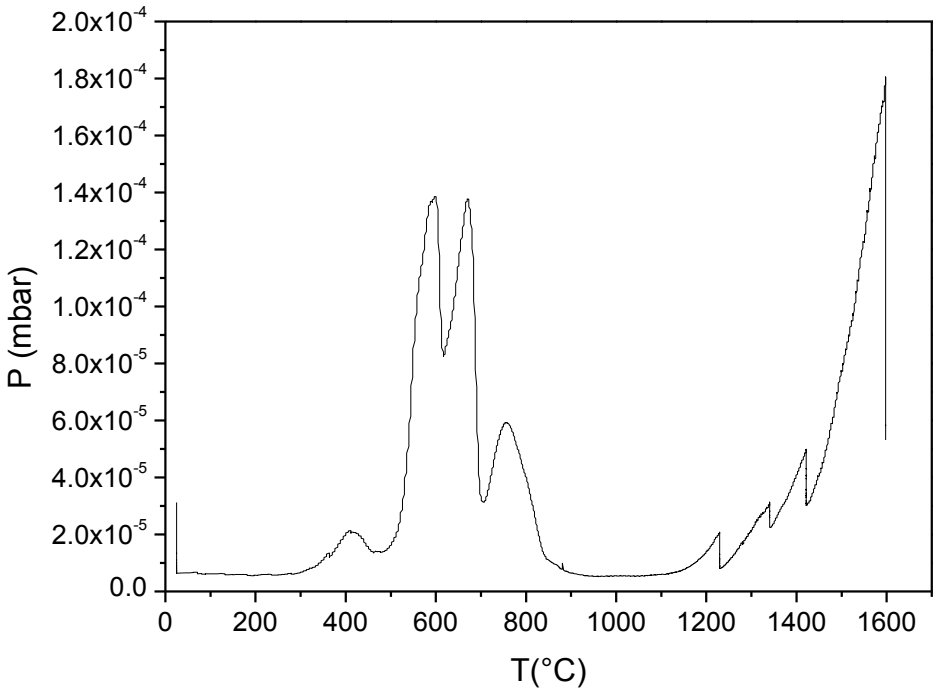

Fig. 80 - Pressure inside the reaction chamber upon carburization and sintering of seven LaC_X discs.

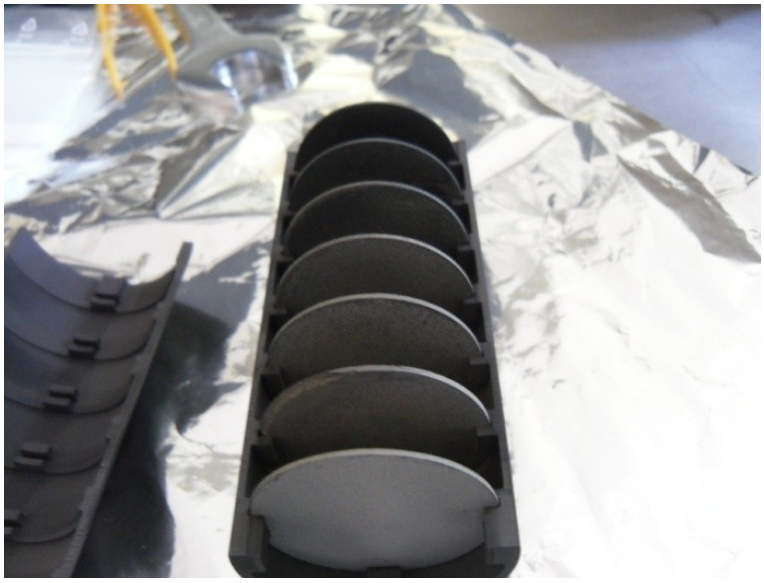

Fig. 81 – Seven LaC_x pellets after the thermal treatment

Fig. 84 shows a SEM image taken on one of the produced samples. The microstructure is similar to that of the "standard" UC_X reported in fig. 28, a dispersion of residual graphite grains in a partially sintered carbide matrix, confirming the analysis already performed on discs of such composition prepared in the high vacuum furnace shown in chapter 3 [86]. The presence of oxygen in the sample was confirmed by EDS analysis reported in fig. 84, where the presence of a residual graphite block is evidenced.

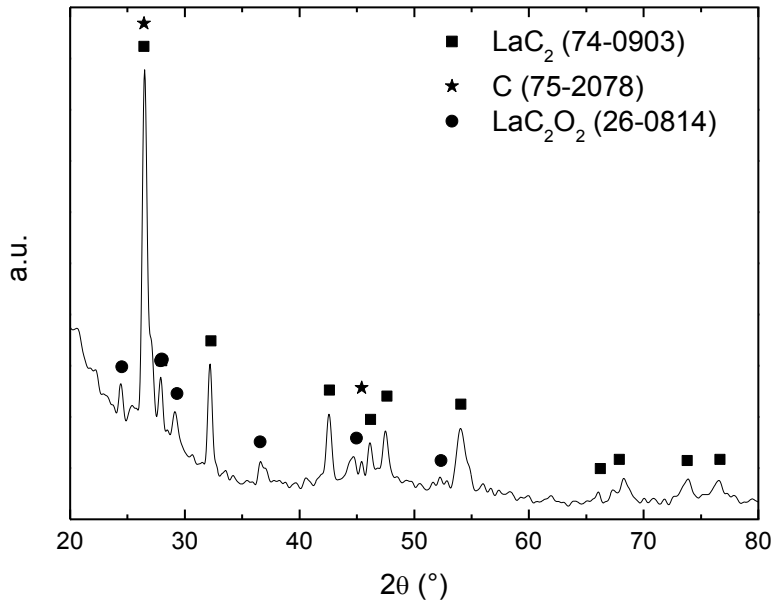

Fig. 82 – XRD patterns of a LaC_X sample.

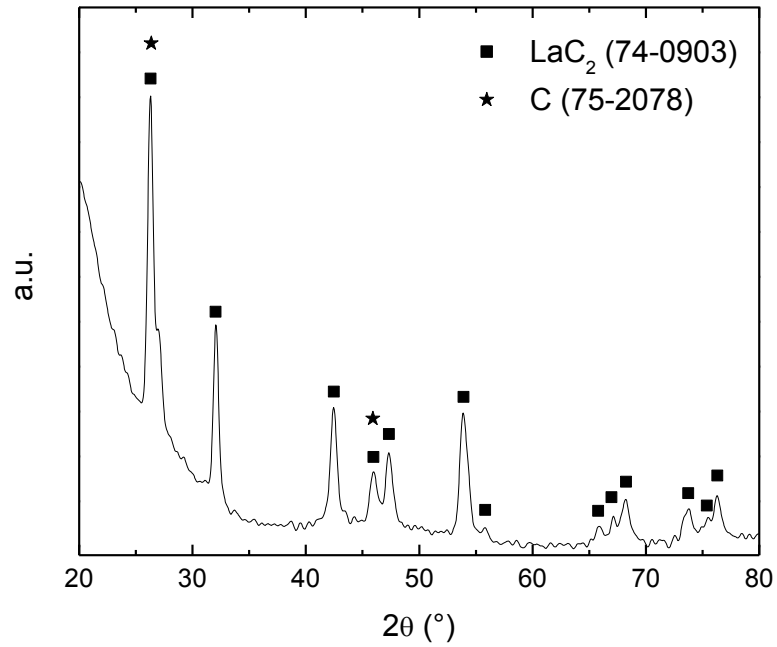

Fig. 83 – XRD patterns of a LaC_X sample stored in a glove box after the thermal treatment.

Table 20 reports some average properties of the produced discs; no significant variations in density and so in total porosity were found between the seven discs, meaning that the experimental setup shown in fig. 78 can guarantee good enough temperature homogeneity along the entire heated zone, to perform the thermal treatment of several samples in one single run. In order to perform the LaC_X synthesis and sintering treatments, a maximum current of 900 A provided by the power supply was necessary. The capability of the system of providing up to

1300 A current should allow for reaching the higher temperatures needed for the UC_X standard production (T up to 1800 °C) and therefore representing a feasible apparatus to perform the target preparation for the SPES facility with limited issues relative to the handling of separately prepared discs made of radioactive material.

A LaC_X sample of reduced dimensions with respect to those above described (30 mm diameter) was prepared under the same processing conditions here described, and dedicated to a thermal conductivity evaluation using the experimental setup described in Appendix B. The results of the measurements are shown in fig. 85, in which the thermal conductivity is reported as a function of the temperature in the 500 ÷ 1100 °C range, together with an indication of the error confidence band (see Appendix B). Even if affected by a non-negligible uncertainty, the obtainment of an experimental evaluation of the thermal conductivity of a lanthanum carbide/carbon sample is extremely important since it seems to be similar to that reported for UC_2 in table 2, thus highlighting once more the key role of LaC_X as a test material to simulate the properties and behavior of UC_X. Moreover, the development of an experimental tool to measure the thermal conductivity will be very useful in characterizing synthesized samples with few or none experimental data available in literature, such as porous UC_X, using the same type of device used for the target production.

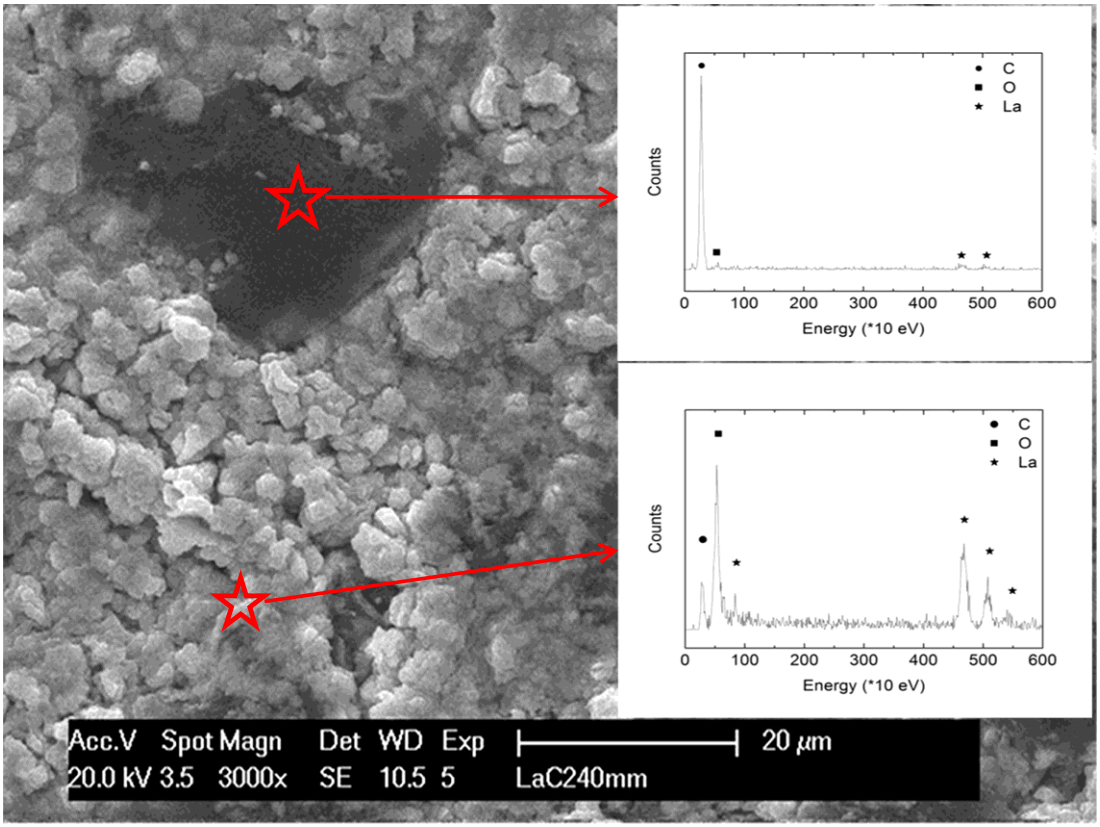

Fig. 84 – SEM-EDS analysis of a partially oxidized LaC_X sample, showing $La(O)C_2$ and graphite separate phases.

Table 20 – Average properties of the LaC_X pellets produced in a single run. [(a)] Calculated as a weighted average between LaC_2 and graphite theoretical densities, with LaC_2+2C stoichiometry

	LaC_X properties
Bulk density (g/cm^3)	2.76 ± 0.06
Theoretical density (g/cm^3)	4.61[(a)]
Disc diameter (mm)	39.67 ± 0.11
Total porosity (%)	40.06 ± 2.04

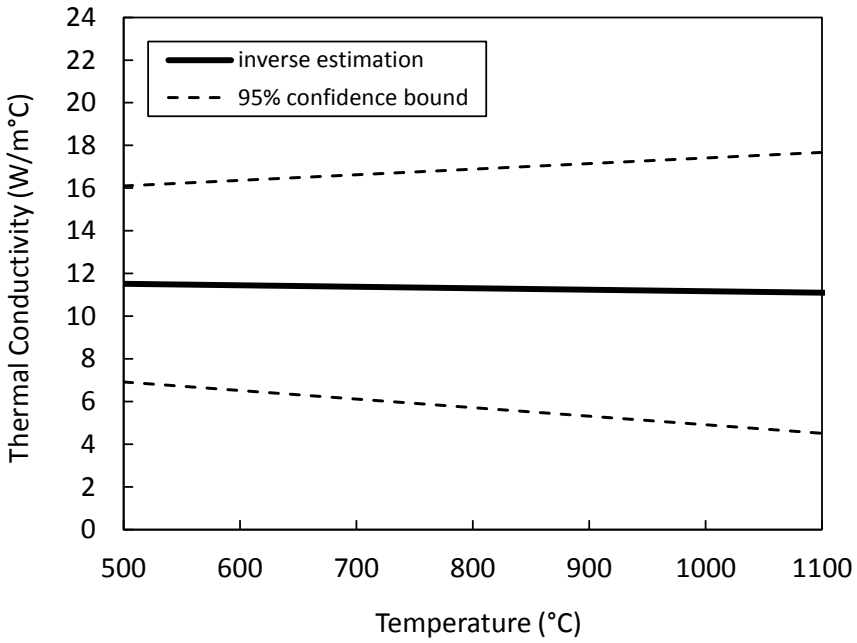

Fig. 85 - Thermal conductivity of LaC_X as a function of temperature. Data obtained by inverse analysis (see Appendix B).

4.3.3. Lanthanum carbide foams

As anticipated in 2.1.3., the effusion of particles from an ISOL target towards the ion source depends mainly on their interaction with the surrounding material, in terms of number of collisions and sticking time. For a ceramic material like those commonly used as targets, the amount of collisions and therefore the release time are clearly related to the porosity level of the material. Moreover, the type of porosity generated during the production process is important in determining the behavior of the material during the isotopes release.

The void fraction of a porous material can be described defining three main pore categories:

- Closed pores, being isolated voids, can only be accessed through diffusion in the solid matrix surrounding them, so not representing a favorable situation for fast release of species since diffusion is slower than effusion.

- Open pores, single or connected, represent void channels that allow for the movement of species from the interior of the solid matrix to the surface, so favorable for isotopes release.

- Permeable pores, which are open channels that connect two surfaces of the medium, so allowing for the release of species without diffusion through the solid matrix.

As reported for the above described materials, the carbothermal reduction synthesis of carbides is invariably characterized by a consistent amount of residual porosity, both deriving from gas generation during the process or by insufficient sintering of the formed grains, which should itself favor the isotopes release. However, if not selectively guided towards open or permeable pores, the increase of porosity within the target structure could have the negative effect of enhancing the free effusion flight path and the number of collisions to the pore walls, resulting in a longer release time, especially for isotopes that are chemically affine to the material matrix. On the other hand, permeable pores should help a direct and faster extraction of exotic species from the target bulk, since they reduce the necessity of successive steps of diffusion through the solid matrix and effusion through the voids, which is the expected sequence in the case of a target matrix containing a similar porosity level but made of closed pores.

Differently from open and closed porosity, which can be investigated by different methods such as helium picnometry, liquid immersion, mercury intrusion, image analysis, mass and bulk volume measurements, the evaluation of the permeability of a material can be carried out with fluid flow experiments, like that described in the following paragraphs, used in this work.

In order to produce highly porous lanthanum carbides with interconnected porosity, a common foaming technique was applied to the lanthanum oxide/carbon system, the sacrificial filler method. The use of this technique represents an interesting approach due its capability to lead to the formation of microcellular interconnected foams [160, 161], thus potentially

favorable for the release of species originated in the ceramic matrix. The production process used to produce LaC_X foams is described as follows.

Material synthesis

LaC_X foams were prepared using polymethilmetacrylate (PMMA, 35μm beads from Altuglas International) as a sacrificial template, while the same lanthanum oxide and phenolic resin above mentioned were used to promote the occurrence of reaction (66), as lanthanum and carbon sources, respectively. The choice of phenolic resin as a carbon source is due to its binding behavior which guarantees the mechanical stability of the pressed pellets during the PMMA burn-out phase (see below). After mixing La_2O_3 and phenolic resin by means of a planetary ball mill, the obtained powders mix underwent several processes and thermal treatments described as follows:

- Curing of the mixture at 180 °C for 3 hours in order to reticulate the phenolic resin and favor the intimate mixing between the two reagents.

- Grinding of the reticulated mass and planetary ball mixing with different quantities of PMMA.

- Cold pressing into 40 mm diameter pellets under a uniaxial 230 MPa pressure.

- Thermal treatment of the pressed discs in a tube furnace under argon flow, following four different steps:

    - Slow heating (0.5 °C/min) up to 350 °C, 3 hours dwelling, in order to completely burn out the PMMA and generate porosity.

    - Heating up to 1200 °C at 2 °C/min in order to decompose the phenolic resin and generate the carbon needed for reaction (66), with a yield of 45% wt. (see fig. 64). The furnace was kept at 1200 °C for 8 hours to slowly promote the occurrence of the carbothermal reaction.

- Heating (2 °C/min) up to 1600 °C, with a 12 hours dwell time, in order to sinter the carbide solid phase.

- Cooling down at 2 °C/min to room temperature.

In order to complete the carburization process, a further high vacuum treatment at 1600 °C would have been necessary, since the above described process in a tube furnace, even if carried out under inert atmosphere, inevitably results in the presence of a remarkable amount of oxygen inside the sample, due to incomplete carbothermal reduction and from unavoidable air contamination. However, in order to perform repeated permeability tests avoiding the problems coming from the reactivity of LaC_2 towards oxygen and water, this second thermal treatment is commonly not carried out, in order to maintain a certain amount of oxygen inside the formed LaC_X foam which could prevent, or at least delay, the degradation of the material (namely referred to as LaOC) during handling and characterization.

Four LaC_X foams compositions were tested, with increasing PMMA content in the starting mixture, to evaluate the dependence of permeability on total porosity. In order to compare the foams characteristics with those of a "standard" SPES target, a lanthanum carbide sample obtained with the methodology shown in 4.3.2. was used as a reference. Table 21 reports the starting composition of the five types of samples. "0LaC" indicates the sample obtained from the carbothermal reduction of La_2O_3 with graphite in high vacuum. The sample was kept under argon after its removal from the furnace in order to preserve it from contact with air and humidity.

Table 21 – Composition of the tested samples.

Sample	La_2O_3 (% wt.)	Graphite (% wt.)	Resin (% wt.)	PMMA (% wt.)
0LaC	71.2	28.8	0.0	0.0
30LaOC	36.8	0.0	33.2	30.0
50LaOC	26.3	0.0	23.7	50.0
70LaOC	15.7	0.0	14.3	70.0
80LaOC	10.5	0.0	9.5	80.0

Permeability measurements

The permeability evaluation of a porous structure is based on the generation of a pressure gradient of a fluid through the thickness of the sample, which results in a flow rate of the gas that is dependent on the morphology, volume and size of permeable channels. The experimental pressure drop can be related to the flow rate by a number of empirical or semi-empirical expressions, which allow to define very specific permeability coefficients. The choice of the correct equation to use to describe a set of experimental data and relate them to the properties of the investigated material is obviously related to the particular conditions of flow which are generated during the experiment.

One of the mostly used expressions that describes with reasonable accuracy the flow resistance through a porous medium for a wide range of fluid velocities is given by Forchheimer's equation, whose integrated form is [162]:

$$\frac{\Delta P}{L} = \frac{\mu}{k_1} v_s + \frac{\rho}{k_2} v_s^2 \tag{67}$$

where L is the sample thickness along flow direction, v_s is the superficial velocity, given by the ratio between the volumetric flow rate and the area of the sample exposed to flow, μ is the absolute fluid viscosity, ρ is the fluid density, k_1 and k_2 are the Darcian and non-Darcian permeability coefficients, respectively, which are considered to be only dependent on the porous structure and not on the fluid or flow conditions [163]. The pressure drop through the sample ΔP can be expressed as:

$$\Delta P = \frac{P_i^2 - P_o^2}{2P} \tag{68}$$

in which Pi and Po are respectively the absolute inlet and outlet gas pressures and P is the reference gas pressure (usually P_i or P_o) used for calculating μ, ρ and v_s.

Forchheimer's equation is based on the assumption of continuum or non-slip flow, valid if the mean free path of the gas molecules is much smaller than the dimension of the permeable voids. In this situation, the loss of pressure accompanying the fluid flow is the sum of two contributions: the linear term in velocity ($\mu v_s/k_1$) represents the energy dissipation by simple viscous action (fluid friction), while the quadratic term ($\rho v_s^2/k_2$) is more important at high flow velocities, where the curvatures, contractions and enlargements of the flow channels, typical of the pore morphology, generate secondary flow patterns and distortions in the pressure and velocity fields at a microscopic scale, intensifying friction. k_1 and k_2 are therefore intimately

related to the characteristics of the porous structure such as the amount, size and morphology of the pores, and so sensitive to variation of the micro morphology of a sample induced by variation in processing parameters or by degradation phenomena.

For the evaluation of the permeability coefficients of LaOC foams, two devices were used:

- Room temperature permeameter, at INFN-LNL, in which the specimen is tightly fixed within a cylindrical aluminum sample holder, shown in fig. 86. The gas used for the analysis (air, argon, helium, etc.) reaches the bottom surface of the cylindrical sample through a hollow tube with an internal diameter of 20 mm, then it flows through the sample until it reaches its top surface. The gas then moves through a symmetrical tube on top of the sample holder, and it passes through a rotameter, in which its flow at the exit of the sample is measured. The flow is then converted to the actual gas velocity v_s dividing it for the area of the sample exposed to flow (which corresponds to the 20 mm internal diameter of the bottom tube).

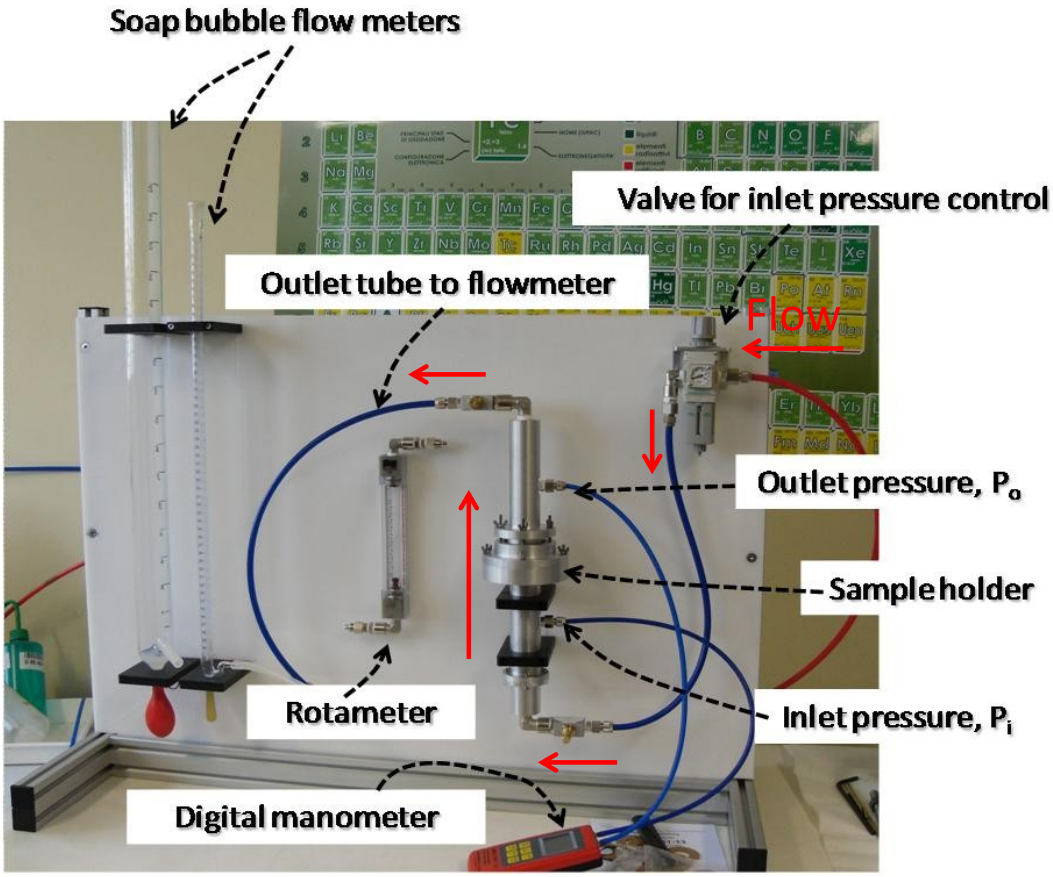

Fig. 86 - Room temperature permeameter at INFN-LNL.

When the gas flow is too low to be detected by the rotameter, a soap bubble meter can be used; it consists of a graduated cylinder in which the gas promotes the formation of bubbles passing through a water-soap solution. In this way, it allows for a direct measurement of the gas velocity. The difference in pressure between sample inlet and outlet is measured by means of a digital differential manometer. In order to have a gas flow going from the bottom to the top surface of the sample, avoiding gas escapes through its lateral walls, particular attention must be done when preparing the specimen for the analysis. First of all, its top and bottom surfaces should be as flat as possible, and parallel to each other. Moreover, the sample should be as thin as possible, so that the path bottom-top surface is shorter than the bottom surface-lateral wall one. A common way to fulfill this requirement is to test samples whose thickness is less than half their diameter. Another practical solution to avoid gas escape is to seal the sample lateral walls using a non-permeable tape. Rubber rings (fig. 87) are placed under and over the sample in order to allow for a tight closing of the system avoiding gas leaks, without resulting in too much pressure on the sample, that could lead to its breakage.

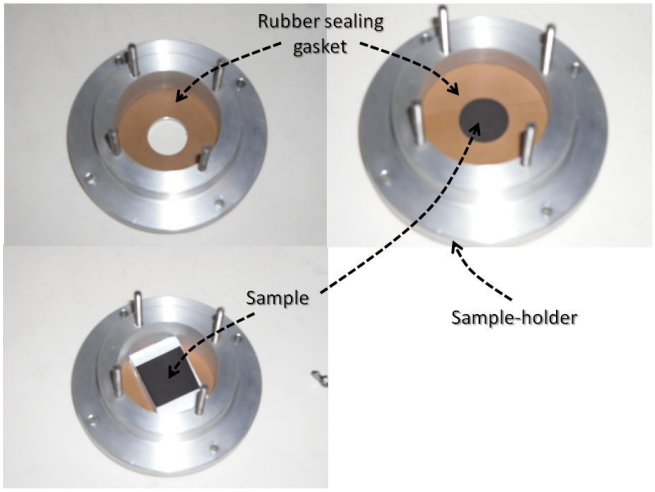

Fig. 87 - Sample holder used int the RT permeameter.

- High temperature permeameter [164], at UNAERP (*Universidade de Ribeirão Preto,* Riberao Preto, Brazil) which has a similar configuration to the room temperature one (fig. 88), but allows for the measurement of permeability coefficients at temperatures up to 700 °C. In this case, the sample holder is made of stainless steel, and it is kept within an electric furnace controlled by a PID system, which permits to realize various temperature-time programs. The gas (usually argon) is pre-heated in a stainless steel coiled tube within the furnace chamber before reaching the sample. Temperature is

measured with K-type thermocouples placed very close to the sample bottom and top surfaces (T_i and T_o, respectively).

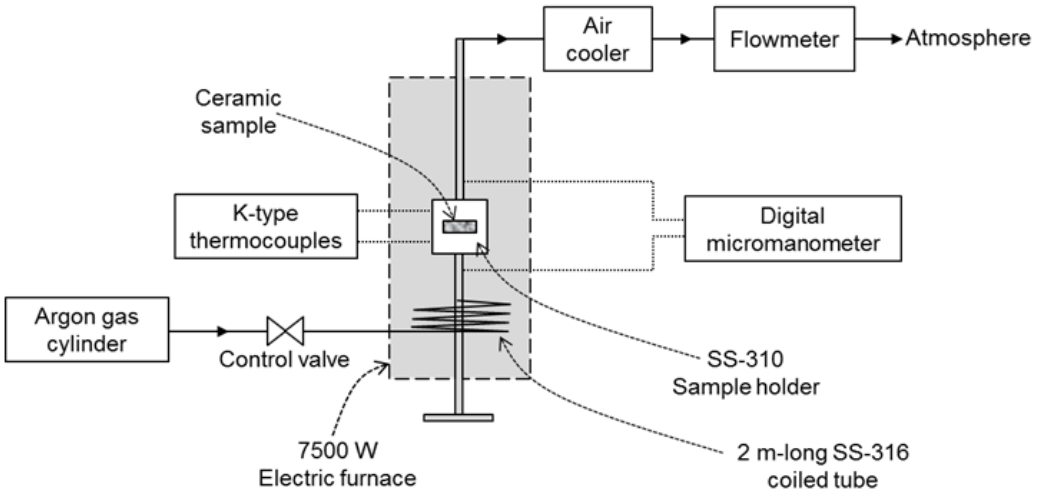

Fig. 88 - High temperature permeameter at UNAERP [164].

To perform the tests, first the temperature is raised to the desired point and then the gas is allowed to flow through the sample with a constant pressure (P_i). When the steady-state regime is reached (constant T_i, T_o, P_i and outlet pressure P_o), the volumetric flow rate Q is measured. The latter measurement is done at room temperature by means of a digital mass flowmeter, after passing the gas through a cooling system. The value of Q is then converted to the value at the sample exit temperature (T_o).

When calculating the permeability coefficients by means of eq. (67), variations in ρ and μ at high temperature must be taken into account, according to (in the case of argon) [163]:

$$\rho_o = \frac{MM_{Ar}}{R}\frac{P_o}{T_o + 273} \tag{69}$$

$$\mu_o = 2.0876 \cdot 10^5 + 7.0219 \cdot 10^{-8} T_o - 3.3071 \cdot 10^{-11} T_o^2 + 2.3196 \cdot 10^{-11} P_o + 2.7082 \cdot 10^{-16} P_o^2 \tag{70}$$

where MM_{Ar} is the molar mass of argon ($39.95 \cdot 10^{-3}$ Kg/mol) and R is the ideal gas constant (62.36 mmHg·L/mol·K), expressing P_o in mmHg and T_o in °C.

Experimental results

Figure 89 shows the effect of the PMMA microspheres addition on the total porosity of the samples (evaluated as in eq.(44)). As reported in table 20, a porosity higher than 40% can be found in samples treated in high vacuum; in the case of the 0LaC samples, an average porosity of about 45% was obtained.

An almost linear increase in porosity was observed with the addition of the sacrificial filler, reaching a maximum of about 89 % for the sample containing a starting 80% wt. amount of PMMA (80LaOC).

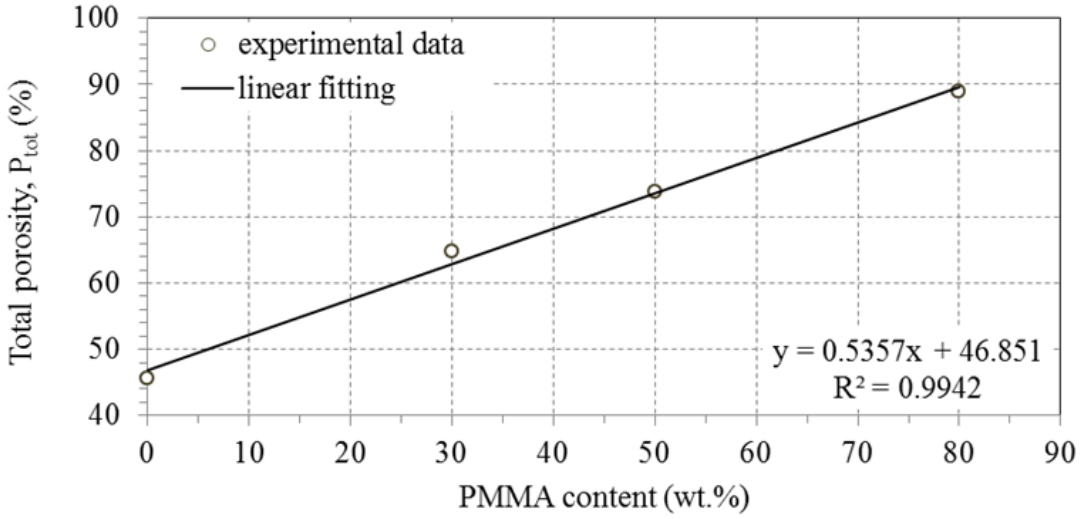

Fig. 89 - Effect of starting PMMA content on the final total porosity of the samples.

SEM images obtained on one of the foams (50LaOC) are shown in figure 90 [165], in which the formation of a porous structure with pores of regular shape is evident. The dimension of the pores ranged from 10 to 30 μm, so compatible with the PMMA used to generate porosity. The struts and cell walls were composed of smooth grains, thus testifying a good degree of sintering. The EDS analysis performed on a strut of the foam (fig. 90d) revealed the presence of C, O and La, analogously to the results shown in fig. 86 for a "bulk" partially oxidized LaC_X sample. In addition to the macropores generated by the PMMA burn-out, holes of smaller dimensions were present on all cell walls, and their presence can be attributed to both the PR decomposition and CO evolution, therefore providing a good degree of interconnectivity among the cells.

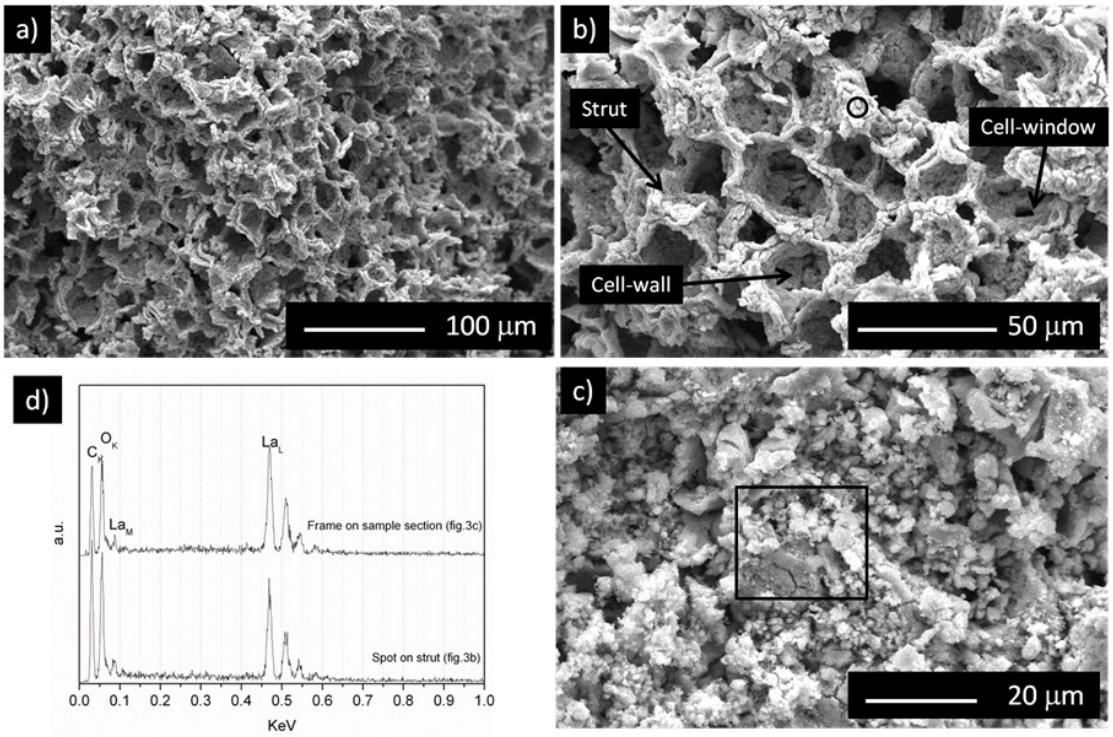

Fig.90 – SEM (a,b,c) – EDS (d) analysis of sample 50LaOC [165].

In figure 91 the isotherm obtained from N_2 physisorption measurements of a 70 LaOC sample is shown. BJH and HK (Saito-Foley modified Horvath-Kawazoe model [166, 167]) methods were used to obtained the meso- and micropores size distribution, respectively, as shown in fig. 92. A clear evidence of the formation of both micro- and mesopores (~ 1.2 and 30 nm, respectively) was found, mainly attributable to the use as a carbon source of phenolic resin [168]. A SSA of about 21 m^2/g was evaluated using the BET method, a value more than 10 times higher than a 0LaC-like sample (1.6 m^2/g, as reported in [87])

In fig. 93, the XRD pattern obtained on powders of a 50LaOC sample is compared to that obtained in the "bulk" 0LaC: in the latter only LaC_2 (and "hidden" graphite peaks as in fig. 83) is present, whereas the former is composed mainly by LaOC (same peaks as the "LaC_2O_2" phase reported in fig. 82, referred to as LaOC in the following) and a minor amount of LaC_2 and unreacted La_2O_3, as expected by using argon flow instead of high vacuum as an environment for the reaction (66). In addition to that, the use of PR in LaOC foams as a source of carbon, instead of graphite, could have contributed to inhibiting carbothermal reaction with La_2O_3, because it shrinkaged and decomposed upon heating creating a certain amount of porosity, thus increasing the distance between the reactants.

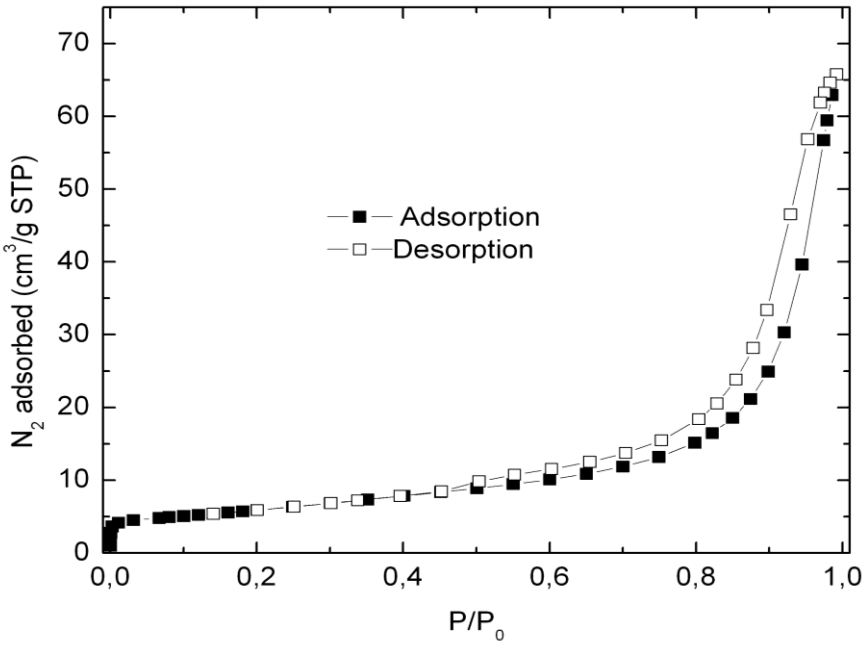

Fig. 91 - N_2 adsorption/desorption isotherm for a 70LaOC sample.

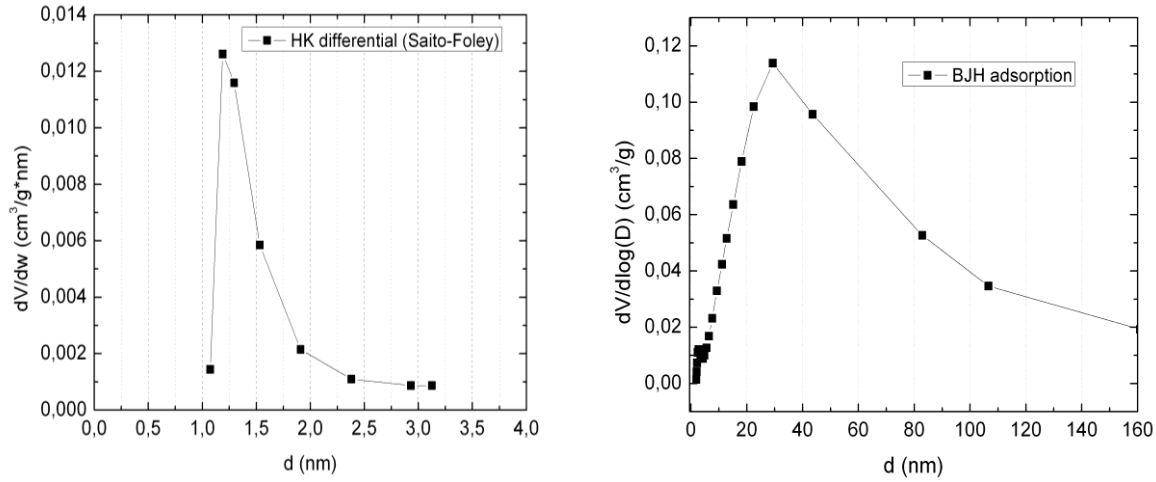

Fig. 92 - Pore size distribution curves for a 70LaOC sample. Left: micropores, right: mesopores.

The permeation curves ($\Delta P/L$ vs. v_s) obtained in the tests with argon flow at room temperature are shown in fig. 94. It is clear that the samples became more permeable with the increase in the PMMA content, since higher gas velocities and smaller pressure gradients were gradually achieved.

The calculated permeability coefficients k_1 and k_2 are reported in fig. 95 (solid lines) as a function of total porosity. The variation of porosity from 45.6% (sample 0LaC) to 88.9% (80LaOC) resulted in an increase of almost 5 orders of magnitude in k_1 and of 8 orders of magnitude in k_2, thus indicating that the inclusion of sacrificial fillers in the lanthanum (oxy)carbide matrix resulted not only in the increase of total porosity, but also in the more

efficient interconnection among the generated voids, enhancing permeability. Fig. 95 shows, as a comparison, a predicted curve (dotted line) based on Ergun-like relationships, which are commonly used to predict the influence of porosity (p) on the permeability coefficients of a porous matrix [162]:

$$k_1 \propto \frac{p^3}{(1-p)^2} \tag{71}$$

$$k_2 \propto \frac{p^3}{(1-p)} \tag{72}$$

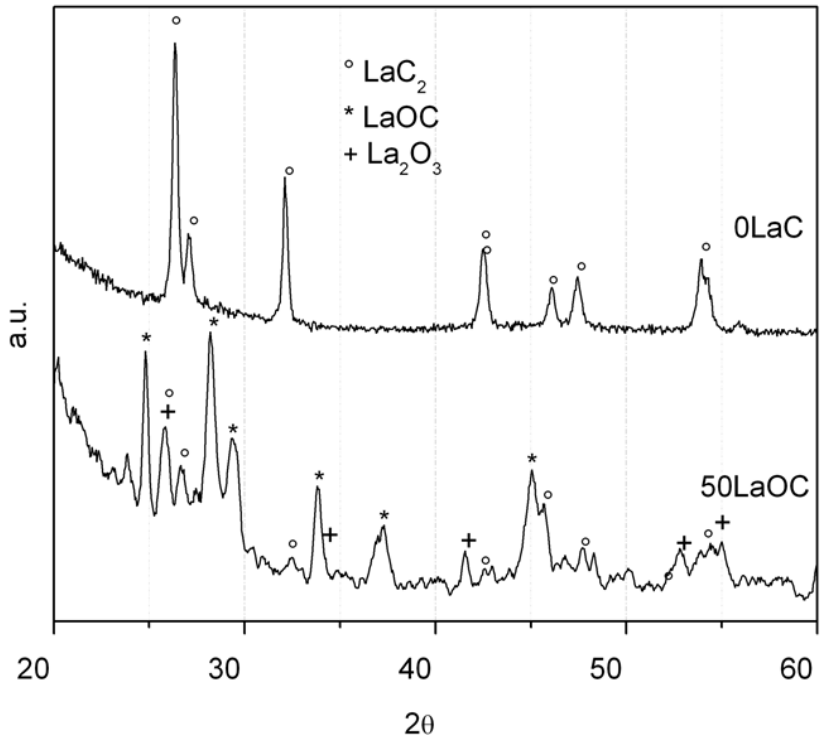

Fig. 93 - Comparison between the XRD patterns of samples 0LaC and 50LaOC [165].

Comparison between the two curves for both k_1 and k_2 show a similar trend of increasing permeability with total porosity. However, since the experimental values were systematically lower than the predicted one, it is likely that a portion of the pores generated by the PMMA burn-out was not permeable.

Fig. 96 [162] shows a "map" of permeability coefficients found for different classes of materials in literature. The permeability coefficients at room temperature found for lanthanum carbide targets processed without PMMA are very low, and comparable to those of concrete, refractory castables and bricks, characterized by a low amount of micro-sized porosity, with k_1

in the order of 10^{-17} m^2. Thus, even if possessing a much higher amount of porosity (45.6%) than those ceramics (5-15%) [169], "bulk" targets like 0LaC were actually very little permeable, denoting the presence of a high percentage of closed pores, or if open, non-interconnected. The use of PMMA on the other hand resulted in a huge increase in both k_1 and k_2, which in the case of 80LaOC resemble those of foams produced by gelcasting and filtering media.

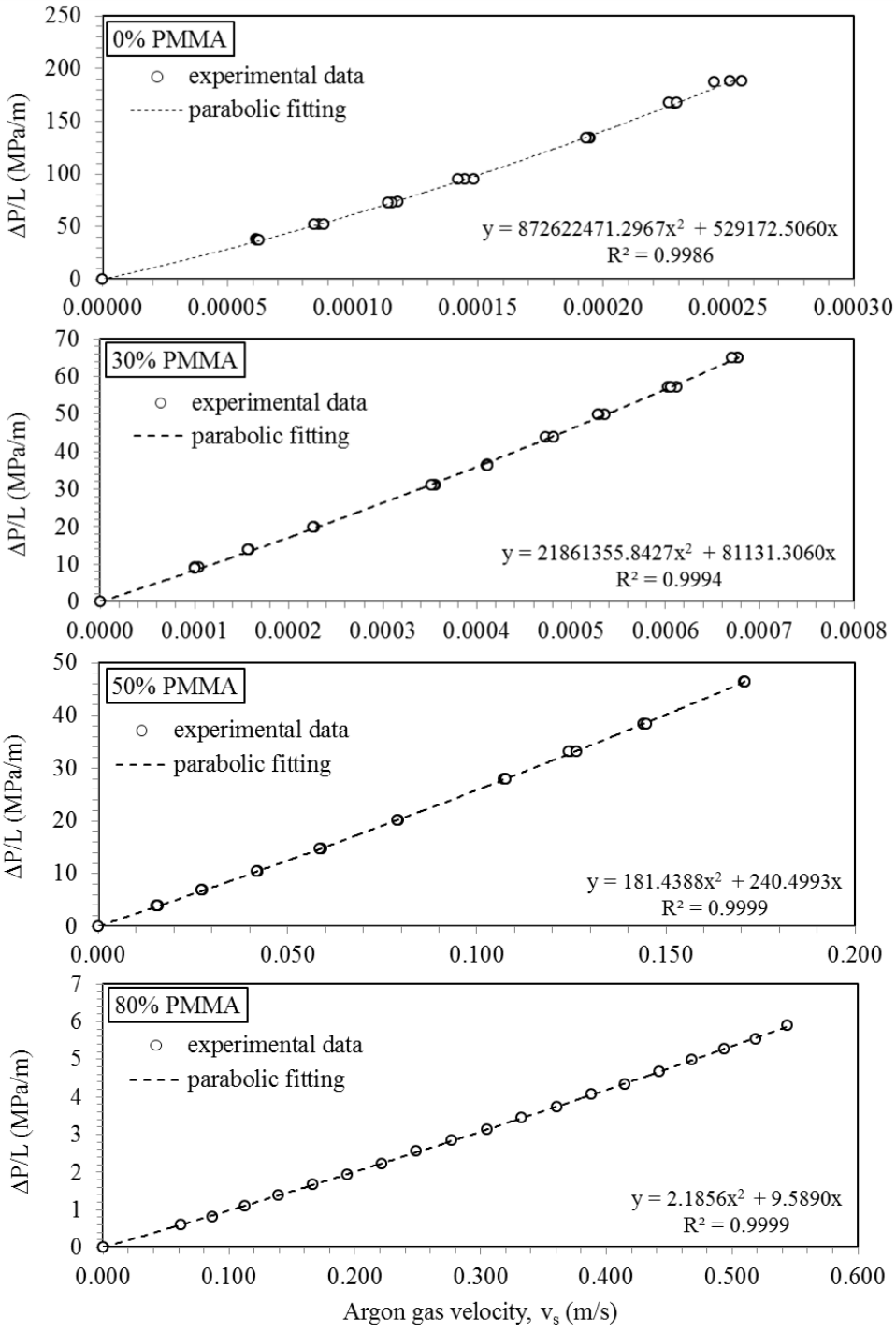

Fig. 94 - Experimental permeation curves at room temperature for lanthanum oxycarbide samples with different PMMA contents [165].

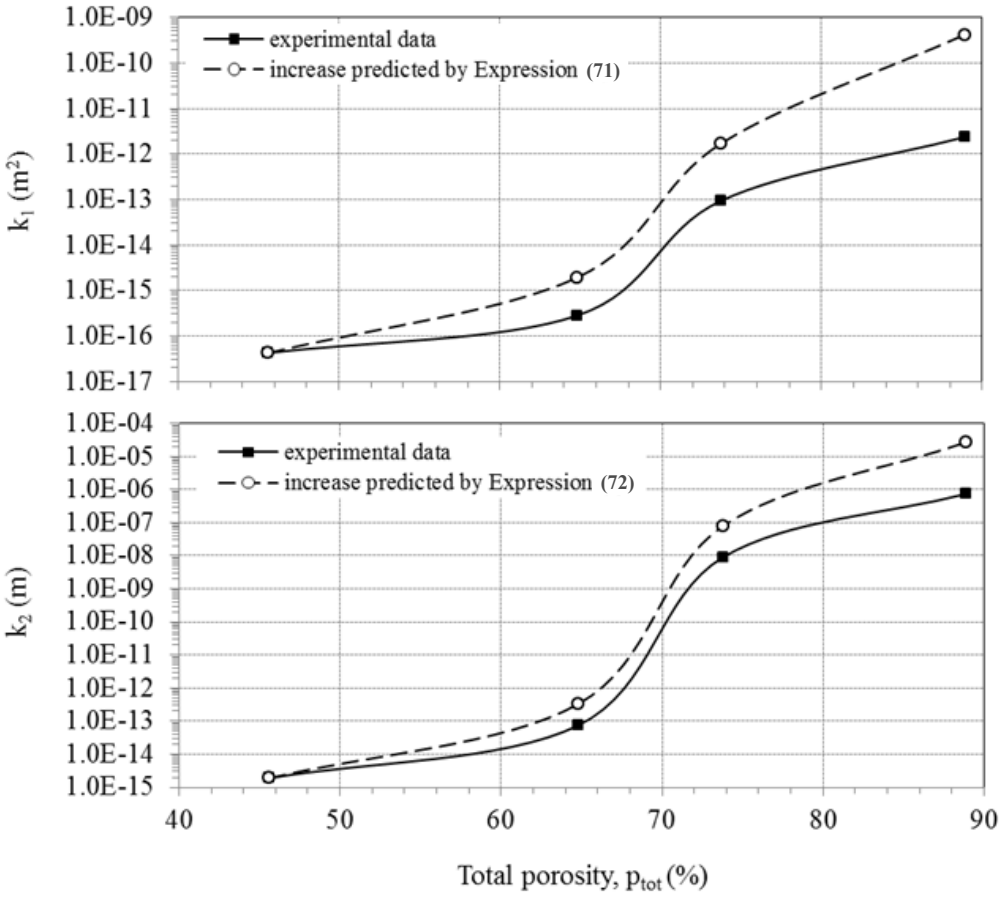

Fig. 95 – Permeability coefficients k_1 and k_2 vs. total porosity for LaOC foams [165].

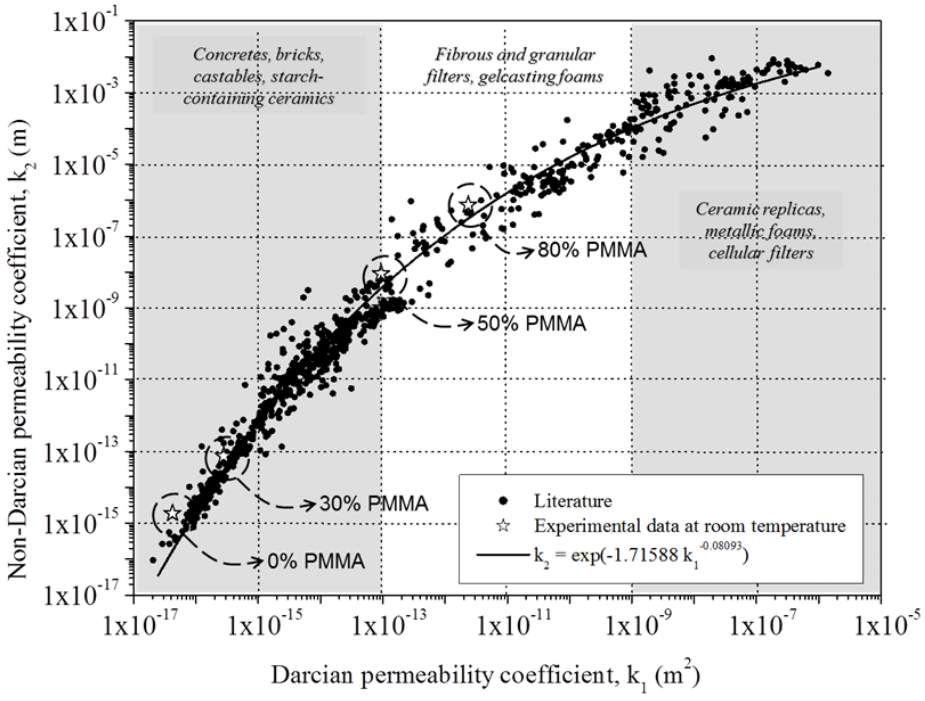

Fig. 96 – k_1 and k_2 coefficients of LaOC foams: comparison with data from different classes of porous ceramics [165].

Figures 97 and 98 show the results of the high temperature tests performed on the 50LaOC and 70 LaOC samples. Due to experimental limitations, the temperature range employed in the tests (30 ~ 450°C) was lower than the common operative temperature of the targets for ISOL facilities (up to 2000°C). However, the obtained data can be used for a preliminary evaluation of the permeation behavior of the LaOC foams.

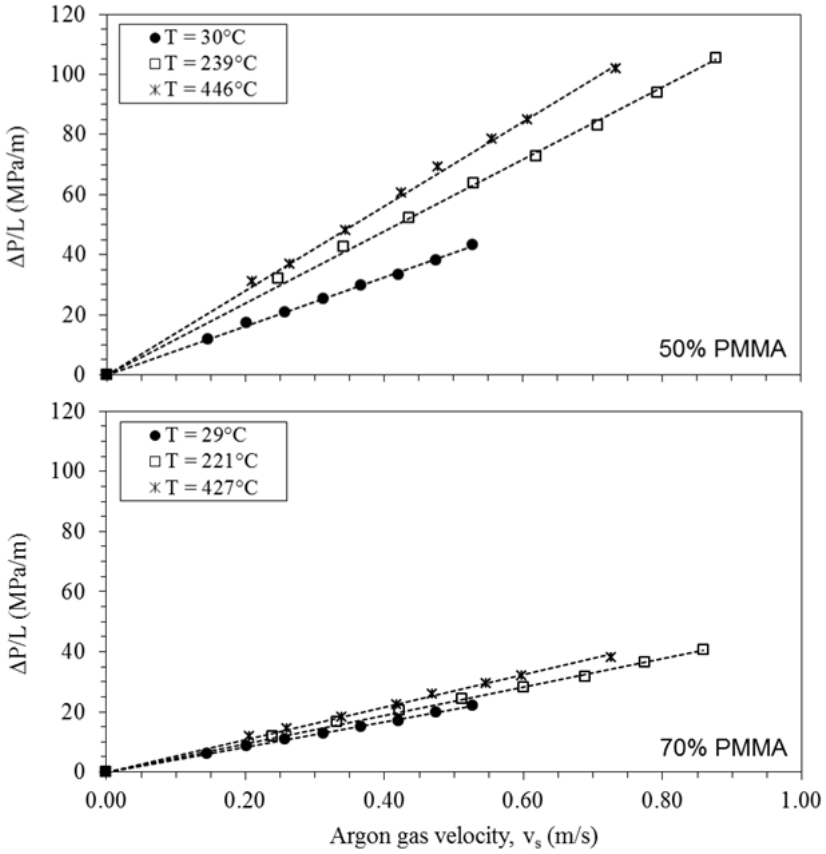

Fig. 97 – Permeation curves for 50LaOC and 70LaOC at different temperatures [165].

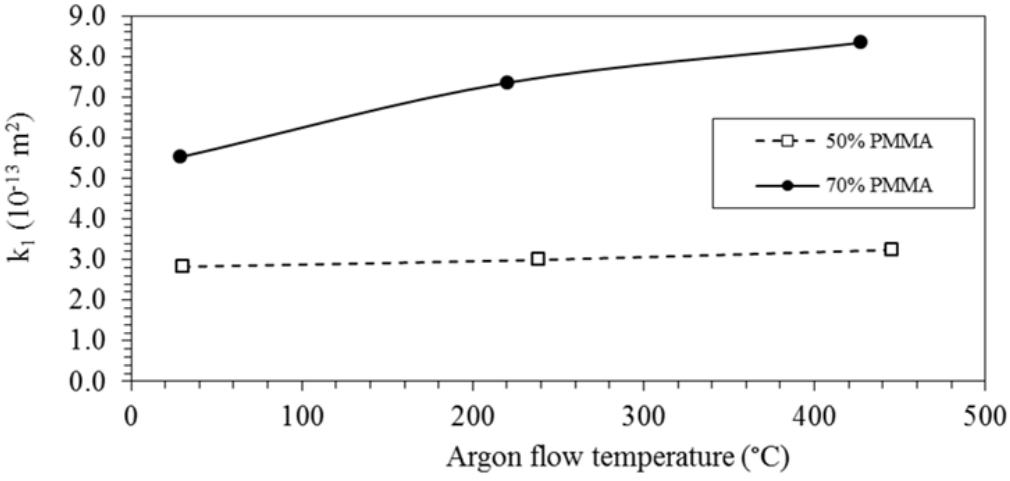

Fig. 98 – Influence of argon temperature on the k_1 coefficient of 50LaOC and 70LaOC [165].

The shift of $\Delta P/L$ vs. v_s curves towards higher ΔP values in the case of the high temperature measurements can be attributed to the variation of gas properties with temperature expressed in eqs. (69) and (70), which has an effect on the viscous ($\mu v_s/k_1$) and inertial term ($\rho v_s^2/k_2$) of eq. (67). Since in the tested gas velocity range (0 – 0.8 m/s) the increase in viscosity is expected to have a greater effect on ΔP than the gas density reduction, the net effect of the increasing temperature is increasing ΔP. On the other hand, also k_1 and k_2 were affected by the gas temperature, since changes in pressure drop curves were more noticeable for sample 50LaOC than for the more porous 70LaOC (fig. 97). Considering that both samples were previously sintered at 1600 °C, such changes up to 450 °C can be considered only to be due to thermal expansion effects. Data reported in the graph of fig. 98 point out that the k_1 coefficient of both samples increased from 30 to 450 °C; the increase was higher (50%) for 70LaOC than for 50LaOC (14%).

The knowledge of k_1 and k_2 can be considered a useful tool to measure and enhance the effectiveness of the interconnected porosity to promote pressure-driven gas flow. The data obtained for lanthanum carbide show that both the inclusion of PMMA and the increase of gas flow temperature up to 450 °C resulted in an enhancement of the pore interconnectivity. On the other hand, k_1 and k_2 absolute values as obtained from the Forchheimer equation can only be used to characterize the gas transport through structures working in conditions of continuous gas flow (the mean free path of the gas molecules is much smaller than the pore diameter), which are actually very far from those of a ISOL target during its operation, in which the mean free path of the permeating rarefied gas (isotopes) becomes comparable to the pore or channel dimensions, since flow is dominated by random collisions of molecules with the wall, rather than by collisions between molecules.

4.4. Conclusions

Among the potential materials to be used at SPES for the production of proton-rich isotopes, boron and lanthanum carbides represent important choices due to their favorable properties, both in terms of physicochemical behavior under extreme conditions and the possibility of tailoring their microstructural properties using different synthetic approaches.

Boron carbide targets, when irradiated with protons, are expected to produce ^{7}Be isotopes which are commonly requested by astrophysicists for several types of experiments. Two different synthesis of carbon dispersed boron carbide targets were proposed and investigated in this work. In both, boric acid acted as a boron source, whereas two different carbon source were used, citric acid and phenolic resin. The techniques were based on the conversion of a starting solution of reagents to intermediate powders, which were then burned to obtain the final carbide and a different amount of residual graphite. In both cases, the desired boron carbide and graphite phases were obtained, but some differences were found in terms of microstructural properties. In particular, a higher but non-organized porosity was obtained in the boric acid-phenolic resin sample, due to the presence of a higher amount of residual carbon. On the other hand, in the boric acid-citric acid sample, a narrow distribution of mesopores was obtained as a result of the gas generation during the boron oxide – boron carbide conversion. Both the types of samples will be tested in order to determine their effective capability of producing and releasing ^{7}Be isotopes under irradiation.

Lanthanum carbide based porous materials have been extensively used in the past few years as test materials to describe different topics relative to the production and characterization of uranium carbides, since the two material are very similar in properties, but lanthanum carbide is not radioactive. In addition to that, lanthanum carbide is a potential material to obtain heavy proton-rich isotopes. Being the synthesis of carbon dispersed lanthanum carbide target prototypes already studied and characterized into detail, in this work the attention was moved to the production of an entire target made of this material, with the final SPES geometrical requirements, in one single run. The fulfillment of this goal required the development of a new production furnace, which was successfully used for this purpose. The developed technique of production will be available for the production and safe handling of uranium carbide targets.

Lanthanum carbide based foams were produced with the sacrificial filler technique, with the aim of obtaining structures with a higher level of porosity and interconnectivity with respect to those obtained from the standard solid state synthesis. To characterize into detail their microstructure, argon permeability measurements were performed at room and high temperature,

using two different devices. The obtained result demonstrated that the addition of polymeric sacrificial fillers to the standard starting mixture of powders not only increased the total porosity of the samples, but also favored the interconnectivity of the pores, resulting in the formation of permeable channels which should favor the isotopes release during operation. Even if the gas flow conditions during the permeability measurements are actually very different from the operative ones, these type of tests can be considered an important source of information about the structural changes in the sample at high temperature.

Conclusions

SPES is a project of INFN which aim is to develop a ISOL facility for the production of Radioactive Ion Beams in one of the four national laboratories of INFN, LNL.

The production of radioactive isotopes will be carried out by irradiating a proper target with a 40 MeV primary proton beam; the produced species will be then extracted from the target, ionized, mass separated and sent to different experimental areas, in which they will be used for nuclear physics, astrophysics, solid state physics and medicine studies.

The core of the project is the production target, in which the nuclear reactions to form the desired isotopes take place. The material it is made of should be able to work in the extreme conditions required to obtain a high production and release of species, without outgassing or undergoing degradation of its thermo-mechanical properties.

The work here reported has been carried out in the framework of the research on materials for the SPES target, focusing on two different categories of materials, depending on the nature of the isotopes which will be produced using them as SPES targets: neutron-rich or proton-rich species.

In the first case, carbon dispersed uranium carbide (UC_X) target prototypes were studied: this material is the most used for the generation of neutron-rich Radioactive Ion Beams with the ISOL technique, due to its excellent thermal properties combined with the possibility to exploit the p-induced uranium fission reaction to generate a huge number of isotopes of several different elements.

In order to have a direct evidence of the performance of UC_X targets produced according to the SPES geometry and layout, two on-line irradiation tests were performed at the HRIBF facility of the Oak Ridge National Laboratory, in similar conditions as those of the future SPES facility. Both the tested materials were obtained from the carbothermal reduction of uranium dioxide, with two different carbon sources: graphite or a 50%-50% wt. mixture of graphite and multi-walled carbon nanotubes.

The experimental results, the first ever obtained on SPES UCX target prototypes, showed that both the targets can be successfully used to produce and release several tens of radioactive isotopes of more than 20 elements, with half-lives from less than one second to up to several hours. The yield vs. temperature and vs. half-life characterization highlighted the importance of working at the highest possible temperature in order to obtain a better release of short-lived

species from the target. Some differences between the isotope yields and release properties of the two targets were found and discussed. They depended both on the actual material microstructure and on the operational anomalies found during the two experimental tests.

Boron and lanthanum carbides are candidate target materials for the production of proton-rich Radioactive Ion Beams at SPES. They can be used under extreme conditions and their microstructural properties can be tailored using different synthetic approaches.

Boron carbide targets are expected to produce ^{7}Be isotopes to be used for astrophysics experiments. In this work, two different synthetic approaches to produce carbon dispersed boron carbide targets were carried out and investigated. In both, boric acid was reacted with two different carbon sources, citric acid and phenolic resin, starting from a solution subsequently converted to reactive powders.

In both cases, the desired boron carbide and graphite phases were obtained, but some differences were found in terms of microstructural properties. In particular, a higher but non-organized porosity was obtained in the boric acid-phenolic resin sample, whereas in the boric acid-citric acid sample a narrow distribution of mesopores was obtained as a result of the gas generation during the boron oxide – boron carbide conversion. The differences between the samples were related to the different residual content in the samples.

Lanthanum carbide synthesis has been already studied and characterized into detail in the last few years; in this work, the attention was moved to the massive production of an entire target made of this material, with the final SPES geometrical requirements, in one single run, in order to develop a technique to be used for the production and safe handling of uranium carbide targets. A new production furnace was developed and successfully used to produce lanthanum carbide targets.

The synthesis of lanthanum carbide foams was studied and developed, using the sacrificial filler technique, with the aim of obtaining structures with a higher level of porosity and interconnectivity with respect to those obtained from the standard target production. Gas permeability at room and high temperature was proposed as a characterization tool to describe the material microstructure and its evolution at high temperature. The use of the sacrificial filler method resulted in samples with increased total porosity and interconnectivity of the pores, leading to the formation of permeable channels which during irradiation should favor the isotopes release.

Both the materials will be tested in order to determine their effective capability of producing and releasing proton-rich isotopes under irradiation.

Appendix A

Yield calculation with γ-ray spectrometry

A.1. Experimental setup

As reported in 3.3.1., a common way to investigate the quality and quantity of the produced and accelerated isotopes in an ISOL facility is to collect them on a moveable tape and to study their gamma emissions by using a high purity germanium detector.

The measurement setup used at OLTF during the UC_X tests reported in Chapter 3 is shown in fig. A.1.

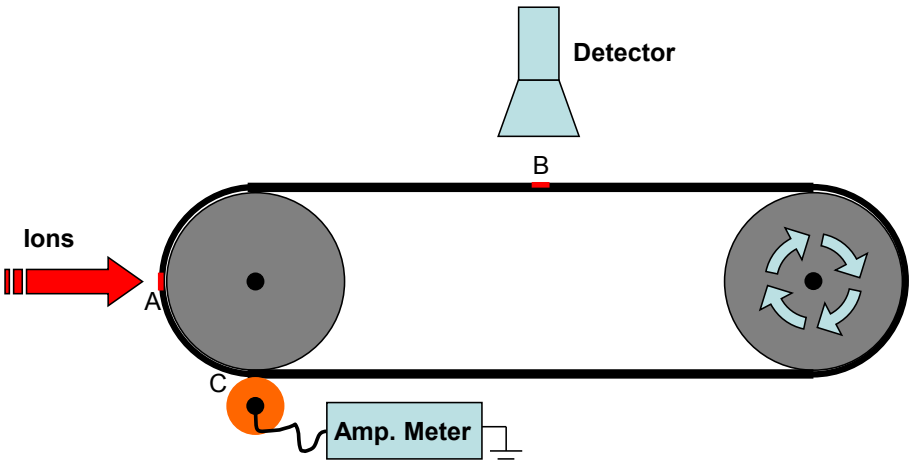

Fig. A.1 – Schematic representation of the γ measurement setup at OLTF [94].

A portion of tape (position A) is exposed to the ion flux for a specific collecting time t_c then quickly moved, by a stepper motor, in front of a Ge detector (position B), where the γ-rays are detected for a fixed observation time, t_o. The measurement is repeated for a number of cycles n_c. The tape is metalized on one side and is incorporated into a Faraday cup, so that current can be measured during collection and during tuning of the RIB. The current signal is collected from the Faraday cup (position C) and connected to a picoammeter.

Appropriate collecting times are used to detect and analyze the presence of isotopes with different lifetimes. Short collection times must be used in the case of short-lived isotopes. On the other hand, with long enough collecting times, most of the contribution to the decay spectra is

due to the isotopes with long half-life. The tape move time, t_m, and any delay time, t_d, between the end of the tape move and the beginning of the observation time, are also important parameters to take into account when calculating the yield.

The yields calculation of different isotopes is carried out analyzing the gamma-ray spectra obtained by coupling the Ge detector with a multi-channel analyzer (MCA), using the Genie™ 2000 Applications Software (Canberra Industries, Inc.), which provides values of peak area and relative uncertainties for each peak analyzed (see fig. A.2).

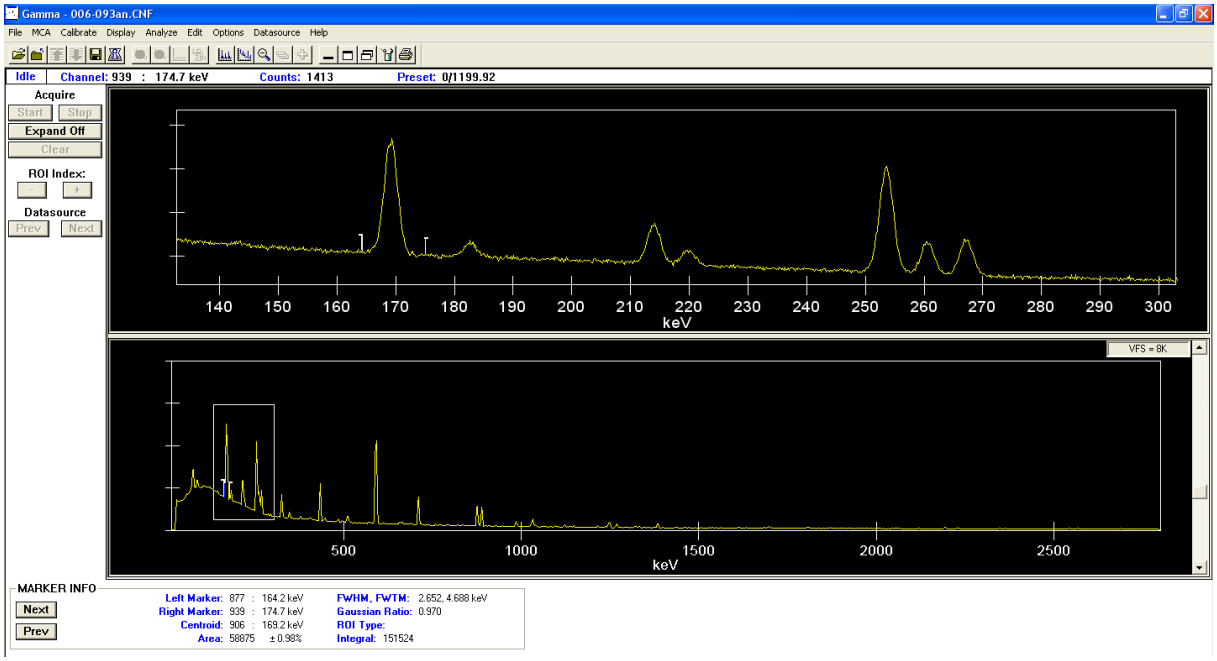

Fig. A.2 – A Genie™ 2000 spectrum for mass 93 during the "standard" UC_X test.

A.2. Yield calculation

After a careful analysis of the γ-ray spectra, it is possible to identify the characteristic γ peaks of a particular isotope, which are generated when it decays into a daughter isotope, or from an excited metastable state to a ground state. To calculate its yield in terms of ions/μC the following expression is used:

$$Y = \frac{N\lambda}{b_\gamma(1 - t_{dead})\varepsilon_\gamma n_c I(1 - e^{-\lambda t_o})(1 - e^{-\lambda t_c})e^{-\lambda(t_m + t_d)}} \qquad \text{(A.1)}$$

in which N is the peak area after background subtraction, $\lambda(s^{-1})$ is the isotope decay constant and b_γ is the γ-branching ratio, i.e. the fraction of decays resulting in an emission of a γ-ray of that energy. t_{dead} is the detector dead time, which represent the fraction of collection time

in which the detector is not able to record the γ-events, whereas I is the primary (proton) beam current. The exponential terms in eq. (A.1) take into account the decay of the isotope during the collection, movement, delay and observation times.

ε_γ, which represents the gamma efficiency of the Ge detector at the different γ-ray energies, can be obtained by placing it close to a standard gamma source of a known activity, and collecting the correspondent γ-spectrum. During an experiment, the detector is commonly moved in different positions with respect to the tape, in order to minimize the dead time during the γ-signals collection. A direct relation between the γ-rays energy (E) and the detector efficiency can be obtained by fitting with fourth-order polynomial the $\log(\varepsilon_\gamma)$ vs. log(E) data revealed using the standard γ-source. An example of efficiency calibration of the detector at two different distances from the γ-source is shown in fig. A.3. The data were obtained using a ^{152}Eu-^{154}Eu-^{155}Eu standard source (MGS-1 from Canberra Industries Inc.), before carrying out the "low density" UC_X irradiation test reported in 3.3.4.

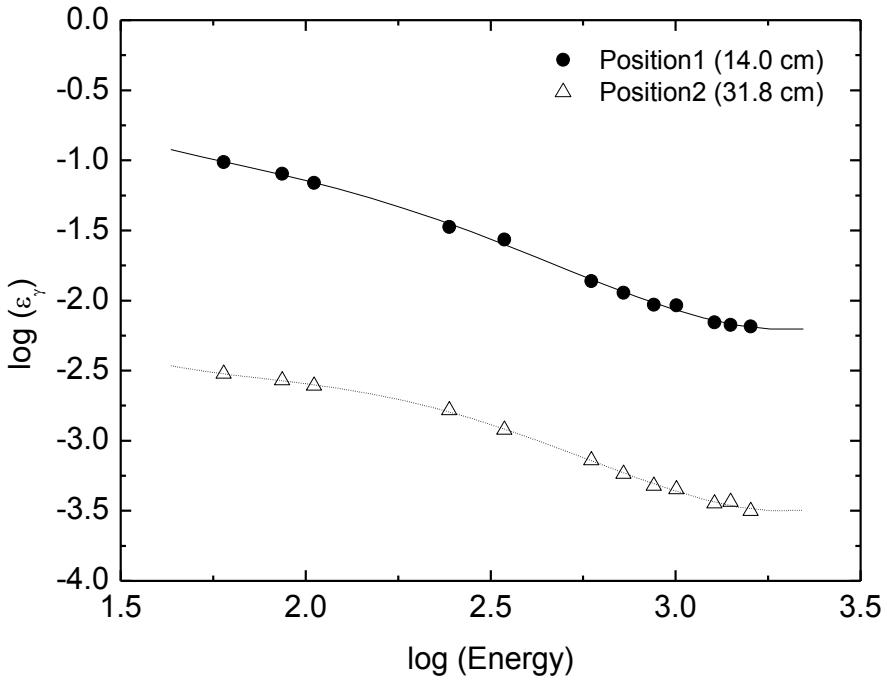

Fig. A.3 – Efficiency calibration of a Ge detector at two different distances from the tape, using fourth-order polynomial fits.

Appendix B
Thermal conductivity estimations for refractory materials

As reported in chapter 3 and 4, very few experimental data are available about the thermal conductivity of the materials used as ISOL targets. Moreover, the data reported in literature are often contradictory one another, or they have been obtained in very different conditions from those encountered by the ISOL target during its operation, so in most cases they cannot be used for thermo-structural predictions of the target behaviour during irradiation. The most common method to perform the thermal conductivity measurements is the "flash-pulse" (or "laser-flash") method [170], in which thermal conductivity is indirectly calculated by measuring the material thermal diffusivity, heat capacity and density.

A new method developed at LNL-INFN [171] allows to determine the thermal conductivity of refractory samples in conditions very similar to those of the final SPES target, without the need of the aforementioned material properties measurements. The technique, based on the inverse analysis method [172], is briefly described as follows.

B.1. Experimental setup

The core of the experimental apparatus developed at LNL for the estimation of thermal conductivity is shown in fig. B.1.

A graphite heater is designed in order to produce on its top round surface (diameter equal to 18 mm) an homogeneous temperature distribution at temperature levels close to 2000 °C, by Joule effect. A 1000A-10V DC power supply feeds the heater by means of two water-cooled copper clamps. Three tungsten bars suspend a sample disc coaxially to the round hot surface of the heater, keeping a small constant spacing of 5 mm between the sample and the hot surface. Bars are accurately inserted in a graphite support positioned below the heater, and the support is in turn placed on a stainless steel main plate. All the components above described are closed inside a water-cooled vacuum chamber. The vacuum is maintained at approximately 10^{-6} mbar

by a rotary pump and a diffusion pump placed in series. A high-temperature infrared pyrometer placed on the top of the vacuum chamber allows the measurement of both temperature and emissivity [41] on the top round surface of the sample disk. Thermal radiation coming from the sample reaches the pyrometer passing through a borosilicate glass window that is almost completely transparent to infrared radiation. Data are collected automatically by making use of a computer connected to the instrumentation by a Programmable Logic Controller (PLC).

The sample geometry takes as reference the SPES target discs, while the heater is designed in order to reproduce in the sample the axially symmetric temperature field (with strong temperature gradients along the radius) that characterizes the SPES target disks during their typical working conditions. This radial temperature gradient in the sample is induced by the fact that the graphite heater has, as mentioned above, in its round top area (facing directly the bottom round area of the sample) an homogeneous temperature distribution. Since the electrical resistivity of graphite is temperature-dependent, the thermal and the electrical problems controlling the system are coupled.

B.2. Direct and inverse problem description

Concerning the thermal field, this is a typical case of coupled conduction/radiation problem. It can be solved using a sequential method [173], so considering iteratively the thermal diffusion and the radiation equations. Fig. B.2 sketches a general coupled conduction/radiation problem, characterized by the diffusion of energy within the solid region V (conductive problem) and the radiative heat transfer between the surfaces forming the enclosure S_{enc} (radiative problem).

The thermal conduction problem is defined by [174]:

$$\frac{\partial}{\partial x}\left(k\frac{\partial T}{\partial x}\right)+\frac{\partial}{\partial y}\left(k\frac{\partial T}{\partial y}\right)+\frac{\partial}{\partial z}\left(k\frac{\partial T}{\partial z}\right)+\dot{q}=\rho c\frac{\partial T}{\partial t} \qquad \text{(B.1)}$$

where T(x,y,z) is the temperature field in the solid region V, t is the time, ρ is the density of the material constituting V, c is the specific heat, k is the thermal conductivity and $\dot{q}$ is the volumetric heat source. A specific solution of eq. (B.1) can be obtained defining both initial and boundary conditions. The surface to surface radiative fluxes q_{enc} constitute the boundary conditions for the surfaces of the enclosure S_{enc} (as shown in fig. B.2).

Assuming that the N surfaces involved in the radiative heat transfer are gray and diffuse and that each one is characterized by a uniform value both for the temperature and the net radiative heat flux, the radiative problem can be expressed as [175]:

$$\sum_{i=1}^{N}\left[\frac{\delta_{i,j}}{\varepsilon_i} - F_{j-i}\left(\frac{1-\varepsilon_i}{\varepsilon_i}\right)\right]\cdot q_{enc,i} = \sum_{i=1}^{N}\left(\delta_{i,j} - F_{j-i}\right)\cdot\sigma\cdot T_i^4 \qquad \text{(B.2)}$$

where δ_{ji} is the Kronecker delta (δ_{ji}=1 if i=j, δ_{ji}=0 otherwise), ε_i is the hemispherical total emissivity of surface i, F_{j-i} is the radiation view factor, $q_{enc,\,i}$ is the net rate of radiative energy loss per unit area (net flux) of surface i, σ is the Stefan-Boltzmann constant ($5.67\cdot10^{-8}$ W/m^{2}K^4) and T_i is the absolute temperature of surface i.

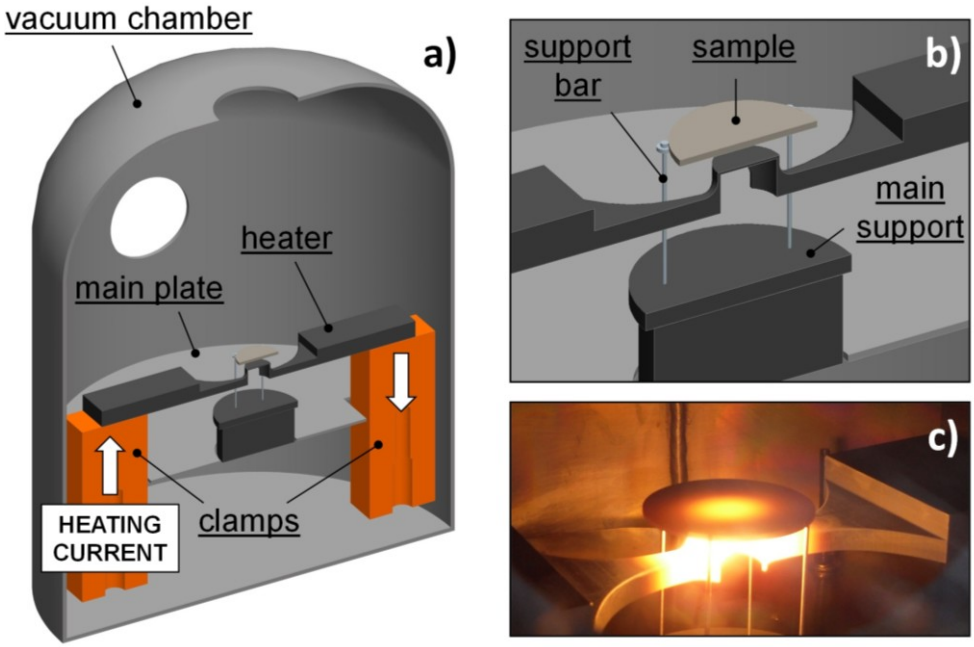

Fig. B.1 – The experimental apparatus used to estimate thermal conductivity: a) general CAD view, b) detailed CAD view of the sample area, c) picture of the sample area at high temperature.

Once obtained the temperatures T_i from the conductive problem solution, in particular the temperatures T_i on the surfaces forming the radiative enclosure S_{enc}, it is possible to construct a system of N explicit eqs. (B.2) delivering the net flux at each surface $q_{enc,\,i}$, which can be applied again to the conductive problem as a known boundary condition.

For the electrical problem, the field of current density **j**(x,y,z) depends on the gradient of the field of the electric potential V(x,y,z) according to Ohm's equation:

$$\mathbf{j} = -\frac{1}{\rho(T)}\nabla V \qquad \text{(B.3)}$$

where ρ(T) is the temperature-dependent electrical resistivity. In the hypothesis of steady-state conditions, the continuity equation for the field **j** is:

$$\nabla \mathbf{j} = 0 \tag{B.4}$$

According to the Joule effect, heat power dissipation in a unit volume of material, $\dot{q}$(x,y,z) in eq. (B.1), can be calculated by the scalar product:

$$\dot{q} = -\nabla V \cdot \mathbf{j} \tag{B.5}$$

Considering exclusively steady state phenomena, the material properties needed to describe the thermal behavior of the system represented in fig. B.1 are thermal conductivities and emissivities. Moreover, since a DC heating current passes through the graphite crucible and the copper clamps, also the electrical resistivity of these materials must be known. All the aforementioned material properties are available in literature or in the manufactory datasheets, with the exception of the sample's thermal conductivity.

In the temperature range investigable using the setup described in B.1, the temperature-dependent thermal conductivity of the sample material (the unknown quantity) is assumed to be linear and represented by the following expression:

$$k = C_0 + C_1 T \tag{B.6}$$

The unknown parameters involved in the inverse problem are two (C_0 and C_1), so the vector of the unknown coefficients can be written as follows:

$$\mathbf{f} = \{f_1, f_2\} = \{C_0, C_1\} \tag{B.7}$$

The inverse problem used by this method is managed in the ANSYS® environment together with the direct problem. The goal of the optimization problem is the consistency between measured and computed temperatures. The quantification of such consistency is represented by the following residual function [172]:

$$\mathrm{J}(\mathbf{f}) = \sum_{i=1}^{N_{HC}} \left[T_{C\_COMP\_i}(\mathbf{f}) - T_{C\_MEAS\_i}\right]^2 + \left[T_{P\_COMP\_i}(\mathbf{f}) - T_{P\_MEAS\_i}\right]^2 \tag{B.8}$$

where N_{HC} is the number of current steps used to power the heater and so to heat the sample, $T_{C\_COMP\_i}$ and $T_{P\_COMP\_i}$ are the computed temperatures at the center and at the periphery of the sample disk, respectively, $T_{C\_MEAS\_i}$ and $T_{P\_MEAS\_i}$ are the correspondent measured values.

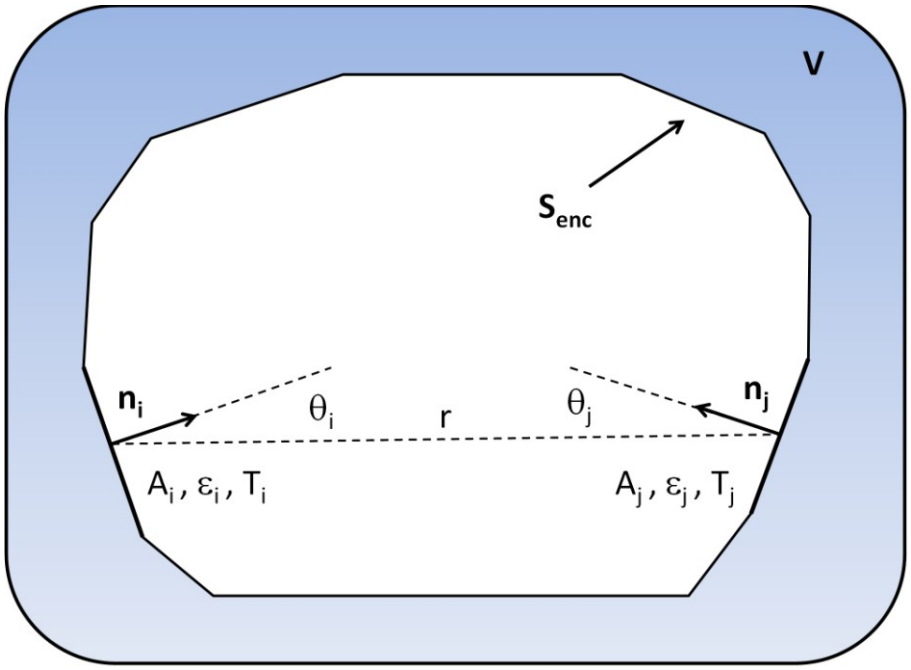

Fig. B.2 – A general coupled conduction/radiation problem.

The error in the k estimation is based on the standard deviation of C_0 and C_1, according to the expression [172, 176]:

$$\sigma_{f_m} = \sigma \sqrt{\left\{\left[\frac{\partial^2 J(\mathbf{f})}{\partial f_p \partial f_q}\right]^{-1}\right\}_{mm}} \qquad \text{for } m = 1,2 \tag{B.9}$$

where σ is the standard deviation of the temperature measurement, $f_1=C_0$ and $f_2=C_1$, as already reported in eq. (B.7). Considering a normal distribution for the measurement errors, confidence intervals at a defined confidence level can be defined. For example, the interval at 95% confidence level for the estimated parameters f_m can be obtained as:

$$f_m - 1.96\sigma_{f_m} < \overline{f_m} < f_m + 1.96\sigma_{f_m} \tag{B.10}$$

where $\overline{f_m}$ is the exact value of the parameter.

B.3. Thermal conductivity of graphite samples

To verify the validity of the numerical model both numerical and experimental tests have to be performed. In the first case, an inverse estimation using simulated numerical temperature data is necessary. In the latter, temperatures are measured on the top surface of the investigated sample, then they are compared to the correspondent numerical ones, which have been obtained

setting for the sample material properties the measured emissivity values and the thermal conductivity as a function of temperature reported in the datasheet of the supplier. Fig. B.3 show and example of the comparison between numerical and measured temperatures of a graphite sample; the temperatures were simulated and measured in the center and in the periphery of the sample, as in eq. (B.8).

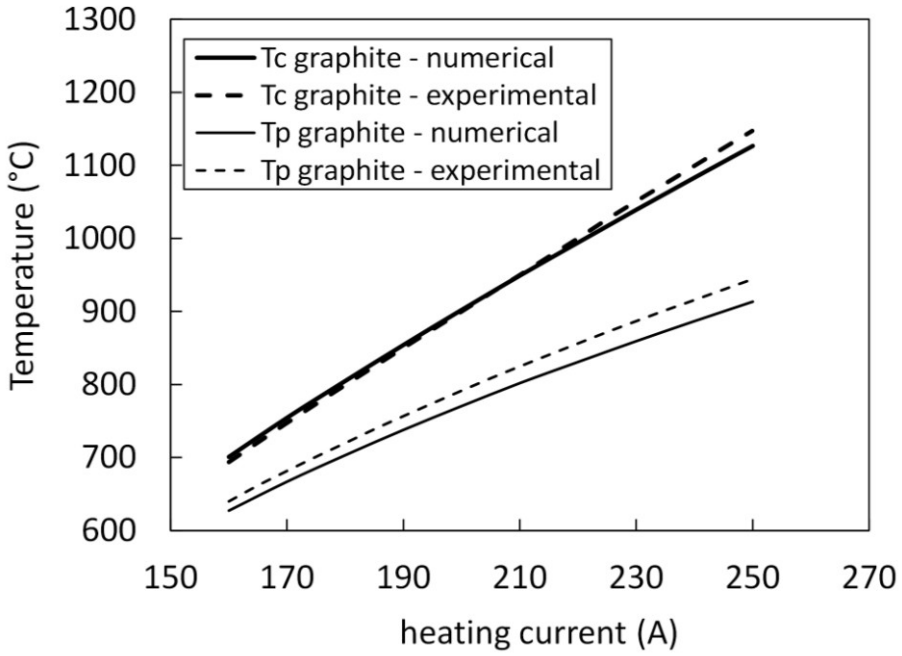

Fig. B.3 – Experimental verification of the numerical model: comparison between experimental and numerical temperatures on the top surface of a graphite sample disc.

Taking into account exclusively numerical data, figs. B.4 and B.5 show the sensitivity of a graphite sample temperature field to relevant variations of the thermal conductivity value. Imposing for the sample material a constant emissivity of 0.8 and considering eq. (B.6) for thermal conductivity, the sensitivity of the system in terms of temperatures (T_c and T_p) is investigated imposing different combinations of C_0 and C_1. Sample temperatures T_c and T_p present significant variations as a function of C_0 and C_1 values, so they can be considered proper thermal conductivity indicators.

Fig. B.6 shows the results of the thermal conductivity inverse estimation carried out on graphite samples, in which a good correspondence with the material data sheet can be found.

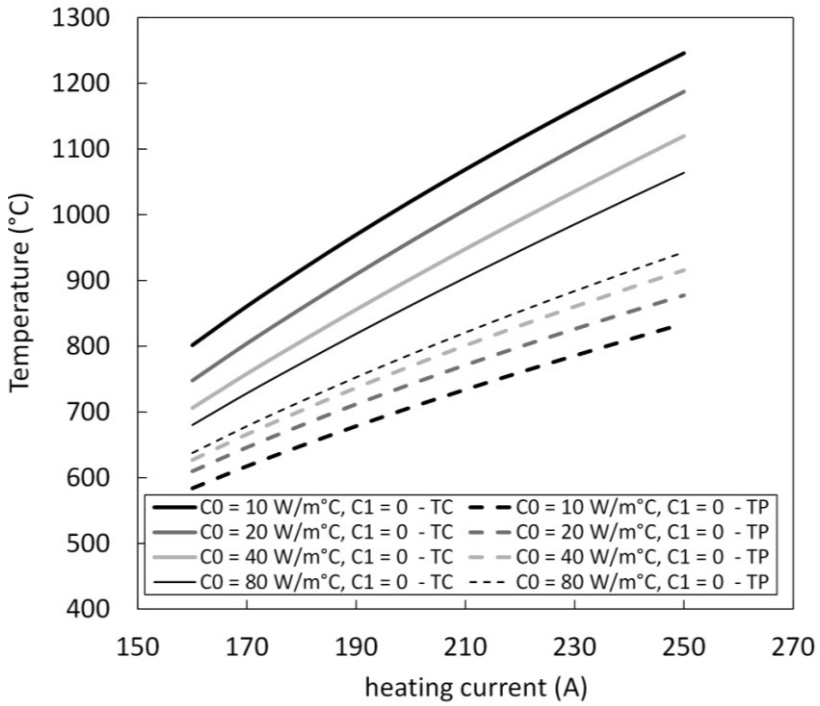

Fig. B.4 – Sensitivity of a graphite sample temperature field (T_c and T_p) to relevant variations of the thermal conductivity value (C_0 variations).

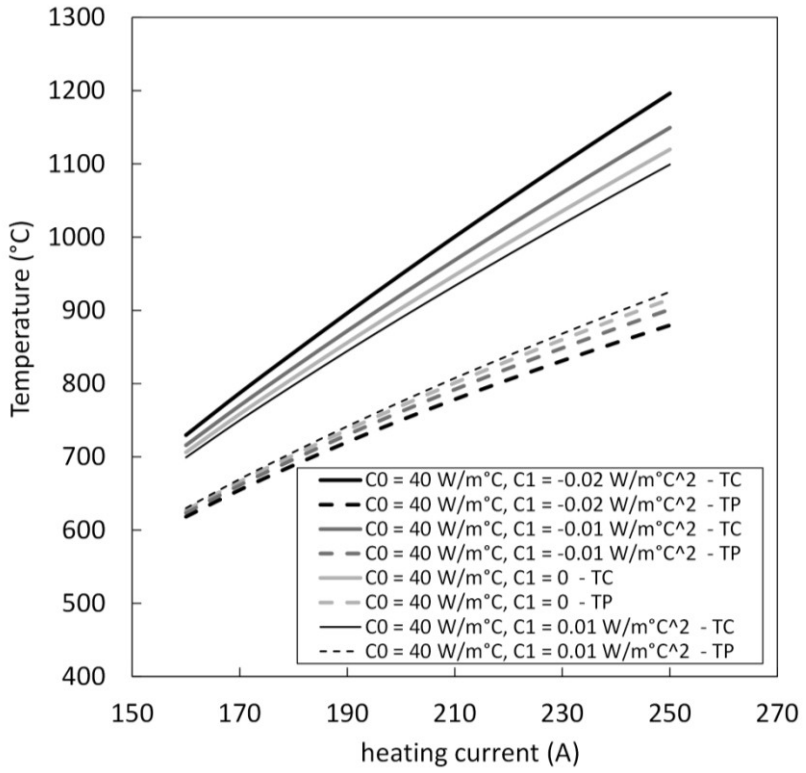

Fig. B.5 – Sensitivity of a graphite sample temperature field (T_c and T_p) to relevant variations of the thermal conductivity value (C_1 variations).

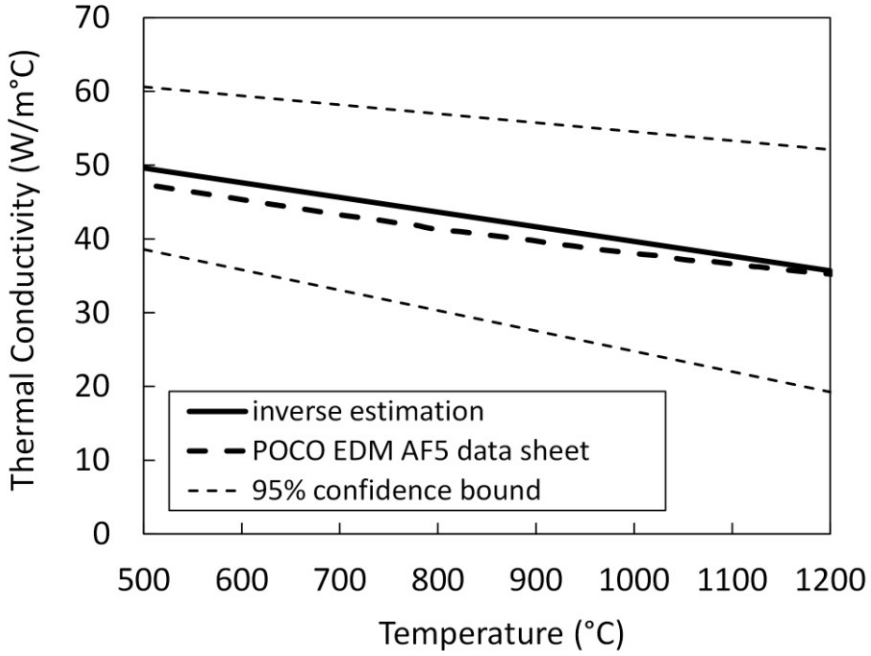

Fig. B.6 – Thermal conductivity of graphite POCO – EDM AF5 as a function of temperature. Comparison between the result of inverse estimation and the data sheet.

References

[1] G.R. Gilmore, *Practical Gamma-ray Spectrometry*, 2nd Edition (John Wiley & Sons., Chichester, West Sussex, UK, 2008).

[2] Eurisol Design Study, www.eurisol.org .

[3] G. Prete, A. Andrighetto, J. Esposito, P. Mastinu, J. Wyss, Physics Procedia **26** (2012) 274-283.

[4] B. Harss, R.C. Pardo, K.E. Rehm, F. Borasi, J.P. Greene, R.V.F. Janssens, C.L. Jiang, J. Nolen, M. Paul, J.P. Schiffer, R.E. Segel, J. Specht, T.F. Wang, P. Wilt, B. Zabransky, Review of Scientific Instruments **71** (2000) 380-387.

[5] M. Manzolaro, *Study, design and test of the Target - Ion Source system for the INFN SPES facility* (PhD Thesis, Università di Padova, Padova, Italy, 2011).

[6] U. Köster, The European Physical Journal A **15** (2002) 255-263.

[7] P. Van Duppen, *Isotope Separation On Line and Post Acceleration* in J. Al-Khalili and E. Roeckl (Eds.), *The Euroschool Lectures on Physics with Exotic Beams, Vol. II*, Lect. Notes Phys. 700 (Springer, Berlin Heidelberg, Germany, 2006).

[8] Y. Jonge, C.M. Lyneis, *Electron Cyclotron Resonance Ion Sources* in I.G. Brown, *The Physics and Technology of Ion Sources* (John Wiley & Sons, New York, USA, 1989).

[9] A. Andrighetto, L. Biasetto, M. Manzolaro, D. Scarpa, J. Montano, J. Stanescu, P. Benetti, I. Cristofolini, M.S. Carturan, P. Colombo, P. di Bernardo, M. Guerzoni, G. Meneghetti, B. Monelli, G. Prete, G. Puglierin, A. Tomaselli, P. Zanonato, Nuclear Physics A **834** (2010) 754c–757c.

[10] G. Meneghetti, M. Manzolaro, A. Andrighetto, Finite Elements in Analysis and Design **47** (2011) 559-570.

[11] M. Barbui, A. Andrighetto, C. Antonucci, S. Carturan, F. Cervellera, S. Cevolani, M. Cinausero, P. Colombo, A. Dainelli, P. Di Bernardo, F. Gramegna, G. Maggioni, G. Meneghetti,

C. Petrovich, L. Piga, G. Prete, V. Rizzi, M. Santana-Leitner, M. Tonezzer, P. Zanonato, D. Zafiropoulos, The European Physical Journal - Special Topics **150** (2007) 275-276.

[12] M. Barbui, A. Andrighetto, C. Antonucci, L. Biasetto, S. Carturan, F. Cervellera, S. Cevolani, M. Cinausero, P. Colombo, A. Dainelli, P. Di Bernardo, M. Giacchini, F. Gramegna, M. Lollo, G. Maggioni, M. Manzolaro, G. Meneghetti, C. Petrovich, L. Piga, G. Prete, M. Re, V. Rizzi, D.W. Stracener, M. Tonezzer, D. Zafiropoulos, P. Zanonato, Nuclear Instruments and Methods in Physics Research B **266** (2008) 4289-4293.

[13] R. Kirchner, Nuclear Instruments and Methods in Physics Research B **204** (2003) 179-190.

[14] R. Kirchner, E. Roeckl, Nuclear Instruments and Methods **33** (1976) 187-204.

[15] G.S. Hurst, M.G. Payne, *Principe and Applications of Resonance Ionization Spectroscopy* (Hilger, London, UK, 1988).

[16] D. Scarpa, J. Vasquez, A. Tomaselli, D. Grassi, L. Biasetto, A. Cavazza, S. Corradetti, M. Manzolaro, J. Montano, A. Andrighetto, G. Prete, Review of Scientific Instruments **83** (2012) 02B317-1–02B317-3.

[17] M. Huyse, The Why and How of Radioactive-Beam Research in J. Al-Khalili and E. Roeckl (Eds.), *The Euroschool Lectures on Physics with Exotic Beams, Vol. I*, Lect. Notes Phys. 651 (Springer, Berlin Heidelberg, Germany, 2004).

[18] I. Tanihata, H. Hamagaki, O. Hashimoto, Y. Shida, N. Yoshikawa, K. Sugimoto, O. Yamakawa, T. Kobayashi, N. Takahashi, Physical Review Letters **55** (1985) 2676-2679.

[19] K. Langanke, F.K. Thielemann, M. Wiescher, Nuclear Astrophysics and Nuclei Far From Stability in J. Al-Khalili and E. Roeckl (Eds.), *The Euroschool Lectures on Physics with Exotic Beams, Vol. I*, Lect. Notes Phys. 651 (Springer, Berlin Heidelberg, Germany, 2004).

[20] H. Hoffsass, Hyperfine Interactions **97-98** (1996) 247-283.

[21] T.H. Schindler, H.R. Schelbert, A. Quercioli, V. Dilsizian, The Journal of the American College of Cardiology **3** (2010) 623-640.

[22] J.R.J. Bennett, Nuclear Physics A **701** (2002) 296c-302c.

[23] L. Winsberg, Nuclear Instruments and Methods **95** (1971) 19-22.

[24] R. Kirchner, Nuclear Instruments and Methods in Physics Research B **70** (1992) 186-199.

[25] M. Portillo, J. Nolen. I. Gomes, V.N. Pantaleev, D.V. Fedorov, A.E. Barzakh, V.I. Beznosjuk, F.V. Moroz, S.Y. Orlov, Y.M. Volkov, Nuclear Instruments and Methods in Physics Research B 194 (2002) 193-206.

[26] L.C. Carraz, I.R. Haldorsen, H.L. Ravn, M. Skarestad, L. Westgaard, Nuclear Instruments and Methods **148** (1978) 217-230.

[27] L.C. Carraz, S. Sundell, H.L. Ravn, M. Skarestad, L. Westgaard, Nuclear Instruments and Methods **158** (1979) 69-80.

[28] D. Bhowmick, D. Naik, M. Eqbal, D. Sanyal, S. Deychoudhury, V. Banerjee, A. Bandyopadhyay, P. Deb, D. Bhattacharya, A. Chakrabarti, Nuclear Instruments and Methods in Physics Research A **539** (2005) 54-62.

[29] M. Santana Leitner, A Monte Carlo Code to Optimize the Production of Radioactive Ion Beams by the ISOL Technique (PhD. Thesis, Technical University of Catalonia, Barcelona, Spain, 2005).

[30] P. Bricault, M. Dombsky, P.W. Schmor, A. Dowling, Proceedings of the 2003 Particle Accelerator Conference **1** (2003) 439-443.

[31] M. Dombsky, P. Bricault, T. Hodges, A. Hurst, P.W. Schmor, Nuclear Physics A **701** (2002) 486c-490c.

[32] C. Benvenuti, *Molecular surface pumping: the getter pumps* in S. Turner (Ed.), Proceedings of the CERN Accelerator School 1999 (CERN, Geneva, Switzerland, 2009).

[33] Y. Zhang, G.D. Alton, Nuclear Instruments and Methods in Physics Research A **521** (2004) 72-107.

[34] G.D. Alton, J.C. Bilheux, A.D. McMillan, Nuclear Instruments and Methods in Physics Research A **521** (2004) 108-125.

[35] D.W. Stracener, G.D. Alton, R.L. Auble, J.R. Beene, P.E. Mueller, J.C. Bilheux, Nuclear Instruments and Methods in Physics Research A **521** (2004) 126-135.

[36] H.L. Ravn, T. Bjornstad, P. Hoff, O.C. Jonsson, E. Kugler, S. Sundell, B. Vosicki and the ISOLDE Collaboration, Nuclear Instruments and Methods in Physics Research B **26** (1987) 183-189.

[37] J.R.J. Bennett, C.J. Densham, P.V. Drumm, W.R. Evans, M. Holding, G.R. Murdoch, V. Pantaleev, Nuclear Instruments and Methods in Physics Research B **126** (1997) 117-120.

[38] B. Mustapha, J.A. Nolen, Nuclear Instruments and Methods in Physics Research B **204** (2003) 286-292.

[39] A. Andrighetto, C.M. Antonucci, S. Cevolani, C. Petrovich, M. Santana Leitner, The European Physical Journal A **30** (2006) 591-601.

[40] W.H. Kohl, *Handbook of materials and techniques for vacuum devices* (American Institute of Physics, New York, USA, 1995).

[41] L. Biasetto, M. Manzolaro, A. Andrighetto, The European Physical Journal A **38** (2008) 167-171.

[42] F.A. Cotton, G. Wilkinson, *Advanced Inorganic Chemistry, 3rd edition* (Interscience, New York, USA, 1972).

[43] H.O. Pierson, *Handbook of refractory carbides and nitrides* (Noyes Publications, Westwood, NJ, USA, 1996).

[44] E.K. Storms, *The refractory carbides* (Academic Press, New York, USA, 1967).

[45] V. Raman, O.P. Bahl, U. Dhawan, Journal of Materials Science **30** (1995) 2686-2693.

[46] N.N. Greenwood, A. Earnshaw, *Chemistry of the Elements* (Pergamon Press, Oxford, UK, 1984).

[47] W. Lengauer, *Transition Metal Carbides, Nitrides and Carbonitrides* in R.Riedel (Ed.), *Handbook of Ceramic Hard Materials, Vol. 1* (Wiley, Weinheim, Germany, 2000).

[48] G.A. Rama Rao, V. Venugopal, Journal of Alloys and Compounds **206** (1994) 237-242.

[49] R.E. Rundle, N.C. Baenziger, A.S. Wilson, R.A. McDonald, Journal of the American Chemical Society **70** (1948) 99-105.

[50] L.M. Litz, A.B. Garrett, F.C. Croxton, Journal of the American Chemical Society **70** (1948) 1718-1722.

[51] D. Manara, F. De Bruycker, K. Boboridis, O. Tougait, R. Eloirdi, M. Malki, Journal of Nuclear Materials **426** (2012) 126-138.

[52] H. Shi, P. Zhang, S. Li, B. Sun, B. Wang, Physics Letters A **373** (2009) 3577-3581.

[53] R. Ducher, R. Dubourg, M. Barrachin, Physical Review B **83** (2011) 104107-1 – 104107-12.

[54] H. Shi, P. Zhang, S. Li, B. Wang, B. Sun, Journal of Nuclear Materials 396 (2010) 218-222.

[55] R. Benz, C.G. Hoffman, G.N. Rupert, High Temperature Science **1** (1969) 342-359.

[56] H. Tagawa, Bulletin of the Chemical Society of Japan **45** (1972) 1069-1072.

[57] D.L. Perry, *Handbook of Inorganic Compounds, 2nd ed.* (CRC Press, Taylor & Francis Group, Boca Raton, FL, USA, 2011).

[58] R.B. Holden, *Ceramic fuel elements, an AEC monograph* (Gordon and Breach Science Publishers, New York, USA, 1966).

[59] M.T. Simnad, *Preparation of Nuclear Ceramic Materials* in J.J. Zuckerman, J.D. Atwood (Eds.) *Inorganic Reactions and Methods: Formation of Ceramics, Volume 18* (John Wiley & Sons, Hoboken, NJ, USA, 1999).

[60] L. Biasetto, P. Zanonato, S. Carturan, P. Di Bernardo, P. Colombo, A. Andrighetto, G. Prete, Journal of Nuclear Materials 404 (2010) 68-76.

[61] R. De Coninck, W. Van Lierde, A. Gijs, Journal of Nuclear Materials **57** (1975) 69-76.

[62] R. De Coninck, R. De Batist, A. Gijs, High Temperatures – High Pressures **8** (1976) 167-176.

[63] R. De Coninck, W. Van Lierde, A. Gijs, Journal of Nuclear Materials **46** (1973) 213-216.

[64] R. Cowan, Journal of Applied Physics 32 (1961) 1363-1369.

[65] J.P. Greene, T. Burtseva, J. Neubauer, J.A. Nolen, A.C.C. Villari, I.C. Gomes, Nuclear Instruments and Methods in Physics Research B **241** (2005) 986-990.

[66] A.L. Bowman, G.P. Arnold, W.G. Witteman, T.C. Wallace, Journal of Nuclear Materials **19** (1966) 111-112.

[67] R. Mendez-Peñalosa, R.E. Taylor, Journal of the American Ceramic Society **47** (1964) 101-102.

[68] R. Mendez-Peñalosa, R.E. Taylor, Journal of the American Ceramic Society **47** (1964) 416-417.

[69] J.L. Henry, R. Blickensderfer, D. Paulson, J.L. Bates, Journal of the American Ceramic Society **53** (1970) 335-339.

[70] K. Maruya, Journal of Nuclear Science and Technology **7** (1970) 13-18.

[71] J.M. Leitnaker, T.G. Godfrey, Journal of Chemical and Engineering Data **11** (1966) 392-394.

[72] L.A. Hanson, Journal of Nuclear Materials **19** (1966) 15-28.

[73] R.M. Dell, V.J. Wheeler, Journal of Nuclear Materials **21** (1967) 328-336.

[74] S. Venter, W.E. Stumpf, Journal of Nuclear Materials **59** (1976) 221-228.

[75] M.J. Bradley, L.J. Ferris, Inorganic Chemistry **1** (1962) 683-687.

[76] M.J. Bradley, L.J. Ferris, Inorganic Chemistry **3** (1964) 189-195.

[77] M.J. Bradley, L.J. Ferris, Inorganic Chemistry **3** (1964) 730-734.

[78] F.H. Pollard, G. Nickless, S. Evered, Journal of Chromatography A **15** (1964) 223-227.

[79] R. Klapisch, J. Chaumont, C. Philippe, I. Amarel, R. Fergeau, M. Salome, R. Bernas, Nuclear Instruments and Methods **53** (1967) 216-228.

[80] S. Borg, I. Bergstrom, G.B. Holm, B. Rydberg, L.E. De Geer, G. Rudstam, B. Grapengiesser, E. Lund, L. Westgaard, Nuclear Instruments and Methods **91** (1971) 109-116.

[81] B. Hy, N. Barré-Boscher, A. Ozgumus, B. Roussiere, S. Tusseau-Nenez, C. Lau, M. Cheikh Mhamed, M. Raynaud, A. Said, K. Kolos, E. Cottereau, S. Essabaa, O. Tougait, M. Pasturel, Nuclear Instruments and Methods in Physics Research B **288** (2012) 34-41.

[82] A. Kronenberg, E.H. Spejewski, B. Mervin, C. Jost, H.K. Carter, D.W. Stracener, J.P. Greene, J.A. Nolen, W.L. Talbert, Nuclear Instruments and Methods in Physics Research B **266** (2008) 4267-4270.

[83] D.W. Stracener, Nuclear Instruments and Methods in Physics Research B **204** (2003) 42-47.

[84] S. Corradetti, L. Biasetto, M. Manzolaro, D. Scarpa, S. Carturan, A. Andrighetto, G. Prete, J. Vasquez, P. Zanonato, P. Colombo, C.U. Jost, D.W. Stracener, unpublished data.

[85] S. Carturan, M. Tonezzer, L. Piga, P. Zanonato, P. Colombo, A. Andrighetto, L. Biasetto, P. Di Bernardo, G. Maggioni, F. Gramegna, G. Prete, Nuclear Instruments and Methods in Physics Research A **583** (2007) 256-263.

[86] L. Biasetto, P. Zanonato, S. Carturan, P. Di Bernardo, P. Colombo, A. Andrighetto, G. Prete, Journal of Nuclear Materials **378** (2008) 180-187.

[87] L. Biasetto, S. Carturan, G. Maggioni, P. Zanonato, P. Di Bernardo, P. Colombo, A. Andrighetto, G. Prete, Journal of Nuclear Materials **385** (2009) 582-590.

[88] B.A. Tatum, Nuclear Instruments and Methods in Physics Research B **241** (2005) 926-930.

[89] M.J. Meigs, D.L. Haynes, C.M. Jones, R.C. Juras, Nuclear Instruments and Methods in Physics Research A **382** (1996) 51-56.

[90] H.K. Carter, J. Kormicki, D.W. Stracener, J.B. Breitenbach, J.C. Blackmon, M.S. Smith, D.W. Bardayan, Nuclear Instruments and Methods in Physics Research B **126** (1997) 166-169.

[91] R. Kirchner, K. Burkard, W. Huller, O. Klepper, Nuclear Instruments and Methods in Physics Research B **70** (1992) 56-61.

[92] D. Scarpa, L. Biasetto, S. Corradetti, M. Manzolaro, A. Andrighetto, S. Carturan, G. Prete, P. Zanonato, D.W. Stracener, The European Physical Journal A **47** (2011) 32-38.

[93] E.H. Spejewski, H.K. Carter, B. Mervin, E. Prettyman, A. Kronenberg, D.W. Stracener, Nuclear Instruments and Methods in Physics Research B **266** (2008) 4271-4274.

[94] S. Corradetti, L. Biasetto, M. Manzolaro, D. Scarpa, A. Andrighetto, S. Carturan, G. Prete, P. Zanonato, D.W. Stracener, The European Physical Journal A **47** (2011) 119-126.

[95] A. Andrighetto, S. Cevolani, C. Petrovich, The European Physical Journal A **25** (2005) 41-47.

[96] G.D. Alton, Nuclear Instruments and Methods in Physics Research A **382** (1996) 207-224.

[97] K. Tsukada, unpublished calculations based on Y.L. Zhao, *Comparison study of mass division phenomena in ^{7}Li-induced ^{232}Th and p-induced ^{238}U-fission systems* (PhD Thesis, Tokyo Metropolitan University, Tokyo, Japan, 1999), communicated by D.W. Stracener.

[98] A.E. Barzakh, V.I. Besnosjuck, I.Y. Chubukov, V.P. Denisov, D.V. Fedorov, V.V. Lukashevich, M.D. Seliverstov, Y.Y. Sergeev, V.I. Tikhonov, Y.M. Volkov, V.M. Zhelesnjakov, Nuclear Instruments and Methods in Physics Research B **126** (1997) 150-153.

[99] Z. Jia, Z. Wang, C. Xu, J. Liang, B. Wei, D. Wu, S. Zhu, Materials Science and Engineering A **271** (1999) 395-400.

[100] Y. Liu, L. Gao, Carbon **43** (2005) 47-52.

[101] Z. Xia, L. Riester, W.A. Curtin, H. Li, B.W. Sheldon, J. Liang, B. Chang, J.M. Xu, Acta Materialia **52** (2004) 931-944.

[102] Y. Morisada, Y. Miyamoto, Materials Science and Engineering A **381** (2004) 57-61.

[103] G. Prete, A. Andrighetto, G. Bassato, L. Biasetto, L. Calabretta, S. Carturan, A. Cavazza, M. Comunian, S. Corradetti, L. Costa, A. Galatà, M. Giacchini, F. Gramegna, A. Lombardi, M. Lollo, J. Montano, M. Maggiore, M. Manzolaro, L. Piazza, M. Poggi, L. Sarchiapone, D. Scarpa, J. Vasquez, D. Zafiropoulos, *The SPES project: an ISOL facility for Nuclear Physics and an Applied Physics research center*, poster presented at the Advances in Radioactive Isotope Science (ARIS) 2011 Conference in Leuven, Belgium.

[104] U.C. Bergmann, L. Axelsson, J.R.J. Bennett, M.J.G. Borge, R. Catherall, P.V. Drumm, V.N. Fedoseyev, C. Forssén, ,L.M. Fraile, H.O.U. Fynbo, U. Georg, T. Giles, S. Grévy, P. Hornshøj, B. Jonson, O.C. Jonsson, U. Köster, J. Lettry, K. Markenroth, F.M. Marqués, V.I. Mishin, I. Mukha, T. Nilsson, G. Nyman, A. Oberstedt, H.L. Ravn, K. Riisager, G. Schrieder, V. Sebastian, H. Simon, O. Tengblad, F. Wenander, K. Wilhelmsen Rolander, Nuclear Physics A **701** (2002) 363c–368c.

[105] H.L. Ravn, R. Catherall, J. Barker, P. Drumm, A.H.M. Evensen, E. Hageba, P. Hoff, O.C. Jonsson, E. Kugler, J. Lettry, K. Steffensen, 0. Tengblad and the ISOLDE Collaboration, Nuclear Instruments and Methods in Physics Research B **126** (1997) 176-181.

[106] U. Köster, R. Catherall, V.N. Fedoseyev, S. Franchoo, U. Georg, M. Huyse, K. Kruglov, J. Lettry, V.I. Mishin, M. Oinonen, H. Ravn, M.D. Seliverstov, H. Simon, P. Van Duppen, J. Van Roosbroeck, L. Weissman, Hyperfine Interactions **127** (2000) 417-420.

[107] U. Köster, U.C. Bergmann, D. Carminati, R. Catherall, J. Cederkäll, J.G. Correia, B. Crepieux, M. Dietrich, K. Elder, V.N. Fedoseyev, L. Fraile, S. Franchoo, H. Fynbo, U. Georg, T. Giles, A. Joinet, O.C. Jonsson, R. Kirchner, C. Lau, J. Lettry, H.J. Maier, V.I. Mishin, M. Oinonen, K. Peräjärvi, H.L. Ravn, T. Rinaldi, M. Santana-Leitner, U. Wahl, L. Weissman, ISOLDE Collaboration, Nuclear Instruments and Methods in Physics Research B **204** (2003) 303-313.

[108] H.-J. Kluge (ed.), *ISOLDE Users' Guide* (CERN, Geneva, Switzerland, 1986)

[109] M. Lindroos, C. Broude, G. Goldring, H. Haas, M. Hass, P. Richards, L. Weissman, Nuclear Instruments and Methods in Physics Research A **361** (1995) 53-59.

[110] U. Köster, V.N. Fedoseyev, A.N. Andreyev, U.C. Bergmann, R. Catherall, J. Cederkäll, M. Dietrich, H. De Witte, D.V. Fedorov, L. Fraile, S. Franchoo, H. Fynbo, U. Georg, T. Giles, M. Gorska, M. Hannawald, M. Huyse, A. Joinet, O.C. Jonsson, K.L. Kratz, K. Kruglov, C. Lau, J. Lettry, V.I. Mishin, M. Oinonen, K. Partes, K. Peräjärvi, B. Pfeiffer, H.L. Ravn, M.D. Seliverstov, P. Thirolf, K. Van de Vel, P. Van Duppen, J. Van Roosbroeck, L. Weissman, IS365, IS387, IS393 and ISOLDE Collaborations, Nuclear Instruments and Methods in Physics Research B **204** (2003) 347-352.

[111] M. Oinonen, Y. Jading, U. Köster, J. Lettry, H. Ravn, J. Äystö, P. Dendooven, J. Huikari, A. Jokinen, P.O. Lipas, A. Nieminen, K. Peräjärvi, T. Siiskonen, P. Baumann, A. Huck, A. Knipper, M. Ramdhane, G. Walter, F. Didierjean, V.N. Fedoseyev, V.I. Mishin, M. Koizumi, W. Liu, E. Roeckl,V. Sebastian, Hyperfine Interactions **127** (2000) 431-436.

[112] F. Gramegna, data presented at the SPES 2010 International Workshop in Legnaro, Padova, Italy.

[113] S. Corradetti, S. Carturan, L. Biasetto, A. Andrighetto, P. Colombo, Journal of Nuclear Materials 432 (2013) 212-221.

[114] U. Köster, M. Argentini, R. Catherall, V.N. Fedoseyev, H.W. Gäggeler, O.C. Jonsson, R. Weinreich, ISOLDE Collaboration, Nuclear Instruments and Methods in Physics Research B **204** (2003) 343-346.

[115] E.G. Adelberger, S.M. Austin, J.N. Bahcall, A.B. Balantekin, G. Bogaert, L.S. Brown, L. Buchmann, F.E. Cecil, A.E. Champagne, L. de Braeckeleer, C.A. Duba, S.R. Elliott, S.J. Freedman, M. Gai, G. Goldring, C.R. Gould, A. Gruzinov, W.C. Haxton, K.M. Heeger, E. Henley, C.W. Johnson, M. Kamionkowski, R.W. Kavanagh, S.E. Koonin, K. Kubodera, K. Langanke, T. Motobayashi, V. Pandharipande, P. Parker, R.G.H. Robertson, C. Rolfs, R.F. Sawyer, N. Shaviv, T.D. Shoppa, K.A. Snover, E. Swanson, R.E. Tribble, S. Turck-Chieze, J.F. Wilkerson, Reviews of Modern Physics **70** (1998) 1265-1291.

[116] P. Fehsenfeld, C. Eifrig, R. Kubat, Nuclear Physics A **701** (2002) 235c-239c.

[117] M. Hoffmann, K. Abbas, T. Sauvage, G. Blondiaux, L. Vincent, M.F. Stroosnijder, Nuclear Instruments and Methods in Physics Research B **183** (2001) 419-424.

[118] M. Menna, Nuclear Instruments and Methods in Physics Research B **184** (2001) 466-468.

[119] L Gialanella, U. Greife, N. De Cesare, A. D'Onofrio, M. Romano, L. Campajola, A. Formicola, Z. Fulop, G. Gyurky, G. Imbriani, C. Lubritto, A. Ordine, V. Roca, D. Rogalla, C. Rolfs, M. Russo, C. Sabbarese, E. Somorjai, F. Strieder, F. Terrasi, H.P. Trautvetter, Nuclear Instruments and Methods in Physics Research B **197** (2002) 150-154.

[120] J.M. Sisterson, K. Kim, A. Beverding, P.A.J. Englert, M. Caffee, A.J.T. Jull, D.J. Donahue, L. McHargue, C. Castaneda, J. Vincent, R.C. Reedy, Nuclear Instruments and Methods in Physics Research B **123** (1997) 324-329.

[121] M.G. Giammarchi, M. Laubenstein, J.P. Meulders, L. Miramonti, A. Formicola, Radiation Measurements **43** (2008) 1390-1395.

[122] T. Inoue, S. Tanaka, Journal of Inorganic Nuclear Chemistry **38** (1976) 1425-1427.

[123] F. Thevenot, Journal of the European Ceramic Society **6** (1990) 205-225.

[124] A.K. Suri, C. Subramanian, J.K. Sonber, T.S.R.C. Murthy, International Materials Reviews **55** (2010) 4-40.

[125] D. Gosset, M. Colin, Journal of Nuclear Materials **183** (1991) 161-173.

[126] N. Froumin, N. Frage, M. Aizenshtein, M.P. Dariel, Journal of the European Ceramic Society **23** (2003) 2821-2828.

[127] M.T. Spohn, American Ceramic Society Bulletin **72** (1993) 88-89.

[128] G. Goller, C. Toy, A. Tekin, C.K. Gupta, High Temperature Materials and Processes **15** (1996) 117–122.

[129] A. Sinha, T. Mahata, B.P. Sharma, Journal of Nuclear Materials **301** (2002) 165-169.

[130] A.M. Hadian, J.A. Bigdeloo, Journal of Materials Engineering and Performance **17** (2008) 44-49.

[131] A.K. Khanra, Bulletin of Materials Science **30** (2007) 93-96.

[132] I. Hasegawa, Y. Fujii, T. Takayama, K. Yamada, Journal of Materials Science Letters **18** (1999) 1629-1631.

[133] S. Mondal, A.K. Banthia, Journal of the European Ceramic Society **25** (2005) 287-291.

[134] I. Yanase, R. Ogawara, H. Kobayashi, Materials Letters **63** (2009) 91-93.

[135] T. Matsui, Y. Arita, K. Naito, H. Imai, Journal of Nuclear Materials **186** (1991) 7-12.

[136] C. Wood, D. Emin, P.E. Gray, Physical Review B **31** (1985) 6811-6814.

[137] G.S. Karumidze, L.A. Shengelia, Diamond and Related Materials **3** (1994) 14-16.

[138] Y. Nishi, Y. Arita, T. Matsui, T. Nagasaki, Journal of Nuclear Science and Technology **39** (2002) 391-394.

[139] K.E. Gilchrist, S.D. Preston, High Temperatures - High Pressures **11** (1979) 643-651.

[140] G.V. Tsagareishvili, T.G. Nakashidze, J.S. Jobava, G.P. Lomidze, D.E. Khulelidze, D.S. Tsagareishvili, O.A. Tsagareishvili, Journal of the Less Common Metals **117** (1986) 159-161.

[141] G.W. Hollenberg, American Ceramic Society Bulletin **59** (1980) 538-541.

[142] B.Z. Dacic, V. Jokanovic, B. Jokanovic, M.D. Dramicanin, Journal of Alloys and Compdounds **413** (2006) 198-205.

[143] R.C. Weast (Ed.), *CRC Handbook of Chemistry and Physics, 70th ed., 1989-1990* (CRC Press, Boca Raton, FL, USA, 1990).

[144] A. Alizadeh, E. Taheri-Nassaj, N. Ehsani, Journal of the European Ceramic Society **24** (2004) 3227-3234.

[145] Y.Q. Li, T. Qiu, Materials Science and Engineering A **444** (2007) 184-191.

[146] K.S.W. Sing, D.H. Everett, R. Haul, L. Moscou, R.A. Pierotti, J. Rouquerol, T. Siemieniewska, Pure and Applied Chemistry **54** (1982) 2201-2218.

[147] S. Brunauer, P.H. Emmett, E. Teller, Journal of the American Chemical Society **60** (1938) 309-319.

[148] E.P. Barrett, L.G. Joyner, P.P. Halenda, Journal of the American Chemical Society **53** (1951) 373-380.

[149] T.K. Roy, C. Subramanian, A.K. Suri, Ceramics International **32** (2006) 227-233.

[150] D.R. Beaman, L. F. Solosky, Analytical Chemistry **44** (1972) 1598–1610.

[151] K. S. W. Sing, D.H. Everett, R.A.W. Haul, L. Moscou, R.A. Pierotti, J. Rouquerol, T. Siemieniewska, Pure and Applied Chemistry **57** (1985) 603-619.

[152] K. Kaneko, Journal of Membrane Science **96** (1994) 59-89.

[153] M. Kruk, M. Jaroniec, Chemistry of Materials **13** (2001) 3169-3183.

[154] F.H. Spedding, K.A. Gschneidner Jr., A.H. Daane, Journal of the American Chemical Society **80** (1958) 4499-4503.

[155] F.H. Spedding, A.H. Daane, K.A. Gschneidner Jr., Transactions of the Metallurgical Society AIME **215** (1959) 192-199.

[156] N.N. Greenwood, A.J. Osborn, Journal of the Chemical Society (1965) 1775-1782.

[157] K.A. Gschneidner, F.W. Calderwood, Bulletin of Alloy Phase Diagrams **7** (1986) 421-436.

[158] A.L. Bowman, N.H. Krikorian, G.P. Arnold, T.C. Wallace, N.G. Nereson, Acta Crystallographica B **24** (1968) 459-460.

[159] L. Qiting, N. Jiansen, W. Yiqing, D. Yanan, D. Weizhong, G. Shuhua, Journal of Rare Earths **29** (2011) 416-419.

[160] P. Colombo, E. Bernardo, L. Biasetto, Journal of the American Ceramic Society **87** (2004) 152-154.

[161] C. Vakifahmetoglu, I. Menapace, A. Hirsch, L. Biasetto, R. Hauser, R. Riedel, P. Colombo, Ceramics International **35** (2009) 3281-3290.

[162] M.D.M. Innocentini, P. Sepulveda, F. Ortega, *Permeability* in M. Scheffler, P. Colombo (Eds.), *Cellular Ceramics: Structure, Manufacturing, Properties and Applications* (Wiley-VCH, Weinheim, Germany, 2005).

[163] M.D.M. Innocentini, A.R.F. Pardo, V.C. Pandolfelli, Journal of the American Ceramic Society **83** (2000) 1536-1538.

[164] S. Barg, M.D.M. Innocentini, R.V. Meloni, W.S. Chacon, H. Wang, D. Koch, G. Grathwohl, Journal of Membrane Science **383** (2011) 35-43.

[165] L. Biasetto, M.D.M. Innocentini, W.S. Chacon, S. Corradetti, S. Carturan, P. Colombo, A. Andrighetto, unpublished data.

[166] G. Horvath, H. Kawatzoe, Journal of Chemical Engineering of Japan **16** (1983) 470-475.

[167] A. Saito, H.C. Foley, American Institute of Chemical Engineers Journal **37** (1991) 429-436.

[168] J.B. Yang, L.C. Ling, L. Liu, F.Y. Kang, Z.H. Huang, H. Wu, Carbon **40** (2002) 911-916.

[169] M.D.M. Innocentini, A.R.F. Pardo, B.A. Menegazzo, L.R.M. Bittencourt, R.P. Rettore, V.C. Pandolfelli, Journal of the American Ceramic Society **85** (2002) 1517-1521.

[170] W.J. Parker, R.J. Jenkins, C.P. Butler, G.L. Abbott, Journal of Applied Physics **32** (1961) 1679-1684.

[171] M. Manzolaro, S. Corradetti, A. Andrighetto, L. Ferrari, unpublished data.

[172] S.K. Kim, B.S. Jung, H.J. Kim, W.I. Lee, Experimental Thermal and Fluid Science **27** (2003) 697-704.

[173] R.E. Hogan, D.K. Gartling, Communications in Numerical Methods in Engineering **24** (2008) 523-542.

[174] F.P. Incropera, D.P. Dewitt, T.L. Bergman, A.S. Lavine, *Fundamentals of Heat and Mass Transfer, 6th ed.* (Wiley, New York, USA, 2007).

[175] R. Siegel, J.R. Howell, *Thermal Radiation Heat Transfer, 4th ed.* (Taylor and Francis, New York, USA, 2002).

[176] M.N.Ozisik, H.R.B. Orlande, *Inverse Heat Transfer: fundamentals and applications* (Taylor & Francis, New York, USA, 2000).